

(2)

SRL 13-F-1992

AD-A256 779



FERRITE RESEARCH AIMED AT IMPROVING INDUCTION  
LINAC DRIVEN FEL PERFORMANCE

Principal Investigator:

Dr. Daniel Birx

SCIENCE RESEARCH LABORATORY, INC.

15 Ward Street  
Somerville, MA 02143

15 October 1992

DTIC  
SELECTED  
OCT 20 1992  
S P D

PHASE II FINAL REPORT

Period for September 15, 1990 to September 30, 1992

Contract Number N00014-90-C-0165

APPROVED FOR PUBLIC RELEASE; DISTRIBUTION UNLIMITED

"Original contains color.  
Plates: All DTIC reproductions  
will be in black and white."

Prepared for

OFFICE OF NAVAL RESEARCH  
800 North Quincy Street  
Arlington, VA 22217-5000

"The views and conclusions contained in this document are those of the authors and should not be interpreted as representing the official policies, either expressed or implied, of the Strategic Defense Initiative Organization or the U.S. Government."

92 1000000000

47557

92-27413



299P8

# **DISCLAIMER NOTICE**



**THIS DOCUMENT IS BEST  
QUALITY AVAILABLE. THE COPY  
FURNISHED TO DTIC CONTAINED  
A SIGNIFICANT NUMBER OF  
COLOR PAGES WHICH DO NOT  
REPRODUCE LEGIBLY ON BLACK  
AND WHITE MICROFICHE.**

## TABLE OF CONTENTS

<u>Section</u>		<u>Page</u>
	EXECUTIVE SUMMARY	1
1	THE SNOMAD-V HIGH GRADIENT ACCELERATOR MODULE	1-1
2	THE SNOMAD-IV 0.5 MeV INJECTOR	2-1
3	SNOMAD-IVB, 1.0 MeV INDUCTION ACCELERATOR MODULE	3-1
4	THE DoE/MIT ECH AND NASA/SELENE PROGRAMS	4-1
	4.1 The MIT ECH Development Program	4-1
	4.2 The NASA SELENE Program	4-3
5	THE DARPA "RED WATER" PROGRAM	5-1
	5.1 Preliminary Comparative Economic Analysis – Capital Costs	5-8
	5.2 Operating Costs	5-10
6	THE ELECTRON BEAM MATERIALS PROCESSING PROGRAM	6-1
	6.1 Graded Alloy Turbine Disks	6-2
	6.2 Surface Heat Treatment	6-8
	6.3 Graded Superalloy Turbine Disk Fabrication	6-12
	6.4 Deep Surface Hardening Using a High Energy Electron Beam System	6-20
7	E-BEAM STERILIZATION EXPERIMENTS USING SNOMAD-IV	7-1
8	TREATMENT OF WASTEWATER AND THE REMOVAL OF SO <sub>X</sub> AND NO <sub>X</sub> FROM STACK GASES	8-1
	8.1 SO <sub>X</sub> and NO <sub>X</sub> Removal from Stack Gases	8-5
	8.2 Brief Review of Electron Beam SO <sub>2</sub> /NO <sub>X</sub>	8-6
9	SOLID STATE ULTRA-WIDEBAND SOURCES	9-1
	9.1 Introduction	9-1
	9.2 SLS-I	9-4
	9.3 Summary of SLS-I Operating Parameters	9-13
	9.4 SLS-II	9-19
	APPENDIX 1: INTRODUCTION TO ELECTROMAGNETIC SHOCK LINES	
	APPENDIX 2: NONLINEAR MAGNETIC MATERIAL SELECTION	
	APPENDIX 3: SCR SELECTION	

## TABLE OF CONTENTS CONTINUED

### Section

- APPENDIX 4: CAPACITOR SELECTION
- APPENDIX 5: TRANSFORMER DESIGN
- APPENDIX 6: NONLINEAR MAGNETIC COMPRESSORS
- APPENDIX 7: COMMAND RESONANT CHARGE SYSTEMS
- APPENDIX 8: THE SNOMAD SCR TRIGGER SYSTEM
- APPENDIX 9: INDUCTION CELL DESIGN
- APPENDIX 10: BEAM BREAK-UP INSTABILITY AND THE GAP FIELD

D-100

3

1

Accession For	
NTIS GSA&I	<input checked="" type="checkbox"/>
DTIC TAB	<input type="checkbox"/>
Unpublished	<input type="checkbox"/>
Justification	
By _____	
Distribution/	
Availability Codes	
Dist	Avail And/or Special
A-1	

## LIST OF ILLUSTRATIONS

<u>Figure</u>		<u>Page</u>
1	Saturation Time Versus $J/m^3$	6
2	Saturation Time Versus % Energy Lost/cm <sup>2</sup>	7
3	Saturation Time Versus H	8
1.1	SNOMAD-VB	1-2
1.2	SNOMAD-V Shock Line System Simplified Schematic	1-5
1.3	SNOMAD-V nonlinear magnetic pulse compressor	1-6
1.4	Field Waveforms @ 40 ft. for SNOMADS 5, 7, and 10 and Bornlea 3153	1-8
1.5	SNOMAD-V Nonlinear Magnetic Compressor and 1 MeV High Gradient Accelerator Section	1-11
1.6	SNOMAD-V, 10 Cell Induction Accelerator	1-12
1.7	SNOMAD-VB Accelerator Module Attached to SNOMAD-VB Driver	1-13
1.8	SNOMAD-VB with Cathode Stalk	1-14
2.1	SNOMAD-IV 0.5 MeV Electron injector module	2-2
2.2	Electrical Schematic of SNOMAD-IV solid-state driver	2-4
2.3	SNOMAD-IV accelerator cell	2-7
2.4	Coupling coefficient, K, versus ferrite core inner radius for beam currents from 1 to 5 kA.	2-12
2.5	Required ferrite core volume, $\nu_{ferrite}$ , versus accelerating gap voltage for $r_i = 0.015, 0.10, 0.15, 0.20, 0.24, 0.30$ meters.	2-13
2.6	Assembly drawing SNOMAD-IV input commutator arms, first compression stage and step-up transformer.	2-14
2.7	Assembly drawing of SNOMAD-IV second compression stage, PFN and output stage.	2-15
2.8	Drawing of SNOMAD-IV 0.5 MeV injector accelerator cell assembly.	2-20
2.9	Preliminary assembly drawing of cathode extraction optics and vacuum pumping port.	2-22
2.10	SNOMAD-IV Enclosure, elevation	2-23

## LIST OF ILLUSTRATIONS CONTINUED

<u>Figure</u>		<u>Page</u>
2.11	SNOMAD-IV Enclosure, plan view	2-24
2.12	Photograph of SNOMAD-IV injector and pulse power supply	2-26
2.13	The 500 kV induction accelerator and x-ray target (inside the blue lead box) assembly in the experiment vault.	2-27
2.14	Current (lower) and voltage (upper) pulse waveforms of the electron beam.	2-28
3.1	SNOMAD-IVB Driver	3-2
3.2	SNOMAD-IVB Accelerator Cells	3-6
3.3	Photograph of Completed SNOMAD-IVB, 1.0 MeV Accelerator Module	3-7
3.4	Photograph of SNOMAD-IVB 1.0 MeV Accelerator Module in Box with Lid Removed	3-8
3.5	Photograph of SNOMAD-IVB; 1.0 MeV accelerator module before installation in box	3-9
3.6	SNOMAD-IVB Voltage Waveform During Initial Tests	3-10
3.7	Charge Module	3-12
3.8	SRL-2650B Control Module Logic Circuit	3-15
3.9	Control Module	3-16
4.1	An Induction Linac Driven Free Electron Laser for ECH Heating	4-4
5.1	Expanded Electron Beam from a 1.5 MeV Induction Accelerator is used to irradiate the Red Water System	5-9
6.1	A typical aircraft gas turbine engine and relative temperature and pressure profiles are shown.	6-3
6.2	Advanced aircraft requirements will require higher engine temperatures and compression ratios.	6-4
6.3	The influence of specimen diameter to mean grain diameter ratio and solution-treatment on the creep properties of wrought superalloy tested at 10 ksi and 870°C. <sup>(3)</sup>	6-7
6.4	A SNOMAD-IV induction accelerator based material processing system	6-11

## LIST OF ILLUSTRATIONS CONTINUED

<u>Figure</u>		<u>Page</u>
6.5	(a) Top view, (b) bottom view and (c) side view of a compacted turbine disk with unremoved can produced by hot isostatic pressing.	6-13
6.6	The process of fabricating a graded alloy turbine disk using HEEB processing is shown.	6-15
6.7	The required HEEB power density for processing the graded alloy turbine disk as calculated by a heat transport code.	6-16
6.8	The required HEEB power for processing the graded alloy turbine disk	6-17
6.9	The temperature history at four radial locations as calculated by a heat transport code.	6-19
6.10	The temperature time history for (a) the surface and (b) 0.5 mm into the steel is shown.	6-22
6.11	The experimentally measured microhardness for the laser surface treated low carbon steel is shown.	6-23
6.12	The maximum temperature and achievable depth of HEEB surface hardening is shown of 1.5, 5.0 and 10.0 MeV beams at 3 kW/cm <sup>2</sup> power density	6-24
6.13	The time history for surface hardening with a 5.0 MeV HEEB system is shown.	6-25
7.1	A 5.2 MeV induction linear accelerator driven x-ray sterilization source is shown.	7-5
7.2	Measured <i>B.pumilus</i> survival curve.	7-9
8.1	The possible benzene decomposition products are shown.	8-2
8.2	EBARA Electron Beam Process (simplified flow diagram)	8-7
8.3	SO <sub>2</sub> and NO <sub>X</sub> Removal Efficiency versus Dose at Process Vessel Outlet	8-7
8.4a	SO <sub>2</sub> Removal Efficiency versus Inlet SO <sub>2</sub>	8-9
8.4b	NO <sub>X</sub> Removal Efficiency versus Inlet SO <sub>2</sub>	8-9
8.5	SRL compact induction accelerators deliver more power than NHV/EPS and dynamitron at one-tenth the cost	8-11
8.6	Model diagram of reaction mechanism	8-13
9.1	Simplified Schematic of Typical, All-Solid-State, Electromagnetic Shock Line System	9-3

## LIST OF ILLUSTRATIONS CONTINUED

<u>Figure</u>		<u>Page</u>
9.2	SLS-I Simplified Equivalent Circuit	9-5
9.3	SLS-I Shock Line System	9-6
9.4	SLS-I, SCR Commutation Module	9-8
9.5	SLS-I, LV Compression Module	9-9
9.6	SLS-I HV Compression Module	9-10
9.7	Cross Section of SLS-I HV Compression Module	9-11
9.8	Operation of SLS-I	9-12
9.9	Typical Transmitted Output Pulse	9-14
9.10	Simplified Schematic of SLS-II	9-20
9.11	SLS-II	9-21
9.12	Nonlinear Magnetic Compression Head	9-22
9.13	Operation of SLS-II	9-23
9.14	Output Pulse of SLS-II	9-24

## LIST OF TABLES

<u>Table</u>		<u>Page</u>
1.1	SNOMAD-V Preliminary Specifications	1-3
2.1	Design Parameters of the SRL Prototype Injector	2-3
2.2	SNOMAD-IV Performance Specifications	2-17
3.1	SNOMAD-IVB Performance Specifications	3-3
5.1	Summary of Percent Removal of Selected Aromatic Compounds Using High-Energy Electrons	5-4
6.1	A comparison of the relative merits of HEEB processing and competing technologies for the fabrication of graded alloy turbine disks and for deep surface heat treatment.	6-6
6.2	The Operating Parameters for a Proposed HEEB Processing System	6-10
6.3	Comparative High Throughput Heat Treatment Technologies	6-28
7.1	Preliminary Design Parameters	7-6
7.2	Cost Comparison for Large $\gamma$ -Ray/X-Ray Sterilization Facilities	7-10
8.1	Electron Beam Treatment of Water Containing Toxic Organic Contaminants	8-2
9.1	SLS-I Preliminary Specifications	9-15
9.2	SLS-IIB Performance Specifications	9-25

## EXECUTIVE SUMMARY

The primary goal of this program was to improve the performance of induction accelerators with particular regards to their being used to drive FELs. The strategy for achieving this end was to first optimize the nonlinear magnetic material used in induction accelerator construction and secondly to optimize the design in terms of cost, size and efficiency.

We began this research effort with an in depth study into the properties of various nonlinear magnetic materials (e.g. various ferrite compositions, Metglas (an amorphous tape composed of steel and glass), and more conventional magnetic materials such as 50/50 Ni-Fe tapes). An all-solid-state, nonlinear magnetic pulse compressor, denoted SNOMAD-V was constructed for this purpose. As more information was obtained the design was optimized with the aim of producing as short an output pulse as possible. This unique pulse generator was finally proven capable of producing gigawatt pulses as short as 2 nanoseconds in duration with risetimes less than 150 picoseconds at repetition rates as high as 10 kHz. Being very proud of this new toy, we leaked work of its existence to an old friend at DARPA (Dr. Bertram Hui). Previous to this conversation we had never even imagined that the services were greatly in need of just such a device. Representatives from the US Army Missile Command immediately descended upon our laboratory and in a joint DARPA/US Army program we have now delivered six sources based on this initial SNOMAD-V design. We have recently been approached by the British Defense Research Agency and have been asked to provide a quotation for the delivery of three sources to that agency.

We then fabricated a high gradient, 1 MeV induction acceleration section and fed it with the output of SNOMAD-V. The results of this experiment greatly excited researchers at UCLA (University of California, Los Angeles). A group in the Center of Advanced Accelerators had need of an electron injector which could inject a single bunch of high brightness electrons into a S-Band collider. This required either a very expensive and complicated injector with a

laser driven cathode or a previously non-existent injector technology which would produce 1 nanosecond duration electron pulses at 1 MeV. The long term goal of their research was to optimize synchrotrons for X-ray lithography and positron sources for the next generation of high energy colliders. This group helped arrange for funding from the DoE and we are nearing the completion of a 1 MeV, 1 nanosecond, 1 kiloampere injector for shipment to their facility.

Producing ridiculously short pulses and using them to accelerate electrons or radiate energy for Ultra-Wideband antennas was certainly a new and exciting technology. It was certainly the first time an all-solid-state pulse generator had ever produced peak output powers of more than a megawatt with pulse lengths less than 10 nanoseconds, and here we were with a gigawatt at pulse lengths down to 1 nanosecond but we still wished to apply what we had learned to more conventional induction accelerator design. We envisioned a new induction accelerator design where all of the components were packaged together in one container. This induction accelerator module would combine an all-solid-state, nonlinear magnetic driver and the induction accelerator cells all in one convenient package. Each accelerator module (denoted SNOMAD-IVB) would produce 1.0 MeV of acceleration with the exception of the SNOMAD-IV injector module which would produce 0.5 MeV of acceleration for an electron beam current up to 1000 amperes. An arbitrary number of modules could be stacked end to end producing any desired electron beam energy.

The completed design package drew considerable interest from the DoE, SDIO, NASA, DARPA, and NSF as well as several commercial interests including EPRI, Merck Pharmaceutical, Johnson and Johnson, RSI (Radiation Sterilization Inc.), RDI (Radiation Dynamics Inc.), and Stericycle Inc. It appeared we had hit a nerve. The long term goals of all these organizations were quite diverse but it appeared that they all had one thing in common and that was the need for a cheap, reliable, high power electron beam. An accelerator construction project akin to the fabrication of "Stone Soup" began with the construction of the 0.5 MeV SNOMAD-IV injector which has been operational now for almost 1 year. The first of the 1.0 MeV SNOMAD-IVB accelerator modules is nearing completion. We will briefly summarize the contributions of the

various agencies who supported this work and describe their goals.

The DoE was looking for a low cost, high repetition rate induction accelerator driven FEL for electron cyclotron heating of the C-MOD Tokamak at the MIT Plasma Fusion Center. They have agreed to make a home for the completed 5 MeV accelerator. Their contribution includes the cost of shielding, prime power, magnet supplies and a location at the Plasma Fusion Center retrofitted for placement of the accelerator.

The SDIO Directed Energy Office was interested in this technology for its long term application to the goals of the SDIO program. They agreed to fund half of the 0.5 MeV SNOMAD-IV injector provided that the SDIO SBIR office would fund the other half. Karl Nelson at the SDIO SBIR office agreed to the arrangement and the SNOMAD-IV injector was added to the work statement of this effort.

NASA was interested in a high power FEL which might beam power into space. The program known as SELENE for SpacE Laser ENEnergy had several goals. First of all by beaming power to satellites when the earth is between them and the sun, their operational life can be greatly extended and many satellites already in orbit with failed batteries could be brought back into service. In the longer term power could be beamed to a colony on the moon greatly decreasing the cost associated with supplying power to the colonists during the 15 day lunar night, and finally power could be beamed to advanced spacecraft and actually used to power a plasma thruster. NASA agreed to fund most of the 1.0 MeV SNOMAD-IVB accelerator module with the understanding that we would use the remaining funds in this contract to complete that module and begin work on the second 1.0 MeV module. The short term goal being to install a 5 MeV accelerator at the MIT Plasma Fusion Center where the ECH experiments would provide a proof of principle demonstration for the feasibility of a low cost, high power induction linac powered FEL.

DARPA was very interested in using this technology for electron beam processing of various construction materials as well as the removal of complex hydrocarbons from a substance known as "Red Water", an unwanted byproduct of high explosives manufacture. They agreed to cover

the costs of operating and testing the first SNOMAD-IV injector module and to fund its temporary installation in SRL's Boston facility. Initial experiments are being conducted on this 0.5 MeV injector module and the temporary installation in the same location of the first 1.0 SNOMAD-IVB accelerator module is scheduled for later this year. Pending the successful conclusion of these initial tests, DARPA has agreed to supply funding for yet another SNOMAD-IVB accelerator module.

The National Science Foundation (NSF) has supplied a low level of funding (Phase - I SBIR) to perform initial experiments using the SNOMAD-IVB accelerator to Sterilize various products.

EPRI has supplied SRL with a small grant to cover experiments aimed at the treatment of industrial wastewater toward the goal of reducing toxicity, and a proposal to investigate the removal of  $\text{SO}_X$  and  $\text{NO}_X$  from stack gases is under consideration by the EPA. Merck has joined with SRL in a program to investigate the use of this technology for the sterilization of medical products. At this time they are participating in experiments using the SNOMAD-IV injector. They have been supplying radiation diagnostic support, samples, and personnel to do analysis and testing. Johnson and Johnson have sent representatives to SRL and are currently working on a plan for performing experiments at SRL with the long term goal of purchasing a 5-10 MeV induction accelerator of the same design. We have had several visits from RSI, and RDI and have performed several experiments on the sterilization of medical waste products with Stericycle as a team member.

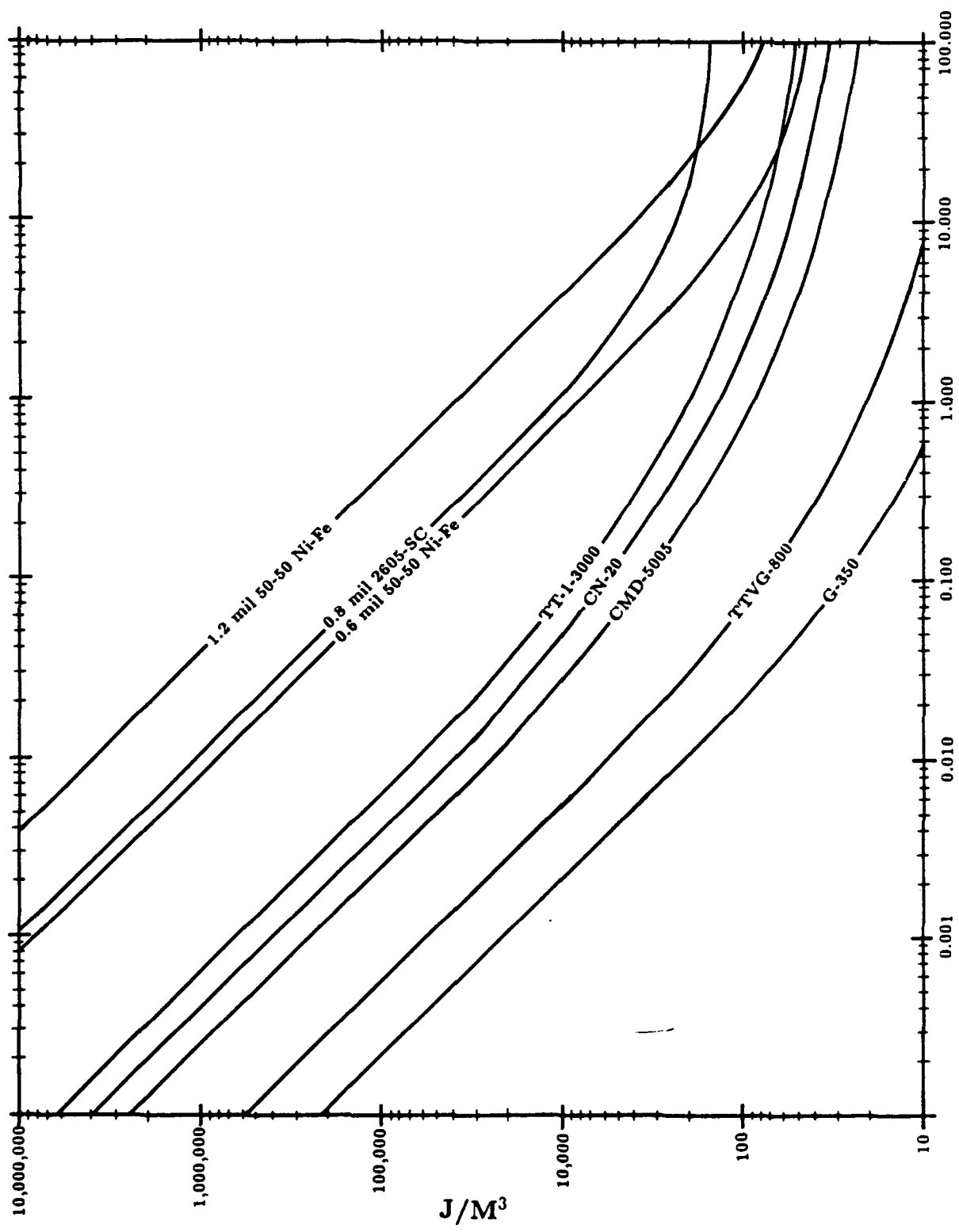
In the remainder of this report we will describe the SNOMAD-V, high gradient accelerator experiment, the SNOMAD-IV 0.5 MeV injector module, and the SNOMAD-IVB 1.0 MeV accelerator module. We will follow this up with a few brief descriptions of some of the co-sponsor's programs and finally we have assembled test data and accelerator design information in the appendices. However, before we proceed with these discussion it is worthwhile to present a brief summary in graphical form of the most relevant test results.

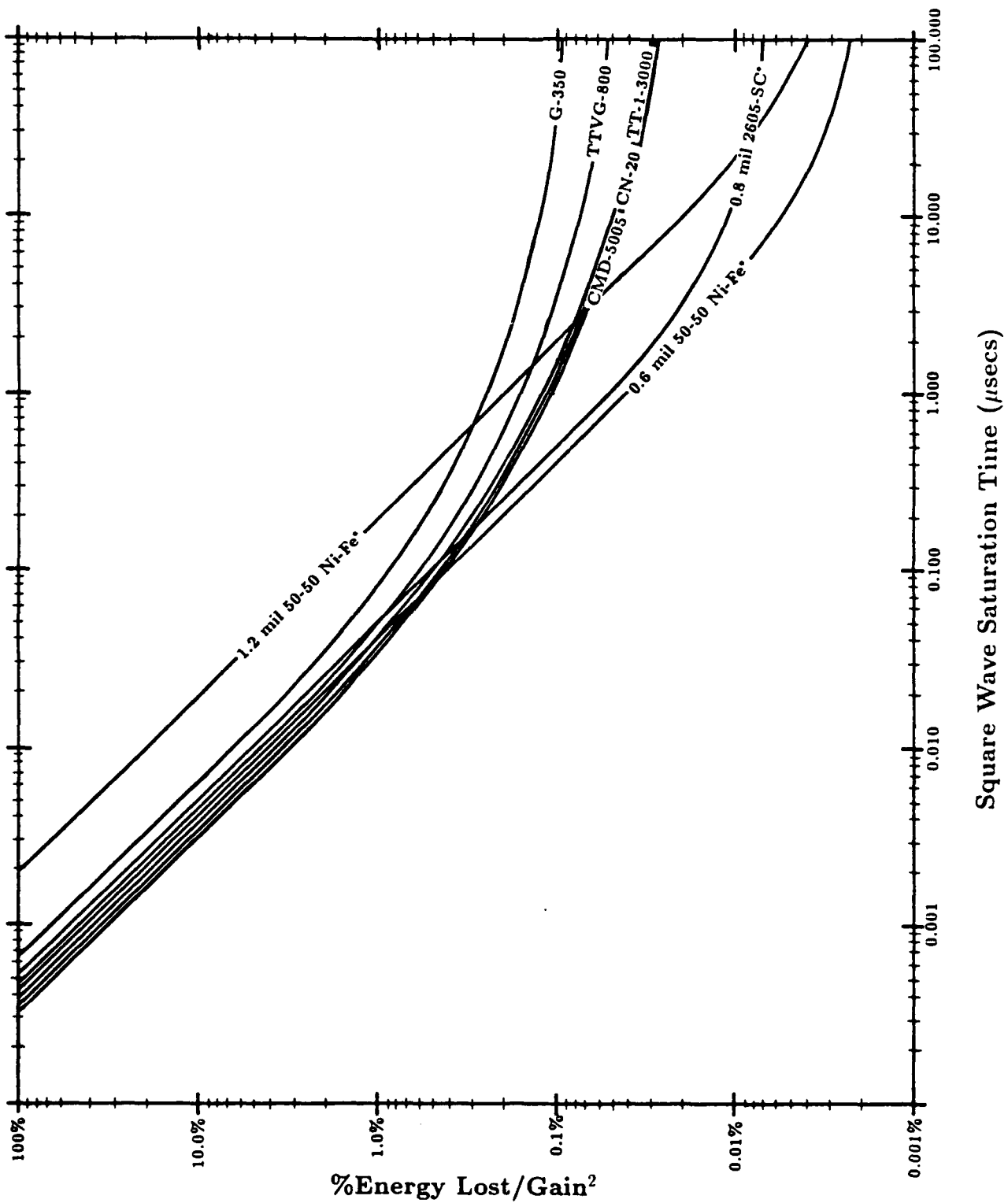
In Fig. 1 we present a curve which plots energy absorbed in various magnetic materials versus saturation time assuming a flux excursion  $\Delta B_s = 2B_s$ . Here we see that as the saturation

time decreases the losses increase linearly as  $1/\tau$ . We have compared what we believe are the most useful nonlinear magnetic materials. Figure 2 supplies a curve of saturation time versus a quantity denoted % Energy Lost/Gain<sup>2</sup>. This is a very important curve for designers of nonlinear magnetic pulse compressors. From this curve the magnetic material losses can easily be determined for a given material, saturation time and temporal compression factor. The curve in Fig. 3 supplies important information to the designer of electromagnetic shock line. The required H field for a given output risetime can easily be determined.

Square Wave Saturation Time ( $\mu$ secs)

Figure 1: Saturation Time Versus  $J/m^3$

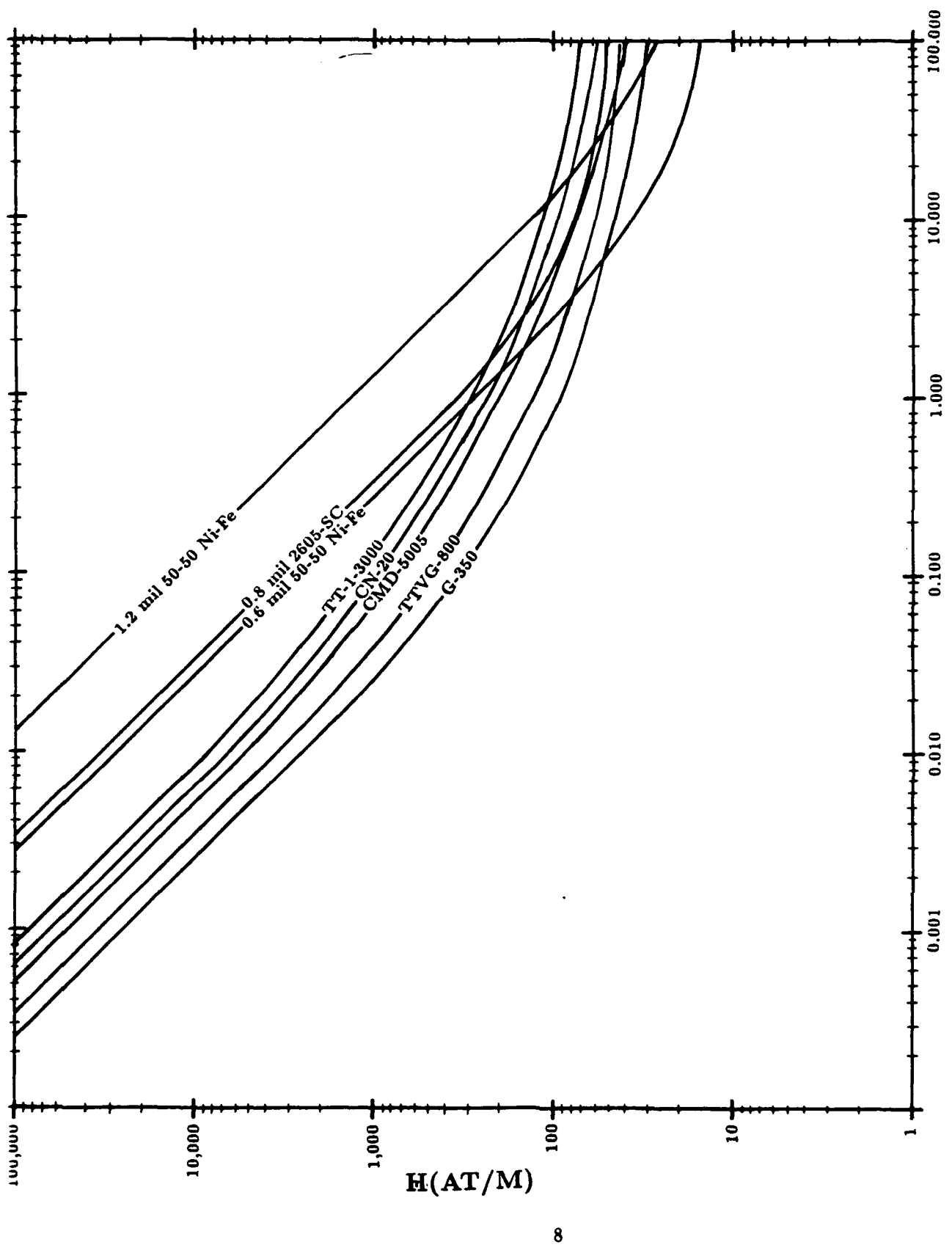




\*Packing Factor=0.7 Assumed, Unity Packing Factor Assumed for all Ferrites

Figure 2: Saturation Time Versus % Energy Lost/cm<sup>2</sup>

SCIENCE RESEARCH LABORATORY

Square Wave Saturation Time ( $\mu$ secs)

## SECTION 1

### THE SNOMAD-V HIGH GRADIENT ACCELERATOR MODULE

The SNOMAD-V high gradient accelerator module consists of the SNOMAD-V driver and a 10 cell induction accelerator. The SNOMAD-V, all-solid-state nonlinear magnetic driver was designed and fabricated first before construction of the 10 cell accelerator. SNOMAD-V was used as a test bed to provide data on the performance of nonlinear magnetic materials at high power levels.

The input energy of SNOMAD-V is  $\approx$ 5 Joules. A picture of SNOMAD-V with the test fixture attached is presented in Fig. 1.1 while the performance specifications are outlined in Table 1.1. A simplified schematic of the SNOMAD-V driver system with an electromagnetic shock line attached appears in Fig. 1.2. An informative although somewhat inaccurate cross-sectional view of SNOMAD-V is shown in Fig. 1.3. The shock line driver resides in an oil filled tank and has an approximate weight of 350 lbs.

The original test configuration of SNOMAD-V included four parallel coaxial transmission lines which could be loaded with ferrite samples. Saturation times as short as 200 picoseconds could be achieved by exposing small toroid samples to voltages as high as 200 kV. An electromagnetic shock wave created in the line assures that the samples are exposed to an almost instantaneously rising HV pulse. This type of arrangement has been called an electromagnetic shock line. The original investigation of this phenomena was performed at low power levels in the Soviet Union. More recently a small British company known as Bournlea corporation has exploited this technology. Before the introduction of SNOMAD-V, the Bournlea, thyratron driven shock line system was the highest power electromagnetic shock line system in the world. Previous to the creation of SNOMAD-V the US Army Missile Command had purchased several Bournlea systems for testing purposes. They had also expended several million dollars in equipping an experimental facility with diagnostic equipment capable of measuring subnanosecond

SCIENCE RESEARCH LABORATORY

Figure 1.1: SNOMAD-VB



**Table 1.1: SNOMAD-V Preliminary Specifications**

**Input Power Requirements:**

Energy/pulse	5.27 joules
PRF	5 kHz
Power	26.4 KW
Voltage	465 volt
Current	56.6 Amps

**Intermediate Storage**

Capacitance	12.3 $\mu$ fd
Voltage	930 volts
Energy	5.27 joules
Stored charge	$1.144 \times 10^{-2}$ Coulombs
$\tau$ discharge	$\leq 5 \mu$ sec
I peak	$3.594 \times 10^3$ Amp
dI/dt	$2.258 \times 10^3$ A/ $\mu$ sec
$I_T$ (RMS)	430 Amps
dI/dt per device	564 A/ $\mu$ sec (4 $\times$ R400 West Code)
Commutation losses	$\sim .27$ joules

**1<sup>st</sup> Stage**

Capacitance	12.5 $\mu$ fd
Voltage	894 volts
Energy	5.0 joules
Core Type	.6 Mil $\times$ 2605 CO
# Turns	1
Core geometry	$1 \times 5.75"$ ID $\times$ 7.0" OD $\times$ 2" Wide
$\int V \cdot dt$	$\sim 2.4 \times 10^{-3}$ Vsecs
Lsat	1.97 nh + 2 nh (STRAY) = 3.97 nh
$\tau$ discharge	494 nsec
Losses	$\sim .20$ joules (.10 cores, .10 caps)
Core volume	$4.1 \times 10^{-4} \text{ m}^3$ , 2.46 kg

**Transformer**

Core Type	2605S3A
# Turns (PRIM)	.50
# Turns(sec)	30
Losses	$\leq .15$ joules
Peak stress	53 kV/cm at 50.5/2 kV (.375" dia. Rod in .875" dia. hole)
Core geometry	$2 \times 10.5"$ ID $\times$ 12.875" OD $\times$ 2" wide

**Table 1.1: SNOMAD-V Preliminary Specifications (Continued)**

<b>2<sup>nd</sup> Stage</b>	Capacitance	3.64 nfd
	Voltage	50.546 kV
	Energy	4.65 joules
	Core type	2605SC METGLASS
	Core Geom.	1×4.25" ID × 5.75" OD × 2" w (.371×10 <sup>-3</sup> M <sup>2</sup> )
	$\int V \cdot dt$	6 Turns × 2.48 Vsecs/Turn = 50.546 kV* (.589 Vsecs/2)
	LSAT	.112 $\mu$ h + .06 $\mu$ h stray $\simeq$ .172 $\mu$ h
	$\tau_{\text{discharge}}$	55 nsec
	Losses	~ .15 joules
<b>Third Stage</b>	Capacitance	3.92 nfd
	Voltage	47.9 kV
	Energy	4.5 joules
	Core type	CMD-5005 Ferrite
	Core Geom.	4×5.0" ID × 8" OD × .5" w
	$\int V \cdot dt$	1 Turns × 1.257 × 10 <sup>-3</sup> Vsecs/Turn
	LSAT	4.7 nh + 1.3 nh (Stray) $\simeq$ 6 nh
	$\tau_{\text{discharge}}$	~ 10.7 nsec
	Losses	~ .4 joules
<b>Fourth Stage</b>	Capacitance	4 nfd
	Voltage	45.27 kV
	Energy	4.1 joules
	Core type	CMD-5005 Ferrite
	Core Geom.	1×5.0" ID × 8" OD × .5" w
	$\int V \cdot dt$	1 Turns × .314 × 10 <sup>-3</sup> Vsecs/Turn
	LSAT	1.17 nh + .3 nh (Stray) $\simeq$ 1.47 nh
	$\tau_{\text{discharge}}$	~ 5.4 nsec
	Losses	~ .4 joules
<b>1:6 Transformer</b>	Core Type	CMD-5005
	# Turns (PRIM)	.16
	# Turns(sec)	1
	Losses	≤ .4 joules
	Core geometry	6×5" ID × 8 " OD × .5" wide
<b>Output Shock Line</b>	Core Type	CMD-5005
	Impedance	37Ω
	Input Pulse Length	5 nanoseconds
	Output Pulse Risetime	≤ .20 nanoseconds
	Output Voltage Level	≤ 200 kV

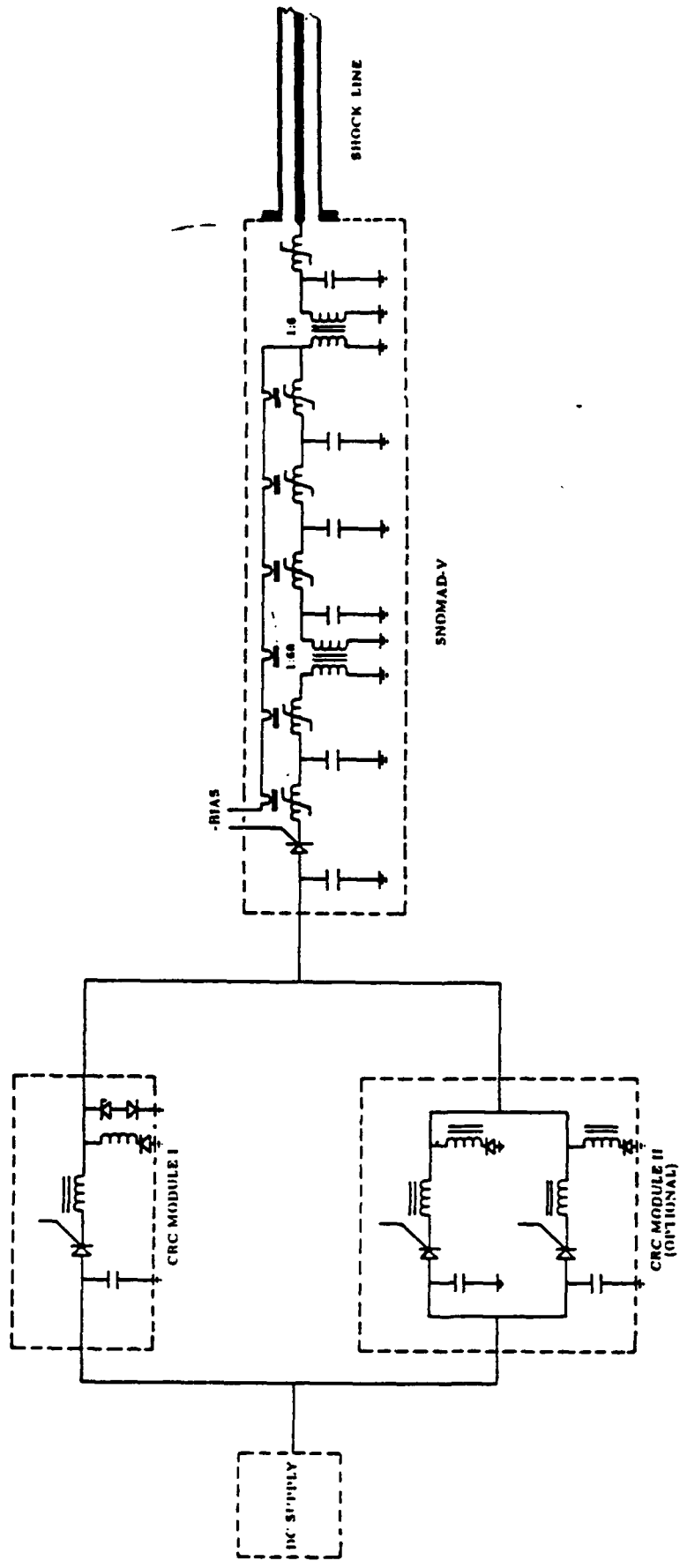


Figure 1.2: SNOMAD-V Shock Line System Simplified Schematic

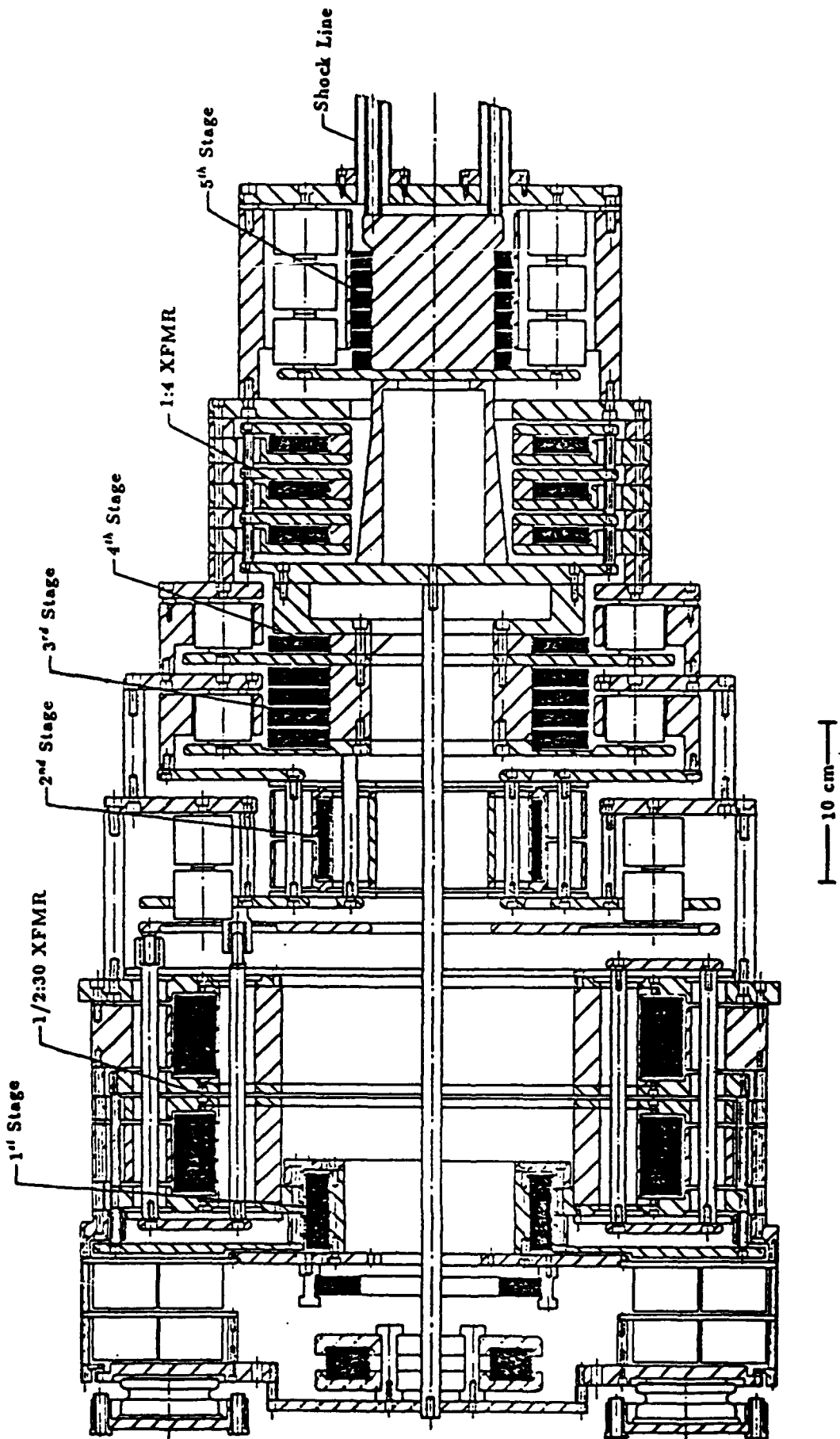


Figure 1.3: SNOMAD-V nonlinear magnetic pulse compressor

pulses.

Measurement of pulses with subnanosecond risetimes is an elaborate and expensive process. To equip ourselves with an accurate measurement system would have cost more than the entire value of this contract. We contacted the US Army and asked if we might make use of their measurement system. They agreed and we travelled with SNOMAD-V to Redstone Arsenal in Huntsville Alabama. The Army measurement technique involved transmitting the output pulse from a high fidelity, TEM horn and measuring the field pattern at ranges of up to 140 ft in a large anechoic chamber. After the initial tests with SNOMAD-V, the personnel at US Army Missile Command became very excited and working with DARPA arranged to fund us for some additional development effort in this area. We later supplied them with the SNOMAD-VII and SNOMAD-X pulsers and finally with the SLS series pulsers described later in this report. SNOMAD-VII and SNOMAD-X were direct descendants of SNOMAD-V.

In Fig. 1.4 we present data taken at Redstone Arsenal. The field measurements from four sources are compared at a range of 40 feet from the antenna. The three all-solid-state nonlinear pulse generators including SNOMAD-V are compared to the highest power, previously existing electromagnetic shock line pulser, the Bournlea 3153. The Bournlea 3153 uses an extremely fast thyratron operating at 20 kV to supply the initial pulse to an electromagnetic shock line. It is important to remember when you make a comparison of the relative field levels from these different sources that the relative output power level scales with the square of the output field.

The SNOMAD-V shock line system is an oil immersion cooled, all-solid-state nonlinear magnetic pulse compressor. Six SCRs are used to transfer 5.27 Joules from the intermediate storage capacitor to the 1<sup>st</sup> stage of the compression network during a 5  $\mu$ sec commutation cycle. The compression circuits take this energy and temporally compress it into a 5 nanosecond pulse at the end of the chain. The voltage is also increased from the input voltage level of a little over 1 kV to the output voltage level of 200 kV. This entire process is completed with a measured efficiency of over 50%. Energy recovery circuits also store the reflected energy from the shock line head and add it to the energy in the next pulse.

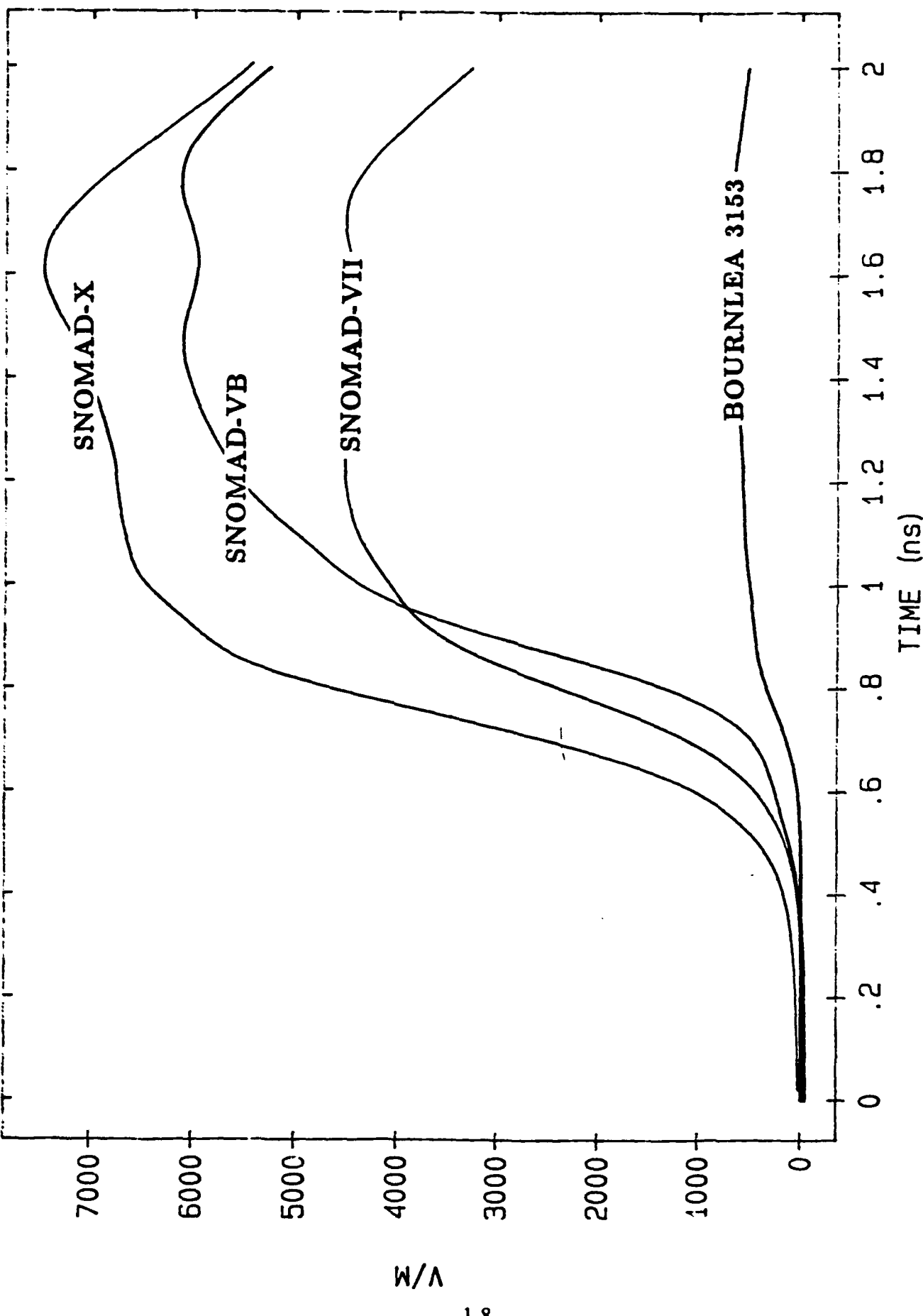


Figure 1.4: Field Waveforms @ 40 ft. for SNOMADS 5, 7, and 10 and Bournlea 3153

SCIENCE RESEARCH LABORATORY

The 123, 0.1  $\mu$ fd Intermediate Storage capacitors in each module are charged to the single pulse energy by either a command resonant charge system or an inverter. Once fully charged to 930 volts, Six R-355 SCRs are triggered. Each SCR commutator arm delivers 0.88 Joules into the first stage energy storage capacitors in 5.0  $\mu$ sec, charging this 12.5  $\mu$ fd capacitor bank to a maximum of 894 volts. This charging time has been selected so as not to exceed the dI/dt capabilities of commercially-available SCRs. Operation at repetition rates in excess of 10,000 pulses per second is possible with devices operating in this regime. The 12.5 $\mu$ fd first stage energy storage and the intermediate storage units are comprised of low loss, high reliability, aluminized polypropylene capacitors with a shot-life demonstrated to be in excess of  $10^{11}$  in these applications. These capacitors are coupled via a low inductance bussing network to a metglass core saturable inductor. This compression reactor has been designed with sufficient VT product ( $\int V \cdot dt = N \cdot \text{Area} \cdot \Delta B_s$ ) so as not to saturate until the termination of the 5.0  $\mu$ sec charging pulse. Once saturated, the energy stored is discharged in 0.5  $\mu$ sec thereby achieving a factor of 10 temporal compression at constant energy. This results in a corresponding increase in the peak power level.

The output of the first stage compression reactor powers a 0.5:30 hybrid transformer. Following this transformer reactor is the 3.64 nfd 2<sup>nd</sup> stage capacitor bank isolated from the 3<sup>rd</sup> stage capacitor bank by a second, metglass-core compression reactor. When the 2<sup>nd</sup> stage core saturates, this energy is delivered in less than 60 nsec to the 3.92 nfd 3<sup>rd</sup> stage capacitor bank.

A final stage of compression, the 4<sup>th</sup> stage, provides a 5.4 nanosecond discharge pulse at >40 kV to the primary of a 1:6 induction style output transformer. This 1:6 step-up transformer is an induction style transformer utilizing a fractional turn primary and single turn secondary. This transformer design was accredited to the Nicholas Christofolis who originally used this innovative design as the basis for high current (> 10 kiloampere) accelerators for use in charged particle beam weapon research. In that case, the single secondary turn was comprised of an accelerating electron beam.

The output from this induction transformer charges the output test cell when SNOMAD-V

is configured for materials testing and can also be reconfigured to drive a 10 cell induction accelerator (Fig. 1.5).

The SNOMAD-V, 10 cell induction accelerator (Fig. 1.6) is a ferrite based induction accelerator with an overall length of approximately 1 foot. It attaches directly to the output of the 1:6 induction transformer of SNOMAD-V (Fig. 1.7). The complete accelerator system is shown operating with a cathode stalk in Fig. 1.8. The addition of the 10 cell induction module loads the output bus of SNOMAD-V to such an extent that the normal 200 kV open circuit voltage is reduced to only 60 kV. The overall accelerating potential never reached the design value of 1 MeV, topping out at 600 kV. Even with this drawback we are planning to deliver an improved version of this system to UCLA later this year. We will discuss that project later in this report.

Once the accelerator tests were completed at SR, we returned the SNOMAD-V pulser to US Army Missile Command in order that we could continue tests on various ferrite samples. SNOMAD-V is still occupied in this function.

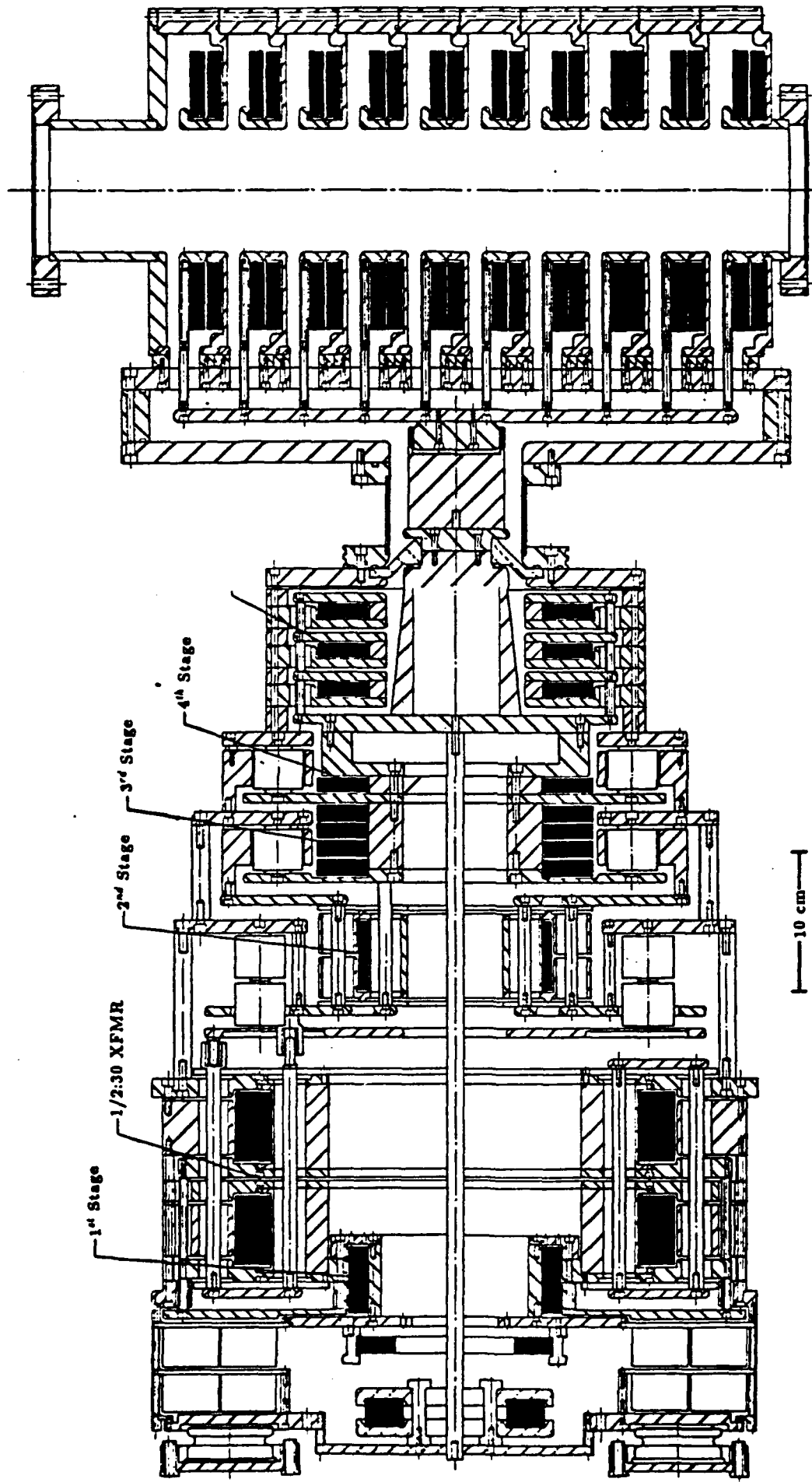


Figure 1.5: SNOMAD-V Nonlinear Magnetic Compressor and 1 MeV High Gradient Accelerator Section

SCIENCE RESEARCH LABORATORY

Figure 1.6: SNOMAD-V, 10 Cell Induction Accelerator



SCIENCE RESEARCH IN SPACE

Figure 1.1. SNO-MAD-VP Accelerator Module Attached to SNO-MAD-VP Unit

Figure 1.8: SNOMAD-VB with Cathode Stalk

## SECTION 2

### THE SNOMAD-IV 0.5 MeV INJECTOR

The SNOMAD-IV induction linear accelerator injector is a self contained 0.5 MeV accelerator module driven by an all solid state nonlinear magnetic pulse compressor. Ten induction cells, each driven at 50 kV, produce a total accelerating voltage of 0.5 MeV. A schematic of this accelerator indicating its physical size and layout is shown in Fig. 2.1. Table 2.1 summarizes the performance specifications of SNOMAD-IV.

The use of solid state devices to replace thyratrons or spark gaps in existing pulse power designs is key to the development of reliable, high average power induction linear accelerators. When combined with the technology of nonlinear magnetic compression circuits, SCR commutated drivers provide operating capabilities at pulse repetition rates and lifetimes greatly exceeding those of thyratron designs. The SNOMAD-IV driver is capable of delivering up to 50 Joules per pulse at a rate of up to 5 kHz (cw), to an induction cell load. A circuit diagram of SNOMAD-IV is shown in Fig. 2.2. Commercially available SCRs are utilized in the command resonant charge and intermediate storage power supply. Thyratron switches have been completely eliminated permitting significantly higher repetition rate operation and a reduction in cost and size.

The input is split into multiple arms, each completely isolated from the other, allowing each SCR to perform individually. Isolation between arms is provided by the saturable inductors in series with each SCR. The commutator arms deliver a 55 Joule energy pulse into the first stage energy storage capacitors,  $C_1$ .  $C_1$  is charged to 1 kV in 10  $\mu$ sec. The charging time has been chosen so as not to exceed the  $dI/dt$  capabilities of commercially available SCRs. Low loss, aluminized polypropylene capacitors are utilized in the first energy storage stage,  $C_1$ . These capacitors are coupled via a low inductance bussing network to a metglass saturable inductor,  $L_1$ .  $L_1$  is designed so that saturation occurs following the termination of the 2  $\mu$ sec charging

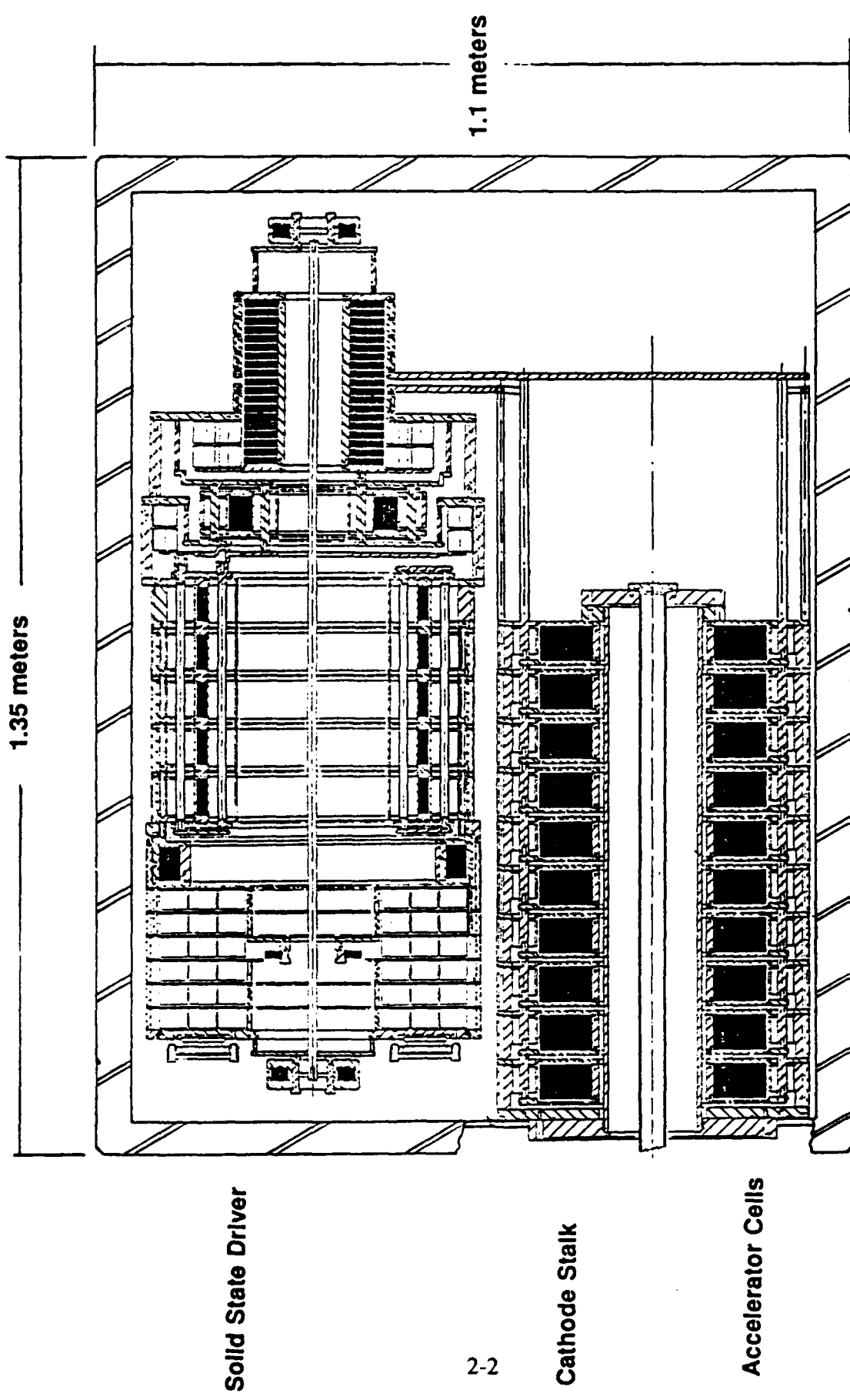


Figure 2.1: SNOMAD-IV 0.5 MeV Electron injector module

**Table 2.1: Design Parameters of the SRL Prototype Injector**

**Accelerator Parameters**

Beam Energy	0.5 MeV
Beam Current	600 amp
Pulse Length	50 nsec
Pulse Repetition Rate	5 kHz
Single Pulse Energy	30 joules
Voltage per Cell	125 kV
Accelerating Gradient	0.5 MeV/meter
Pipe Radius	6.35 cm
Gap Field Stress	150 kV/cm
Cathode	3.5" $\phi$ Dispenser

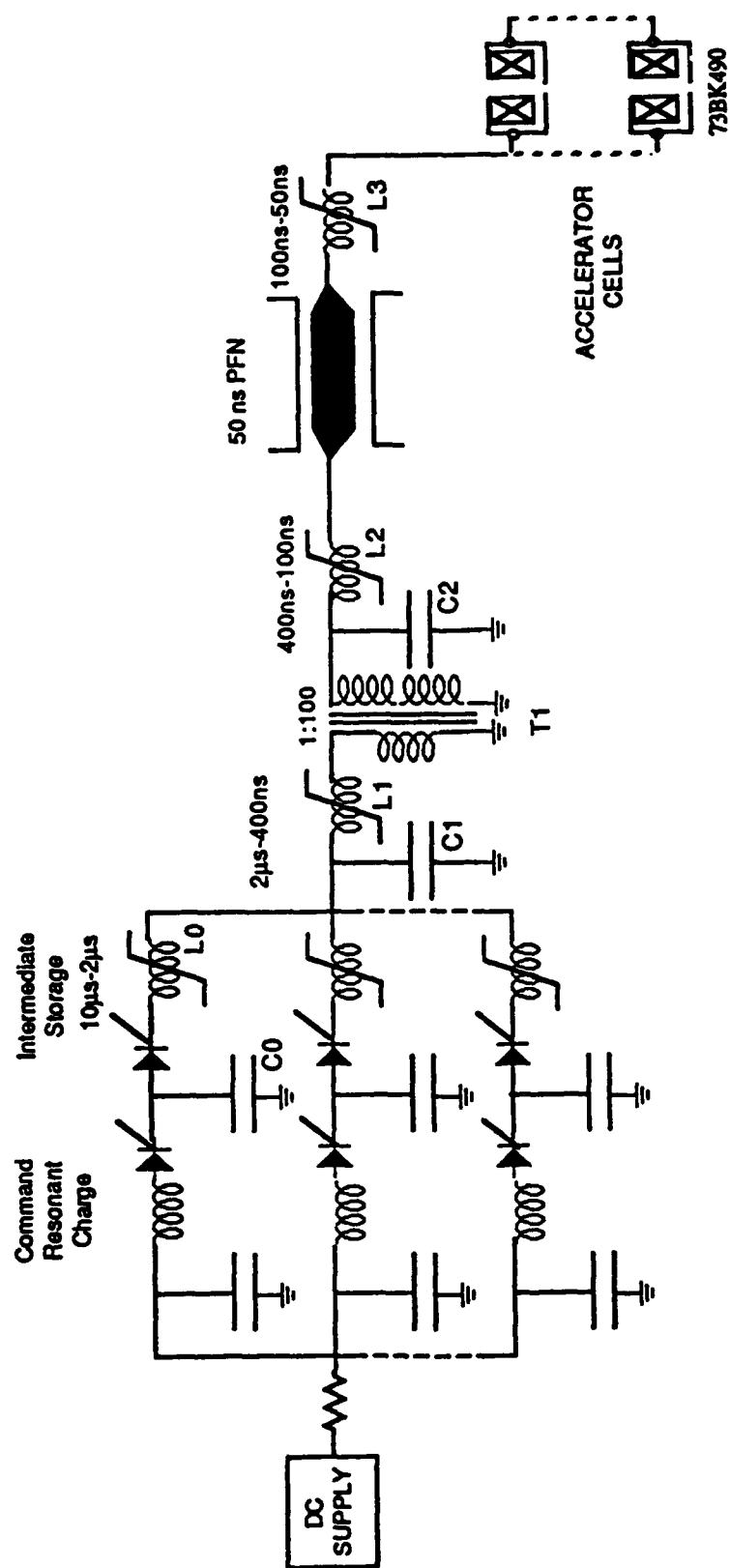


Figure 2.2: Electrical schematic of SNOMAD-IV solid-state driver

pulse. Once saturated, the energy stored in  $C_1$  is discharged into the primary of a 1:100 step-up pulse transformer,  $T_1$ , in 400 ns thereby achieving a temporal compression of 5. This results in a corresponding increase in the peak power level.

The secondary of  $T_1$  charges a bank of strontium titanate capacitors,  $C_2$ , to 100,000 volts.  $T_1$  and the second stage compression inductor,  $L_2$ , both utilize metglas cores. Metglas is a silicon-iron alloy, developed by Allied Chemical Co, with a resistivity that is three times higher than most ferro-magnetic materials.  $L_2$  has a charging time of 400 ns and a discharge time of 100 ns. This is the last stage in the compression chain where metglas can be employed. A saturation time of less than one microsecond results in excessive losses due to eddy currents. The second stage inductor,  $L_2$  feeds a 50 ns pulse forming network (PFN) to 100 kV in 100 ns. Input coupling to the PFN is accomplished at its electrical midpoint which allows for charging twice as fast as could be accomplished by coupling to either end. However, if the charging time becomes too short with respect to the output pulse length, remnants of the charging waveform can appear on the output pulse as voltage fluctuations. The output inductor stage,  $L_3$ , is a ZnNi ferrite saturable inductor which delivers the 50 kV pulse to the output transmission line.  $L_3$  has been carefully designed to take advantage of the high dielectric constant ( $\epsilon_r \approx 12$ ) of the ferrite. This single turn compression stage operates to some extent as a shock line. Once saturated, the ferrite forms the medium for a transmission line with an impedance close to that of the PFN.

Special care has been taken in the design of SNOMAD-IV to minimize the saturated inductance of the compression reactors  $L_1$ ,  $L_2$  and the transformer windings of  $T_1$ . The ferrite core volume, required to obtain a given temporal compression,  $\tau_c$ , in a nonlinear magnetic pulse compression stage is proportional to the square of the saturated inductance.

$$V_{ferrite} = \tau_c^2 E \frac{\mu_0 \pi^2}{4 B_{sat}^2 P_f^2}$$

where  $B_{sat}$  is the available flux swing of the ferrite,  $P_f$  is the packing factor and  $E$  is the single pulse energy. The packing factor is defined as the ratio of the ideal toroidal inductance to the actual device inductance including stray inductance. It is essential to minimize the core volume

if efficient operation is to be achieved since the energy lost in the compression reactor scales linearly with the core volume.

The SNOMAD-IV accelerator cell design is shown in Fig. 2.3. This design has been optimized for accelerating beam currents of 1 kA or less with pulse durations of 50 to 100 nsec. Each cell utilizes a metglas core measuring 6.75 inches I.D. by 12.75 inches O.D. by 2.0 inches in length. The cells are fed by a common bus which supplies 50 kV of drive from the SNOMAD-IV driver. Several innovative features have been incorporated into the mechanical design of the accelerator cell assembly to simplify the construction and lower its cost. In the injector accelerator cells, a quartz tube separates the evacuated beam pipe from the freon or oil filled accelerator gap and core region of the cell. In conventional accelerator cell designs, the gap and core winding are placed in the high vacuum region shared by the beam. This requires that these materials have ultra-high vacuum compatibility and that the electric field strengths be maintained below the vacuum break-down limit. Isolating these materials from the vacuum permits less expensive materials to be utilized and allows an insulating dielectric liquid to fill the high field gap region. The induction cells used in the 1 MeV accelerating modules will use more conventional ceramic alumina rings to provide the vacuum interface in the accelerator gap region.

An induction cell is a high impedance transmission line transformer filled with ferrimagnetic or ferromagnetic materials with the electron beam forming the single turn secondary winding. The e-beam gains energy equal to the drive voltage as it passes through each cell and appears as a resistive load in parallel with the accelerator cell impedance.

If the accelerator is to be efficient, the losses in the accelerator core must be negligible in comparison to the energy coupled into the electron beam. This requires that the characteristic impedance of the transmission line,  $Z_{line}$ , which forms the cell must be large compared to the impedance of the beam,  $Z_{beam} = V_{line}/I_{beam}$ . Typically, vacuum filled accelerator cell has a characteristic line impedance,  $Z_{line}$ , of less than 100 ohms.

The impedance of an accelerator cell can be increased significantly by one of two methods: by filling the cell with a high permeability, low permittivity material,  $(\mu_r/\epsilon_r)^{1/2} > 1$  or operating

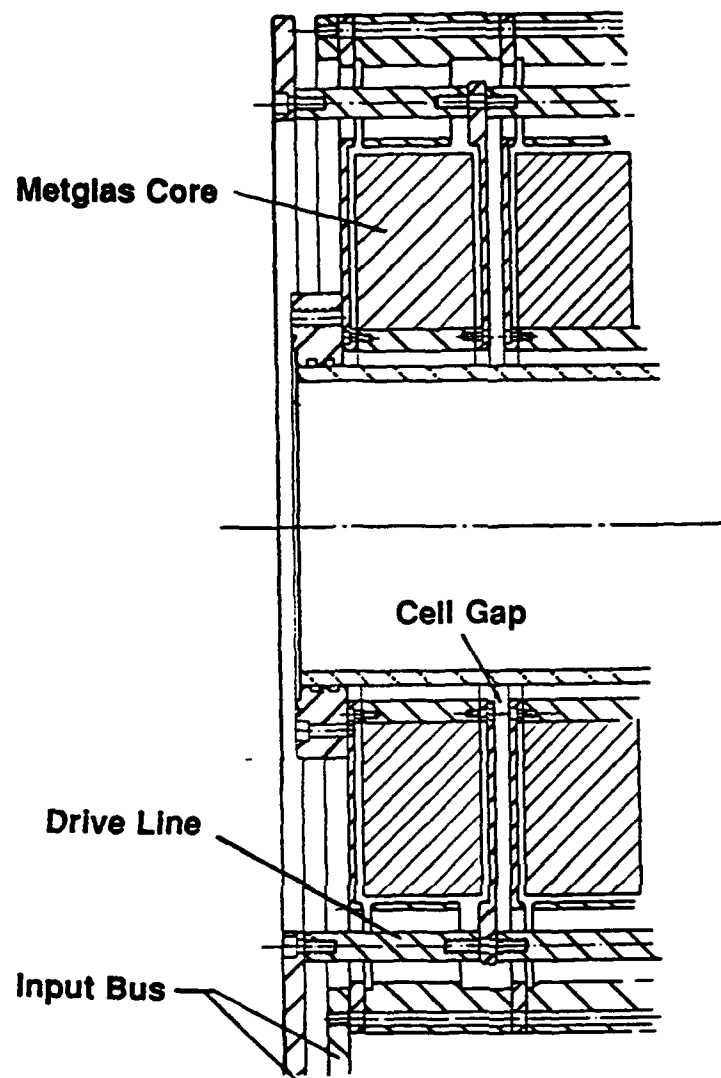


Figure 2.3: SNOMAD-IV accelerator cell

the cell as a resonant transmission line. The disadvantage of resonant structures is that the cavity is never resonant with a single mode. Wake fields produced by the electron beam can feed energy into spatially antisymmetric modes which can steer the beam electrons off axis. This sets an upper limit to the total charge which can be accelerated during an rf cavity decay time.

An induction cell is a non-resonant transmission line and, if properly designed, stores neither the drive fields nor the beam wake fields. This dramatically increases the practical operating e-beam current of the induction cell over that of the rf resonant cavity. However, it also constrains the minimum efficient operating current. Induction linacs which provide short pulses ( $\leq 50$  ns), are usually filled with ferrimagnetic material (ferrite) to increase the impedance of the cell; for long pulses ( $50 \text{ nsec} \leq \tau_p \leq 1 \mu\text{sec}$ ) ferromagnetic materials such as Si-Fe, metglas, or superpermalloy are employed. Most high frequency ferrites have dielectric constants of order  $\epsilon_r \approx 10$  and permeabilities of order  $\mu_r \approx 1000$ . With ferrite as a medium, the characteristic transmission line impedance is increased over the vacuum value by a factor of  $(\mu_r/\epsilon_r)^{1/2} = 10$ , yielding an effective shunt impedance as high as several hundred ohms. The use of ferrite also shortens the required physical length of the transmission line since the group velocity,  $v_g = c/(\mu_r \epsilon_r)^{1/2}$ , in a ferrite filled transmission line is decreased by 100 fold.

The design of an induction accelerator cell is governed by the basic operating principles discussed above. The length ( $h$ ) of the ferrite loaded transmission line is determined by the pulse length and the electrical characteristics of the ferrite.

$$2h \geq \tau_p \frac{c}{\sqrt{\epsilon_r \mu_r}} \approx \frac{\tau_p c}{100} \quad (1)$$

In practice, the best performance is achieved by setting  $h = \tau_p c/100$ , thereby setting the line length equal to a single transit time rather than a round trip time. The reason is that ferrite properties are field dependent and the minimum ferrite volume is achieved by designing for a single transit time. However, the additional size and cost of achieving this improvement in performance may not be required. Making  $h$  longer than a transit time has no benefit since the additional ferrite will not be used during the pulse.

The radial dimensions of the ferrite ( $r_o - r_i = \Delta R$ ) is set by the drive voltage and the maximum flux swing available in the ferrite. The ferrite must not be permitted to saturate as the wave generated by the drive pulse is transmitted down the line. The magnetic flux density,  $B$ , in the ferrite is related to the drive voltage,  $V_{cell}$ , and cross sectional area of the ferrite,  $A$ , by the following relationship

$$V_{cell} = \oint \mathbf{E} \cdot d\mathbf{l} = -\frac{d}{dt} \int_A \mathbf{B} \cdot d\mathbf{A}$$

$|B|$  must be maintained below the saturation flux density,  $B_{sat}$ , of the ferrite. Thus, the minimum size of the ferrite which fills the accelerator cell must then satisfy the relationship

$$V_{cell} < B_{sat} v_g r_i \ln \left( \frac{r_o}{r_i} \right) \quad (2)$$

Typically,  $B_{sat} \simeq 0.6 \text{ Wb/m}^2$ .

The beam pipe radius,  $R_{pipe}$ , is determined by three competing requirements: reducing growth of the beam break-up instability; designing for high shunt impedance; and designing for minimum cost and weight of the accelerator cell.

The beam break-up (BBU) instability arises from the excitation of azimuthally asymmetric cavity modes in the accelerator cell. These modes are characterized by asymmetric longitudinal electric fields and transverse magnetic field on axis which cause sweeping of the electron beam tail. This instability sets the minimum pipe radius and is therefore critical in determining the cost of the accelerator cells. The radial displacement of the beam,  $\xi$ , resulting from the beam break up instability depends on the pipe radius,  $R_{pipe}$ , gap width,  $w$ , total accelerating voltage,  $V_{acc}$ , beam current,  $I_{beam}$ , gap electric field,  $E_g$ , and focusing magnetic field,  $B$ .

$$\xi \propto \exp(I_{beam} w \Psi V_{acc} / B E_g R_{pipe}^2)$$

The quantity  $\Psi$  depends on the beam interaction with the  $TM_{1n0}$  beam break-up modes of the accelerator cell. The beam interaction with the cell must be minimized by reducing the beam coupling to the cell and lowering the  $Q$  of the cavity. This is accomplished by insuring that the beam induced fields are coupled out of the cell via the accelerator gap and damped in the ferrite.

If a ceramic interface is used its angle is also chosen so that all  $TM$  modes excited by the beam will pass through the ceramic into the ferrite. To preserve beam quality and insure good transmission of the beam through the accelerator, an overall amplification of beam displacement due to BBU of less than five must be maintained.<sup>(7)</sup>

In theory it should be possible to offset the effects of a small beam pipe diameter by arbitrarily increasing the focusing magnetic field. In practice, however, as the focusing field is increased to suppress beam break-up, the number of betatron wavelengths in the accelerator increases. This leads to cork screwing and increased beam break-up excitation. Tuning becomes more complicated as the radial position of the beam becomes a rapidly oscillating function of time.

The operating current, total accelerator voltage, and pulse length of an induction linac are usually restricted by the requirements of the microwave generation device. However, the accelerator cell gap voltage remains an unspecified parameter. The accelerator gradient is linearly proportional to the gap voltage and, therefore, designing for a high gap voltage yields the shortest accelerator. However, the accelerator weight and cost increases rapidly with increasing acceleration gradient. The coupling coefficient (defined as the fraction of electrical pulse energy deposited in the beam) is independent of the gradient and therefore the only penalty paid for reducing the accelerating gradient is an increase in overall length of the accelerator. Additionally, for constant BBU growth the accelerator weight and cost increase exponentially with  $I_{beam}^{1/2}$ . These design considerations are discussed in detail below.

The coupling coefficient,  $K$ , for an induction accelerator cell is found by computing the shunt impedance,  $Z_{shunt} = Z_{line}$ , of the ferrite filled transmission line and the load imposed by the e-beam,  $Z_{beam}$ .

$$K = \frac{Z_{shunt}}{Z_{beam} + Z_{shunt}}$$

where

$$Z_{shunt} = \frac{1}{2\pi} \sqrt{\frac{\mu}{\epsilon}} \ln \left( \frac{r_o}{r_i} \right)$$

$$Z_{beam} = \frac{V_{cell}}{I_{beam}}$$

Under the assumption that the cell gap voltage is related to the minimum ferrite radius by Eq. (2), the shunt impedance and coupling coefficient can be written,

$$Z_{shunt} = \frac{1}{2\pi} \mu \frac{V_{cell}}{B_{sat} r_i}$$

$$K = \frac{1}{1 + \frac{2\pi B_{sat} r_i}{\mu I_{beam}}}$$

A plot of  $K$  versus ferrite core inner radius,  $r_i$ , for several beam currents from 1 kA to 5 kA is shown in Fig. 2.4. The coupling coefficient increases with increasing beam current and decreasing inner radius.

The total cost and weight of the accelerating structure is linearly proportional to the volume of the ferrite core,  $V_{ferrite}$

$$V_{ferrite} = \frac{V_{acc}}{V_{cell}} h \pi (r_o^2 - r_i^2) \quad (3)$$

Using Eq. 2 to solve for  $r_o$  in terms of  $V_{cell}$  and  $B_{sat}$  and substituting into Eq. 3 yields

$$V_{ferrite} = \frac{V_{acc}}{V_{cell}} v_g \tau_p \pi r_i^2 \left( \exp \left( \frac{2V_{cell}}{B_{sat} v_g r_i} \right) - 1 \right) \quad (4)$$

The ferrite core volume required per MeV of acceleration is plotted as a function of accelerator cell gap voltage for several accelerator cell inner radii,  $r_i$ . For large values of the exponential argument in Eq. 4, the ferrite core volume increases exponentially with gap voltage. For a specified gap voltage, there exists an inner radius,  $r_i$ , which yields the smallest ferrite core volume according to Fig. 2.5. Likewise, we can see that the minimum ferrite core volume required is achieved by operating with the lowest possible gap voltage. Other constraints (i.e. restricting the overall length of the accelerator) may restrict the gap voltage to be larger than some minimum value. Figures 2.5 and 2.6 show that designing for the smallest inner core radius and lowest gap field will always yield the most economical design. However, arbitrarily reducing these parameters at fixed beam current will result in the onset of the beam break-up instability.

An assembly drawing of the SNOMAD-IV driver is shown in Fig. 2.6 and Fig. 2.7. Five hundred volt DC power enters through the eight command resonant charge SCRs which are mounted on the left deck of the driver assembly. Eight Intermediate storage SCRs are mounted

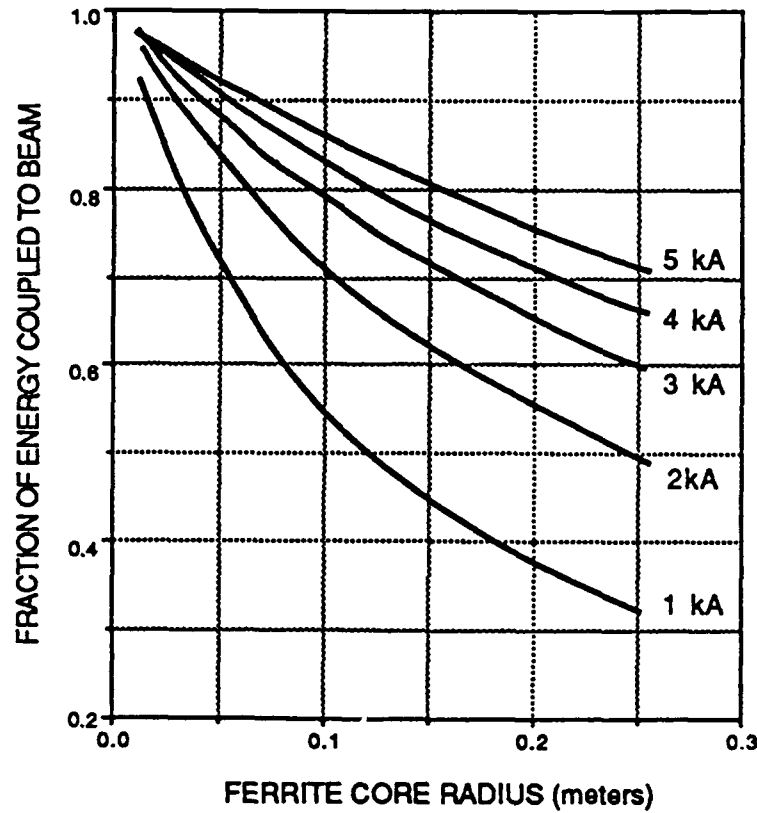


Figure 2.4: Coupling coefficient, K, versus ferrite core inner radius for beam currents from 1 to 5 kA. Ferrite parameters:  $\mu_r = 400$ ,  $\epsilon_r = 12$ .

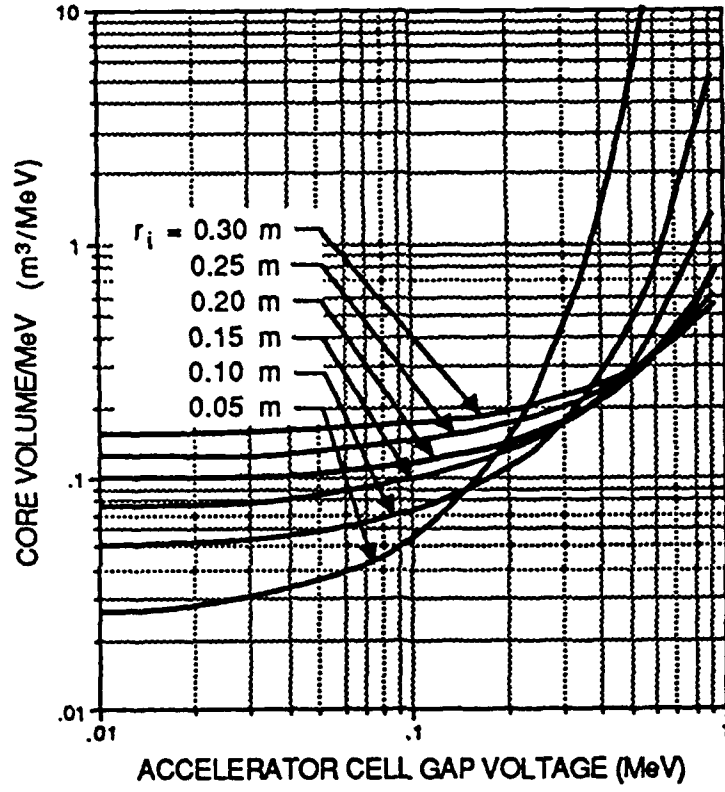
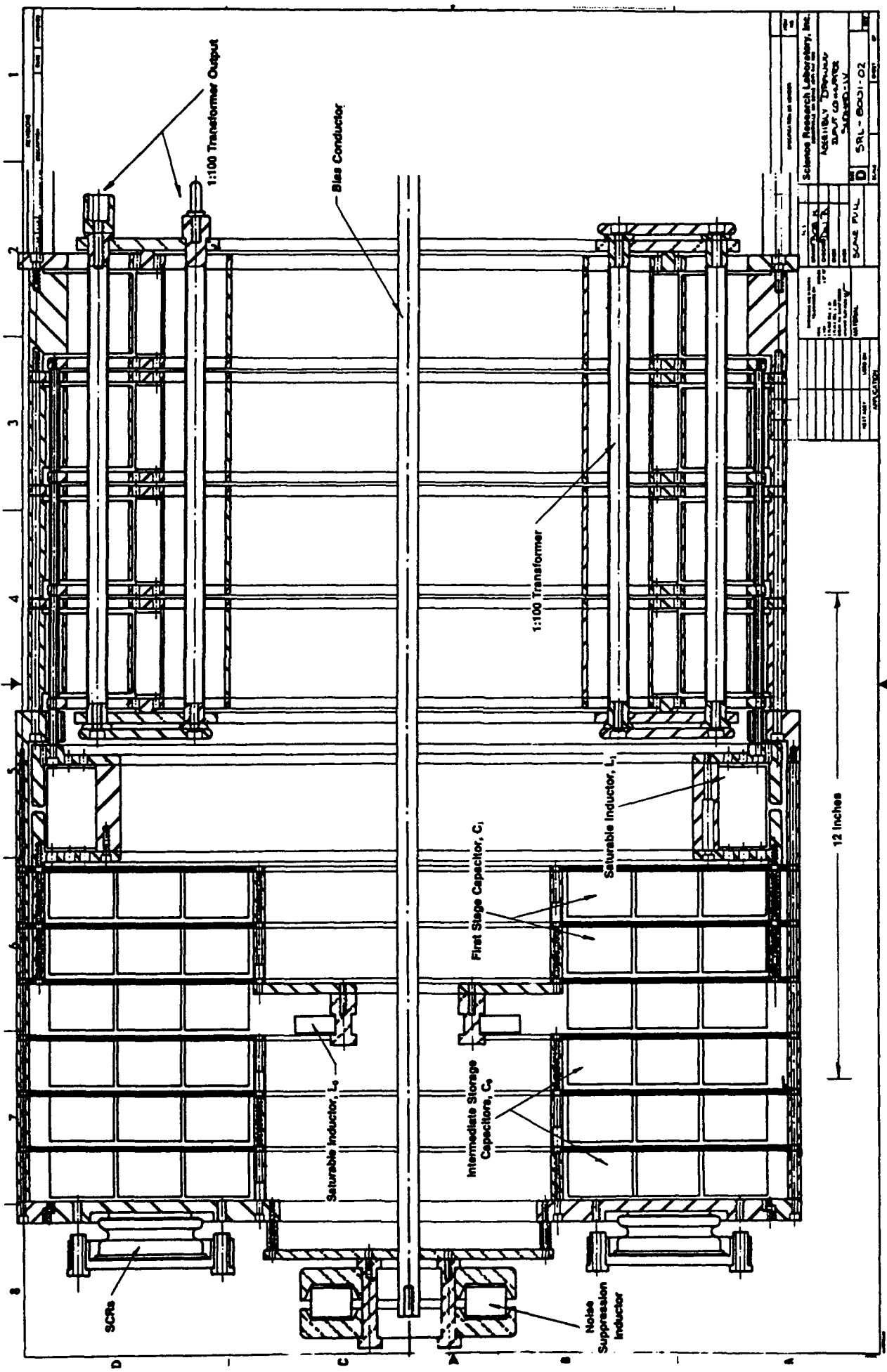


Figure 2.5: Required ferrite core volume,  $\nu_{\text{ferrite}}$ , versus accelerating gap voltage for  $r_i = 0.05, 0.10, 0.15, 0.20, 0.24, 0.30$  meters. Ferrite parameters:  $\mu_r = 400$ ,  $\epsilon_r = 12$ ,  $\tau_p = 50$  nsec.

SCIENCE RESEARCH LABORATORY



# SCIENCE RESEARCH LABORATORY

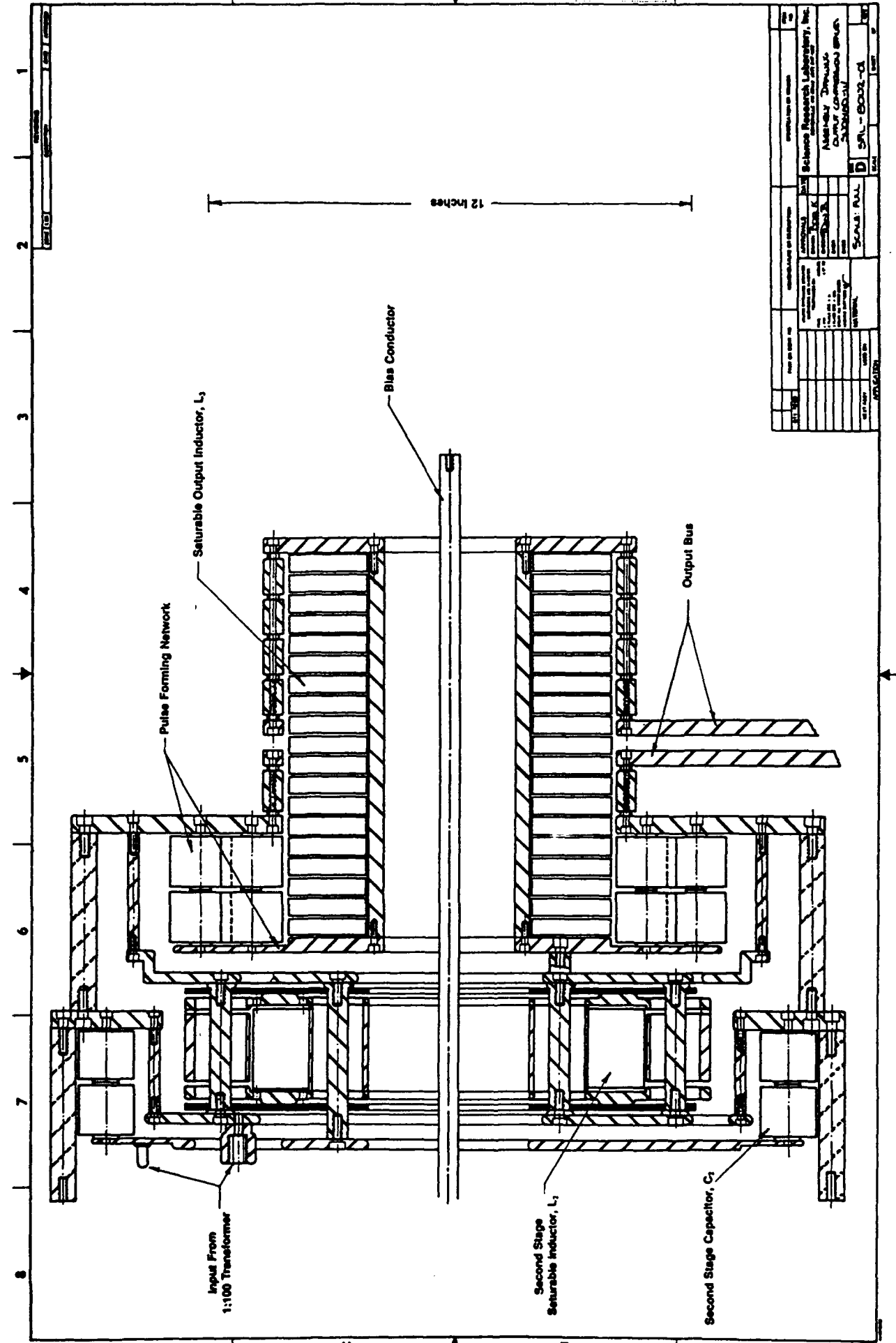


Figure 2.7: Assembly drawing of SNOMAD-IV second compression stage, PFN and output stage.

in reverse polarity from the same deck. The number of SCRs has been chosen so that the dI/dt rating of each device is not exceeded. The saturable inductors, labeled  $L_0$ , isolate the branches of the intermediate storage power supply. These are all wound from a common toroidal core which is mounted on the first compression stage capacitor bank,  $C_1$ . The first stage saturable inductor,  $L_1$ , is single turn design which will utilize a 0.6 mil toroidal metglas core. The discharge of  $C_1$  through  $L_1$  and  $T_1$  to  $C_2$  results in a 5 to 1 temporal compression with a voltage gain of 100. The 1:100 step-up transformer will be wound on four metglas toroidal cores. The design achieves a large step-up ratio with a twenty five turn secondary and fractional, one quarter turn, primary made possible by the use of four transformer cores.

In the second compression stage, high voltage strontium titanate ceramic capacitors,  $C_2$ , will be used. Unlike barium titanate, strontium titanate does not suffer from piezoelectric mechanical failure under high repetition rate operation. The second stage saturable inductor,  $L_2$ , will be a ten turn toroidal inductor wound on a 6.75 inch I.D. X 9.65 inch O.D. X 2 inch wide core.  $L_2$  discharges  $C_2$  into a pulse forming network with a electrical length of 25 nsec. The PFN is a hybrid design consisting of lumped capacitors and distributed inductance. This permits the design to be significantly more compact than either a water filled transmission line or a lumped PFN and allows the electrical length to be varied by the addition of capacitive elements. The output saturable inductor,  $L_3$ , serves as a passive high speed switch to discharge the PFN into the accelerator cell load.  $L_3$  will be constructed using nineteen toroidal ferrite pancakes. A zinc-nickel ferrite has been selected for the output stage to minimize losses and provide fast switching.

A bias conductor, placed on the axis of the driver, will be used for biasing the metglas and ferrite inductor cores into saturation and to provide the reset current between pulses. Both ends of the bias conductor will be terminated with a powdered iron core noise suppression inductor. This prevents electrical noise, generated inside the driver, from being transmitted out along the bias conductor. The assembled driver will be 20 inches in diameter and an overall length of 44 inches. Table 2.2 summarizes the design specifications of the SNOMAD-IV driver.

**Table 2.2: SNOMAD-IV Performance Specifications**

**Input Power Requirements:**

Energy/pulse	57.5 joules
PRF	5 kHz
Power	287.5 KW
Voltage	600 volt
Current	481 Amps

**Command Resonant Charge**

Capacitance	$4 \times 640 \mu\text{fd}$
Voltage	600 volts
Energy	922 joules
Stored charge	1.54 Coulombs
$\tau$ charge	$\leq 120 \mu\text{sec}$
I peak	$1.3 \times 10^3$ Amp
dI/dt	$3.4 \times 10^1$ A/ $\mu\text{sec}$
$I_T$ (RMS)	650 Amps
dI/dt per device	$8.5 \text{ A}/\mu\text{sec}$ (4 $\times$ West Code)
Commutation losses	$\sim 2.5$ joule
Charge Core Type	Powdered Iron
# Turns Charge Core	4 $\times$ 20
Charge Core geometry	$4 \times 4 \times 3.0"$ ID $\times$ 5.218" OD $\times$ .8" Wide
E.R. Core Type	Powdered Iron
# Turns E.R. Core	60
Core geometry	$4 \times 2 \times 3.0"$ ID $\times$ 5.218" OD $\times$ .8" Wide

**Intermediate Storage**

Capacitance	$90.8 \mu\text{fd}$
Voltage	1,100 volts
Energy	55 joules
Stored charge	$10.0 \times 10^{-2}$ Coulombs
$\tau$ discharge	$\leq 7.5 \mu\text{sec}$
I peak	$20.9 \times 10^3$ Amp
dI/dt	$8.77 \times 10^3$ A/ $\mu\text{sec}$
$I_T$ (RMS)	2773 Amps
dI/dt per device	$1096 \text{ A}/\mu\text{sec}$ (8 $\times$ West Code)
Sat. Asst. Core Type	CMD-5005
# Turns	16 $\times$ 5
Core geometry	3.5" ID $\times$ 5.8" OD $\times$ .5" Wide
Commutation losses	$\sim 2.5$ joule

**1<sup>st</sup> Stage**

Capacitance	$90.8 \mu\text{fd}$
Voltage	1075 volts
Energy	52.5 joules
Core Type	.6 Mil $\times$ 2605 CO

**Table 2.2: SNOMAD-IV Performance Specifications (Continued)**

# Turns	1
Core geometry	$1 \times 15.3'' \text{ ID} \times 17.8'' \text{ OD} \times 2'' \text{ Wide}$
$\int V \cdot dt$	$\sim 4 \times 10^{-3} \text{ Vsecs}$
Lsat	$1.588 \text{ nh} + .4 \text{ nh (STRAY)} = 1.988 \text{ nh}$
$\tau$ discharge	944 nsec
Losses	$\sim 1.275 \text{ joules (.675 cores, .6 caps)}$
Core volume	$21.557 \times 10^{-4} \text{ m}^3, 10.8 \text{ kg}$
<b>Transformer</b>	
Core Type	2605S3A
# Turns (PRIM)	1/5
# Turns(sec)	20
Losses	$\leq .5 \text{ joules}$
Peak stress	76.7 kV/cm at 107/2 kV (.5" dia. Rod in 1.50 " dia. hole)
Core geometry	$5 \times 12'' \text{ ID} \times 13.5'' \text{ OD} \times 2'' \text{ wide}$
<b>2<sup>nd</sup> Stage</b>	
Capacitance	8.96 nfd
Voltage	106.4 kV
Energy	50.72 joules
Core type	2605 CO Metglass
Core Geom.	$1 \times 6.75'' \text{ ID} \times 9.65'' \text{ OD} \times 2'' \text{ w}$ ( $1.224 \times 10^{-3} \text{ M}^2$ )
$\int V \cdot dt$	$12 \text{ Turns} \times 4.80 \text{ Vmsecs/Turn} =$ 106 kV <sup>*</sup> (1.082 usecs/2)
LSAT	.556 $\mu\text{h}$ + .1 $\mu\text{h}$ stray $\simeq .656 \mu\text{h}$
$\tau$ discharge	170.7 nsec
Losses	$\sim 1.05 \text{ joules}$
<b>Output Stage</b>	
Capacitance	9.4 nfd
Voltage	102.8 kV
Energy	49.67 joules
Core type	CN-20 Ferrite
Core Geom.	$18 \times 4'' \text{ ID} \times 8'' \text{ OD} \times .5'' \text{ w}$
$\int V \cdot dt$	$1 \text{ Turns} \times 8.16 \times 10^{-3} \text{ usecs/Turn} =$ 102 kV (160 nsec/2)
LSAT	31.2 nh
$\tau$ discharge	$\sim 40 \text{ nsec into } 6 \text{ nfd}$
Losses	$\sim 2 \text{ joules}$

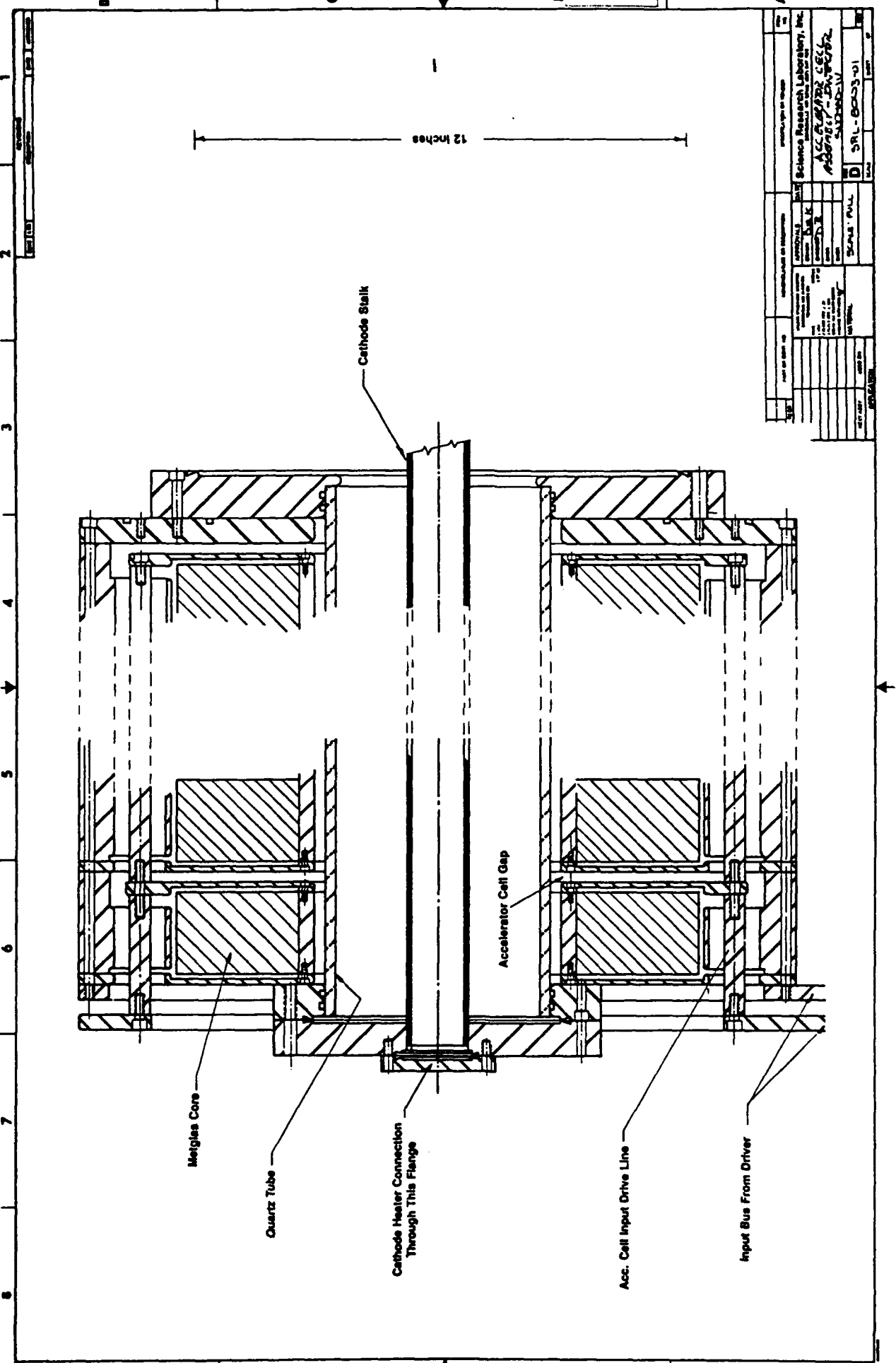
The SNOMAD-IV driver is capable of powering a 0.5 MeV injector induction cell assembly. In the injector these cells utilize metglas core induction cells. An assembly drawing of the injector showing the induction cells, drive line, cathode stalk and input bus from the driver is shown in Fig. 2.8.

Each induction cell uses a metglas core measuring 6.75 inches I.D. X 12.75 inches O.D. X 2 inches wide. The choice of metglas over ferrite was chosen as a core material for several compelling reasons. The saturation flux density of metglas is a factor of five times higher than nickel-zinc ferrites, allowing a significantly more compact design. In addition, a significant cost savings is realized by using metglas and large toroidal cores are more easily fabricated than ferrite cores. The primary disadvantage of a metglas filled induction cell design are limitations imposed by its electrical pulse performance characteristics. A metglas filled cell exhibits characteristics which are inductive rather than transmission like. As a result, the electrical impedance of the cell decreases as a function of pulse duration. In contrast, the ferrite filled cell presents a constant impedance for the duration of the pulse. This difference can manifest itself by producing an inductive voltage droop during the pulse. The impact is severe on the pulse shape. The square output pulse from the SNOMAD-IV driver is rounded at the beginning by the capacitance of the metal tape wound cores and then the lumped inductance causes a droop toward the end of the pulse. For purposes such as X-ray sterilization and E-Beam processing these effects cause little trouble. For the purposes of an FEL the results are quite serious.

The injector assembly and the 1 MeV module assembly will differ in design in two significant ways. The injector will utilize a quartz tube as the vacuum interface. This design eliminates many sealing joints and simplifies the construction, cooling and insulation of the accelerator cells. The simplified design is made possible because there is no electron beam present in the injector cells. Electron beam propagation in the accelerator cells require that the walls be of a conducting material to prevent charge accumulation which results from lost beam electrons. Therefore, the accelerator modules will employ o-ring sealed ceramic insulators in each of the accelerator gap. In addition, each induction cell used in the accelerator module will be fitted

SCIENCE RESEARCH LABORATORY

Figure 2.8: Drawing of SNOMAD-IV 0.5 MeV injector accelerator cell assembly.



with a solenoidal focusing magnet which is required for the propagation of high current e-beam propagation.

The injector module will be fitted with a cathode assembly and vacuum pump housing as shown in Fig. 2.9. A 3.5 inch diameter dispenser cathode will be mounted at the end of the cathode stalk and will supply up to 600 amps of electron beam current. The cathode, cathode shroud and anode ring geometry establish the charged particle extraction optics. The radius of curvature of the cathode surface determines the degree of convergence of the extracted beam.

The SNOMAD-IV driver and accelerator cell assembly is housed in a rectangular aluminum enclosure which supplies cooling and electrical shielding to both units. All high voltage bus connections between the driver and induction cells will be made within enclosure forming a self contained 1 MeV accelerator module. External connections to the module will include: 500 volt DC prime power, low voltage timing signals, and entrance and exit ports for the beam.

Several concepts have been investigated for providing cooling and electrical insulation for the driver and accelerator components within the enclosure. A freon vapor environment is sufficient to provide the necessary peak electric field break-down strength of 70 kV/cm, and will permit the accelerator to operate at a repetition rate of 20 kHz for several seconds or an average repetition rate of up to 1 kHz for an indefinite period of time. Heat removal is accomplished by transferring heat to the aluminum tank without additional heat exchangers or coolers. Filling the tank with liquefied freon or transformer oil will permit the accelerator to operate at an average repetition rate of 5 kHz for an indefinite period. In this mode of operation, the aluminum tank can not dissipate sufficient heat and must be assisted by a water cooled heat exchanger mounted within the tank.

For applications such as ECH in present generation tokamak devices, the most likely operating scenario for the proposed accelerator would require very high repetition rates (20 kHz) for short periods of time (up to several seconds) followed by extended inoperative periods (several minutes). Vapor cooling or passive oil cooling will provide sufficient heat removal for this mode of operation. Assembly drawings of the enclosure are shown in Figs. 2.10 and 2.11.

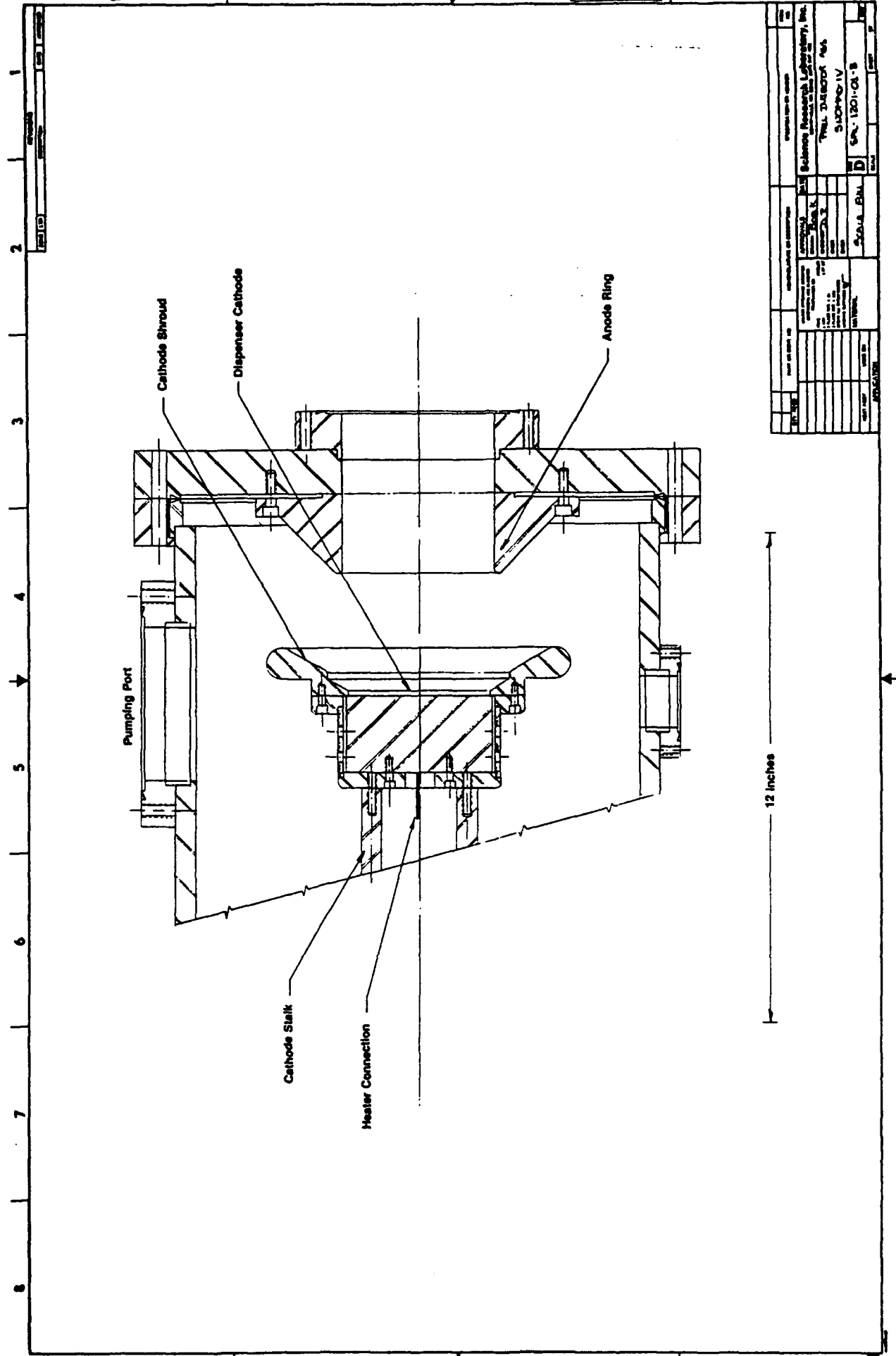
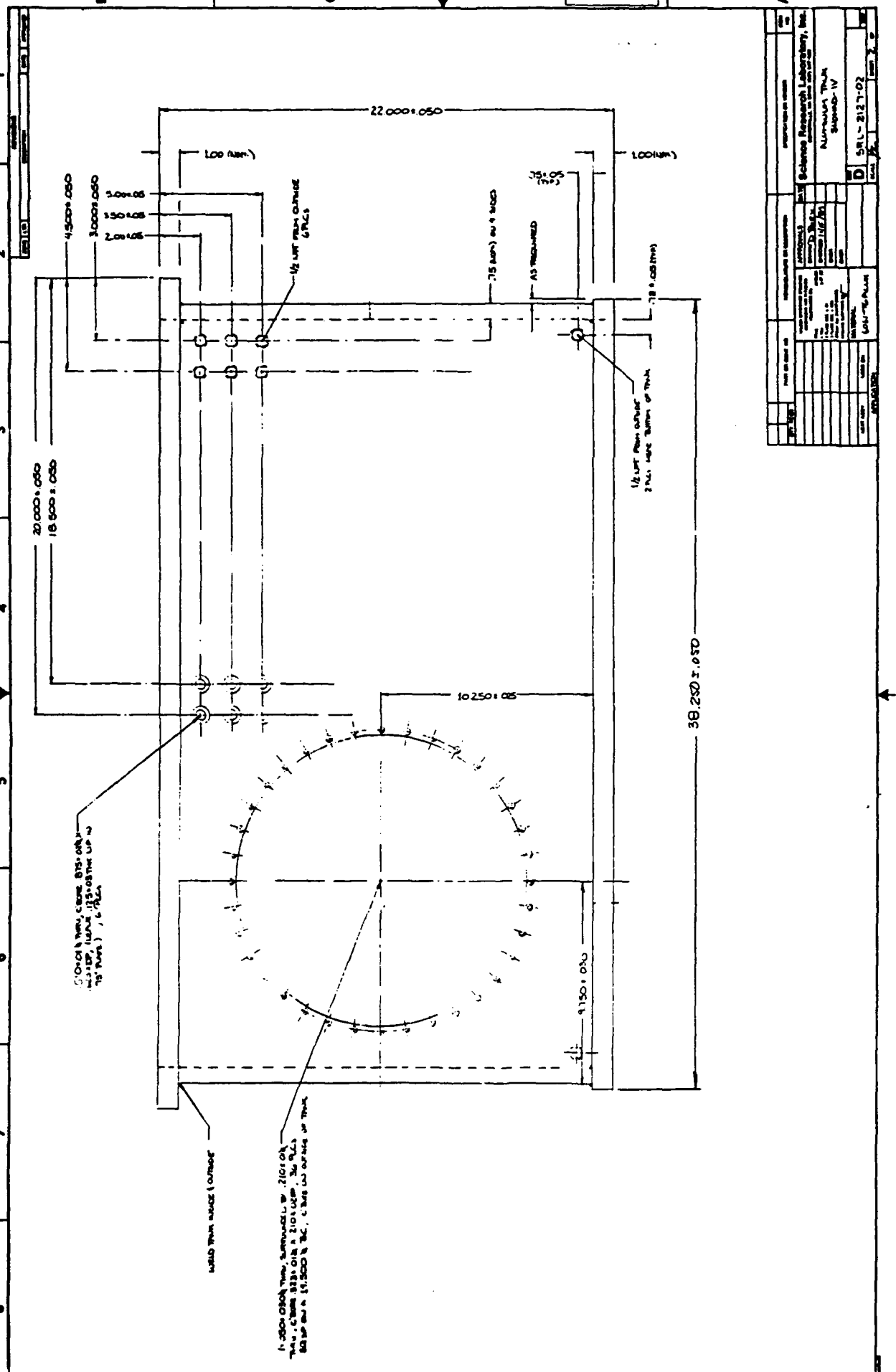


Figure 2.9: Preliminary assembly drawing of cathode extraction optics and vacuum pumping port.

# SCIENCE RESEARCH LABORATORY

Figure 2.10: SNOMAD-IV Enclosure, elevation

SNOMAD-IV Enclosure		Dimensions	
Overall dimensions		Dimensions	
Length	22.000 ± 0.050	Width	10.000 ± 0.050
Height	18.900 ± 0.050	Depth	10.250 ± 0.050
Door dimensions		Door dimensions	
Width	18.900 ± 0.050	Height	7.750 ± 0.050
Floor dimensions		Floor dimensions	
Width	18.900 ± 0.050	Length	38.250 ± 0.050
Ceiling height		Ceiling height	
1.500 ± 0.050		1.500 ± 0.050	
Floor area		Floor area	
18.900 ± 0.050		10.250 ± 0.050	
Volume		Volume	
19.500 ± 0.050		10.250 ± 0.050	
Weight		Weight	
1000 kg		1000 kg	
Material		Material	
Aluminum		Aluminum	
Design		Design	
SNOMAD-IV		SNOMAD-IV	
Date		Date	
10/27/02		10/27/02	



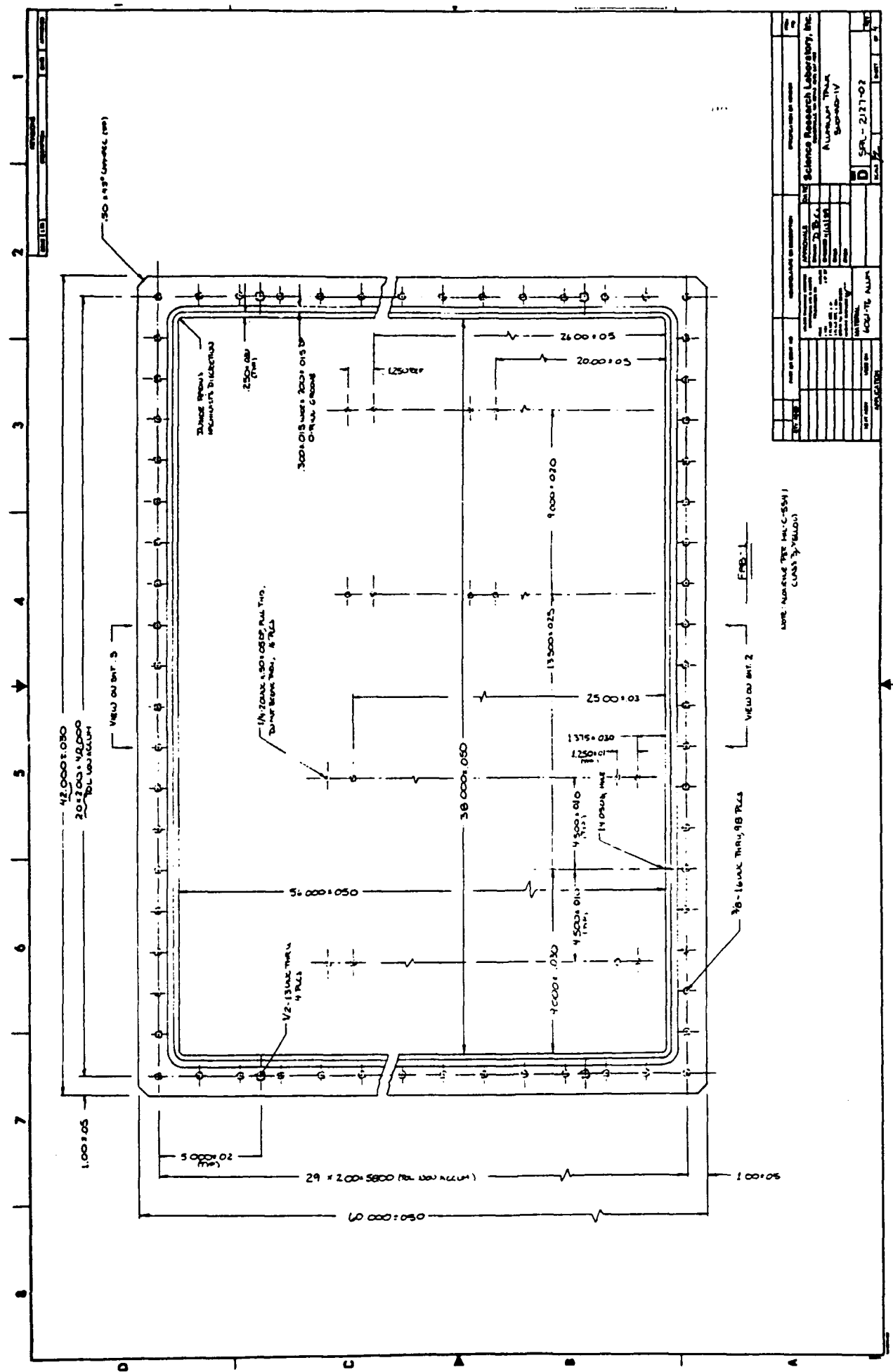


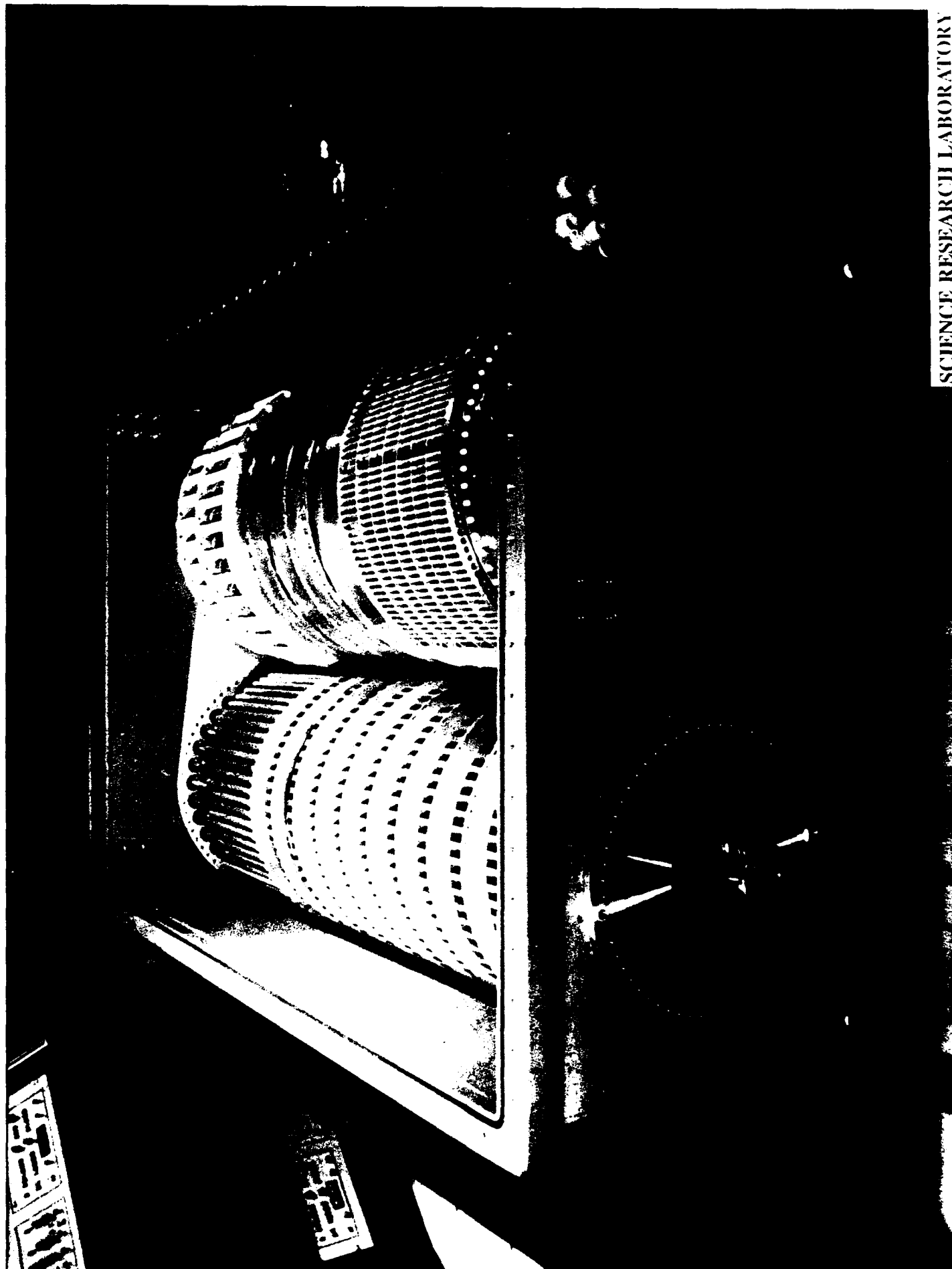
**Figure 2.11:** SNOMAD-IV Enclosure, plan view

SCIENCE RESEARCH LABORATORY

It is planned that after fabrication, assembly and high repetition rate testing of the SNOMAD-IV injector module, the device will be installed in a laboratory at the MIT Plasma Fusion Center which is equipped to provide power, radiation shielding and computerized control. Under the supervision of Dr. Richard Temkin, the accelerator will be made available to research members of the Fusion Center for developing and testing high power millimeter wave sources. SRL will assist in training MIT personnel in the operation and maintenance of the accelerator. The goal of this task will be to gain field experience in operating and maintaining a production prototype of the accelerator module. Information and experience gathered in this effort will be used to improve upon subsequent accelerator designs.

The nearly completed SNOMAD-IV injector is pictured in Fig. 2.12 as is appeared in SRL's Oakley, California facility before shipment. SNOMAD-IV is now housed temporarily in a shielded pit at SRL's Boston, Mass. facility (Fig. 2.13). Here it is being used for a variety of experiments until its new home is completed at the MIT Plasma Fusion Center.

The operating parameters of the SNOMAD-IV injector are represented by the oscilloscope traces in Fig. 2.14. The ringing on the voltage waveform is an artifact of the voltage diagnostic as indicated by the current waveform which should scale as directly as  $V^{1.5}$ . The droop caused by the Metglas accelerator cores is plainly evident on the current waveform.



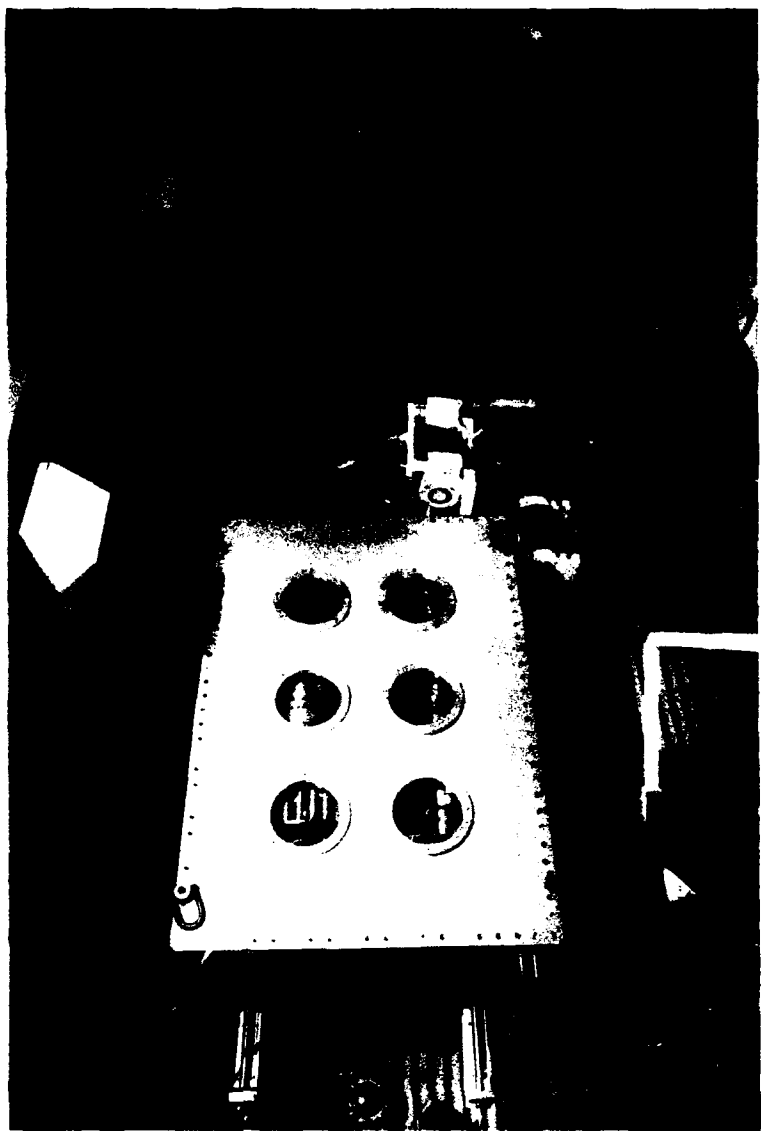


Fig. 2.13 :The 500 kV induction accelerator and x-ray target (inside the blue lead box) assembly in the experiment vault.

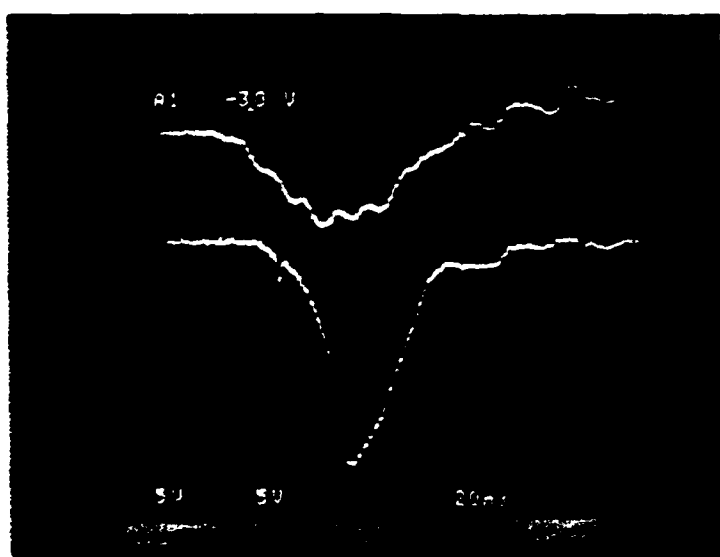


Figure 2.14: Current (lower) and voltage (upper) pulse waveforms of the electron beam. The peak voltage and current are 493 kV and 406 A, respectively.

## **SECTION 3**

### **SNOMAD-IVB, 1.0 MeV INDUCTION ACCELERATOR MODULE**

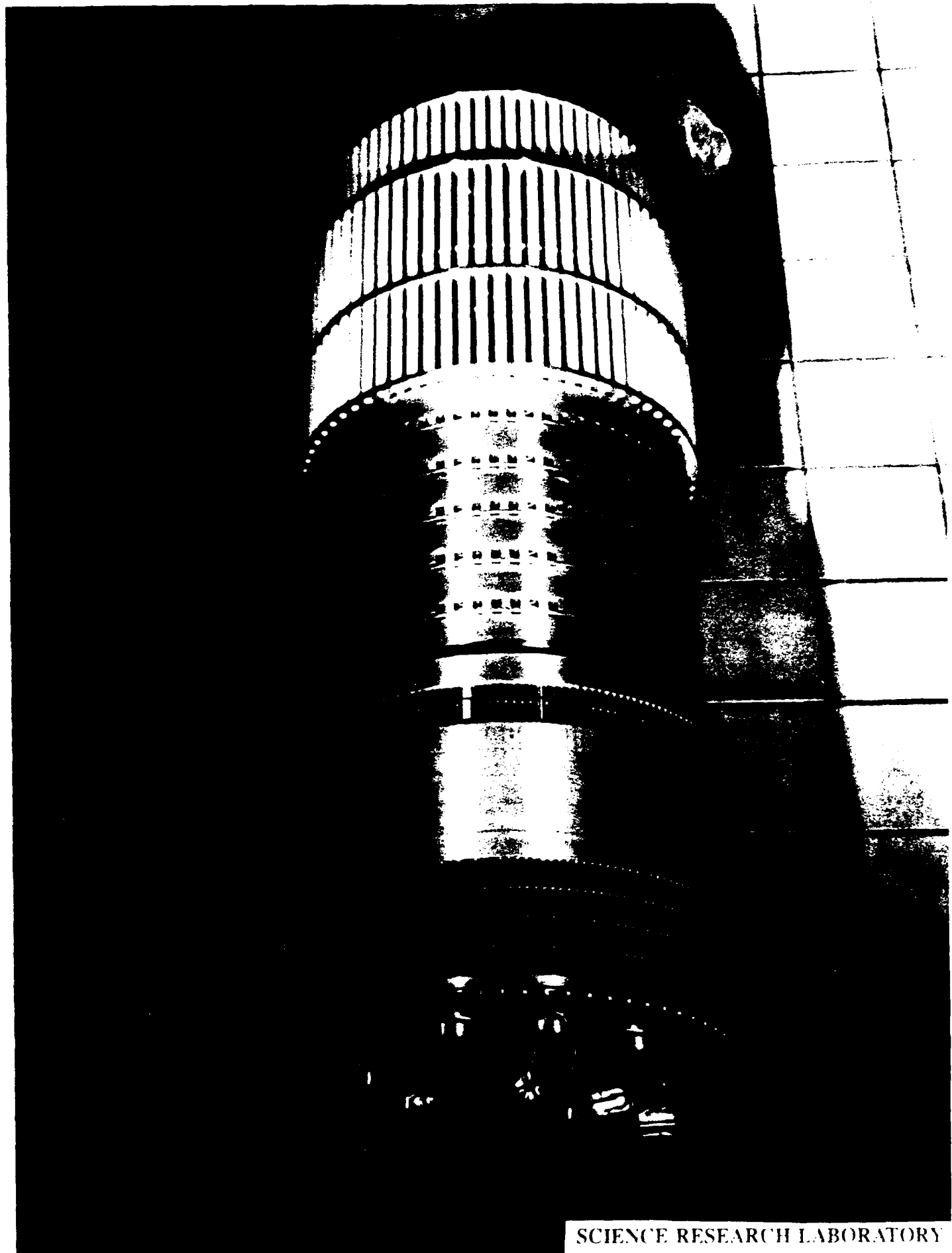
The first SNOMAD-IVB 1.0 MeV accelerator module is nearing completion. When it is finished it will be temporarily installed in line with the SNOMAD-IV injector at SRL's Boston facility. This will result in an upgrade from 0.5 MeV to 1.5 MeV for that facility. As with the SNOMAD-IV injector, the long term goal is to install this module at the MIT Plasma Fusion Center. In the meantime it will be used for studies on e-beam processing.

The SNOMAD-IVB driver (Fig. 3.1) is somewhat larger than the SNOMAD-IV and supplies more than 1.5 times the output energy. A list of specifications for the SNOMAD-IVB driver is supplied in Table 3.1.

The fourteen SNOMAD-IVB accelerator are each designed to operate at 70 kV. Unlike the SNOMAD-IV injector, we have learned our lesson and have returned to the use of ferrite in the accelerator cells. Sometime in the future it is likely that we will upgrade the injector with ferrite loaded induction cells. A picture of three induction cells during assembly is provided in Fig. 3.2. The photographs presented in Figs. 3.3-3.5 show the SNOMAD-IVB module in various stages of assembly.

To date we have not installed this new module on the beamline for final testing but we did manage to run it for a while as it stood in the assembly area. Unfortunately we were not able to evacuate the e-beam transport tube and the end result was the breakdown in the 1 Atm air limited operation to less than 600 kV. The voltage waveform measured during these tests appears in Fig. 3.6.

Aside from the higher operating energy, the operation of the SNOMAD-IVB accelerator modules is virtually identical to that of the SNOMAD-IV injector. With this in mind we will avoid a repetition of the description provided in the previous section and jump to one of the more recent advances incorporated with SNOMAD-IVB. Previously we have always used a simple



SCIENCE RESEARCH LABORATORY

Figure 3.1: SNOMAD-IVB Driver

**Table 3.1: SNOMAD-IVB Performance Specifications**

**Input Power Requirements:**

Energy/pulse	75 Joules
PRF	5 kHz
Power	375 KW
Voltage	600 volt
Current	625 Amps

**Command Resonant Charge**

Capacitance	$4 \times 640 \mu\text{fd}$
Voltage	600 volts
Energy	922 Joules
Stored charge	1.54 Coulombs
$\tau$ charge	$\leq 120 \mu\text{sec}$
I peak	$2.14 \times 10^3$ Amp
dI/dt	$5.6 \times 10^1$ A/ $\mu\text{sec}$
$I_T$ (RMS)	1073 Amps
dI/dt per device	14 A/ $\mu\text{sec}$ (4 $\times$ West Code)
Commutation losses	$\sim 2.5$ Joule
Charge Core Type	Powdered Iron
# Turns Charge Core	4 $\times$ 20
Charge Core geometry	$4 \times 4 \times 3.0"$ ID $\times$ 5.218" OD $\times$ .8" Wide
E.R. Core Type	Powdered Iron
# Turns E.R. Core	60
Core geometry	$4 \times 2 \times 3.0"$ ID $\times$ 5.218" OD $\times$ .8" Wide

**Intermediate Storage**

Capacitance	150 $\mu\text{fd}$
Voltage	1,000 volts
Energy	75 Joules
Stored charge	$15.0 \times 10^{-2}$ Coulombs
$\tau$ discharge	$\leq 10.0 \mu\text{sec}$
I peak	$23.5 \times 10^3$ Amp
dI/dt	$7.39 \times 10^3$ A/ $\mu\text{sec}$
$I_T$ (RMS)	3602 Amps
dI/dt per device	924 A/ $\mu\text{sec}$ (8 $\times$ West Code)
Sat. Asst. Core Type	CMD-5005
# Turns	16 $\times$ 5
Core geometry	3.5" ID $\times$ 5.8" OD $\times$ .5" Wide
Commutation losses	$\sim 5$ Joule

**Table 3.1: SNOMAD-IVB Performance Specifications (Continued)**

**1<sup>st</sup> Stage**

Capacitance	160 $\mu$ fd
Voltage	935 volts
Energy	70 Joules
Core Type	.6 Mil $\times$ 2605 CO
# Turns	1
Core geometry	$1 \times 14.875"$ ID $\times$ 17.8" OD $\times$ 2" Wide
$\int V \cdot dt$	$\sim 4 \times 10^{-3}$ Vsecs
Lsat	$1.888 \text{ nh} + .4 \text{ nh (STRAY)} = 2.288 \text{ nh}$
$\tau$ discharge	1344 nsec
Losses	$\sim 3.275 \text{ Joules (1.675 cores, 1.6 caps)}$
Core volume	$21.557 \times 10^{-4} \text{ m}^3, 10.8 \text{ kg}$

**Transformer**

Core Type	2605S3A
# Turns (PRIM)	1/7
# Turns(sec)	20
Losses	$\leq 1.5 \text{ Joules}$
Peak stress	93.2 kV/cm at 130/2 kV (.5" dia. Rod in 1.50 " dia. hole)
Core geometry	$7 \times 12"$ ID $\times$ 13.5" OD $\times$ 2" wide

**2<sup>nd</sup> Stage**

Capacitance	8.16 nfd
Voltage	126.4 kV
Energy	65.2 Joules
Core type	2605 SC Metglass
Core Geom.	$2 \times 6.75"$ ID $\times$ 9.65" OD $\times$ 2" w ( $2.448 \times 10^{-3} \text{ M}^3$ )
$\int V \cdot dt$	12 Turns $\times$ 8.23 Vmsecs/Turn = 126 kV* (.157 usecs/2)
LSAT	$1.098 \mu\text{h} + .3 \mu\text{h stray} \simeq 1.398 \mu\text{h}$
$\tau$ discharge	237 nsec
Losses	$\sim 2.05 \text{ Joules}$

**3<sup>rd</sup> Stage**

Capacitance	8.4 nfd
Voltage	122.6 kV
Energy	63.15 Joules
Core type	2605 SC Metglass
Core Geom.	$1 \times 5.0"$ ID $\times$ 6.8" OD $\times$ 2" w ( $.546 \times 10^{-3} \text{ M}^3$ )
$\int V \cdot dt$	6 Turns $\times$ 2.55 Vmsecs/Turn = 122.6 kV* (.250 usecs/2)
LSAT	$.118 \mu\text{h} + .05 \mu\text{h stray} \simeq .168 \mu\text{h}$
$\tau$ discharge	83.4 nsec
Losses	$\sim 2.0 \text{ Joules}$

**Table 3.1: SNOMAD-IVB Performance Specifications (Continued)**

**Output Stage**

Capacitance	8.6 nfd
Voltage	119.25 kV
Energy	61.15 Joules
Core type	CN-20 Ferrite
Core Geom.	$13 \times 4'' \text{ ID} \times 8'' \text{ OD} \times .5'' \text{ w}$
$\int V \cdot dt$	$1 \text{ Turns} \times 5.04 \times 10^{-3} \text{ usecs/Turn} = 120 \text{ kV (85 nsec/2)}$
LSAT	23 nh
$\tau_{\text{discharge}}$	$\sim 31 \text{ nsec into } 8.6 \text{ nfd}$
Losses	$\sim 2 \text{ Joules}$

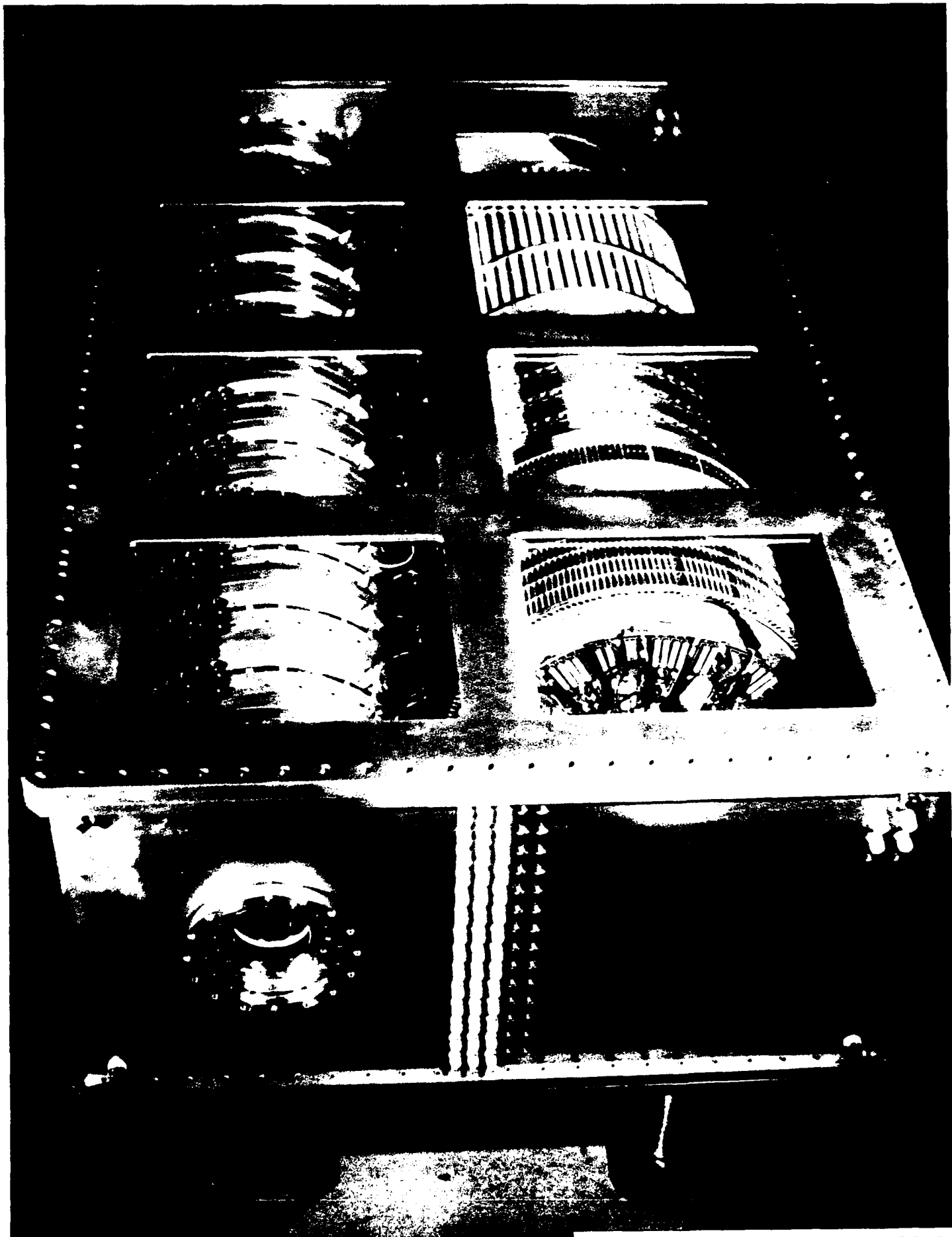
**Peaking Switch**

Peaking Capacitance	1.3 nfd
Voltage	120 kV
Energy	9.36 Joules
Core type	CMD-5005 Ferrite
Core Geom.	$3 \times 4'' \text{ ID} \times 8'' \text{ OD} \times .5'' \text{ w}$
$\int V \cdot dt$	$1 \text{ Turns} \times 1.15 \times 10^{-3} \text{ usecs/Turn} = 120 \text{ kV (18 nsec/2)}$
LSAT	5.28 nh
$\tau_{\text{rise}}$	$\sim 1.5 \text{ nsec into } 3.75 \Omega$
Losses	$\sim 1 \text{ Joules}$



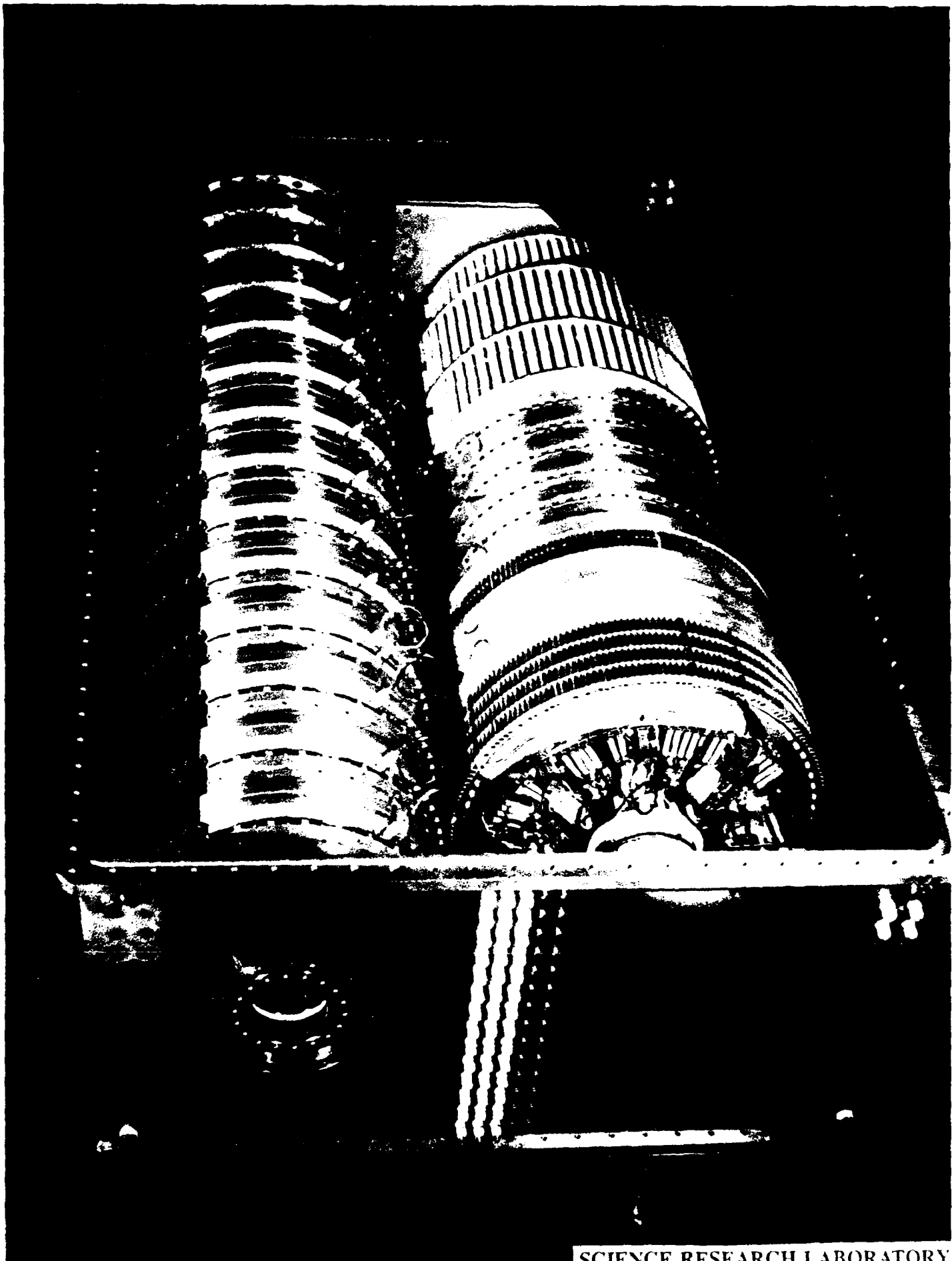
SCIENCE RESEARCH LABORATORY

Figure 3.2: SNOMAD-IVB Accelerator Cells



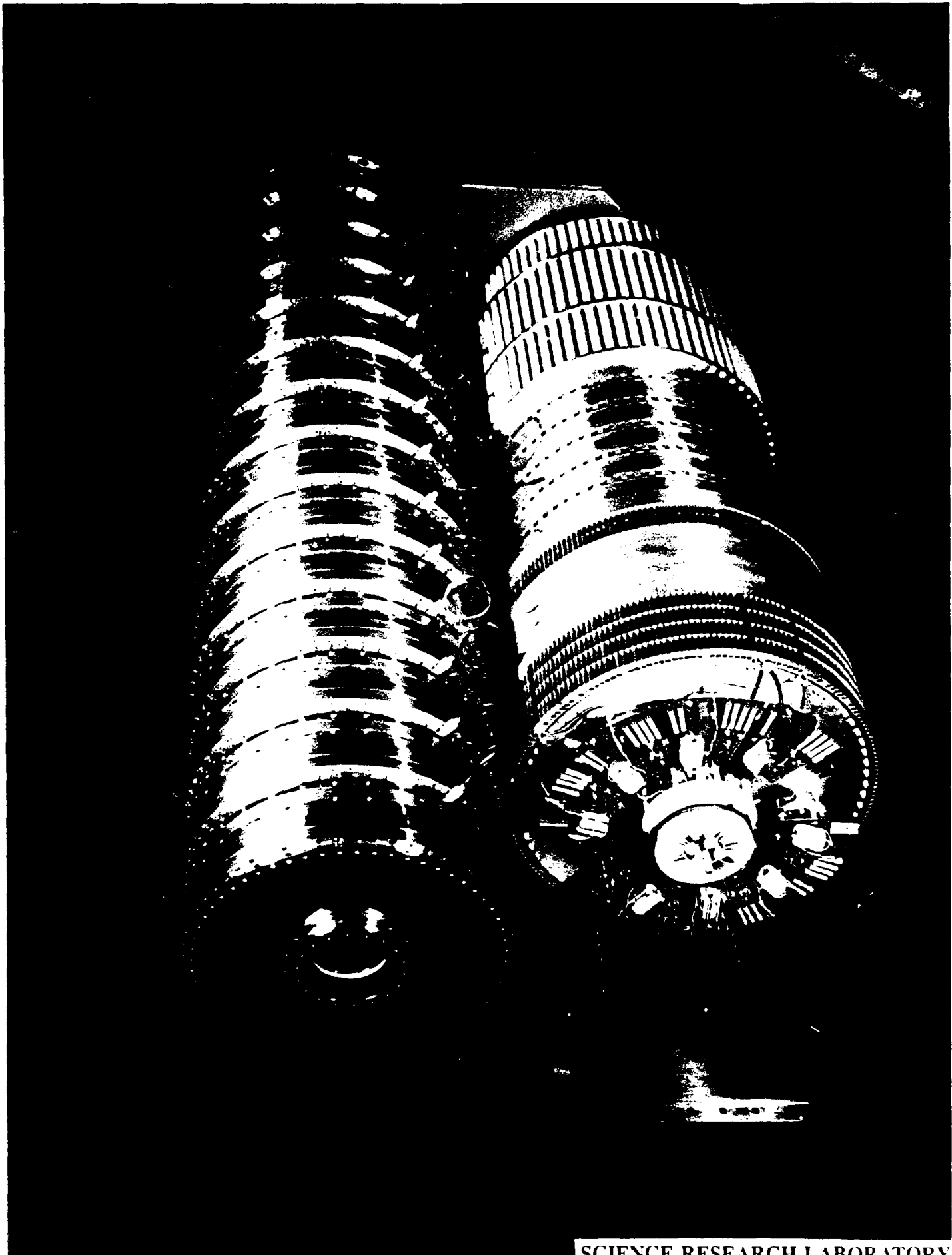
**SCIENCE RESEARCH LABORATORY**

Figure 3.3: Completed SNOMAD-IVB, 1.0 MeV Accelerator Module



**SCIENCE RESEARCH LABORATORY**

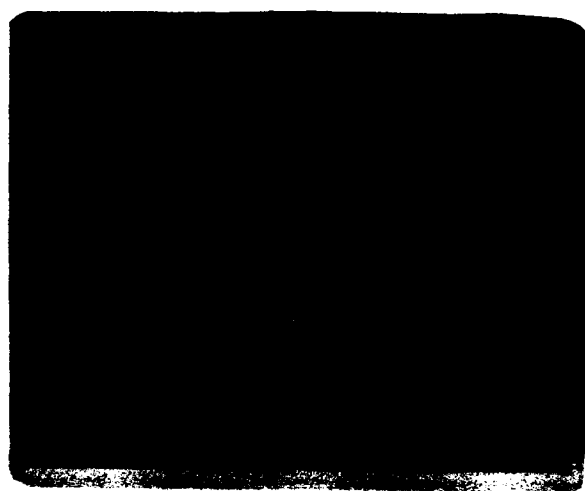
Figure 3.4: SNOMAD-IVB, 1.0 MeV Accelerator Module in Box with Lid Removed.



SCIENCE RESEARCH LABORATORY

Figure 3.5: SNOMAD-IV; 1.0 MeV Accelerator Module Before Installation  
in Box

**SNOMAD-IVB Voltage Waveform During Initial Tests\***



**250kV/d , 20ns/d**

**Figure 3.6**

\*Voltage was limited by electrical breakdown in unevacuated transport tube.

Command Resonant Charge scheme for supplying the per pulse energy to these accelerator modules. Any variations in the supply voltage appeared as a variation in accelerating potential. We have recently developed a controlled charging scheme based on IGBTs (Insulated Gate Bipolar Transistors).

The charge module bears the responsibility of charging the intermediate storage capacitor in SNOMAD-IV accelerator module to a predetermined voltage between output pulses. It was also acquire the reflected energy from the accelerator and add it to the energy required for the next pulse immediately following each discharge cycle.

The charge module must provide the same voltage on the intermediate storage capacitor for each succeeding pulse independent of power supply variations and changes in the reflected power. The charging level is controlled by varying the On-state duration of an IGBT. A photograph of the SNOMAD-IVB charge module appears in Fig. 3.7.

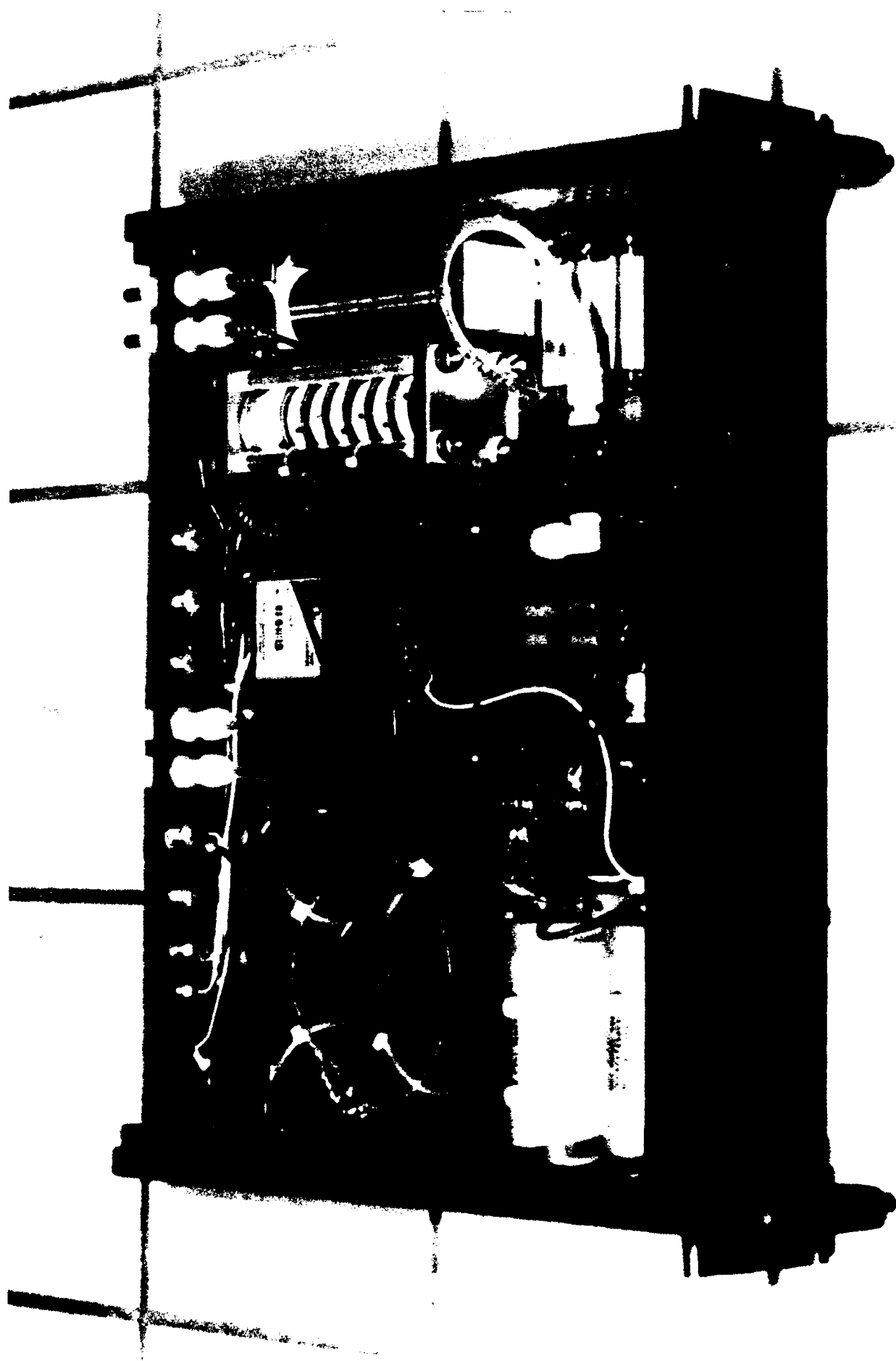
On a scale of peak-power-handling, IGBTs fit in the region between MOSFETs and SCRs. MOSFETs and IGBTs can operate as opening switches and SCRs cannot. An SCR can only be brought out of conduction by reducing the conducted current to near zero. IGBTs (MOSFETs) can be brought out of conduction even at the full current rating by simply reducing the voltage to zero on the Gate-Emitter (Gate-Source) connections.

IGBTs differ from MOSFETs in that MOSFETs are a majority carrier device and IGBTs are minority carrier device like all bipolar transistors. Majority carrier devices offer low drive requirements and high switching speeds but high conduction losses and a dangerous positive temperature coefficient of the on-state resistance. That is, as the junction temperature of a majority carrier device rise so does the on-state resistance and therefore the voltage drop increases at a given current as the temperature rises. The hotter the device becomes the more power is dissipated and therefore the hotter it becomes.

IGBTs, like conventional bipolar transistors, are a minority carrier device and exhibit a negative temperature coefficient of on-state resistance. As the junction temperature rises the on-state resistance decreases and therefore the voltage drop decreases at a given current with increasing

SCIENCE RESEARCH LABORATORY

Figure 3.7: Charge Module



temperature. The hotter the device becomes the less power is dissipated. Historically, the disadvantage of bipolar transistors has been the enormous drive requirements. IGBTs eliminate the large drive requirement by incorporating a MOSFET driver on the same chip with the bipolar transistor. This MOSFET supplies the drive to the bipolar transistor and we wind up with a device which provides the best of both worlds. The input drive requirements and turn-on characteristics match the superior performance of a MOSFET while the power handling capability models that of a bipolar transistor. Because of this IGBTs are rapidly replacing MOSFET in inverter power supply and many other applications.

When the IGBT is brought out of conduction the charging cycle can not be immediately terminated. There is energy stored in the charging inductor and that energy must go somewhere. The incorporation of a free wheeling diode to ground allows the energy stored in the charge inductor to be transferred into the intermediate storage capacitor after the IGBT conduction cycle is terminated. The final charge voltage will not be simply determined by the intermediate storage capacitor voltage level when the IGBT is brought out of conduction but will also hinge on the current level flowing in the charge inductor at that time.

The SNOMAD-IVB control module must base its decision on two input variables. It must measure the current flowing in the inductor and the voltage appearing on the intermediate storage capacitor. It is simple to show be energy conservation the

$$1/2CV_f^2 = 1/2CV_i^2 + 1/2LI^2$$

and the current can easily be determined by applying the rule that

$$I = CdV/dt .$$

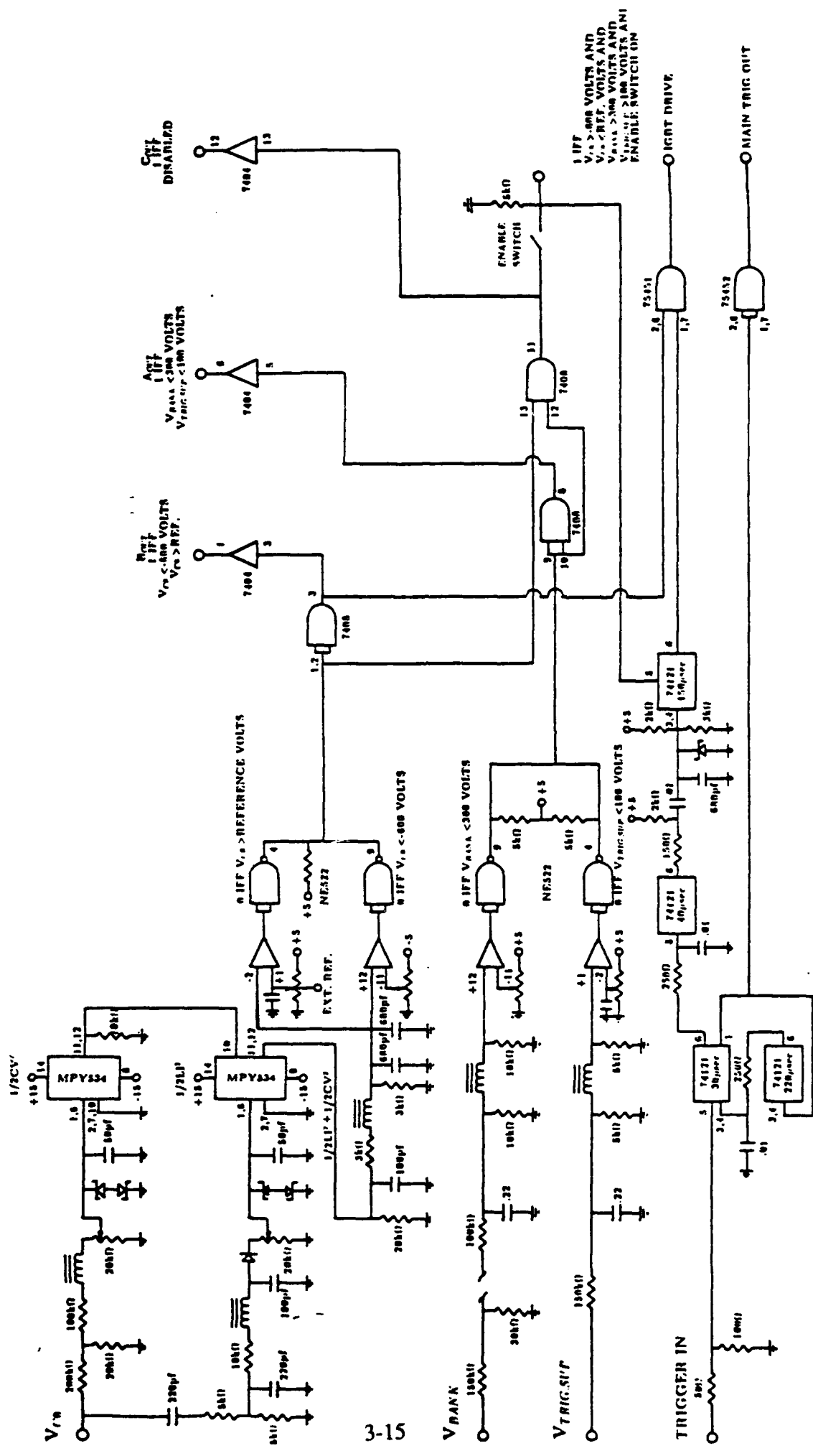
The SNOMAD-IVB control module contains a small analog computer which precisely measures the voltage and its derivative and then makes the determination of the final charge voltage based on the following equation.

$$V_f = \sqrt{V_i^2 + L(dV/dt)^2}$$

The SNOMAD-IVB control module also compares power supply levels and intermediate storage charging levels to predetermined limits and discontinues the driver operation if these levels fall outset these limits. It also bears responsibility of triggering the SCRs in the SNOMAD-IVB compression module at the appropriate time.

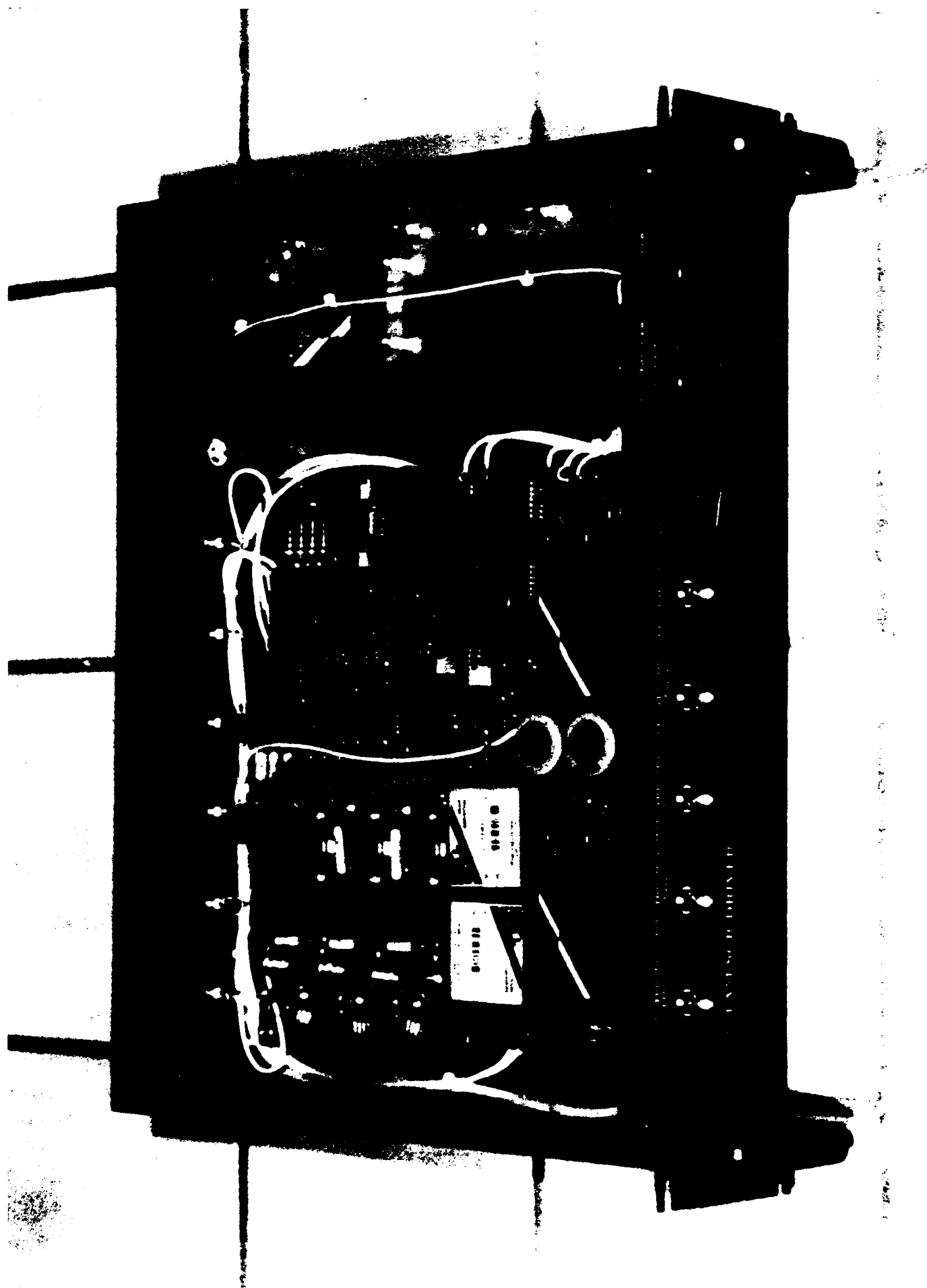
A simplified schematic of the control circuitry found in the SNOMAD-IVB control module can be found in Fig. 3.8 while a photograph of the assembled unit appears in Fig. 3.9.

Figure 3.8: SRLL-2650B Control Module Logic Circuit



SCIENCE RESEARCH LABORATORY

Figure 3.9: Control Module



## SECTION 4

### THE DoE/MIT ECH AND NASA/SELENE PROGRAMS

In this section we discuss the objectives of the two primary co sponsors for the construction phase of a 5.5 MeV induction accelerator facility to be located at the MIT Plasma Fusion Center. MIT has agreed to fund the required conventional facility improvements and site the accelerator. NASA has contributed part of the funds to build the first SNOMAD-IVB 1.0 MeV induction accelerator module. We begin with the long terms goals of MIT.

#### **4.1 The MIT ECH Development Program**

Among the various auxiliary heating methods for tokamak plasmas, electron cyclotron heating (ECH) offers many advantages and is currently favored as the primary heating technique for future tokamak devices (CIT and ITER). These advantages include: 1) controlled localization of power deposition through choice of radiation frequency; 2) ease of access through vacuum vessel ports; 3) precise control of launching; 4) minimal interaction with plasma edge and vacuum vessel; 5) potential to control disruptions; 6) ability to provide cw current drive. The Department of Energy has been engaged in the development of high power, high frequency microwave devices for several years. Research in gyrotrons, FELs, and most recently cyclotron auto resonance masers (CARMS) is presently being pursued by the DOE ECH Technology Development Program. A recent Panel XXI report<sup>(1)</sup> presented to the Magnetic Fusion Advisory Committee (MFAC) recommends continued DOE support for the development of high power ECH sources.

Next generation Tokamaks will operate with a central magnetic field of up to 10 Tesla, requiring 280 GHz for fundamental heating and 560 GHz for second harmonic. A total of 10 MW of auxiliary heating for several seconds will be required. The ideal ECH source will be capable of generating this power in 0.5-5.0 MW modules, and be frequency tunable over a sufficient range to provide profile heating control and operation over a range of tokamak magnetic fields. A recent ECH technology review report<sup>(2)</sup> recommends that the source be step

tunable by 30% and dynamically tunable by 5-10% on a time scale of tens of milliseconds. Tunable FELs and CARMs are being developed to satisfy there performance requirements. The CARM is an attractive alternative to the FEL because of its lower e-beam energy requirement and overall simplicity of design. However, little experimental data is available on the performance of CARMs in this frequency and power range.

The success of ECH will require reliable and economical radiation sources at the appropriate frequencies and power levels. High power FELs and CARMs suitable for ECH applications rely on accelerator facilities to provide high energy (1-10 MeV), high average power (2-10 MW), electron beams. Consequently, the development of economical FELs and CARMs for ECH will require low cost, high efficiency accelerator technology. The induction linac is unique in its ability to accelerate high peak currents ( $> 1000$  amps) to several MeV with a high repetition rate ( $> 1000$  Hz); delivering electron beams with multi-megawatt power levels to an FEL wiggler or CARM resonator. However, the complexity and cost of induction linac facilities has, thus far, restricted the development of millimeter wave sources based on this technology to the national laboratories. Recent advances by Science Research Laboratory (SRL) in the design and development of SCR commutated magnetic pulse compression power systems and compact accelerator cells has significantly reduced the cost and improved the reliability of high repetition rate induction linacs.

This report has described the development of a high repetition rate induction linear accelerator optimized for driving ECH sources. The objective of the research program has been to develop a low cost and highly reliable accelerator suitable for driving high frequency ( $> 250$  GHz), high average power ( $> 1$  MW) radiation sources. In the future these advanced induction accelerator modules will be installed in the high power microwave laboratory at the MIT Plasma Fusion Center where it will be available for millimeter wave source development.

The induction linac offers the promise of generating very high average power electron beams of sufficient brightness to drive millimeter wave radiation sources. The present generation of induction linacs have been operated with peak currents of 1-10 kA, 50 nsec pulse lengths and

beam energies of up to 50 MeV. These accelerators are powered by thyratron commutated magnetic pulse compression circuits, and are designed to operate at up to 5 kHz pulse repetition rate. Continuous pulse rates of 10 pps have been demonstrated and initial demonstration experiments of high repetition operation are planned for 1990.<sup>(3)</sup> Reliable high repetition rate operation will be required to satisfy the demands of ECH sources.

The development of a reliable high repetition rate thyratron pulse compression driver poses a difficult challenge and constitutes a significant fraction of the cost and size of present generation induction linear accelerator.

All-solid-state SCR commutated magnetic pulse compression circuits offer significantly higher repetition rate operation, improved reliability and a significant reduction in cost and size over thyratron-based designs. High repetition rate operation of an accelerator has recently been demonstrated using this technology.<sup>(4)</sup>

A block diagram for the future planned accelerator installation at MIT is provided in Fig. 4.1. Operating costs and the fabrication of both the low power, 280 GHz local oscillator and the FEL will be the responsibility of DoE/MIT.

#### 4.2 The NASA SELENE Program

The 5.5 MeV induction accelerator powered FEL to be sited at MIT offers a unique opportunity for NASA as a technology demonstration experiment. NASA has initiated a program known by the acronym SELENE (SpacE Laser ENergy) which would employ this technology to beam power into space. To understand why laser power beaming to space is important, consider the alternatives. All present space applications utilize either solar photovoltaics cells, batteries, fuel cells, nuclear energy sources, or combinations thereof. All of these technologies are relatively heavy per kilowatt of power generated. In laser power beaming the heavy and complex components all stay on the ground where they can be easily maintained and where power is relatively inexpensive. The new optics, laser, and photovoltaic cell technologies being developed in the Laser Power Beaming program could deliver more than ten times the power of present space systems at a fraction of the size and weight. The laser driven photovoltaic cells have more than

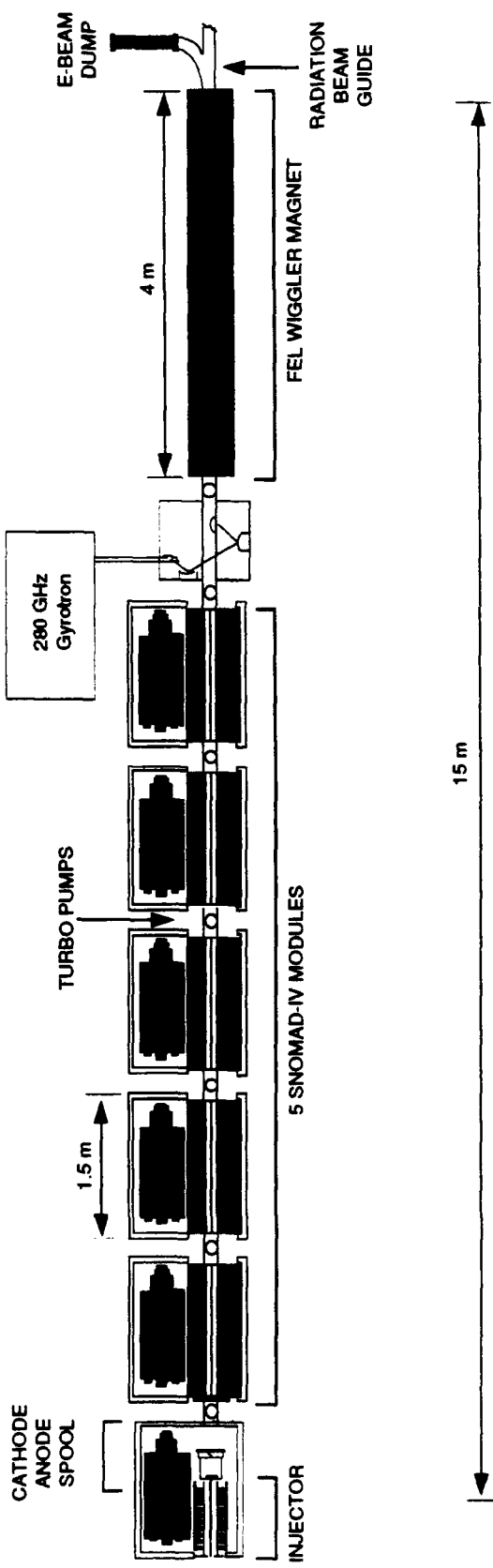


Figure 4.1: An Induction Linac Driven Free Electron Laser for ECH Heating

246 dB 001  
SCIENCE RESEARCH LABORATORY

twice the efficiency of solar cells and the light would be focused to give five times more energy density than sunlight. Not only does this make high power applications possible in space, but it might also make high thrust, electric propulsion feasible. It appears likely that the cost of transporting substantial payloads from low Earth orbit to high orbital locations can be reduced by a factor of three to four.

Even a very limited power beaming capability is of great interest to organizations such as COMSAT who dismay at satellites in their ownership which sit in orbit unable to provide service at night due to failed battery storage systems. The battery lifetime is a major limitation in existing as well as future planned satellites. A laser power source which could deliver energy to the solar arrays of these satellites during the period in which the Earth occludes their sunlight would bring some satellites back into service and extend the life of others.

In the much longer term, a high power, laser power beaming facility would eliminate one of the major impediments to establishing a colony on the Moon. There is presently no realistic solution to the problem of supplying power to this colony during the 15 day lunar night.

NASA has performed a fairly in depth study on the economic impact of laser power beaming and I have included some of the key charts from a recent advocacy briefing.

#### References

- 1) J. Leiss, D. Baldwin, L. Berry, N. Luhmann, T. Marshall, D. Montgomery, R. Parker, R. Prater, P. Sprangle, K. Thomassen, J. Watson, H. Weitzner, Electron Cyclotron Heating Requirements for the Fusion Program, Panel XXI Report to Magnetic Fusion Advisory Committee, December 6, 1988.
- 2) T. Marshall, J. Lebacqz, T. Godlove, Electron Cyclotron Heating Technology Review, U.S. DoE, Office of Energy Research, Office of Fusion Energy, Division of Development and Technology, May 1987.
- 3) K. Thomassen, Lawrence Livermore National Laboratory, Livermore, CA, LLL-PROP-00202, 1986.
- 4) R.E. Klinkowstein, D. Birx, A Low Cost Induction Linac for High Power Electron Cyclotron Heating Millimeter Wave Sources, Bul. Am. Phys. Soc., 34, 1987 (1989).

# SELENE

## Space Laser Electric Energy

# Applications



Sandy Montgomery  
Program Development  
George C. Marshall Space Flight Center  
National Aeronautics and Space Administration

SM060892-1400

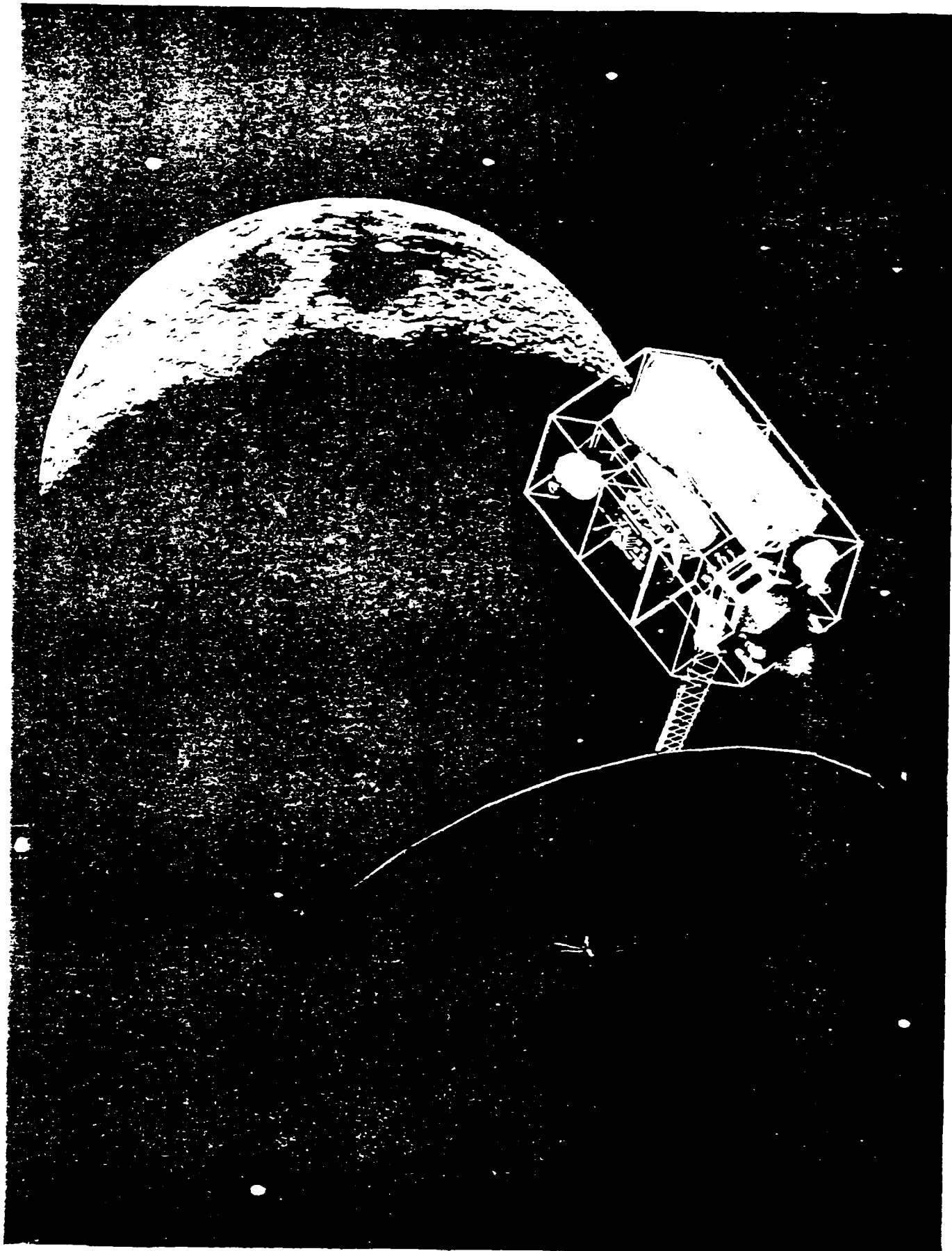


Three Space Applications of Beamed Power

## Space Transportation

## Spacecraft Power

## Surface System Power



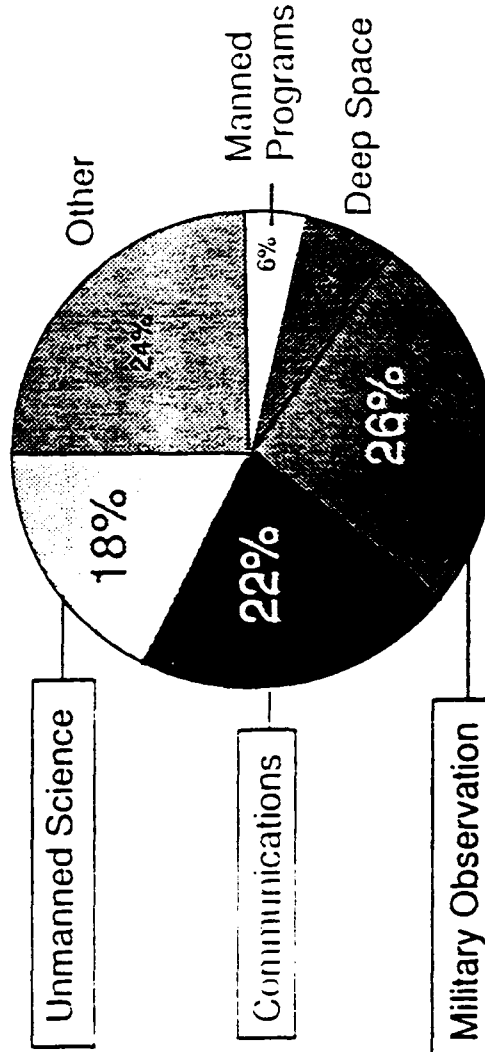


## The Transportation Market

- Potential laser EOTV missions:
  - Geostationary delivery/retrieval
  - Cis-lunar transport
  - Interplanetary departure/return

US Civil Commercial  
US Civil Scientific  
US Military  
International Commercial  
International Scientific

Payload Missions (1955-1988)

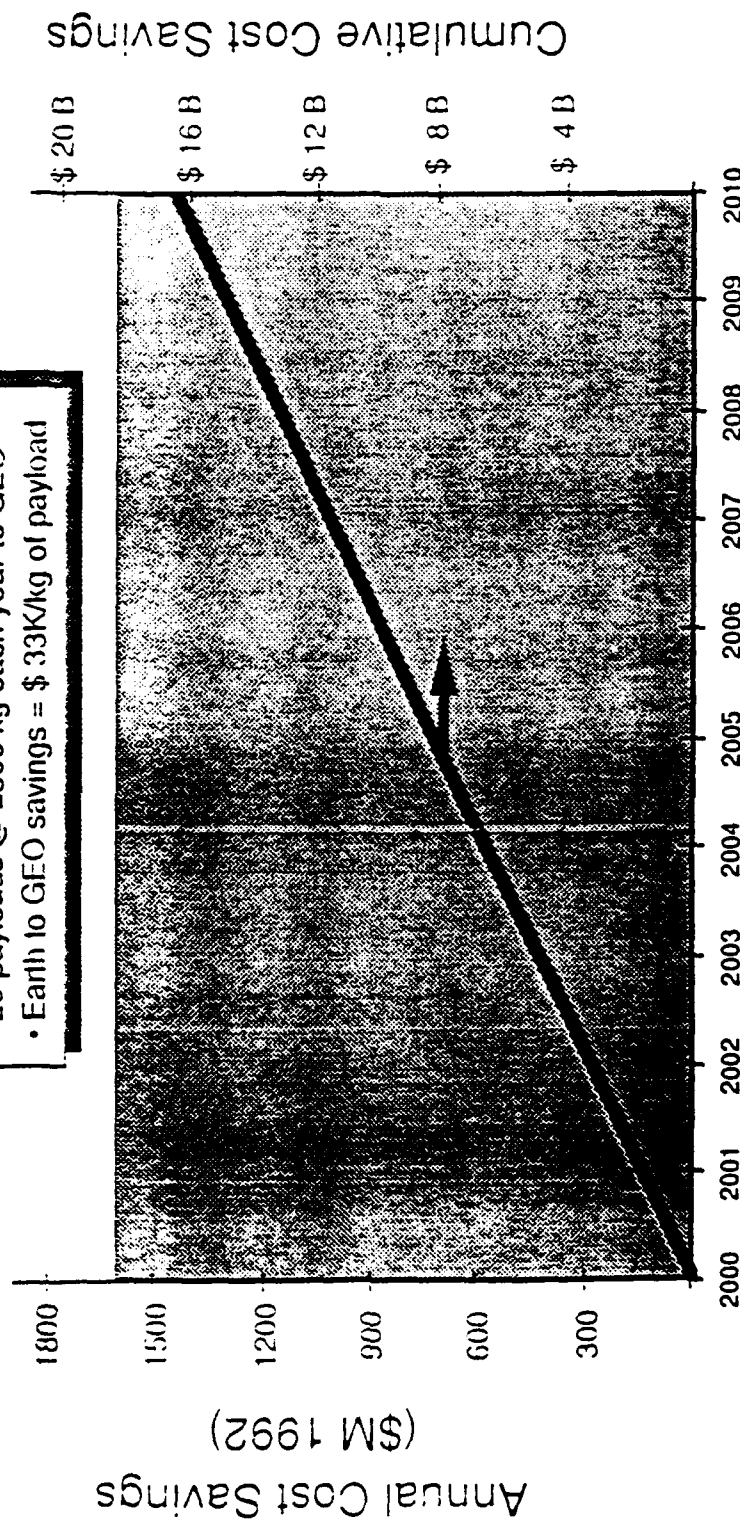


Two thirds of all payloads launched are unmanned, near-earth satellite missions.



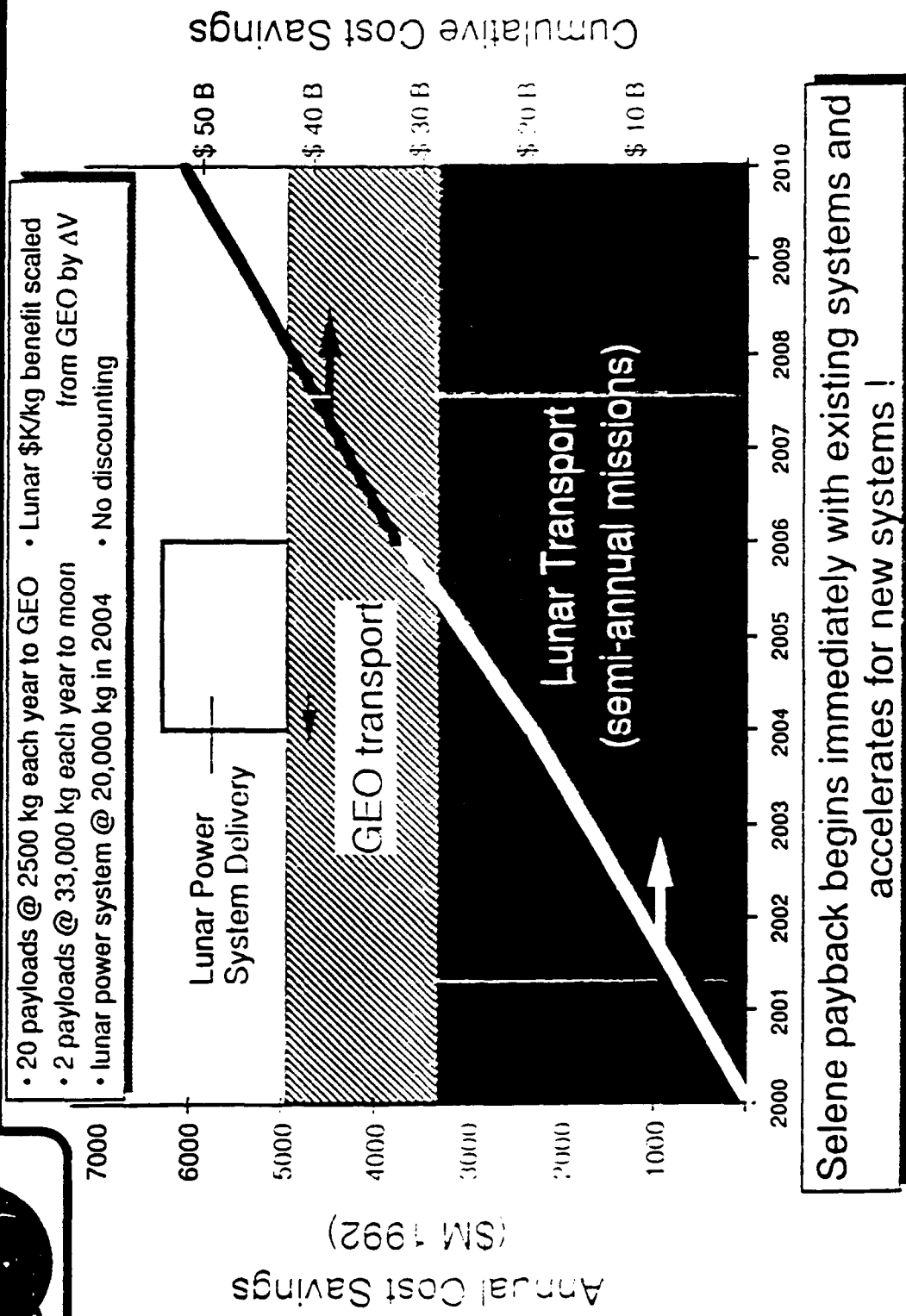
## Transport Benefit Projection

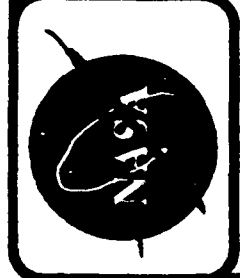
- 20 payloads @ 2500 kg each year to GEO
- Earth to GEO savings = \$ 33K/kg of payload



Selene payback begins immediately with existing systems and accelerates for new systems !

# Transport Benefit Projection





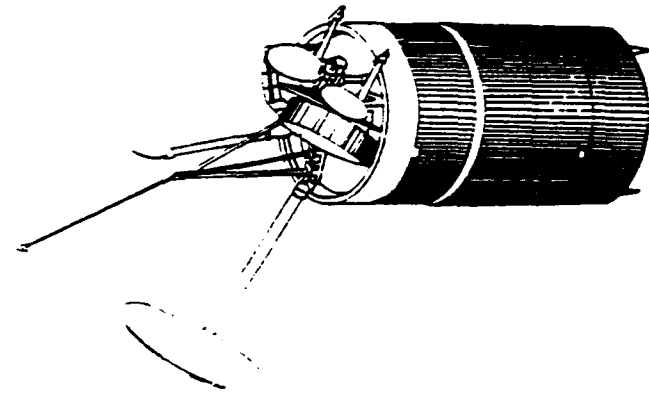
## GEO Transport Vehicle Comparisons

	<u>Chemical</u>	<u>Laser Electric</u>
<b>Specific Impulse:</b>	480	5,500
<b>Mass (kg)</b>		
Propellant	9,180	941
Vehicle	1,023	2,890
Payload	2,500	2,500
<b>Total</b>	<b>12,703</b>	<b>6,331</b>
<b>Delivery Time (days):</b>	0.5	39
<b>Vehicles Produced:</b>	20	4
<b>Total Mass Lifted to LEO</b>	<b>2,356,000 kg</b>	<b>699,560 kg</b>
<b>Cost (\$M):</b>		
Development	133	Including <sup>4</sup> Ground Sites
Production	409	Transport Systems Only
ETO Launch (\$11K/kg)	25,921	376
<u>Transit Time &amp; Operations</u>	<u>3</u>	<u>2,491</u>
<b>Total</b>	<b>26,465</b>	<b>7,696</b>
<b>Payload transport cost (\$K/kg)</b>	<b>53</b>	<b>1,785</b>
		<b>25</b>
		<b>18</b>
		<b>8,854</b>

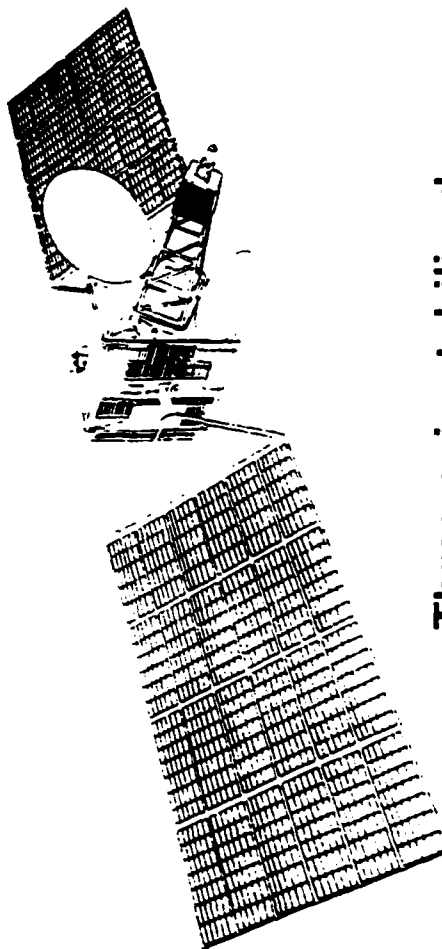


## Commercial GEO Communications Satellites

	First Generation	Second Generation	Current Generation
Power	1955-70 <500 watts	1970-76 <1000 watts	1976- <b>92</b> 1.3 kW
Mass	<500 kg	<1000 kg	1000- <b>2500 kg</b>
# Operating	20	48	<b>58</b>
Design Life	-	8-9 years	10-15 years



Spinners

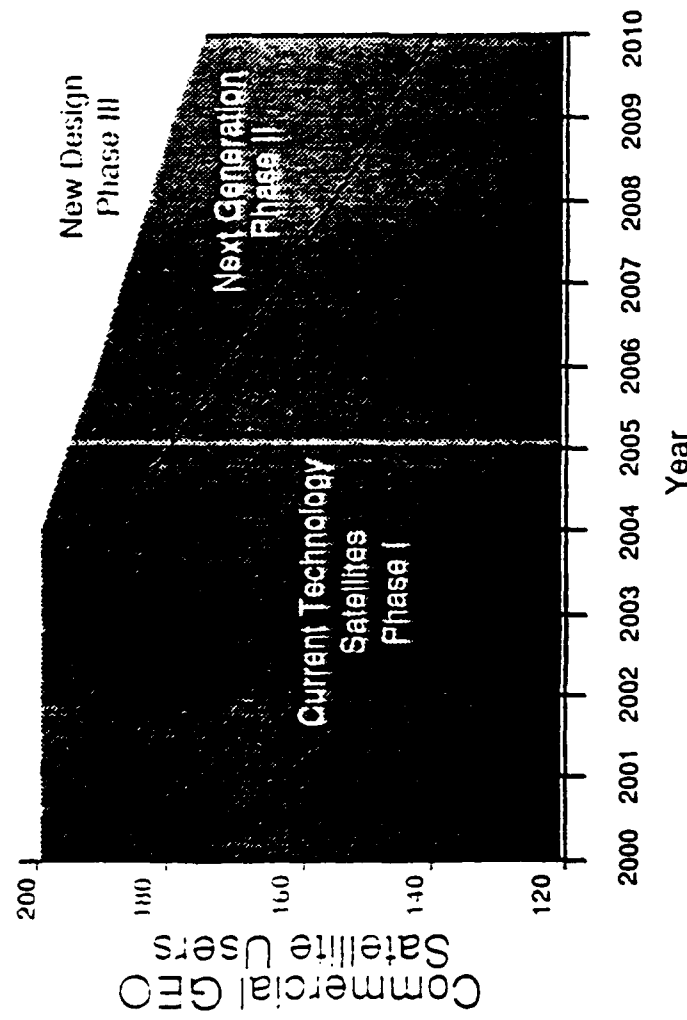


Three-axis-stabilized

Commercial satellites are increasing in performance and numbers



## GEO Commercial User Projection



### Annual Geostationary Traffic & Market

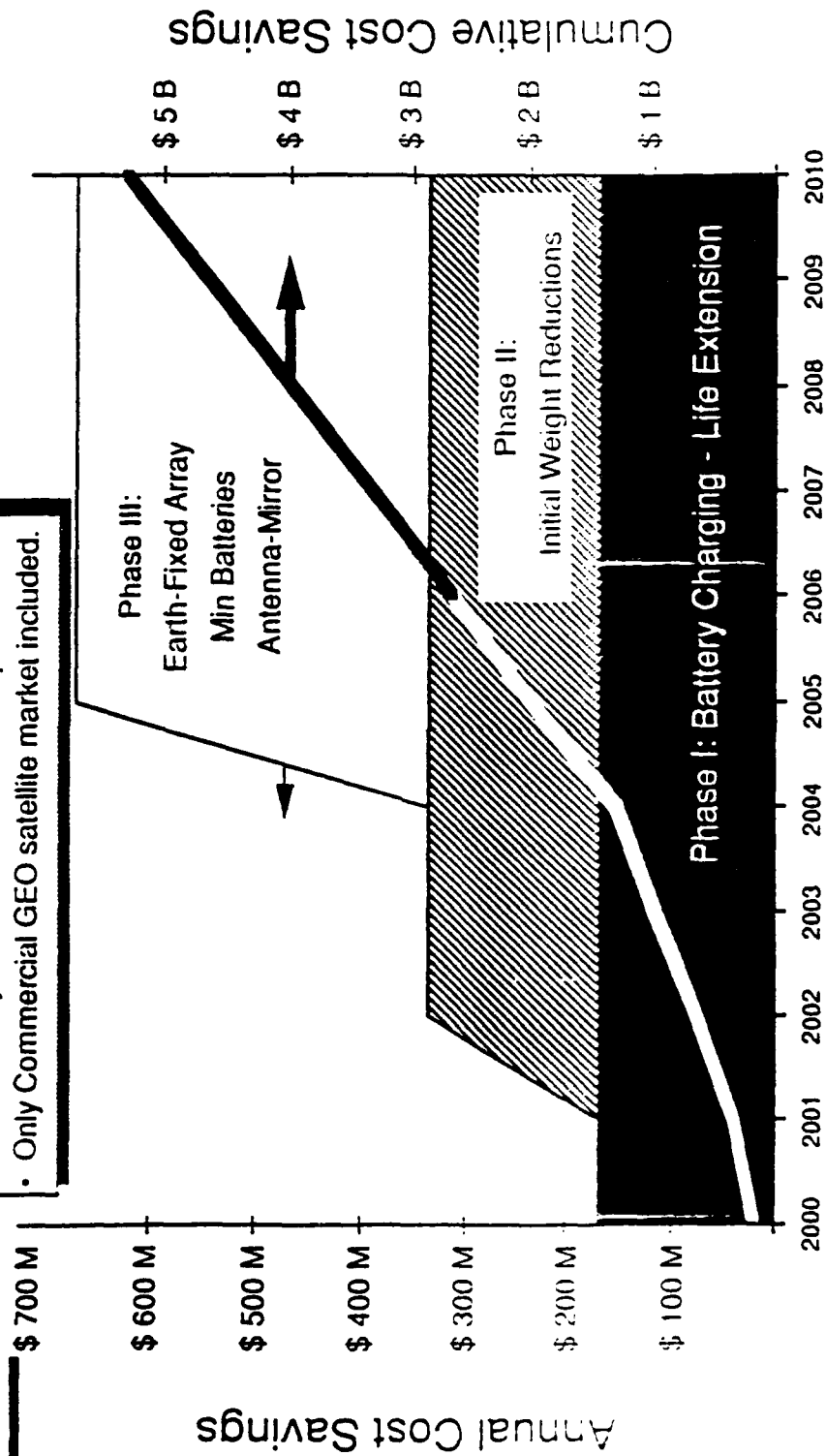
New Satls/year	~10
Avg Mass/Sat	~2500 kg
Total Value of Operating Commercial Satellites	\$ 10.2 B
1980	1990
\$ 3.9 B	\$ 10.2 B

SELENE support begins immediately with existing systems  
and gracefully leads system growth !

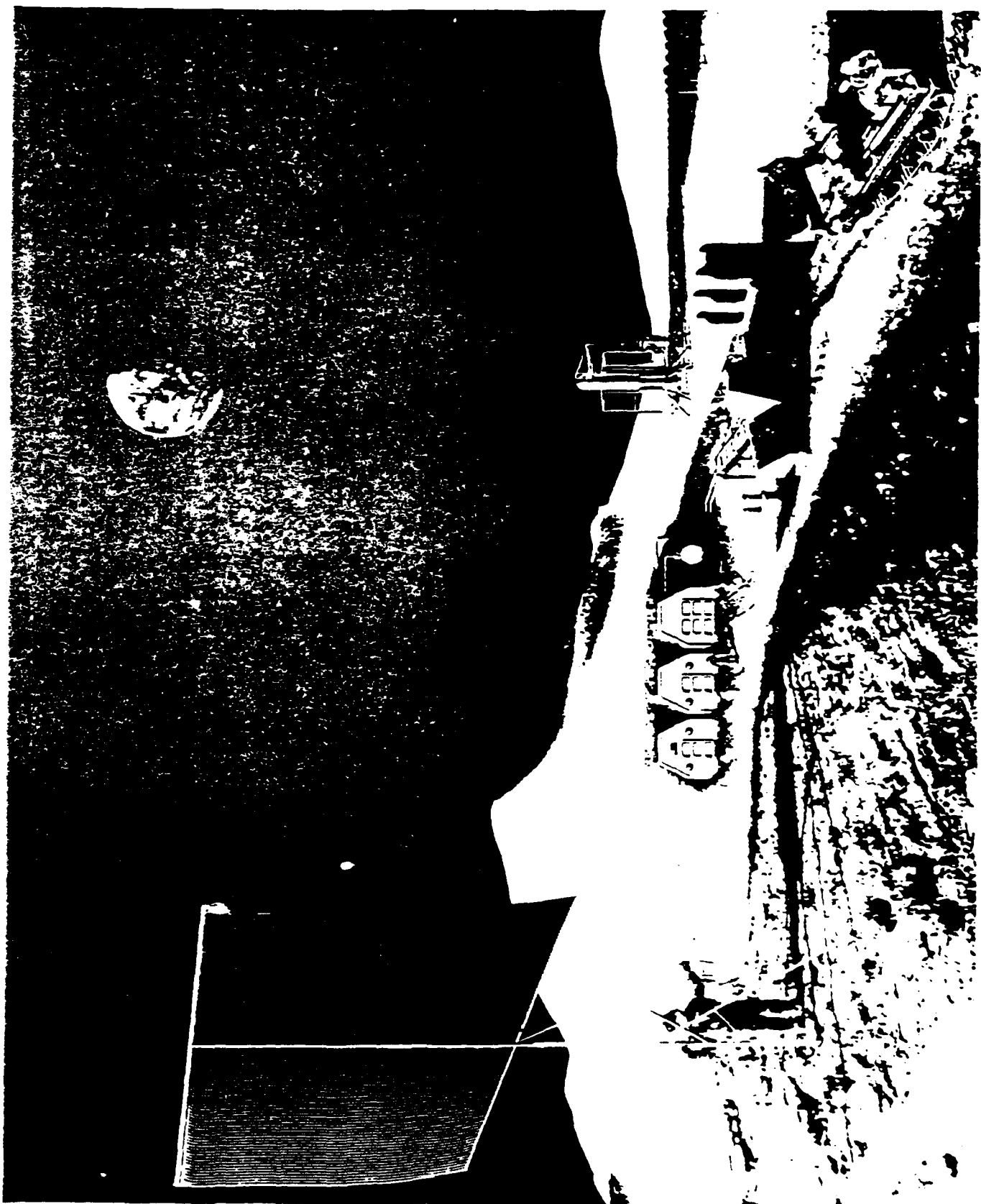


## GEO Commercial Benefit Projection

- Assumes only 50% of User Market Captured.
- Only Commercial GEO satellite market included.

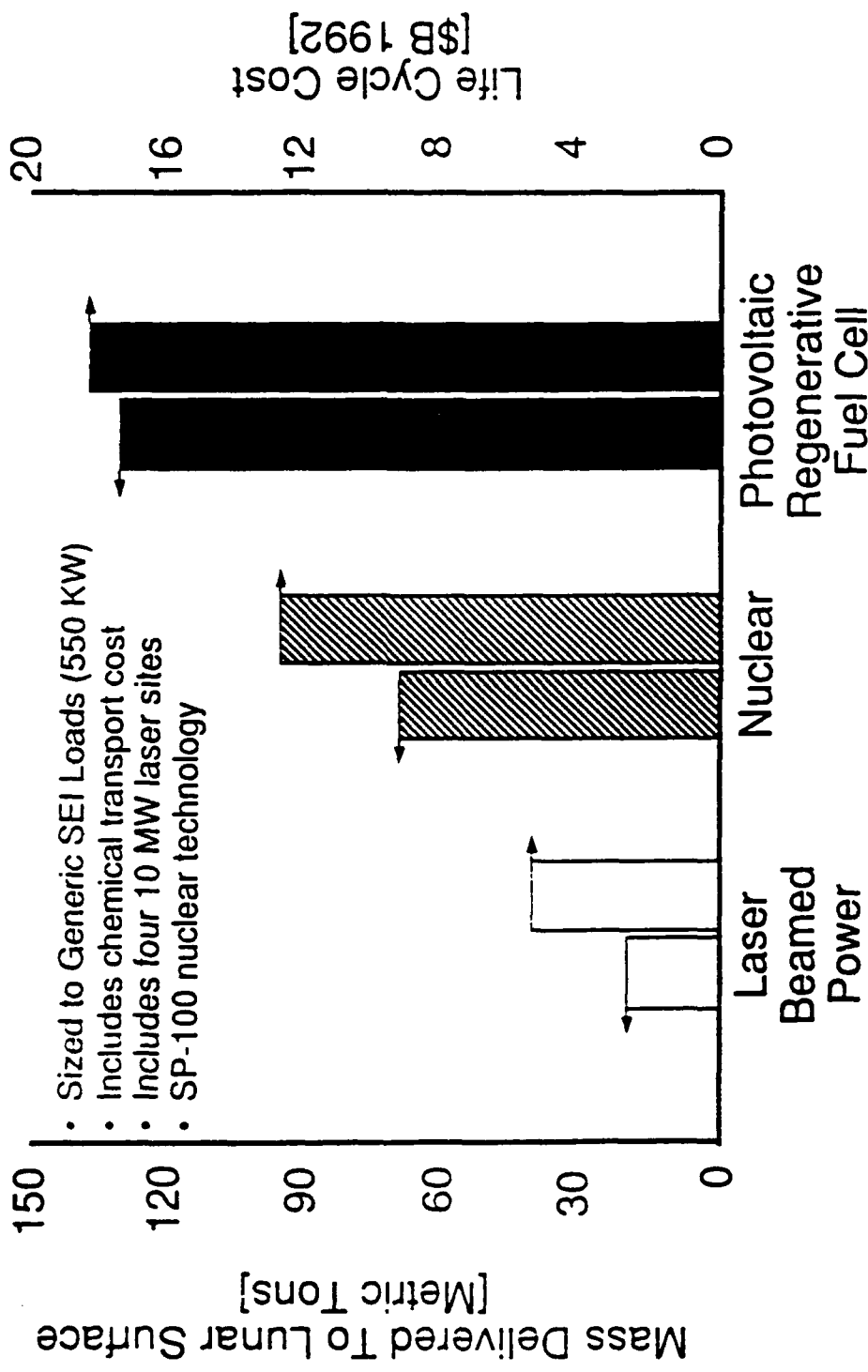


Selene payback begins immediately with existing systems and accelerates for new systems !





## Lunar Surface Power System Comparison



SM060892-1400  
[Rev J.H. Smith/JPL]

## What is the total User Picture ?



- Satellite power customers: (2000-2010)
  - 200 operational satellites in GEO - assume 50% of market
  - Sats with reduced shielding/batteries (Phase II) start 2002.
  - Earth-fixed arrays & antenna/mirror sats (Phase III) in 2005.
  - Reflects only GEO commercial market. Others ?
- Transportation (2000-2010)
  - 20 GEO satellites replaced every year (2500 kg per trip)
  - Revisit lunar outpost on 6 month intervals (33,000 kg per trip)
  - Deliver lunar power expansion system (20,000 kg)
  - Undetermined: Interplanetary, plane change, near-earth
- Lunar Base Power utility
  - Growth benefit from laser power (25 to 550 kw continuously)

- No application requires a fully dedicated single laser site.
- All applications studied are compatible with multiplexing ground sites and targets.



## Selene Spin-off Potential

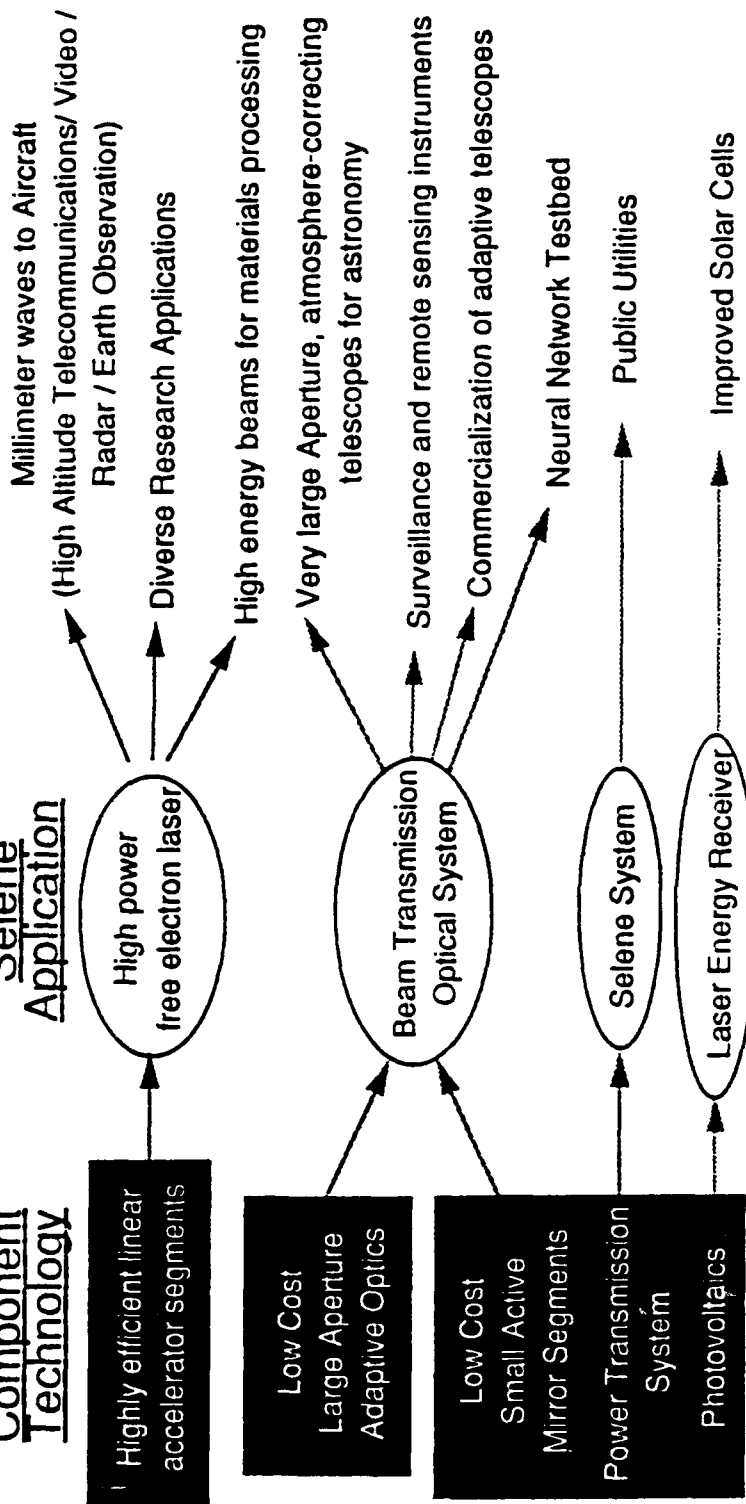
### Component Technology

Highly efficient linear  
accelerator segments

### Selene Application

High power  
free electron laser

### Other Applications



The technologies developed in the Selene program will revolutionize scientific fields from astronomy to materials engineering and create new industries !



# Conclusions

- The Development of a laser power beaming capability for space applications will pay for itself many times over.
- Positive cash flow will be achieved quickly.
- Science/technology spin-offs are as significant as the direct economic benefits.
- Any of the applications taken individually result in \$ benefits at least on par with required investment.
- Together, the four applications studied may have a ten-fold ROI.

## Recommendations



- NASA should lead the aggressive development of the first ground site
  - in conjunction with DoD and DoE
- The development of the technology should begin immediately
  - GEO delivery opportunities and satellite life are being lost now.
- The revolutionary nature of a laser power beaming capability makes it important to focus near-term attention on its development - before other costly R&D expenditures are made obsolete.
- New NASA technologies point the way to substantially reduced cost for ground and space based systems.

## SECTION 5

### THE DARPA "RED WATER" PROGRAM

DARPA has funded a program in which the SNOMAD-IV accelerator will be used to experimentally treat red water, an unwanted byproduct of TNT production. Initial experiments have already been conducted using the SNOMAD-IV, 0.5 MeV injector and future experiments are planned which will use the 1.5 MeV output of the SNOMAD-IV injector - SNOMAD-IVB accelerator module package. Red water processing is a serious concern to the services.

Environmental concerns regarding red water, a hazardous by-product of TNT production, have forced the closing of all of the TNT production facilities in the US including the primary two production lines at the Radford Army Ammunition Plant (RAAP). RAAP personnel are presently performing preliminary planning for acquisition of a conventional, fossil-fuel powered incinerator for red water disposal. However, environmental concerns regarding NO<sub>X</sub> and SO<sub>2</sub> emissions from this incinerator together with the high capital (\$20M) and operating cost (>\$34,000 per day) of this incinerator have led the Army to investigate alternative red water disposal technologies. Other technologies being investigated include wet air and supercritical water oxidation. However, the capital costs of these techniques are likely to exceed the capital costs of conventional incinerator approaches while their operating costs (which are dominated by fuel costs) are somewhat lower or comparable to the incinerator approach.

In this experiment, DARPA has funded SRL to perform proof-of-principle experiments to determine the technical and economic viability of using electron beam irradiation to decompose the hazardous nitro bodies in red water. The technical objective of this effort is to measure the efficiency of nitro body decomposition with electron beams and also to determine the decomposition byproducts. Nitro body decomposition products are likely to be primarily NO<sub>2</sub>, sodium salts such as sodium sulfite and sodium sulfate and toluene mixed with water. The NO<sub>2</sub> gas can be contained and perhaps recycled to make nitric acid which is used in the nitration of toluene

as part of the TNT production process. Sodium salts, dissolved in water, can be sold to paper mills and toluene, which is easily separated from the water, can be recycled and used as fuel.

The capital cost of the electron beam red water treatment system is estimated to be \$4M – a factor of 5 times lower than other red water disposal systems. Operating costs depend critically on the electron beam dose required to decompose the nitro bodies. With an electron beam decomposition efficiency,  $\eta$ , a dose of  $30/\eta$  Mrad corresponding to 300 Joules/gram is required to decompose the nitro bodies in undiluted red water. This dose gives an operating cost of  $\$1680/\eta$  per day for which all of the nitro bodies produced by the two TNT production lines at RAAP can be decomposed. At near unity nitro body decomposition efficiencies, this operating cost would be a factor of 11 times lower than operating costs associated with a conventional incinerator. To put these costs into perspective, the two TNT production lines at RAAP produce a total of 100 tons of TNT per day and generate 17,000 gallons of red water in the TNT purification process.

Trinitrotoluene (TNT) is by far the most important explosive used for blasting charges in military weapons. It is extremely stable, neutral and does not attack metals. It can be charged by casting as well as by pressing. In addition, TNT is insensitive and does not require phlegmatizers to avoid accidental detonation. It is utilized in its pure form, or mixed with ammonium nitrate to form Amatols, with aluminum powder to form Tritonal, with RDX to form Cyclonite and Composition B and is used in combinations to form Torpex, HBX and Trialene. Moreover, TNT is an important component of many industrial explosives.

TNT is produced by nitration of toluene with mixed nitric and sulfuric acid in several steps. The trinitration step uses highly concentrated mixed acids with free SO<sub>3</sub>. Batchwise and continuous nitration methods are used with the latter being the method of choice for the large quantities manufactured at military production sites. Military forms of TNT are freed from isomer forms other than 2,4,6 TNT ( $\alpha$ -TNT). TNT purification is done by recrystallization in organic solvents. The non-symmetrical isomers are destroyed by washing with an aqueous sodium sulfite solution – a process whose byproducts are responsible for the large quantities of

red-colored waste water (red water). The red color is generated by sodium sulfonates of the various TNT isomers.

The purity of the product, 2,4,6 trinitrotoluene, can be estimated from its solidification point. The minimum value for solidification of the TNT used for military purposes is 80.2°C and the value for the pure 2,4,6 isomer is 80.8°C. The pourability of TNT at 81°C makes it extremely attractive for military applications. Fine crystalline cast charges of TNT are used in shells, mines and bombs. High loading densities of TNT provide high brisance.

Unfortunately, all of the US military production facilities for TNT including the primary site at the Radford Army Ammunition Plant (RAAP) in Radford, VA have been closed. RAAP is a GOCO which provides TNT and other explosives for military arsenals throughout the US. Closure has been mandated until methods have been developed and deployed for environmentally acceptable disposal of the red water by-product of TNT production.

The Army is currently performing a preliminary design of an incinerator approach to red water disposal. Discussions with cognizant RAAP personnel have revealed that this incinerator will cost approximately \$20M when it is equipped with the environmental pollution control systems required for NO<sub>X</sub> and SO<sub>2</sub> abatement. Serious issues remain in obtaining the US Army, including personnel at Piccatinny Arsenal (Dr. Bob Goldberg) and at RAAP (Mr. Chip Batton), are extremely interested in more cost-effective, more environmentally acceptable solutions to the red water disposal issue. They have obtained a samples of red water from the ICI explosives facility in Canada and have shipped it to SRL for experimentation.

Science Research Laboratory is performing proof-of-concept experiments which will determine the feasibility of decomposing the primary organic constituents of red water with a high energy (1.5 MeV) electron beam generated by an induction accelerator. In these feasibility experiments, an existing 500 keV electron beam is being used to compose the complex nitro bodies which are the primary unacceptable constituents of red water. These nitro bodies are listed in Table 5.1 which summarizes the various concentrations by weight of red water solids. The primary constituents to be decomposed are the sodium sulfonates of TNT isomers, the  $\alpha$ -TNT-sellite

**Table 5.1:**  
**Summary of Percent Removal of Selected Aromatic Compounds Using High-energy Electrons**

Compound	Detection Limit (nm)	Initial Conc. (nm)	Percent Removal at Various Radiation Doses (krads)				
			41	79	131	195	388
Benzene	0.128	1420	47.719	61.276	84.388	93.021	95.907
Toluene	0.108	1094	50.955	64.494	83.395	90.009	96.557
Chlorobenzene	0.088	1049	42.387	55.208	76.065	86.969	95.516
Ethylbenzene	0.94	1003	51.078	61.0334	77.375	86.766	90.138
1, 2-Dichlorobenzene	0.068	1126	35.681	41.653	63.178	75.757	82.061
1, 3-Dichlorobenzene	0.068	1077	39.222	46.752	64.794	77.365	79.431
1, 4-Dichlorobenzene	0.068	773	35.818	43.127	60.744	73.965	80.723
m-Xylene	0.094	905	52.541	64.725	79.425	87.906	88.085
o-Xylene	0.094	1088	48.087	56.539	76.579	86.144	90.128
							92.057

complex and the trinitro-benzene salts and alcohols. These substances are the primary hazardous constituents of red water and their decomposition would solve the red water disposal problem.

Through the process of radiolysis, electron beams can be used to break the bonds which attach the  $\text{NO}_3$  and  $\text{NaSO}_3$  to the toluene base molecule. Direct radiolysis involves a direct interaction between the electron beam and the nitrobodies in which the electron beam deposits energy in the nitrobody to break chemical bonds. With indirect radiolysis, the electron beam deposits its energy primarily in the water molecules to form reducing radicals ( $e_{aq}^-$ ,  $\text{H}$ ), oxidizing radicals ( $\text{OH}$ ), ions ( $\text{H}_3\text{O}^+$ ) and molecules ( $\text{H}_2$ ,  $\text{H}_2\text{O}_2$ ) which then attack and decompose the nitrobodies. At high concentrations of nitrobodies (8% by weight in red water direct from TNT purification), the radiolysis is primarily indirect but has a significant direct component. At lower concentrations, the radiolysis is essentially all indirect.

Electron beams have been demonstrated to be extremely effective in decomposing trace quantities of benzene and toluene in dilute aqueous solution by indirect radiolysis as shown in Table 5.1. At the large concentrations of the toluene-based hazardous substances in red water (8% in weight), however, it may be more effective and efficient to simply remove  $\text{NO}_2$  and  $\text{NaSO}_3$  from the toluene base by a combination of both direct and indirect radiolysis. For the sodium sulfonates of TNT isomers and the  $\alpha$ -TNT-sellite complex, this would leave toluene with gaseous  $\text{NO}_2$  (which bubbles out of the solution) and the  $\text{NaSO}_3$  radical which ultimately would react to form sodium sulfite and remain in solution. If this can be accomplished with the electron beam at a reasonable efficiency, this process will be significantly less costly – both in terms of capital and operating costs – than incineration or wet air oxidation.

In addition, the  $\text{NO}_2$  which is evolved can be recovered and then reacted with water to form nitric acid. This nitric acid can be recycled and used in the nitration stage of the TNT production process. A nitric acid reconstitution facility is already in place at RAAP, but its throughput would likely have to be increased if the  $\text{NO}_2$  evolved from the electron beam decomposition step proves to be sufficiently pure. The  $\text{NaSO}_3$  together with other inorganic salts which are in red water could be either recycled, sold to the paper industry or dumped. Finally the toluene, if sufficiently

pure could be easily separated from the water, reprocessed and used on site as fuel or sold.

The TNT facility at Radford Army Ammunition Plant consists of 2 production lines each of which manufacture 50 tons of TNT per day. Each of these lines also produces 8500 gallons of red water per day. Red water solids account for 15% by weight of the aqueous solution. approximately 55% by weight of the solids are nitrobodies while the remainder of the solids are inorganic sodium salts. Consequently, nitrobodies comprise 8% by weight of the red water.

Three other plants, which are typically closed but represent a surge capability in times of conflict, are located in Maryland, Tennessee and Illinois. These plants each contain 10 lines, each capable of manufacturing 50 tons of TNT per day. Although presently idle, these plants are maintained in a state of readiness and will likely be equipped with red water disposal technology once it is available.

The key issue in determining the economic viability of red water disposal via electron beam irradiation is the efficiency with which the  $\text{NO}_2$  and  $\text{NaSO}_3$  bonds to the toluene molecule can be broken with electron beam irradiation. These bond strengths can be estimated based on the strength of similar bonds and from the temperature at which TNT starts to decompose.

Typical  $\text{NO}_2$  bonds with aromatic hydrocarbons (eg. benzene) have bond strengths of 300 kJ/mol. The bond strength between the toluene molecule and  $\text{NO}_2$  is therefore likely to be approximately 3.1 eV.  $\alpha\text{-TNT}$  starts to decompose at a temperature of 523°K, although the decomposition rate remains a strong function of temperature. Assuming a decomposition energy which is 30 times this threshold temperature gives a rough estimate of bond strength as 1.35 eV. In the remainder of this discussion, we will assume bond strengths for the  $\text{NO}_2$  and  $\text{NaSO}_3$  of approximately 3 eV. Since three bonds must be broken per molecule, the energy which must be supplied to the molecule by electron beam irradiation is  $10 \text{ eV}/\eta$ , where  $\eta$  is a measure of the electron beam irradiation coupling efficiency to the nitrobodies. The mass density of nitrobodies in undiluted red water is  $8.8 \times 10^{-2} \text{ g/cm}^3$ . Assuming an average molecular weight of 275 for these nitrobodies, the density of nitrobodies is found to be  $1.92 \times 10^{20} \text{ molecules/cm}^3$ . With a decomposition energy of  $10/\eta$  eV per molecule, the electron beam must deliver  $1.92 \times 10^{21}$

eV/cm<sup>3</sup> or approximately  $300/\eta$  Joules/gram into the undiluted red water. Consequently the electron beam dose must be a minimum of  $30/\eta$  MRad for red water with 8% nitrobodies by weight. For red water diluted with water to 0.8% nitrobodies, the electron beam must deliver  $3/\eta$  MRad. Of course, in this case, the total throughput of diluted water per production line increases to 85,000 gallons per day and the total electron beam energy requirements remain the same. Dilution will only be used if the overall efficiency of nitrobody decomposition is enhanced or if the viscosity of the red water must be decreased to facilitate electron beam irradiation.

Assuming an electron beam dose of  $30/\eta$  MRad, a total electron beam energy of  $1.1 \times 10^{10}/\eta$  Joules per line must be generated per day, since 8,500 gallons of diluted red water weighs approximately  $3.6 \times 10^4$  kilograms. With a 300 kW electron beam power, derated to 150 kW by the electron beam extraction efficiency of 50%, the 8,500 gallons of undiluted red water from one TNT production line can be processed in approximately  $20/\eta$  hours of continuous operation. With a 50% electron accelerator efficiency (from wallplug to electron beam),  $1.2 \times 10^4$  kW-hrs of electricity would be used per line per day. At \$0.07/kW-hr, the cost of electricity per line would be approximately \$840/line/day.

Incinerators which thermally decompose all of the organic compounds in red water operate at 1000°C. Sufficient residence time at 1000°C for the nitrobodies is accumulated in the incinerator by operating with a kiln length of approximately 8 meters. The heat input (enthalpy) required by the red water in reaching 1000°C from 20°C is more than 4,000 Joules/gram as compared with approximately  $300/\eta$  Joules/gram with radiolysis by an electron beam. For the wet air oxidation approach, the red water is pressurized with oxygen or air and heated to ~320°C at constant volume. This process requires pressure vessels capable of withstanding more than 1600 psia (>100 atmospheres). The heat input (enthalpy) required by the red water in this process is approximately 2400 Joules/gram. Consequently, the electron beam irradiation technique for decomposing red water has the potential to be 10 times more energy efficient than wet air oxidation and 20 times more efficient than incineration. The key issue is the efficiency of coupling the electron beam energy to the bonds which must be broken in these complex molecules.

Induction accelerators represent the only electron beam accelerator technology which can be scaled to the high average powers required for red water disposal. As shown above, a single TNT production line requires approximately 300 kW of average electron beam power to process the daily production of red water.

With near unity nitrobody decomposition efficiency,  $\eta$ , as well, two 1.5 MeV, 300 kW electron beam accelerators would be required to process the red water produced at RAAP. Electron beam powers of 300 kW are readily available from 1.5 MeV induction accelerators as shown in Fig. 5.1. However, 1.5 MeV electrostatic or RF accelerators are scalable to only 50 kW of electron beam power. Consequently 12 of these accelerators would be required to meet the processing demands from the 2 TNT production lines at RAAP. These accelerators cost \$10 per electron beam watt and consequently the capital cost for these accelerators alone would be approximately \$6M. Scalable induction accelerators are being developed which can deliver electron beam power at \$3.50/watt which implies a \$2M capital cost for the accelerators required at RAAP. With the balance of the red water processing equipment likely to cost \$2M, an induction accelerator-based system could be developed to handle the red water problem at RAAP for ~\$4M in capital costs. Electrostatic and RF accelerators are therefore neither economically competitive nor scalable to the average electron beam power required to provide cost-effective processing of red water.

### **5.1 Preliminary Comparative Economic Analysis – Capital Costs**

The electron beam red water treatment system can be installed at a capital cost of \$4M. These costs include \$2M for the two 300 kW induction accelerators, \$1.8M for construction of the weir red water delivery system, and red water handling system, and \$200K for installation and x-ray personnel shielding. The accelerator costs are based on actual costs incurred in the construction of the existing SNOMAD-IV Induction Accelerator module. The cost of the weir delivery system and the red water handling systems are engineering estimates. This treatment system is sized to irradiate either 17,000 gallons of red water per day with a dose of 30 MRad or 170,000 gallons of diluted red water per day with a dose of 3 MRad.

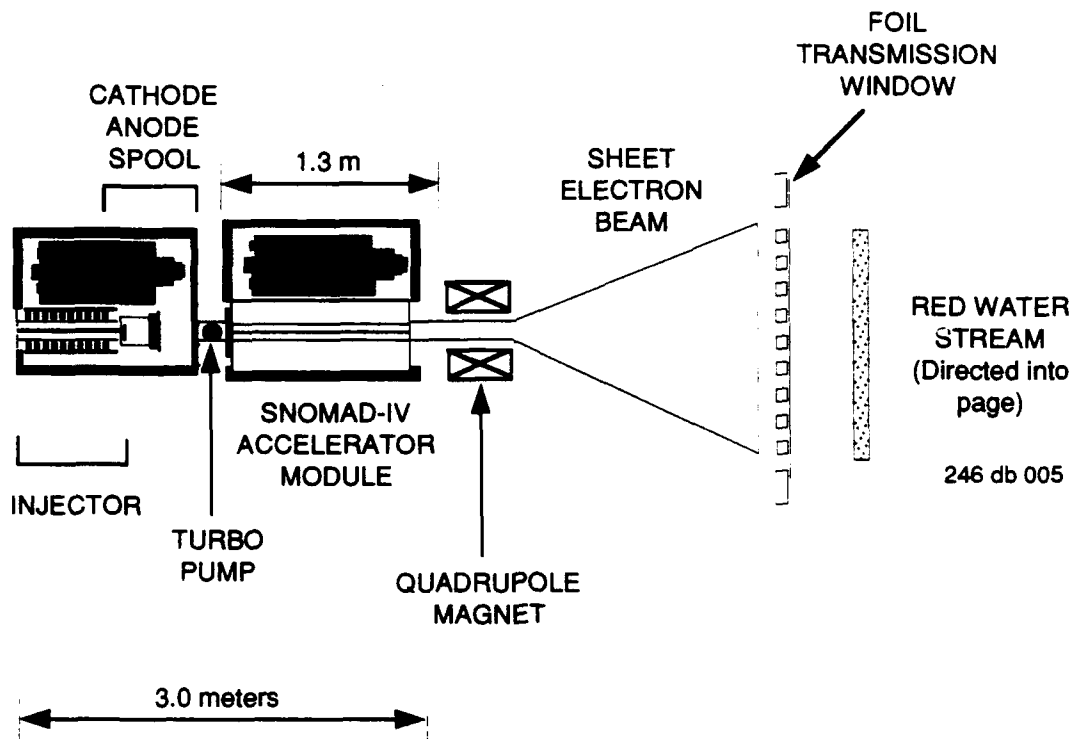


Figure 5.1: Expanded Electron Beam from a 1.5 MeV Induction Accelerator is used to irradiate the Red Water Stream.

SCIENCE RESEARCH LABORATORY

An incineration system based on a rotary kiln construction is estimated by Hercules Aerospace (Mr. Chip Batton) to cost \$20M installed. This cost is believed to include the cost of the NO<sub>x</sub> and SO<sub>2</sub> emission control systems. This incineration system, which operates at 1000°C, will also handle the entire red water production volume from the 2 TNT production lines at RAAP.

## 5.2 Operating Costs

The operating cost of the electron beam treatment system is dominated by the cost of the electricity to drive the accelerators. With a 50% accelerator efficiency, the electrical costs for operating two 300 kW induction accelerators for 20 hours per day is  $\$1680/\eta$  (24,000 kW-hrs @ \$0.07 per kW-hr). This corresponds to a red water clean up operating cost of  $\$16.80/\eta$  per ton of TNT produced. The cost of replacement cathodes (\$4000 per 2000 hours of operation) and capacitors ( $10^{11}$  shots equals 1 year of operation) are negligible. Based on a working year of 251 days, the yearly operating costs of the accelerator-based red water treatment system is thus  $\$421K/\eta$ .

Operating costs of the incinerator will also be dominated by the cost of the electricity to heat the rotary kilns. The most efficient method of heating red water and the kiln is by using microwaves. Microwaves are twice as efficient in these applications than simply burning fossil fuels on site. This is the primary reason that industry is converting to microwave systems for heat intensive drying operations where possible. Use of microwaves will also obviate environmental issues which may arise from burning fossil fuels locally. Standard high power magnetrons, operating at 2.45 GHz, directly deposit heat into resonance levels of water and consequently can deliver heat to the red water at approximately 50% efficiency. This compares to an overall efficiency of 25% for the induction accelerator in delivering electron beam power to the red water. However, although microwave heating is twice as efficient electrically, the microwave driven incinerator system must deliver 4,300 J/g to the red water, vice  $300/\eta$  J/g with the accelerator. Consequently, the electrical costs for the microwave driven incinerator system will be \$11.78/day or \$2.96M/year. This corresponds to a red water clean-up cost of \$117.78 per ton of TNT produced. These operating cost estimates for a microwave-driven incinerator compare

favorably to the cost of a fuel-oil-driven incinerator. According to Mr. Chip Batton, the operating cost associated with a conventional incinerator is nominally \$2/gallon of red water (his range was \$1.5 to \$2.5 per gallon). This unit cost gives a daily cost of red water disposal of \$34,000 per day and a yearly cost of \$8.53M. When I mentioned the possibility of microwave incineration, Mr. Batton was intrigued, since the operating cost of his baseline incinerator, driven by fuel oil, was totally dominated by the cost of the fuel oil. In fact, an operating disposal cost of \$2 per gallon of red water, implies that approximately 2 gallons of fuel oil must be burned for every gallon of red water which is destroyed! In the following total yearly cost estimates, the lower microwave incineration costs are once again used for comparison.

Yearly operating costs must, of course, also include amortization of the capital costs of these two systems. Amortized over 20 years at 10% interest per year gives a total yearly cost of  $\$232/\eta$  K (for the accelerator) plus \$232K (for balance of facility) per year for the \$4M electron beam treatment facility and \$2.32M for the \$20M incinerator facility. Consequently, the total yearly cost (amortized capital cost plus operating cost) for the electron beam treatment facility is given by

$$\text{Yearly Cost of Electron Beam Treatment Facility} = \frac{\$653K}{\eta} + \$232K$$

By comparison, the total yearly cost of the incinerator system is \$5.28M. These costs are equal at an efficiency,  $\eta$ , of approximately 0.13. Consequently the electron beam facility is more cost effective for electron beam coupling efficiencies of greater than 13%. At  $\eta = 0.1$ , an electron beam dose of 3,000 J/g (or 300 MRad) would be delivered to the undiluted red water. At these extreme dose levels, it would be unlikely that the red water nitro bodies are not fully decomposed.

It is interesting to note that a fuel oil powered incinerator would have a total cost (amortized capital cost of \$20M plus operating cost) of \$10.85M. This yearly operating cost becomes equal to the cost of electron beam red water treatment at an efficiency,  $\eta$ , of 0.06 or 6%.

## SECTION 6

### THE ELECTRON BEAM MATERIALS PROCESSING PROGRAM

DARPA has funded experiments in electron beam materials process on the SNOMAD-IV accelerator. Some portions of these experiments will have to be postponed until more accelerator modules are completed but the initial experiments are now being conducted using the 0.5 MeV SNOMAD-IV injector.

The use of high energy ( $E \sim 1\text{-}5 \text{ MeV}$ ) electron beams (HEEB) at high average power ( $P \sim 200 \text{ kW} - 1 \text{ MW}$ ) allows the cost effective processing and fabrication of unique graded composition materials which are not economically viable using conventional fabrication methods. Examples of such materials are superalloys and metal-matrix composites with graded thermal and mechanical properties. A graded nickel-based superalloy jet aircraft turbine disk fabricated using HEEB powder metallurgy techniques would operate at higher temperatures with the improved deformation resistance needed for the High Speed Civilian Transport and next generation fighter aircraft. A HEEB material processing system would also allow cost effective surface hardening of steel up to depths of 5 mm. By hardening rail steel on long haul rail lines, costly repair and replacement can be avoided.

High energy electron beams propagate significant distances in air, allowing for processing at long working distances. The average power levels now available using HEEB are 5-25 times higher than competing processing technologies such as laser layer glazing and plasma spraying. High average power contributes to high throughput and cost effective HEEB material processing systems. High energy electron beams (HEEB) propagate significant distances in air, allowing processing such as surface heat treatment or deep penetration welding at atmospheric pressure. High average power also promises high throughput operation, with the deposited energy used efficiently before heat conduction can take place.

## **6.1 Graded Alloy Turbine Disks**

The fabrication of graded alloy turbine disks needed for the next generation of high performance aircraft is an example where the high average power capability of HEEB reduces the fabrication time from weeks to hours. HEEB processing makes possible material properties long desired by, but not previously available to, aircraft engine designers.

A schematic of a gas turbine engine with relative temperature and pressure profiles is shown in Fig. 6.1. The turbine rotor disk, shown at the right, is typically composed of a nickel- or nickel-iron-based superalloy to withstand the extreme operating stresses at elevated temperatures. Turbine disk operating temperatures in modern aircraft are approximately 1400°F (760°C) at the rim in the area of the turbine blade attachment, with lower temperatures toward the hub.

Operating stresses due to the centrifugal loads in these rotating components are high at the rim and still higher at the hub where operating stresses greater than 70,000 psi are encountered. Hub materials, therefore, require very high tensile strength at hub operating temperatures for burst protection and high creep strength at the high temperature rim operating conditions. Also, good fatigue resistance, both low and high cycle are required. The importance of turbine disk material properties was graphically illustrated by the Sioux City, Iowa plane crash of 1988. The disaster occurred when the turbine disk cracked, destroying the engine and much of the plane in midair.

Advanced, high efficiency aircraft engine designs operate at ever increasing temperatures and require higher performance materials. The temperatures and compression ratios for turbine engines manufactured by General Electric Co. for military and civilian applications are shown in Fig. 6.2. Also listed are the requirements for the national High Speed Civilian Transport (HSCT) planned for the year 2005 and the Advanced Supersonic Transport (AST) planned for 2010. Materials with higher temperature capability, higher strength and lower density are needed for both military and civilian applications of advanced high performance aircraft engines.

Turbine disks are currently fabricated using either conventional ingot-fed rolling or by powder metallurgy (P/M) techniques. In either case, the billet undergoing closed die forging is made of

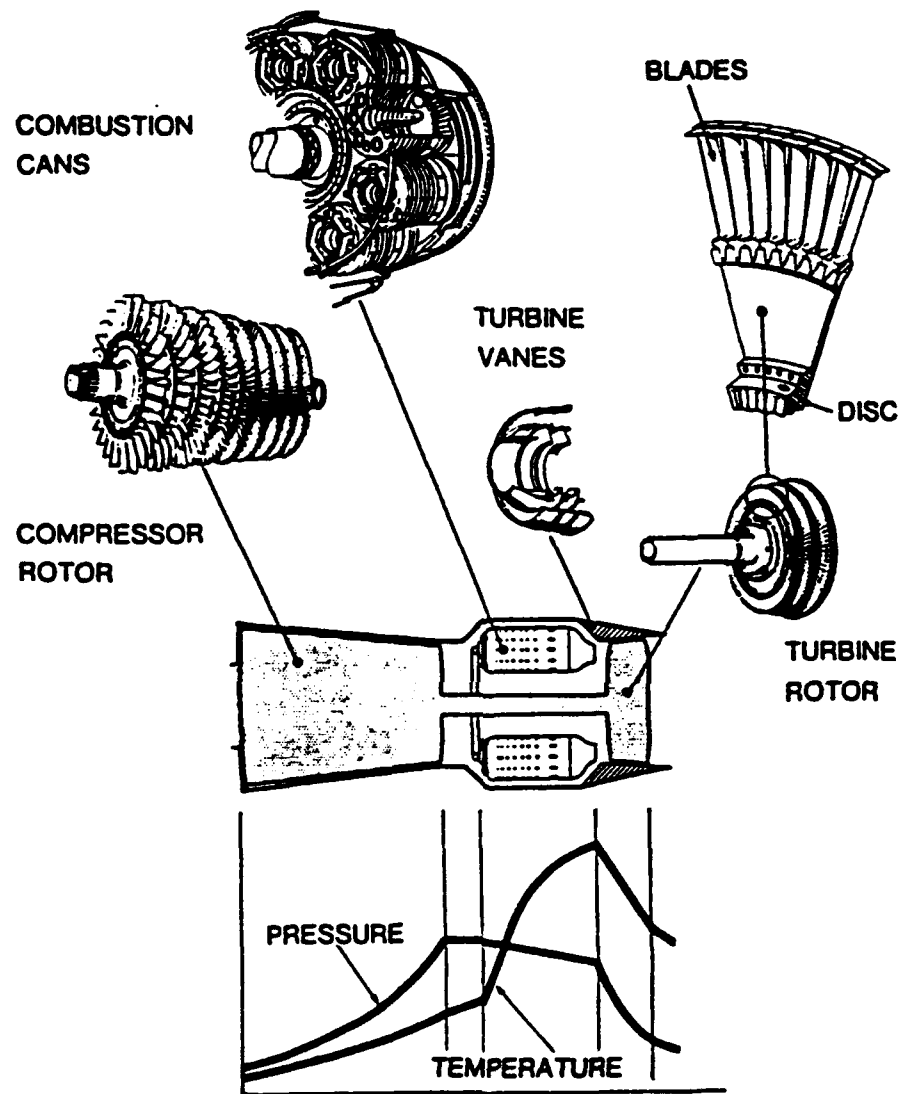
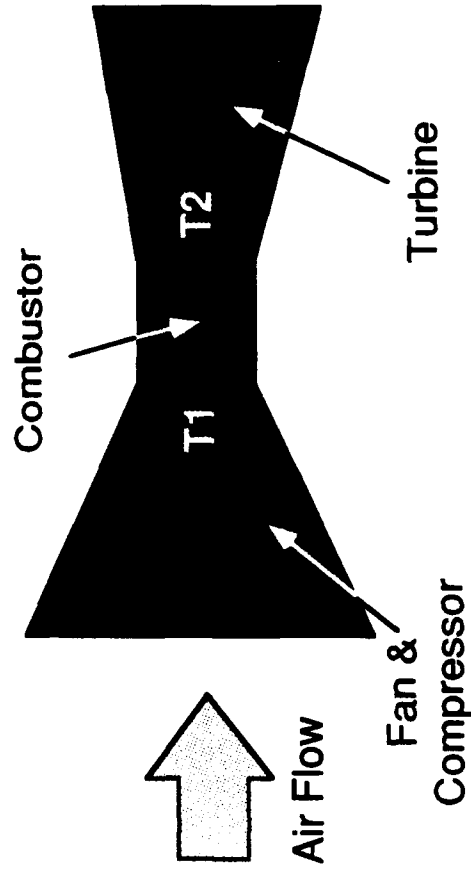


Figure 6.1: A typical aircraft gas turbine engine and relative temperature and pressure profiles are shown.



Year	OPR	Max. T <sub>1</sub> (°F)	Max. T <sub>2</sub> (°F)
1970	15:1	1100	2450
1994	38:1	1280	2600
≈ 2005 HSCT	25:1	1250	2900
≈ 2010 AdvS	75:1	1500	3200
			246 dg 004

Figure 6.2: Advanced aircraft requirements will require higher engine temperatures and compression ratios. [1]

a single alloy. This alloy has properties which represent a compromise between the high tensile strength needed at the disk center and the high temperature creep and fatigue resistance required at the rim.

Ideally, the composition of the disk would be a graded alloy with properties which vary continuously with radius. Three possible methods to fabricate such a disk utilize plasma spraying, laser layer glazing and high energy electron beams. Relative process merits are shown in Table 6.1. Plasma spraying is a slow process, which would require days to build up a turbine disk. Plasma spraying also does not allow the alloy cooling rate to be controlled over the range needed for turbine disk fabrication.

Laser layer glazing is even slower than plasma spraying. Available laser power is limited to 15 kW, and significant power is lost to reflection, with only about 30 percent of the power absorbed. To achieve melting, laser operation requires a high power density, resulting in significant vaporization. Preferential vaporization at power densities of  $3000 \text{ W/cm}^2$  and above can alter alloy chemistry as well as presenting problems with condensate fall in. Like plasma spraying, inadequate available power limits the range of available alloy cooling rate.

There are several advantages to fabrication of graded turbine disks using the HEEB powder metallurgy process. Manufacture of a 500 lb., 40 inch diameter disk using a 250 kW, 2.5 MeV HEEB requires only two hours. Because the HEEB penetrates to a depth of a few millimeters rather than depositing power on the surface, vaporization is minimized. Experiments have shown that electron beam power deposition at densities below  $3000 \text{ W/cm}^2$  range produces negligible vaporization.

The strength of superalloys is very dependent on grain size and its relation to component thickness. Figure 6.3 shows that rupture life and creep resistance increase as component thickness to grain size ratio increase. With a wrought superalloy, provided the ratio was kept constant, fatigue and creep resistance increased with grain size. For a graded superalloy turbine disk, control of grain size is vital. Excessively fine grains decrease creep and rupture strength while excessively large grains harm tensile strength and yield properties.

Key	+ = Advantage 0 = Neutral - = Disadvantage	HEEB	Laser Glazing	Plasma Spray
Graded Alloy Fabrication	Total Power	250 kW - 1 MW	15 kW	50 - 100 kW
Melt Depth	Travel Speed	++	++	-
Vaporization	Melt Depth	+	-	+
Cooling Rate Control	Vaporization	++	-	0
Production Rate	Cooling Rate Control	+	-	-
Production Limitation	Production Rate	250 lbs/hr	10 lbs/hr	25 - 50 lbs/hr
Fundamental Limitation	Production Limitation	Conductive Heat Flow Out of Metal	Power, Vaporization	Cooling Rate
Efficiency	Fundamental Limitation	Conductive Heat Flow	Surface Melting	NA
	Hardening Depth	~ 50%	< 30%	NA
				NA

Table 6.1: A comparison of the relative merits of HEEB processing and competing technologies for the fabrication of graded alloy turbine disks and for deep surface heat treatment.

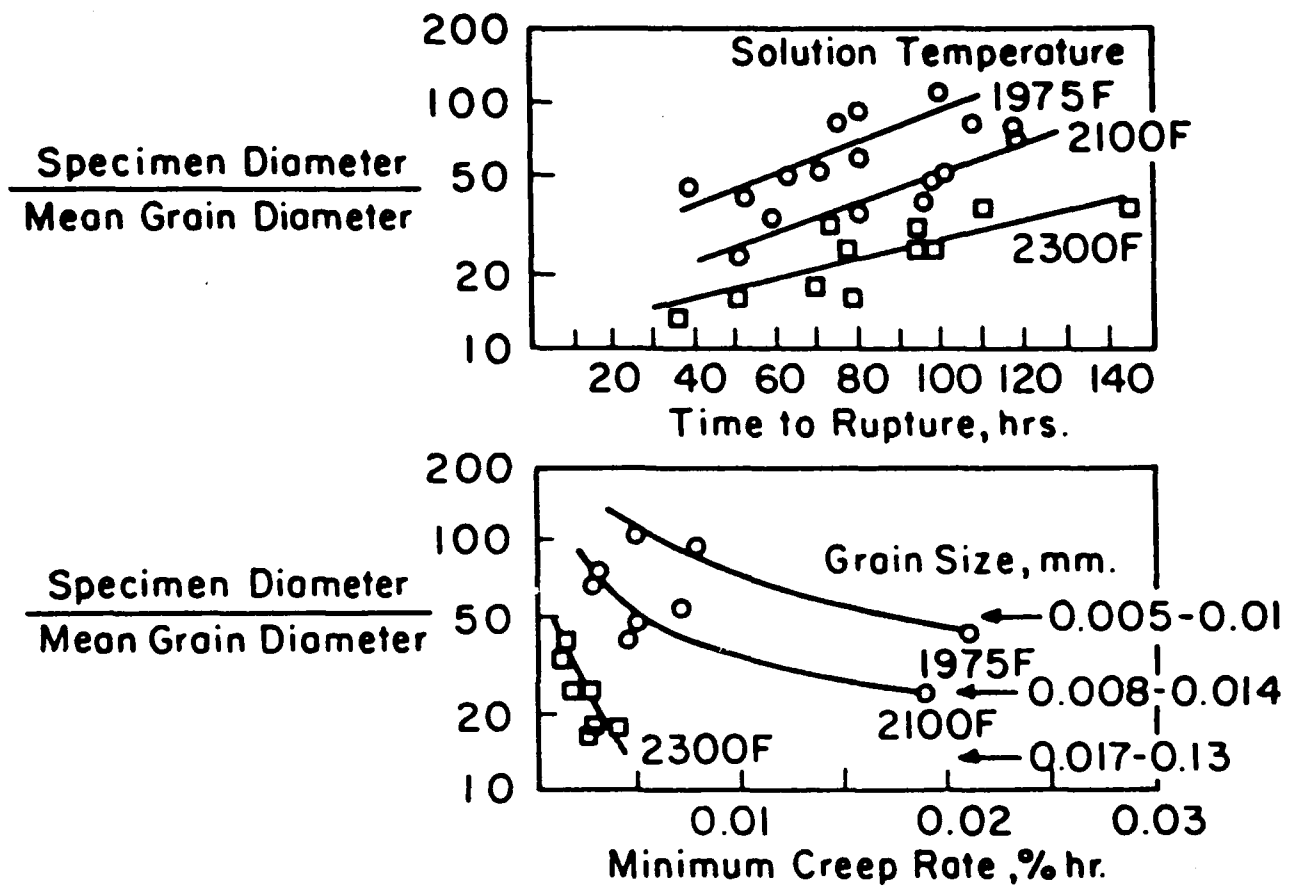


Figure 6.3: The influence of specimen diameter to mean grain diameter ratio and solution-treatment on the creep properties of wrought superalloy tested at 10 ksi and 870°C.<sup>(3)</sup>

Grain size depends in a complicated way on cooling rate for each alloy, but in general increases for slower cooling rates. Finer grain size ( $\sim 2\mu\text{m}$ ) and faster cooling rate is needed near the bore, and larger grain size ( $\sim 200\mu\text{m}$ ) is required near the rim. The absolute cooling rate as a function of radius for HEEB powder metallurgy fabrication is controllable, with the relative cooling rate decreasing outward due to conduction to the water cooled mandrel. Although the exact cooling rate profile needs to be tailored to a particular alloy, the shape and slope of the cooling rate is correct and can be controlled to provide unprecedented process latitude.

Graded alloy fabrication using HEEB powder metallurgy is performed in vacuum. With the possibility of keeping the extruded powder under vacuum at all times, maximum cleanliness is possible. Indeed, electron beams are presently used as the heat source in the purification of powers. Process parameters including the time dependent energy and energy density, mandrel rotation speed, solidification rate and cooling rates have been calculated and are possible only with the electron beam energy and average power available using SRL linear induction accelerator technology.

The processing system described in this proposal can also be used for fabrication of a variety of other novel materials. One promising possibility is to introduce particulate or continuous reinforcement into the disk to manufacture metal-matrix composite (MMC) disks.

## 6.2 Surface Heat Treatment

An important additional advantage of HEEB processing is the ability to process materials in air, and process to significant depth. A second example of a process which will be investigated in this effort is the heat treatment of steels for deep surface hardening.

High energy electron beams also offer significant advantages over conventional heat treatment methods for deep metal surface hardening and wear resistance. The high energy electrons penetrate into the metal, depositing their energy into volumetric rather than surface heating. This raises the temperature of the treated layer above the required transitional (austenitizing) temperature without melting the surface. Hardening depths of 5 mm are possible using HEEB, compared to 1 mm or less using conventional methods, such as lasers which only deposit energy

on the surface. Perhaps more critical is the extremely short dwell time and high throughput that deep penetrating HEEB systems can deliver without causing surface melting. This advantage of HEEB systems occurs because the depth and processing rate of conventional heat treatment surface hardening systems are limited by the slow rate of thermal diffusion into the metal. The megawatt total power available leads to ultra-high throughput processing and a significantly lower cost per unit surface area treated.

Hardening of rail steel is one application of HEEB surface hardening. Hardening depths between 1 and 10 mm are required depending on the application. For example, the crane rails of the Altair Radar System (Kwajalein Island near Guam) have a requirement for a 10 mm hardening depth due to operation in stress-limited conditions. Commuter rail steel requires approximately 2 mm hardening depth for abrasion resistance and freight haul rails require 3-4 mm. These hardening depths can only be achieved with high energy (5-10 MeV) electron beam treatment systems. The advantages of HEEB systems for graded alloy fabrication and surface hardening are summarized in Table 6.1.

Table 6.2 shows the operating parameters for a proposed HEEB material processing experiment with an electron beam produced by SRL SNOMAD-IV induction accelerator modules.

The possibility of cost effective production of graded alloy materials and of high throughput surface heat treatment at atmospheric pressure using HEEB represents a significant opportunity for innovation in material processing.

A conceptual design for the overall system is shown in Figure 6.4 and the processing system parameters are listed in Table 6.2.

Modifications to the system required to convert from graded alloy fabrication to HEEB deep surface hardening will also be determined. The modifications will be primarily be in the electron beam focusing and the target block transport systems.

Surface heat treatment of steels is a much faster process than graded alloy fabrication, requiring only one pass of the electron beam. Fabrication of a graded alloy block will take several minutes of processing time. The electron beam power density is in the  $100\text{-}1000 \text{ W/cm}^2$

**TABLE 6.2: THE OPERATING PARAMETERS FOR A PROPOSED HEEB  
PROCESSING SYSTEM ARE LISTED**

	<b>Graded Alloy Fabrication</b>	<b>Heat Treatment Surface Hardening</b>
Beam Energy	2.5 MeV	2.5 MeV
Beam Current	500 A	500 A
Pulse Length	50 ns	50 ns
Repetition Rate	4000 pps	4000 pps
Average Power	250 kW	250 kW
Power Density	0.1 - 1 kW/cm <sup>2</sup>	1 - 10 kW/cm <sup>2</sup>
Penetration Depth	3 mm	3 mm
Surface Temperature	1200 - 1400 °C	1450 - 1650 °C
Processing Rate	250 lbs/hr	80 cm <sup>2</sup> /sec

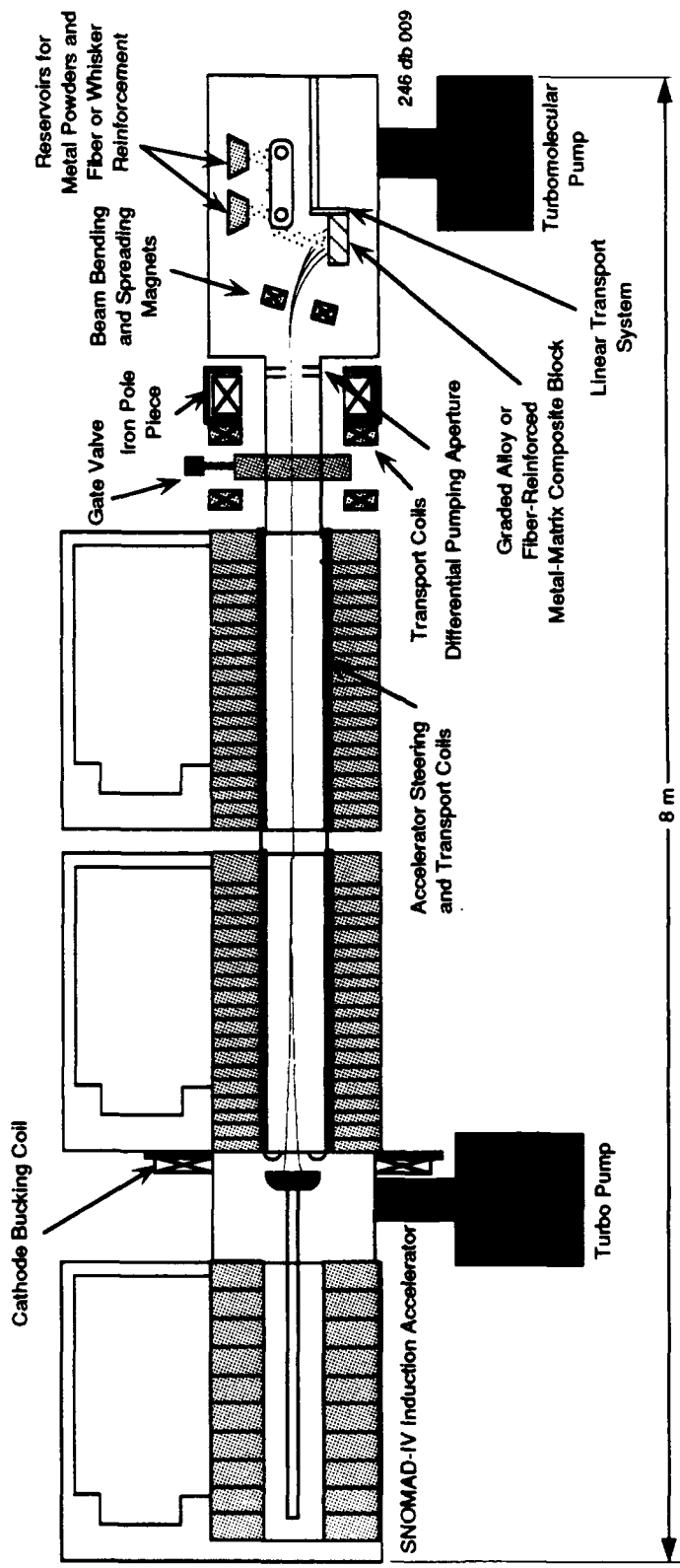


Figure 6.4: A SNOMAD-IV induction accelerator based material processing system

range for graded alloy fabrication and approximately  $3000 \text{ W/cm}^2$  for surface heat treatment. To achieve uniform heating and cooling rates, careful tailoring of the power deposition profile is required. Design tradeoffs between solenoidal/quadrupole beam spreading and oscillatory beam motion will be examined in the experimental system design study.

### 6.3 Graded Superalloy Turbine Disk Fabrication

The aircraft turbine rotor shown in Figure 6.1 consists of the central turbine disk surrounded by the turbine blades. The rotor is typically fabricated from a single nickel-based superalloy using either conventional ingot-fed rolling or powder metallurgical techniques. Powder Metallurgical (P/M) techniques offer both economic and structural advantages. Near net shape technology ensures more efficient material utilization, which is important for these high cost materials. Metallurgical benefits include improved homogeneity and control of microstructure to achieve enhanced mechanical properties. A near-net-shape turbine disk fabricated using hot isostatic pressing is shown in Figure 6.5.

The principal use of powder made by inert gas atomization has been for the production of gas turbine disks. The process facilitates the use of high-strength alloy compositions that are not workable by conventional techniques. Nickel-based superalloys for turbine disk fabrication consist of 50-75% nickel with significant amounts (5-15%) of chromium and cobalt and lesser amounts (2-5%) of molybdenum, tungsten, tantalum, titanium and aluminum. Trace amounts ( $\sim 0.1\%$ ) of carbon, boron and zirconium are also present. Use of the HEEB P/M process to fabricate graded alloy turbine disks will require optimization of the superalloy compositions. Staff members of the Alloy and Process Development Department of the General Electric Aircraft Division have expressed interest in P/M development which will occur after the HEEB P/M fabrication process is demonstrated.

Graded alloy turbine disks will have higher tensile strength at hub operating temperatures and higher deformation resistance at rim operating conditions. These improved material properties will allow for higher operating temperatures and compression ratios for next generation aircraft. An HEEB P/M process for fabricating graded alloy turbine disks is shown schematically in

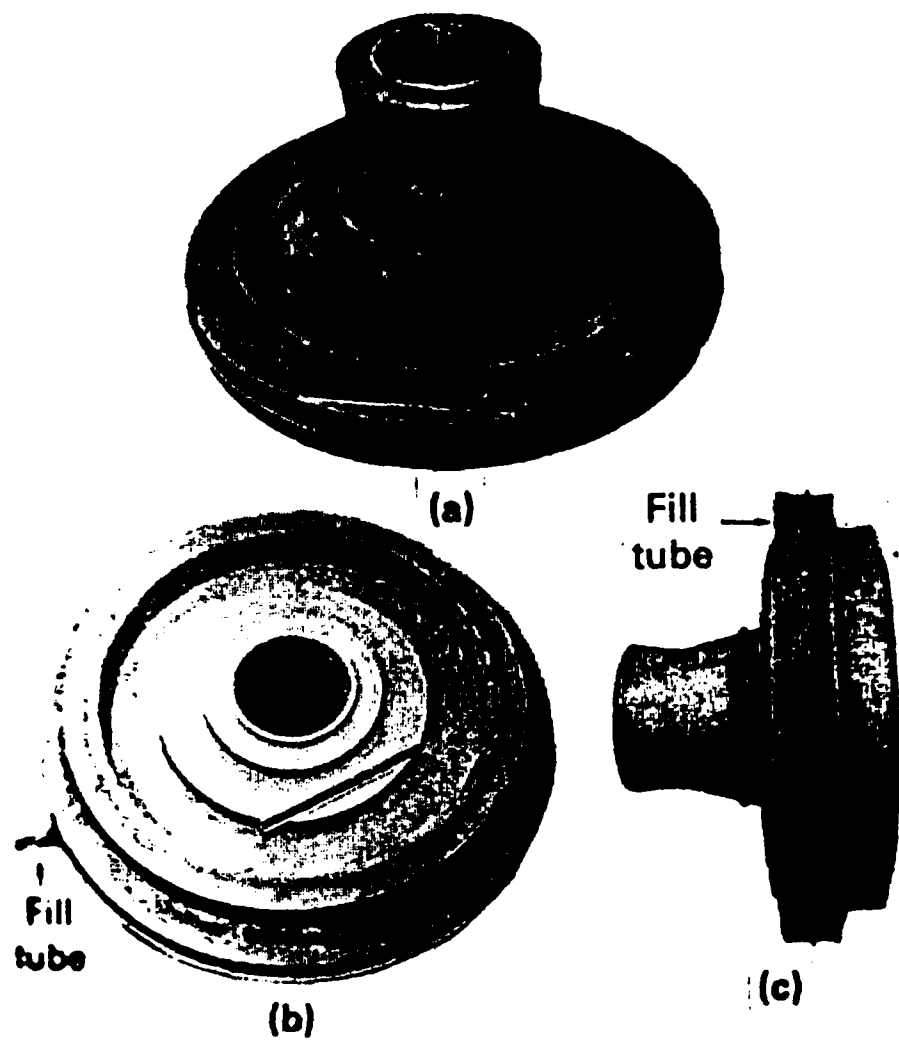


**Figure 6.5:** (a) Top view, (b) bottom view and (c) side view of a compacted turbine disk with unremoved can produced by hot isostatic pressing. The disk consists of a single composition nickel-based superalloy powder compressed to about 98% theoretical density.

**Figure 6.6.**

The nickel-based superalloy mandrel is surface heated to melting temperature ( $T \sim 1450^\circ\text{C}$ ) by the 250 kW, 2.5 MeV electron beam with a power density of 500-1000 W/cm<sup>2</sup>. Disk buildup begins using alloy powder of the same composition as the mandrel. The powder is melted to the mandrel and superheated to approximately 1650°C. Alloy powder sizes smaller than the electron penetration depth (1-2 mm) ensures uniform power deposition. The powder composition, applied electron beam power and cooling rate are varied as the disk is built up to achieve increasing grain size and high temperature deformation resistance, and decreasing tensile and yield strength. A 500 lb, 40 inch diameter disk would require two hours to fabricate using a 250 kW HEEB system.

The required HEEB power density and total beam power as a function of time are shown in Figures 6.7 & 6.8. These projections were computed using a simulation code which includes the temperature-dependent thermal properties (thermal conductivity, diffusivity, specific heat and heat of fusion) of the nickel-based superalloy. Conductive heat transport from the surface melt zone to the water-cooled mandrel determines the solidification rate and the rate at which powder is added. The code includes power losses due to both conduction and radiation in a one-dimensional cylindrical geometry. Heat transport across the thin superheated melt zone occurs quickly due to convection, with the liquid assumed isothermal. The temperature drop to melting temperature occurs across a thin boundary layer at the solid-liquid interface.

Figure 6.7 shows the HEEB power density required to fabricate this turbine disk. The initial surface heating to nickel melting temperature (1450°C) requires 500-1000 W/cm<sup>2</sup>. The initial buildup phase, while the disk increases from 6 to 20 cm radius, requires power densities in the 150-300 W/cm<sup>2</sup> range. After the first ten minutes, power densities of approximately 100 W/cm<sup>2</sup> are required, balancing losses due to radiation as well as conduction to the mandrel. The ability to vary the power density over a wide range (100-1000 W/cm<sup>2</sup>) is necessary for processing, and unique to the HEEB technology. Laser glazing is forced to operate at maximum power density, due to low ( $\leq 15$  kW) total power. Plasma spraying operates over a narrow range of power

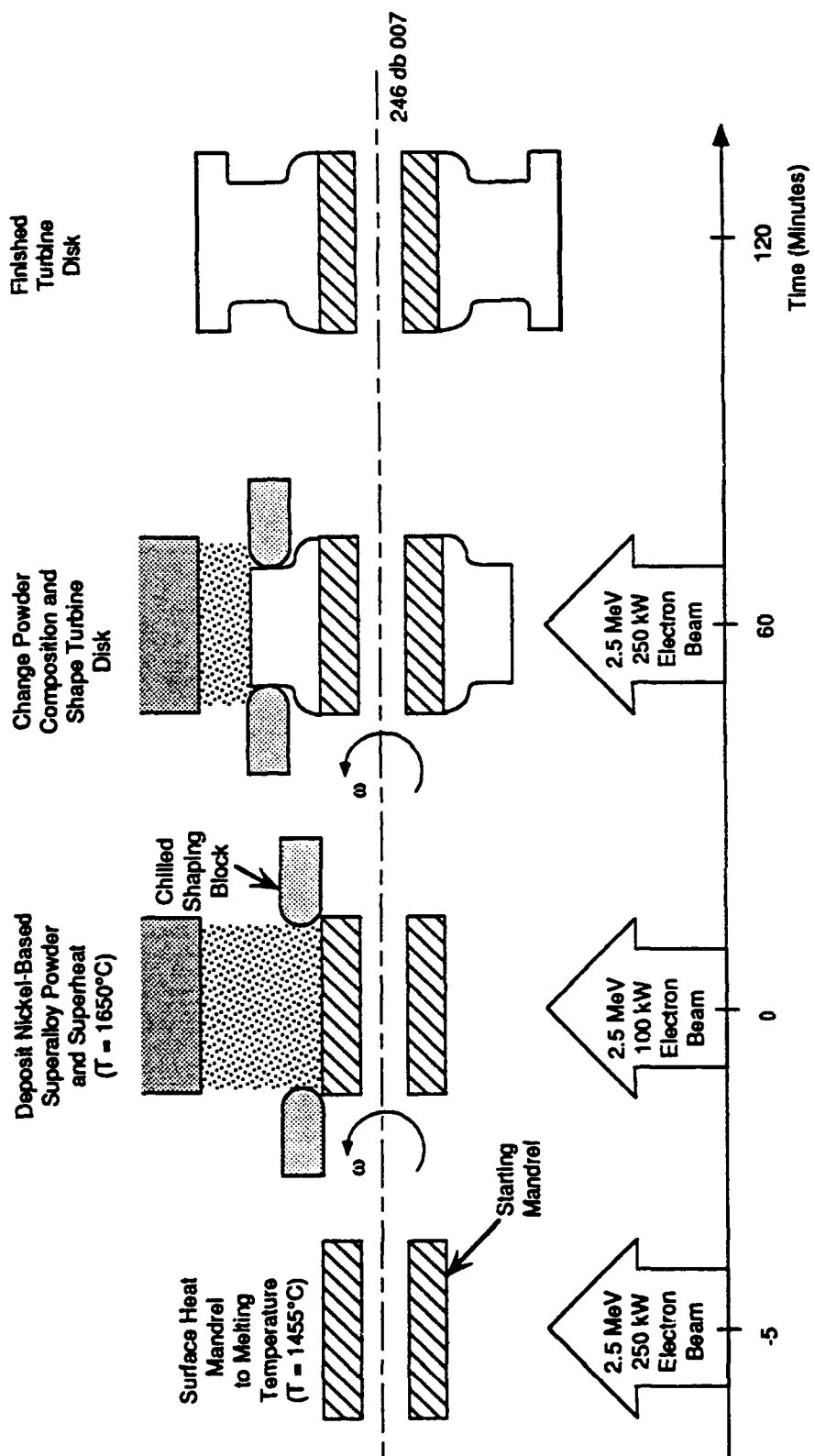


Figure 6.6: The process of fabricating a graded alloy turbine disk using HEEB processing is shown. The mandrel is water-cooled at the center. The alloy powder composition and HEEB power is varied in time to produce a graded composition with the varying mechanical and thermal properties. Fabrication of a 5000 lb. disk requires approximately two hours to complete.

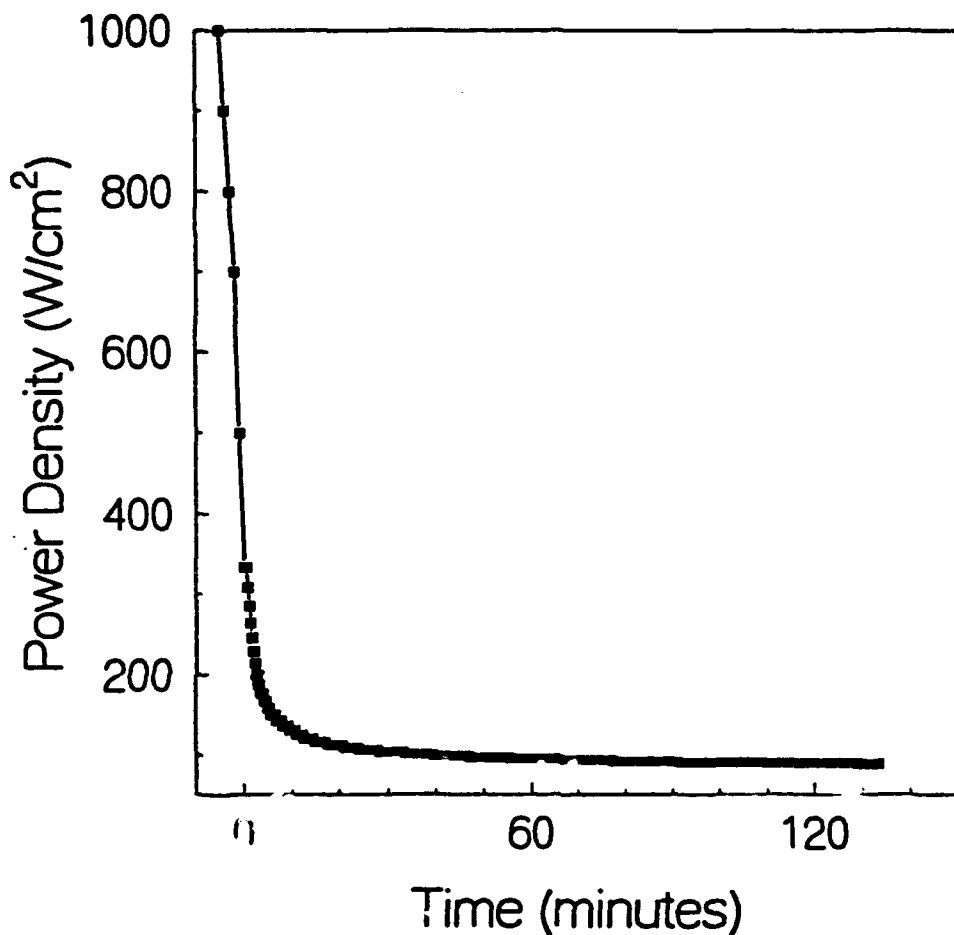


Figure 6.7: The required HEEB power density for processing the graded alloy turbine disk as calculated by a heat transport code. A wide range of total power and power densities is required, which can be easily achieved by varying the HEEB repetition rate.

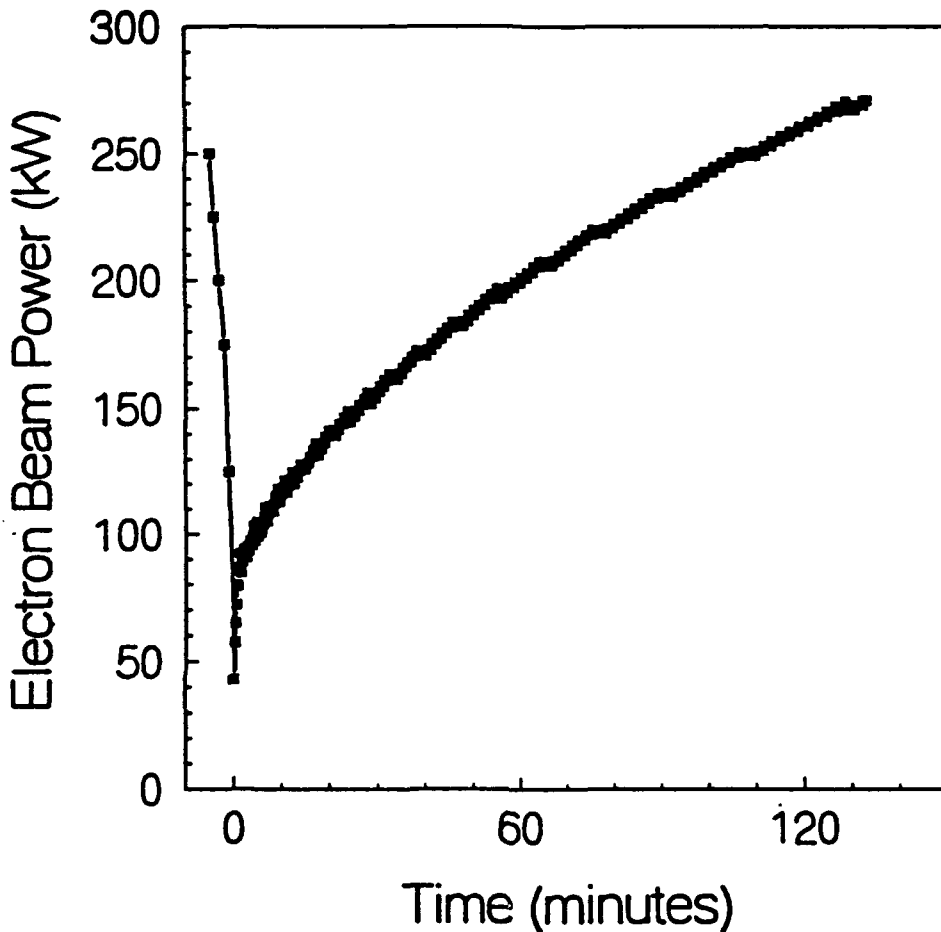


Figure 6.8: The required total HEEB power for processing the graded alloy turbine disk. The required power is considerably larger than the 15 kW available from CO<sub>2</sub> laser layer glazing or the 50-100 kW available from plasma spraying.

densities, controlled primarily by travel speed. A comparison of these process features is shown in Table 6.1.

Figure 6.8 shows the total HEEB power required during the two hour fabrication process. Preheat power of 150-250 kW is required. Less power (50-100 kW) is required early on, with power requirements rising to 250 kW as the total disk surface area increases with radius. The disk shape used is that of a fighter aircraft turbine engine, with a disk length ranging from 5 inches at the bore to 2 inches at the rim. Power requirements for other size turbine disks scale roughly as the total disk surface area.

Figure 6.9 shows the calculated temperature time history at four radial locations. The initial cooling rate is rapid near the disk center ( $r = 8$  cm) and slower at the edge. The high central cooling rate of several °C/s is caused by rapid heat conduction to the water-cooled mandrel and will result in small grain size and high tensile strength. The slower cooling rate at the rim will result in larger grain size and increased high temperature deformation resistance. The cooling rate can be varied over a wide range by adjusting the HEEB power density and the alloy powder deposition rate. The desired grain size is  $\sim 20\mu\text{m}$  at the bore and  $\sim 200\mu\text{m}$  at the rim.

The mandrel rotation rate is an additional process parameter that can be controlled. Rotation rate should be sufficiently fast so that the metal is still molten by the time the next layer is deposited, but not so fast as to spin off molten metal. The first requirement is determined by the code to require a rotation rate greater than approximately 0.5 RPM. To prevent splashing, the bond number  $B_0$  must be less than unity:

$$B_0 = \frac{\rho(g + \omega^2 r)h}{2\gamma/h} < 1$$

where  $\rho$  is the metal mass density,  $g$  is the acceleration due to gravity,  $\omega$  is the rotation rate,  $r$  is the disk radius,  $h$  is the melt depth and  $\gamma$  is the surface tension coefficient. To prevent splashing, melt depths less than 0.6 cm and rotation rates less than 20 RPM are required.

The electron beam requirements for high throughput graded alloy turbine disk fabrication are consistent with operating parameters of the SRL SNOMAD-IV based induction linear accelerator.

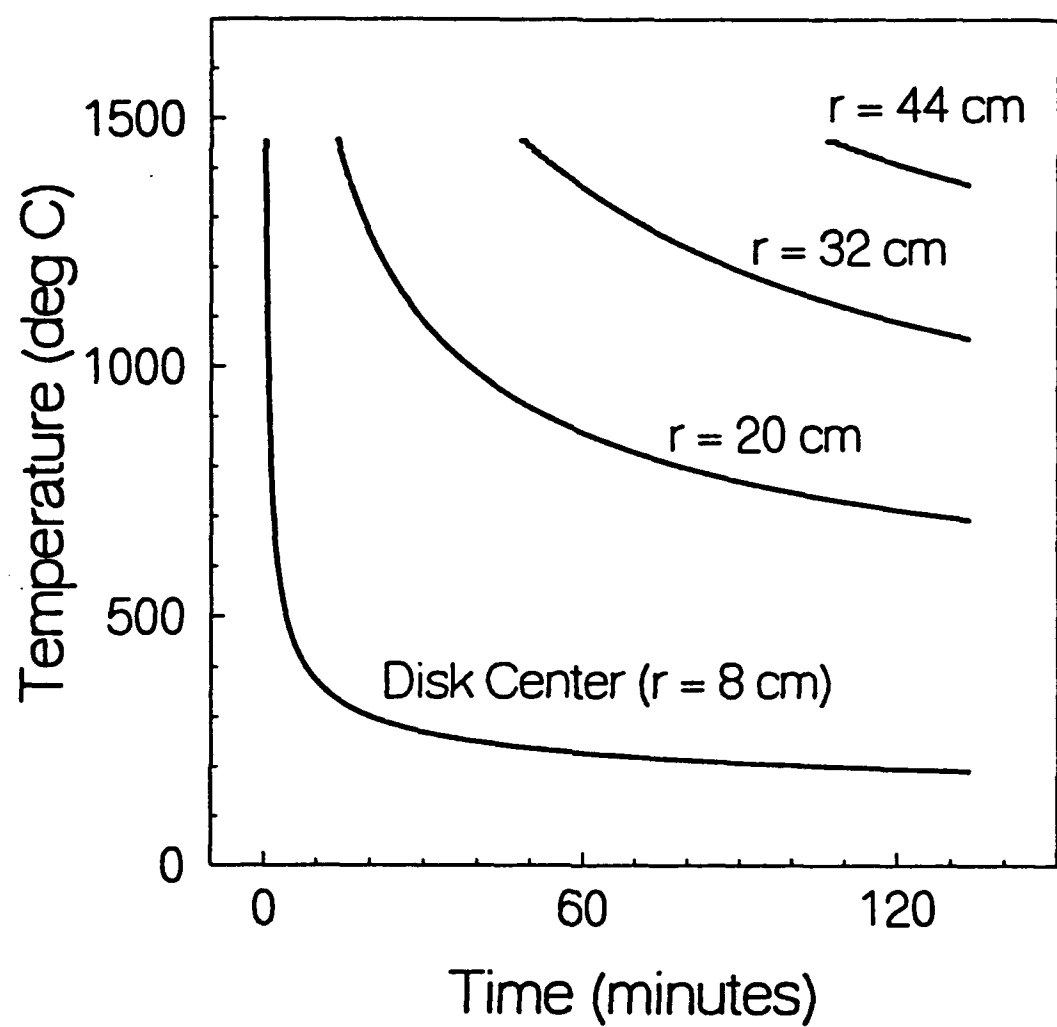


Figure 6.9: The temperature history at four radial locations as calculated by a heat transport code. The initial cooling rate is fastest in the center, resulting in small grain size and high tensile strength.

This process is entirely consistent with computer control, with the electron beam power density effectively controlled by varying the repetition rate of the accelerator and the spatial power deposition profile of the electron beam. The alloy cooling rate and the dependence of cooling rate on radial position are in the correct range to produce the necessary mechanical and thermal properties. The system will require alloy powder deposition rate of approximately 4 lbs. per minute and a mandrel rotation rate of a few RPM.

#### **6.4 Deep Surface Hardening Using a High Energy Electron Beam System**

Efficient deep surface hardening of metals at high process throughput is an application of high energy electron beams which cannot be achieved using any other method. As shown in this section, the surface hardened layer produced by processing with electron beams in the 1.5-10 MeV energy range will be 2-5 times deeper than previously achieved using purely surface heat sources such as CO<sub>2</sub> lasers and low energy electron beams. The opportunity for low cost surface hardening with low residual stresses and material distortion as well as extremely high throughput are additional advantages of HEEB processing when compared with conventional hardening methods.

During surface hardening, the outer layer of an already machined part or structure is heated above the critical temperature for phase transformation (about 730°C for low carbon steel), held at temperature for a short time to austenitize (dissolve carbon and/or carbides) and then quenched. A second low temperature (300-400°C) cycle for tempering may also be included, although it is typically not required.

Conventional methods of surface heat treatment include low energy density processes such as inductive skin depth heating and high energy density methods such as laser and low energy electron beam processing. Low energy density methods are slow and cause material distortion which forces the reworking of hardened parts. High energy density methods, especially laser processing, are now used for a wide variety of high volume surface hardening applications in the aerospace, tooling and automotive industries.

In high energy density heat treatment, the surface is heated above the austenitizing temper-

ature. When the source of energy is removed, the part self-quenches owing to the diffusion of heat into the volume of the part. This is made possible by the extremely rapid heating rate of laser and low energy electron beam sources at the surface.

Figure 6.10 shows the details of a laser surface heating experiment including the temperature time history and isothermal transformation diagram for a low carbon (0.2%) steel. The temperature at (a) the surface and (b) a depth of 0.5 mm shows that heat is conducted into the steel with a thermal diffusion coefficient of approximately  $0.12 \text{ cm}^2/\text{s}$ . The power density of  $3 \text{ kW/cm}^2$  temperature applied for a 0.2 second dwell time heats the surface up to  $1100^\circ\text{C}$ , well below the  $1500^\circ$  melting temperature. The temperature at a depth of 0.5 mm is raised above the  $730^\circ$  austenitizing temperature and is subject to a fast quenching rate which strongly favors martensite formation. Figure 6.11 shows the measured profile of microhardness versus depth after laser surface hardening. A hardness above HV 700 to a depth of 0.6 mm is measured, compared with a bulk hardness of HV 250.

As the applied power density in laser and low energy electron beam hardening systems is increased, shorter dwell times are required to prevent surface melting with a resulting limit in the depth of hardening. For heat treatment hardening by these methods, where power is deposited only on the surface, power densities in the  $10^3 - 10^4 \text{ W/cm}^2$  range and dwell times of 0.01 to several seconds are typically used.

High energy density surface hardening is not used at power densities below  $1 \text{ kW/cm}^2$  because the long processing time leads to low throughput and also because radiative and convective heat losses make the process inefficient. High energy ( $E > 1.5 \text{ MeV}$ ) electron beams deposit energy over a profile in depth rather than at the surface. Because the power is not deposited at the surface, HEEB hardening is limited neither by surface melting nor by the speed of heat diffusion. Large power densities ( $10^3 - 10^4 \text{ W/cm}^2$ ) can be combined with short dwell times and deep penetration to process at high throughput.

HEEB surface hardening was modeled at SRL using a time dependent heat transport code, with the results shown in Figures 6.12 & 6.13. Figure 6.12 shows a comparison of the maximum

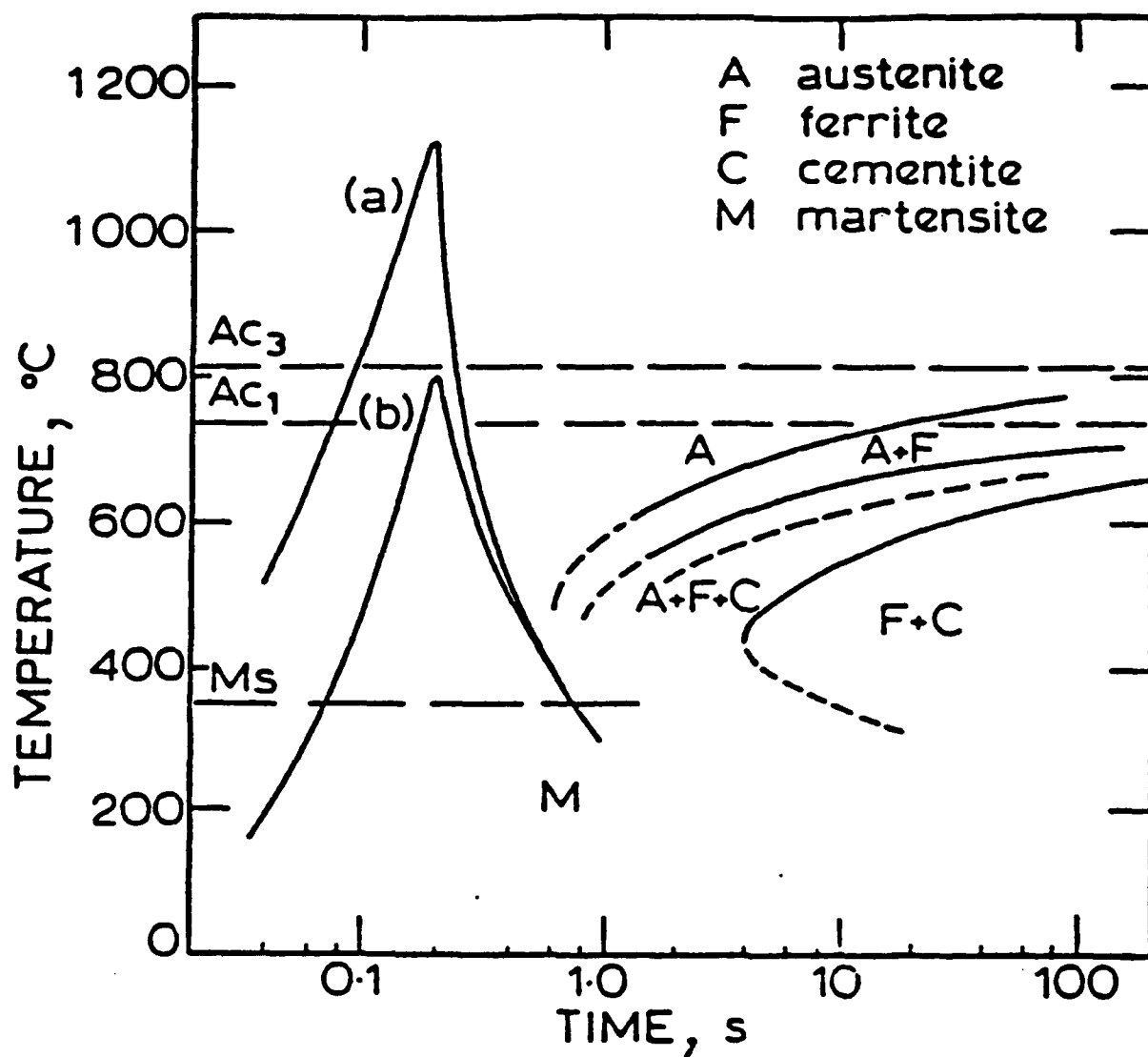


Figure 6.10: The temperature time history for (a) the surface and (b) 0.5 mm into the steel is shown. A power density of  $3 \text{ kW/cm}^2$  was applied for 0.2 seconds. An isothermal transformation diagram is also shown.

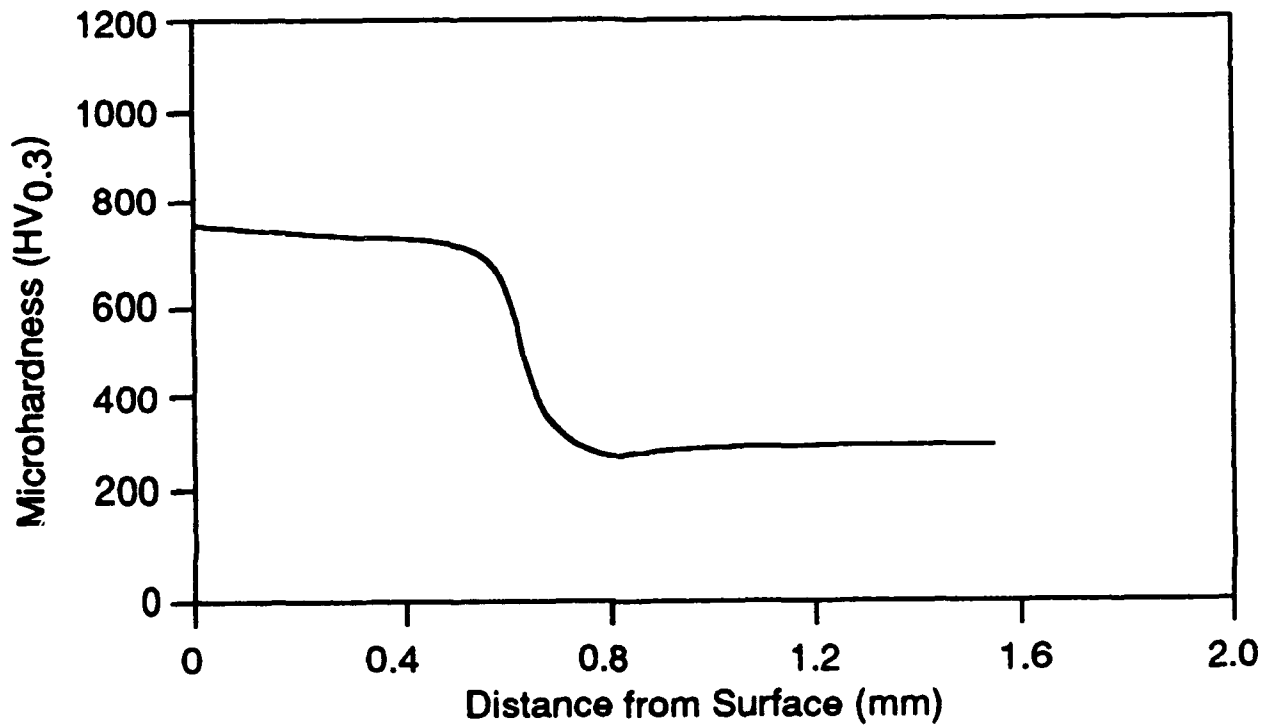


Figure 6.11: The experimentally measured microhardness for the laser surface treated low carbon steel is shown.

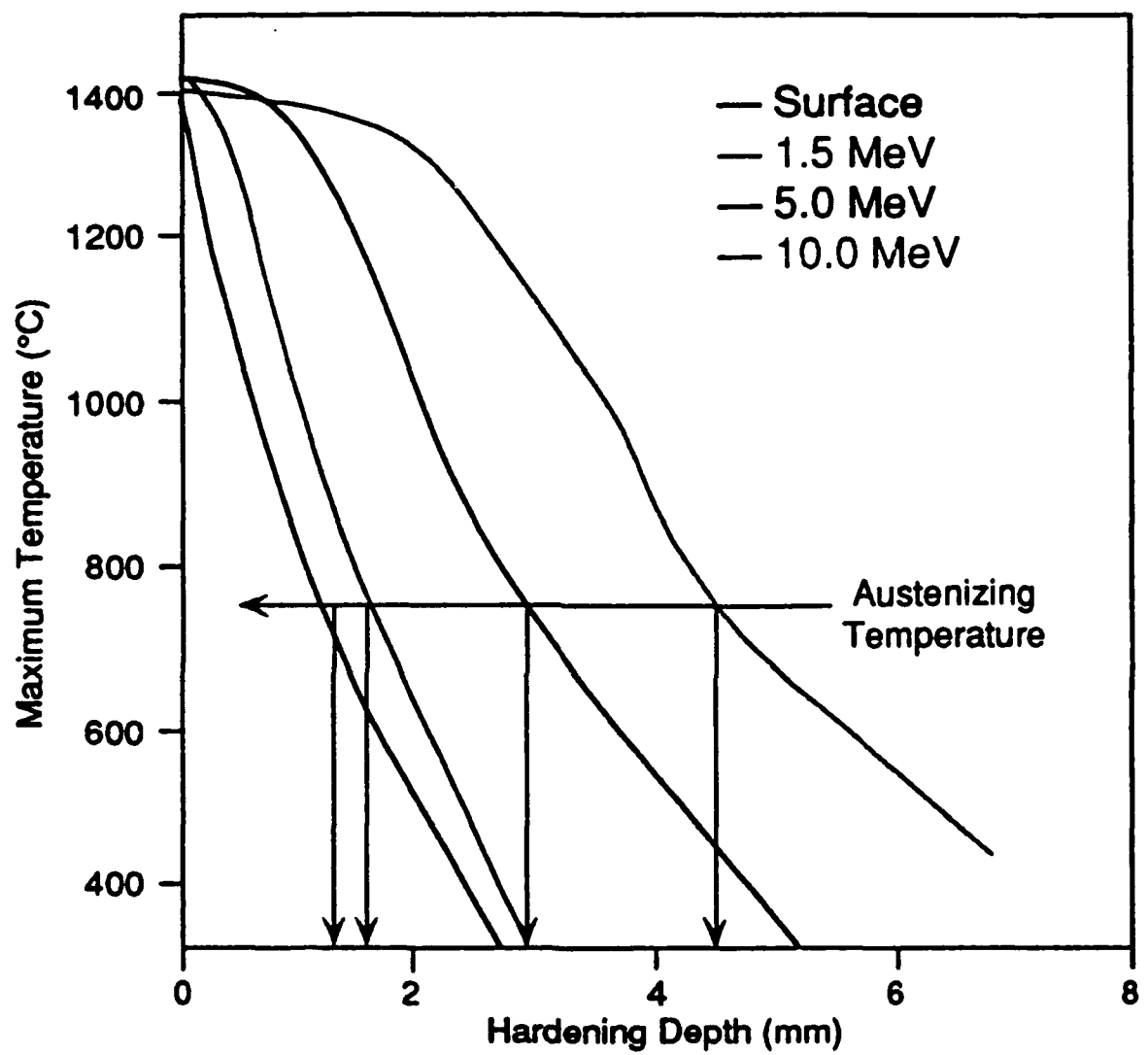


Figure 6.12: The maximum temperature and achievable depth of HEEB surface hardening is shown of 1.5, 5.0 and 10.0 MeV beams at 3  $\text{kW}/\text{cm}^2$  power density.

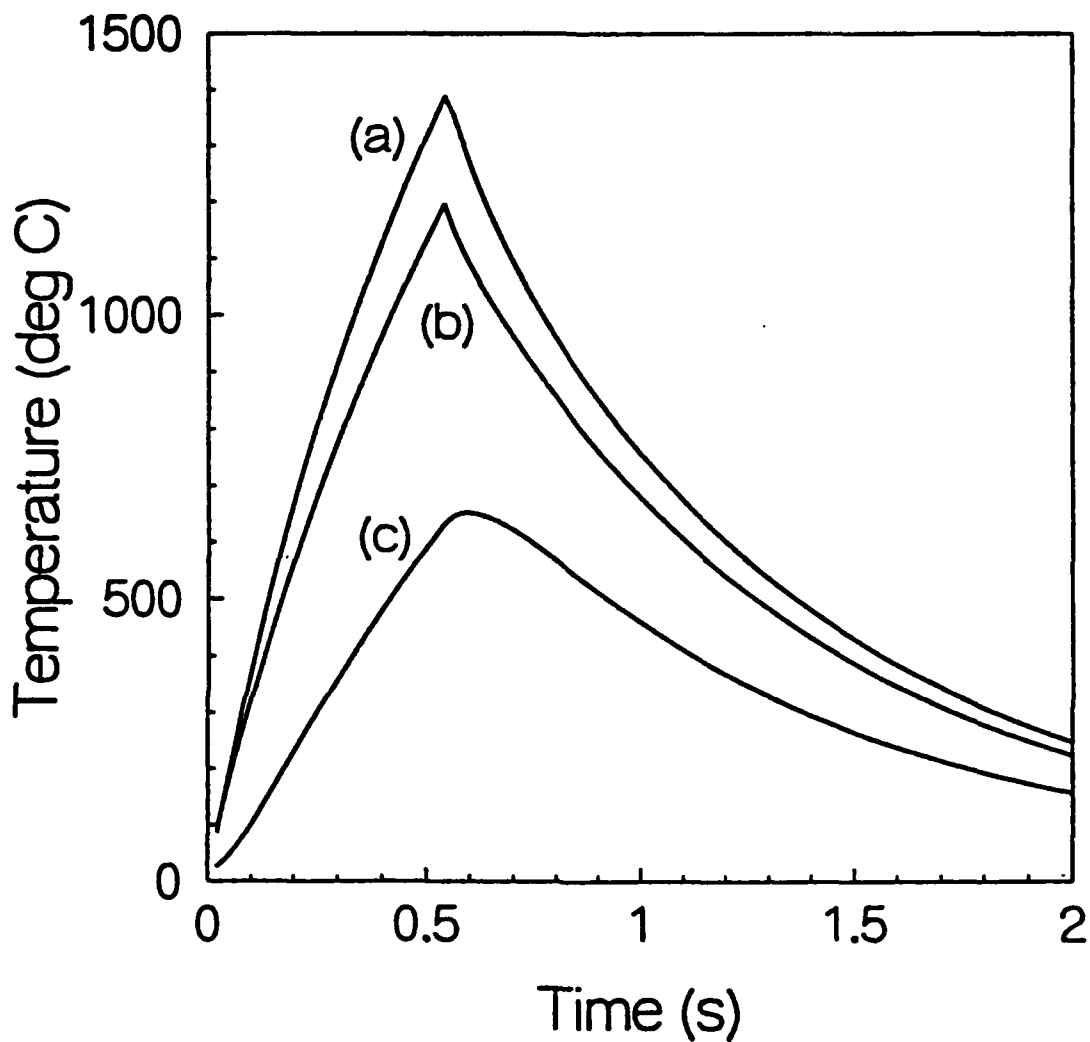


Figure 6.13: The time history for surface hardening with a 5.0 MeV HEEB system is shown. A power density of  $3 \text{ kW/cm}^2$  was applied. Temperatures at (a) the surface, (b) 1.5 mm and (c) 3 mm depths are shown.

temperatures attained with surface and volumetric heating methods. The first curve shows that using lasers or low energy electron beams, diffusive heat conduction allows a hardening depth of slightly more than 1 millimeter. The other three curves show maximum temperature profiles for 1.5, 5.0 and 10.0 MeV electron beam systems. The applied power density in all four cases is  $3 \text{ kW/cm}^2$ , with the dwell times adjusted to prevent surface melting.

Deeper surface hardening than shown in the curves of Figure 6.12 are possible if a combination of volumetric heating and conduction is used. One possible method is to oscillate the beam allowing the bulk metal to heat up. This method is presently used in conventional heat treatment. A second method is to "clamp" the surface temperature using a carefully regulated fine water spray.

The experimental setup for HEEB surface hardening is very similar to the system which will be used for HEEB graded "o" fabrication shown in Figure 6.4. Heat treatment will be done at atmospheric pressure in the same chamber and using the same positioning system. The electron beam power density will be increased from the  $100\text{-}1000 \text{ W/cm}^2$  level used in graded alloy fabrication to approximately  $3 \times 10^3 \text{ W/cm}^2$ , with an electron beam spot radius of several centimeters. The same beam bending and spreading magnet system can be used for both experiments.

Three steels which will be surface hardened to a 3 mm depth using the 2.5 MeV HEEB system include AISI C1060, 4340-H and 1020. The AISI C1060 is a standard high carbon steel with similar specifications to the steel used for railroad rails. The high carbon content indicates that the steel is hardenable, but none of the plain carbon steels will harden all the way through, even when drastically quenched (unless manufactured in very small sections). By HEEB deep heat treatment this less expensive carbon steel, initially inferior to the alloy steel in strength and elastic properties, can be strengthened to a hardness close to that of a hardened alloy steel to a 2 mm depth.

The AISI 4340 is a deep hardening (Rockwell 53-60) alloy steel similar to that used in gun barrels. AISI C1020 is a low carbon steel, which has the lowest initial hardness, commensurate

with its low carbon content. It is expected that this steel will show a large, easily measurable hardness increase when treated using the HEEB system.

After processing with the HEEB, diagnostic tests will be performed on the metallurgical samples to determine the microstructure, properties, residual stresses and distortion resulting from the HEEB hardening process. The microstructure will be characterized by metallographic polishing and etching as well as microhardness profiles. Appropriate samples will be selected for evaluation of mechanical properties, including yield strength, tensile strength, elongation, reduction in area, fracture mode and impact energy.

Distortion resulting from samples processed by the HEEB will be compared to similar samples produced by conventional heat treatment processes, including arc, laser and low energy electron beam processing. Residual stresses will be estimated by sectioning the samples and measuring the elastic springback. As with the distortion samples, the HEEB residual stress measurements will be compared to the stresses produced by conventional heat treating processes.

A preliminary cost comparison of HEEB and laser hardening is given in Table 6.3. For a laser hardening system based on a 15 kW CO<sub>2</sub> laser (the largest commercially available), the unit treatment cost is \$12.80/m<sup>2</sup> for hardening to a depth of 1 mm. The hardening costs for an envisioned 1 MW 10 MeV system is \$0.22/m<sup>2</sup> for hardening to 5 mm. The dramatic difference in cost is due both to the higher electron beam generation efficiency and the high throughput possible with volumetric HEEB power deposition. The unit treatment costs include amortized capital costs plus operational costs such as prime electrical power (\$0.07/kWh) and maintenance costs (5% of capital costs per year). Facility costs and labor are not included but are expected to be comparable on a unit basis.

The hardening cost for a particular application will of course depend on the metal geometry. However, for typical plate and rail geometries, electron beam hardening costs are considerably less than the difference between the cost of factory hardened and unhardened steel. In addition, for many applications where unhardened steel is already in place (such as heavily used rail lines), the cost of hardening preexisting steel will be much less than the cost of replacement.

Process Parameters	CO <sub>2</sub> Laser (15 kW)	Electron Beam Source (10 MeV)
• Penetration Depth	≤ 1 mm	≤ 5 mm
• Beam Generation Efficiency	15%	50%
• Beam Power	15 kW	1 MW
• Process Throughput	4.1 cm <sup>2</sup> /sec	273 cm <sup>2</sup> /sec
• Capital Cost	\$500K	\$3M
• Unit Treatment Cost	\$12.8/m <sup>2</sup>	\$0.22/m <sup>2</sup>

246 db 010

Table 6.3: Comparative High Throughput Heat Treatment Technologies



GE Aircraft Engines

---

General Electric Company  
P.O. Box 156301, One Neumann Way  
Cincinnati, OH 45215-6301  
513-243-2000

January 8, 1992

Dr. Dan Goodman  
Science Research Laboratory  
15 Ward St.  
Somerville, MA 02143

Dear Dan,

As we have discussed in detail over the last month, although there are a large number of challenging issues to address, I believe the concept of a graded alloy turbine disk manufactured by HEEB has significant potential. As you know, increasing the temperature and load carrying capabilities of turbine disks is probably the most critical materials development required for advanced engines in the early 21st century. Preliminary design for the advanced subsonic transport currently predicts turbine disk temperatures around 1500°F, over 200°F above our current materials capability. Consequently, development of a process for making higher temperature disks is important for GE Aircraft Engines. If I can be of any further assistance please do not hesitate to call.

Richard G. Menzies

Dr. Richard G. Menzies, Manager  
Alloy & Process Development

Ext. Lit RGM - 6

## SECTION 7

### E-BEAM STERILIZATION EXPERIMENTS USING SNOMAD-IV

The National Science Foundation (NSF) has partially funded an experimental program which utilizes the SNOMAD-IV to perform experiments in bulk sterilization. Additional support is provided by MERCK and BARD. This additional support is supplied in the form of technical assistance. Personnel from these companies supply samples, assist in the experiments and analyze the data.

Bulk sterilization of disposable medical products is a rapidly growing industry that presently utilizes ethylene oxide (EtO) gas<sup>(1,2)</sup> or gamma radiation from radioactive emitters such as Cobalt-60.<sup>(3)</sup> These sterilization methods are becoming economically unattractive and their byproducts are becoming increasingly unacceptable to regulatory agencies of the Federal Government. Ethylene oxide is a toxic, explosive gas which is stabilized with chlorofluorocarbons (CFCs). Standard sterilization mixtures now contain 12% EtO in a stabilizing buffer of 88% CFCs. The Montreal Protocol (February 13, 1989) restricts the generation and use of ozone depleting CFCs. Surcharges of \$3.00 per kilogram, which essentially double the cost of CFCs, and of EtO mixtures were imposed on CFCs in January, 1990. In addition, these protocols mandated essentially complete recovery of the CFCs. Two agencies of the Federal Government are investigating the carcinogenic properties of EtO in connection with its use as a bulk sterilization source.<sup>(4,5)</sup> The bulk sterilization industry is now attempting to convert to pure EtO and EtO/N<sub>2</sub> mixtures but the cost of the required new equipment as well as safety and health issues will eventually limit the market to only essential uses of EtO; that is, applications where gamma radiation cannot be used.

The most widely used radioactive isotope for sterilization is Cobalt-60, which is produced from stable Cobalt-59 by neutron absorption in nuclear reactors. Cobalt-60 emits two gamma rays with photon energies of 1.17 and 1.33 MeV and has a half-life of 5.3 years. A modern high throughput Cobalt-60 sterilization facility uses approximately 4 MCi of Cobalt-60 (~0.8

MCi/year) which in turn produces 56 kilowatts of gamma ray power.

The largest vendor of Cobalt-60 is Nordion International which is a crown corporation of the Canadian government. Nordion supplies over 80% of the market, approximately 40 MCi per year and is now in the process of privatizing the production of encapsulated Cobalt-60 sources. Increased Cobalt-60 costs to the user are expected because of privatization and because of increased costs associated with the storage, handling and disposal of Cobalt-60 once its activity has reached uneconomic levels. Cobalt-60 used in bulk sterilization plants now costs \$1.62 per Curie which represents a 100% increase in cost over the past 3 years. A cost of \$2.00 per Curie is expected once privatization is complete.

Alternate existing methods for bulk sterilization of medical products are at present not competitive with chemical and radioisotopic methods. These alternate methods are based on electrostatic (Cockcroft-Walton) or rf accelerators which generate high energy (5 MeV) electron beams for direct use or for subsequent conversion to X-rays to allow deep penetration of medical products in bulk. These existing accelerator technologies were developed in the 1960's and do not produce sufficient average electron beam power to service a modern bulk sterilization facility. Commercially available electrostatic accelerators provide only 200 kW at beam energies up to 5 MeV while rf accelerators provide only 50 to 100 kW at 5 to 10 MeV. These technologies are neither economically competitive nor scalable to the average electron beam power required to exploit the economies of scale enjoyed by large facilities which process 4 million cubic feet of product per year.

The all-solid-state, SNOMAD-IV accelerator technology offers many advantages for bulk sterilization of medical products. These accelerators are reliable and significantly less expensive than electrostatic or rf accelerators. Unlike electrostatic and rf accelerators, induction accelerators are scalable to average electron beam powers of more than 800 kilowatts at beam energies ranging from 5-10 MeV, providing up to 100 kilowatts of x-rays in the x-ray conversion mode.

A single induction accelerator can provide a direct electron beam irradiation mode for medical products which can be penetrated with 5 to 10 MeV electrons as well as the x-ray conversion

mode required for sterilization of medical products in bulk. Bulk sterilization requires the significantly greater penetration depth provided by 5-7 MeV x-rays. These US built accelerators are also competitive with respect to EtO, Cobalt-60 and commercially available electron accelerators in terms of both capital and operating costs. Our economic analyses indicate that induction accelerators can sterilize medical products in bulk for \$0.51 per cubic foot in the x-ray mode. Current costs for EtO and Cobalt-60 based sterilization is \$0.71 per cubic foot while comparable costs using the Sumitomo Heavy Industries Dynamitron accelerator is \$0.81 per cubic foot in the x-ray mode. RF accelerators, which are not scalable to average powers greater than 100 kW are even less competitive than electrostatic accelerators. Finally, bulk sterilization with induction accelerator sources is readily adapted to current US regulatory requirements regarding safety, Good Manufacturing Practices (GMP's) and dose setting methodologies.

Both the direct damage to microorganisms by ionizing radiation and radiological reactions due to radical molecules, excited atoms and ions are important in the sterilization process.<sup>(6,7)</sup> This radiolysis process, which is dependent on the densities of intermediate radiation products, results in a dose-rate-dependent sterilization efficiency. At low radiation dose rates when the densities of free radicals are small, the probability of radical-radical interaction is low and interactions are primarily between radicals and molecules. Sterilization by radiation at low dose rate is then proportional to the integrated dose and independent of the dose rate, provided that the dose rate is not so low that microorganism have time to regenerate.

When the dose rate is sufficiently high, several non-linear effects may occur. Higher radical densities may result in two or more radicals simultaneously interacting with one microbe and increase the lethality of the radicals. But when the densities of the radicals are high, there is also a higher probability that the radicals will interact with themselves. This radical-radical interaction will reduce the radical population and could result in an inefficiency.

It has been observed that higher dose rate generally improves the efficiency of sterilization of microorganisms.<sup>(8,9)</sup> However, some experiments have reported smaller material degradation in samples irradiated with electrons at very high dose rates (100 MR/s or higher).<sup>(10-12)</sup> These

seemingly contradictory observations were probably caused by the difference in molecule sizes between microorganism and the base materials. Higher dose rate results in higher radical densities and shorter lifetimes as a result of radical-radical interactions. This leads to a situation where the absolute radical densities are higher but the total number of radicals interacting with molecules are smaller for a fixed total dose. For large molecules in microorganisms the probability of multi-radical interaction is relatively high and the higher radical density increases the lethality of the radiation. For the smaller molecules in the base materials, multi-body interactions are unlikely and fewer radical-molecule interactions result in less material damage and material property changes.

A schematic diagram showing the components of the linear induction accelerator is provided in Fig. 7.1. The 500 keV electron beam injector uses induction accelerator cells with the voltage of each accelerator gap added in series on the central stalk which is attached to a long-life, dispenser cathode. The electron beam formed at the cathode surface is then accelerated to 5.2 MeV by five identical accelerator modules as shown in Fig. 7.1. The injector and accelerator modules are each powered by an all-solid-state driver based on branched SCR-commutation of the 500 VDC input power followed by four stages of nonlinear magnetic pulse compression. Accelerator parameters are listed in Table 7.1. Preliminary calculations predict that an average electron beam power of 800 kilowatts will generate 56 kW of forward directed X-rays.

While the throughput of sterilized medical products allowed by this accelerator is equivalent to that provided by a 4 MCi Co-60 gamma facility, the projected capital cost of the bulk sterilization source based on a linear induction accelerator (\$1.5M) is approximately 4 times less than a comparable 4 MCi Cobalt-60 source. The capital cost of the most powerful electrostatic accelerator available - a 200 kW Cockcroft-Walton accelerator (Dynamitron) manufactured by Radiation Dynamics Inc. - is \$2.5M. An 800 kW electrostatic accelerator system based on four of these accelerators would have a total capital cost of \$10M. The development of an induction linac based system is thus the only cost effective alternative to 4 MCi Cobalt-60 sterilization facilities for which the cost of the Cobalt-60 alone is \$6.5M.

SCIENCE RESEARCH LABORATORY

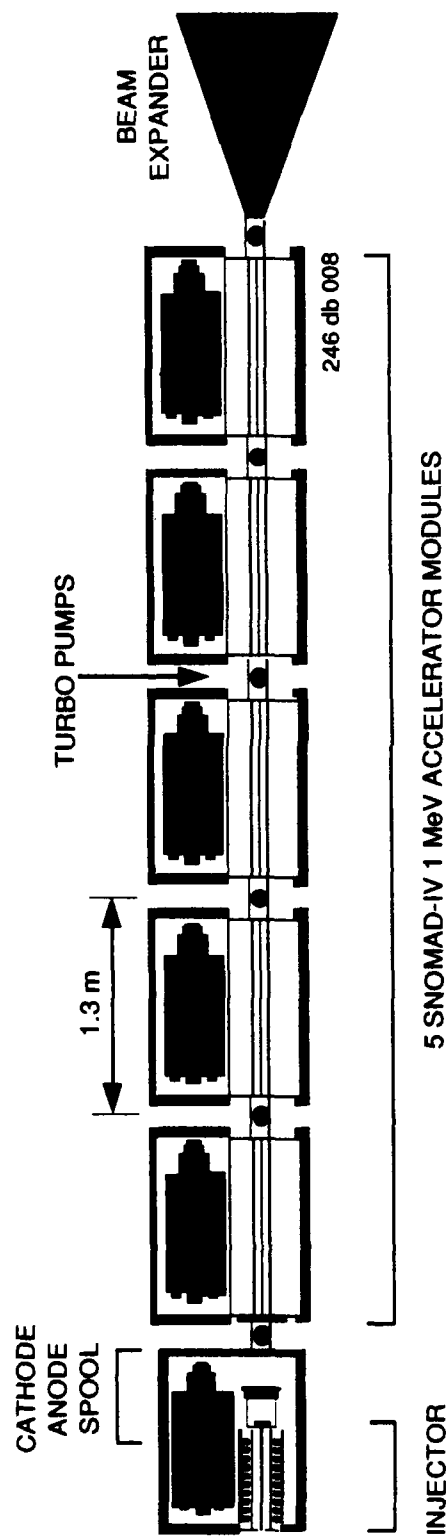


Figure 7.1: A 5.2 MeV induction linear accelerator driven x-ray sterilization source is shown.

**Table 7.1: Preliminary Design Parameters**

<b>Linear Induction Accelerator</b>	
Average Beam Power	800 kW
Beam Energy	5.2 MeV
Beam Current	800 A
Normalized Beam Emittance	$50 \pi \text{ mrad cm}$
Repetition Rate	2.75 kHz
Pulse Length	70 ns
Duty Factor	$1.9 \times 10^{-4}$

Successful completion of the program will allow the existing EtO and Co-60 bulk sterilization technologies to be supplemented and/or replaced by a sterilization source which is economically more attractive, environmentally cleaner and inherently safer for employees and the surrounding neighborhood. This technology will help alleviate the growing inventory of nuclear waste materials generated as part of the existing gamma irradiation process using Cobalt-60 sources.

A primary research objective of these experiments is to demonstrate that the high dose radiation from the induction accelerator can efficiently sterilize medical products. To date the method used to sterilize medical products is based on radioactive Cobalt-60. These systems produce continuous radiation with dose rates of  $10^{-3}$  MR/s or less compared with the pulsed induction accelerator which produces an x-ray peak dose rate of tens to hundreds of MR/s. Before these accelerators will be accepted by industrial users, the effectiveness of high dose rate x-rays for bulk sterilization must be demonstrated and their effect on the medical products and material properties assessed. An additional research objective is to study how a uniform x-ray radiation field can be generated inside a sterilization test chamber. As described in the next section, this requires research in the areas of beam optics, x-ray target design and heat transport as well as diagnostic (dosimetry) design.

Preliminary experiments to determine the utility of SRL's linear induction accelerators for sterilization of bulk medical products have been performed in using the SNOMAD-IV 0.5 MeV accelerator. These experiments were performed in conjunction with the Merck and C.R. Bard companies.

Because the x-ray yield is such a strong function of e-beam energy, the x-ray intensity from this 500 kV accelerator is small relative to that required for a practical sterilization radiation source. It is therefore necessary to arrange the samples close to the x-ray target to utilize the maximum available x-ray intensity. Using a tungsten x-ray target approximately 2.6% of the electron beam energy is converted to x-rays. Allowing for the self-absorption of the x-rays in the target, peak dose rates at the sample locations are between 0.6 MR/s and 41 MR/s, and average x-ray dose rates range from 0.1 kR/s to 8 kR/s.

The experimental results are plotted in Fig. 7.2. Here we see that at least the preliminary findings would indicate that high dose rate x-rays are actually more effective at sterilization

Presently the North American market for bulk sterilization of new single use, disposable medical products is approximately 1.3 million tons per year. Approximately 45% of the market, or 560 thousand tons (90 million cubic feet of product) per year is serviced by Cobalt-60 radiation processing plants. There are now more than 120 cobalt 60 irradiators and 10 electron beam accelerator facilities in the North American continent representing an annual service market of \$40,000,000. These facilities are typically regional toll centers to which suppliers send medical products for bulk sterilization under contract. The medical products sterilized by the service sterilization companies include surgical instruments, sutures, syringes, bandages, gloves, catheters, and labware. These products cannot tolerate high temperature sterilization and the present use of reactive gas (ethylene oxide) is being made unattractive based on growing environmental concerns. As a consequence, the medical sterilization industry is turning its attention to Cobalt-60 sources and electron beam generated X-ray devices. The service market for bulk sterilization by radiation is predicted to grow 8-10% annually for the next decade, presenting a unique opportunity for a start up company that makes use of SRL's linear induction accelerator (LIA) technology.

Science Research Laboratory has performed a preliminary economic analysis to determine the commercial viability of Induction-Accelerator-based X-ray sources for bulk sterilization of medical products. The competing technologies are Cobalt-60 gamma ray sources, and Electrostatic-Accelerator-based X-ray sources. The analysis presented here is similar to that of Cleland and Pageau.<sup>(15)</sup>

The capital costs associated with a 4 million ft<sup>3</sup>/y, 2.5 Mrad facility are given in Table 7.2(a) for each of the three sterilization source technologies. In this analysis, we have used a capital cost of \$1.62/Ci for Cobalt-60 and have used a cost of \$1.5M for an 800 kW 5 MeV Linear Induction Accelerator and a cost of \$10M for four 200 kW/5 MeV Electrostatic Accelerators (Dynamitrons commercially available from RDI).

### B. pumilus Survival Curve

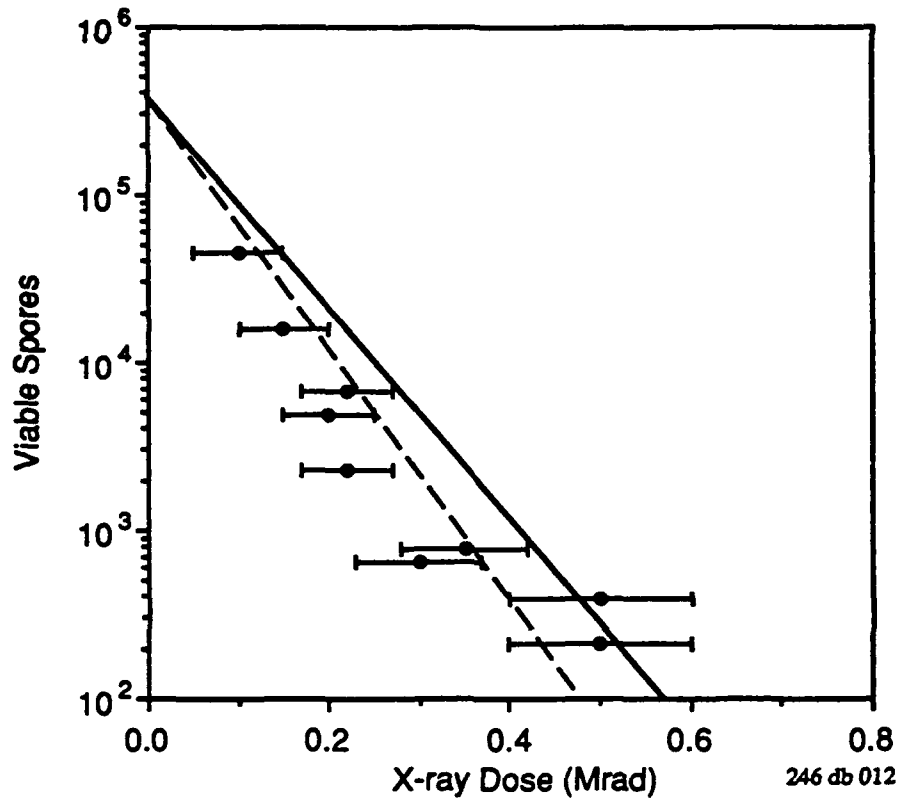


Figure 7.2: Measured B.pumilus survival curve. The solid line is the survival curve for typical gamma-ray sterilization process at a dose rate of 1 krad/sec (with a  $D_{10}$  value of 0.16 Mrad). The dashed line is a least-square fit of the data and it corresponds to a  $D_{10}$  value of 0.134 Mrad).

**TABLE 7.2: Cost Comparison for Large  $\gamma$ -Ray/X-Ray Sterilization Facilities**

a) Capital Costs:

Capital Costs	Gamma Rays Cobalt-60 (\$K)	X-Rays SRL Accel. (\$K)	X-Rays Dynamitron (\$K)
Building (15 k sq. ft.)	600 k	600 k	600 k
Radiation Shield	600 k	450 k	450 k
Irradiation Equipment	1,200 k	1200 k	1200 k
HVAC & Utilities	100 k	300 k	300 k
Engineering & Fees	300 k	400 k	400 k
Land & Permitting	<u>200 k</u>	<u>150 k</u>	<u>150 k</u>
Total Facility Cost	3,000 k	3,100 k	3,100 k
Radiation Source Cost	<u>6,480 k</u>	<u>1,500 k</u>	<u>10,000 k</u>
Total Investment	9,480 k	4,600 k	13,100 k

b) Annual Costs:

Operating Costs	Gamma Rays	X-Rays SRLs Accel.	X-Rays Dynamitron
Debt Service	1,366 k	663 k	1,887 k
Co-60 Decay	835 k	—	—
Electricity	—	560 k	560 k
Maintenance	25 k	200 k	200 k
Overheads	300 k	300 k	300 k
Labor	<u>310 k</u>	<u>310 k</u>	<u>310 k</u>
Total Annual Costs	2,836 k	2,033 k	3,257 k
Unit Cost/cu ft	\$0.71	\$0.51	\$0.81

• Present Sterilization Cost

1 - 1.25/cu ft

In Table 7.2(b), the total annual costs and the unit costs (\$/cubic ft. of sterilized product) are calculated for each of the three sterilization source technologies. The capital investments for both the facility and the radiation sources are amortized over 15 years at 12% interest. For Cobalt-60 sources, replenishment of the Cobalt-60 which has decayed (12.4% per year) is made annually at a cost of \$1.62/Ci plus \$25K for transportation and loading. Maintenance of the LIA is based on a shot life of  $10^{11}$  for the capacitors and a dispenser cathode lifetime of 2000 hrs. Maintenance costs for the 4 RDI Dynamitrons are not known. Therefore we have very conservatively assumed that maintenance costs for these 4 electrostatic accelerators are equivalent to those for the LIA. The cost of electricity for the accelerators is assumed to be \$0.07/kW-h and the efficiency of converting electricity to average electron beam power is taken to be 80% in each case.

As shown in Table 7.2(b), the total annual savings associated with the LIA based radiation source is \$826K/year in comparison with the Cobalt-60 source and \$1.23M in comparison with a sterilization facility based on Dynamitron accelerators. The unit sterilization costs are \$0.51/cu. ft. for the SRL LIA, \$0.71/cu. ft. for the 4 MCi Cobalt source and \$0.81/cu. ft. for the Dynamitron accelerators. It should be noted that the total price to the consumer for sterilization is now approximately \$1/cu. ft. It is clear from this analysis that the cost of a bulk sterilization facility based on Dynamitron accelerators is not cost competitive with Cobalt-60 sterilization facilities. As a direct result, Cobalt-60 facilities are still being built.

## REFERENCES

1. K. Kereluk and R. S. Lloyd 1969. Ethylene oxide sterilization. A current review of principles and practices. *J. Hosp. Res.*, 7, 7-75.
2. CSA 1979. Industrial sterilization of medical devices by the ethylene oxide process. Canadian Standard Association Z314. J.
3. AAMI 1981. Process control guidelines for radiation sterilization of medical devices. Arlington, VA, Assoc. for the Adv. of Med. Instrum.; AAMI Guideline for E-Beam Rad. Med. Dev. Sterilization (1990).
4. OSHA 1979. Occupation Safety and Health Administration: OSHA Safety and Health Standards. Sub part 2-Toxic and Hazardous Substances. 29 CFR 1910:1000, p. 591.
5. NIOSK 1981. Ethylene oxide (ETO). Current Intelligence Bulletin 35. Washington, DC, Nat. Inst. for Occup. Safety and Health. DHHS (NIOSK,) Pub. No. 81-130.

6. J. C. Arthur 1971. Reactions induced by high-energy radiation. In Cellulose and Cellulose Derivatives, ed. N. M. Bikales and L. Segal, Wiley-Interscience, NY, pp. 937-971.
7. A. J. Swallow, (1973) Radiation Chemistry William Clowers & Sons, London.; A. J. Swallow 1977. Chem. effects of irradiation. In Rad. Chem. of Major Food Components. P. S. Elias and A. J. Cohen, eds., Elsevier Publ. Co., N.Y., p. 5.
8. W. D. Bellamy and E. J. Lawton 1955. Studies on factors affecting the sensitivity of bacteria to high velocity electrons. Ann. NY Acad. Sci., 59, 595.
9. T. F. Midura, L. L. Kempe, J. T. Graikoski and N. A. Milone 1965. Resistance of Clostridium perfringens Type A spores to  $\gamma$ -radiation. Appl. Microbiol. 13, 224.
10. F. A. Bovey 1958. The Effects of Ionizing Radiation on Natural and Synthetic High Polymers. Interscience, NY.
11. E. Czerniawski and L. Stolarczyk 1974. Attempt to establish the ionizing radiation dose in the sterilization of one-use medical equipment. Acta Microbiol. Pol. Ser. B6, 177.
12. D. M. Sandila and M. Shamin 1972. Effect of Gamma Rays Irradiation on Cotton Fibre and Yarn. Pakistan J. Sci. Ind. Res. 15 1-2:127-130.
13. M. Farahani, F.C. Eichmiller, and W.L. McLaughlin (1990). Measurement of Absorbed Doses Near Metal and Dental Material Interfaces Irradiated by X- and Gamma Ray Therapy Beams, Physics in Medicine and Biology, 35, pp. 369-385.
14. M.C. Saylor, T.T. Tamargo, W.L. McLaughlin, H.M Kahn, D.F. Lewis, and R.D. Schenfele (1988). A Thin Film Recording Medium for Use in Food Irradiation, Rad. Chem. and Phys., 31 (4-6), pp. 529-536.
15. M.R. Cleland and G.M. Pageau, "Radiation Processes of Medical Devices and Food", 20<sup>th</sup> Mid-Year Topical Meeting of the Health Physics Society (February 1987).

MERCK PHARMACEUTICAL MANUFACTURING DIVISION

DIVISION OF MERCK & CO., INC.

WEST POINT, PENNSYLVANIA 19486

June 13, 1991

Dr. Jonah Jacob  
President  
Science Research Laboratory, Inc.  
15 Ward Street  
Somerville, MA 02143

Dear Dr. Jacob:

I am pleased to learn of your efforts to develop compact, low cost, induction accelerator technology for sterilization applications. As we have discussed, MPMD is considering on-line sterilization as a way of improving our product quality and value. The induction-accelerator-based radiation device you propose would seem to have the potential for performing on-line sterilization with x-rays and could replace our current sterilization methods for selected applications. I envision numerous applications for on-line sterilization of products or components which are currently either steam, dry heat, or ETO sterilized here, or gamma irradiated off-site. As I understand it, these applications would require a compact accelerator capable of delivering approximately 200 kilowatts of electron beam power at a beam energy of between 0.5 - 1 MeV. This requirement can apparently be met by accelerator technology which you are proposing to develop under NSF SBIR.

As we have discussed, Merck plans to visit your facility with sample products to be exposed to varying doses of x-rays to evaluate the effectiveness of the sterilization and determine the deleterious effects the radiation may have on the containers. If the advantages of your sterilization technology are demonstrated, Merck would then consider installation of prototype sterilization equipment.

I would be pleased to meet with cognizant NSF personnel and provide them with an overview of potential uses of this new sterilization technology. Please keep me informed of further developments regarding this exciting opportunity.

Sincerely,



Dennis Thompson  
Project Process Engineer

DKT/ts/212

USCI Division  
C.R. Bard, Inc.  
1200 Technology Park Drive  
P.O. Box 7025  
Billerica, MA 01821  
508 667-1300



June 11, 1991

Dr. Jonah Jacob  
President  
Science Research Laboratory, Inc.  
15 Ward Street  
Somerville, MA 02143

Dear Dr. Jacob:

C.R. Bard, a leading supplier of medical products, is interested in developing new low cost sterilization sources to complement or replace the existing ETO based units.

To evaluate the new accelerator-based radiation sources, C.R. Bard will conduct bulk sterilization tests on SRL's SNOMAD induction accelerator. As I understand it, this accelerator is under development and its beam energy will be increased to 1.5 MeV with an additional 1 MeV accelerator module.

Upon installation of this equipment, C.R. Bard will provide resources to conduct sterilization experiments with simulated bulk pallets and diagnose the spatial profile of the x-radiation in the pallet vicinity.

C.R. Bard will use the above results to perform the design of a high throughput bulk sterilization facility, conduct a quantitative sterilization economic analysis for induction accelerator driven x-ray sources keeping in mind that such a sterilization unit will be configured to fit in an existing C.R. Bard facility.

Please keep me informed of the developments on this NSF SBIR proposal.

Sincerely,

A handwritten signature in black ink, appearing to read "Tim Moutafis".  
Tim Moutafis  
Project Manager

BARD

## SECTION 8

### TREATMENT OF WASTE WATER AND THE REMOVAL OF SO<sub>X</sub> AND NO<sub>X</sub> FROM STACK GASES

SRL has been funded by the Electric Power Research Institute (EPRI) to experimentally investigate utilizing the SNOMAD-IV accelerator to clean up contaminated waste water. At the same time SRL has proposed to the Environmental Protection Agency a program for applying a similar procedure to the removal of SO<sub>X</sub> and NO<sub>X</sub> from stack gases.

Electron beam irradiation is an effective method of treating a wide variety of organic matter and chemicals in water including the disinfection of municipal wastewater and the destruction of toxic organic contaminants in industrial wastewater. It is safe, compatible with high throughput operation and has already been demonstrated effective for the disinfection of water<sup>(1,2)</sup>. A dose of 50 kRads is sufficient to reduce the coliform and salmonella organisms in wastewater by a factor of 1000, yet raises the temperature of water by only a quarter of a degree<sup>(3)</sup>.

Pulsed electron beam systems such SNOMAD-IV can quickly respond to changes in wastewater flow rate or contaminant concentration. This compensation is accomplished by adjusting the pulse repetition rate, leading to a system response rate orders of magnitude faster than that of biological treatment systems.

It has been observed that electron irradiation can destroy trace organic contaminants present in water, such as benzene and trichloroethylene (TCE) as shown in Table 8.1<sup>(4-7)</sup>. Initially, the irradiation process destroys the contaminant and produces new compounds, most of which are more polar and therefore more soluble in water (i.e. less lipophilic) than the original contaminant. Upon further irradiation, these contaminant daughter products are themselves degraded, and the process can be continued until all undesirable solutes have been eliminated from the water.

When a high energy electron strikes a water molecule either an excited water molecule or an H<sub>2</sub>O<sup>+</sup> ion and a secondary electron is produced. Both primary and secondary electrons have

TABLE 8.1: ELECTRON BEAM TREATMENT OF WATER  
CONTAINING TOXIC ORGANIC CONTAMINANTS

Compound	Percent Removal	Required Dose (kRads)
Carbon Tetrachloride	> 99	50
Trichloroethylene (TCE)	> 99	500
Benzene	> 99	650
Tetrachlorethylene (PCE)	> 99	500
trans-1,2-dichloroethene	93	800
1,1-dichloroethene	> 99	800
1,2-dichloroethane	60	800
hexachloroethane	> 99	800
1,1,1-trichloroethane	89	650
1,1,2,2-tetrachloroethane	88	650

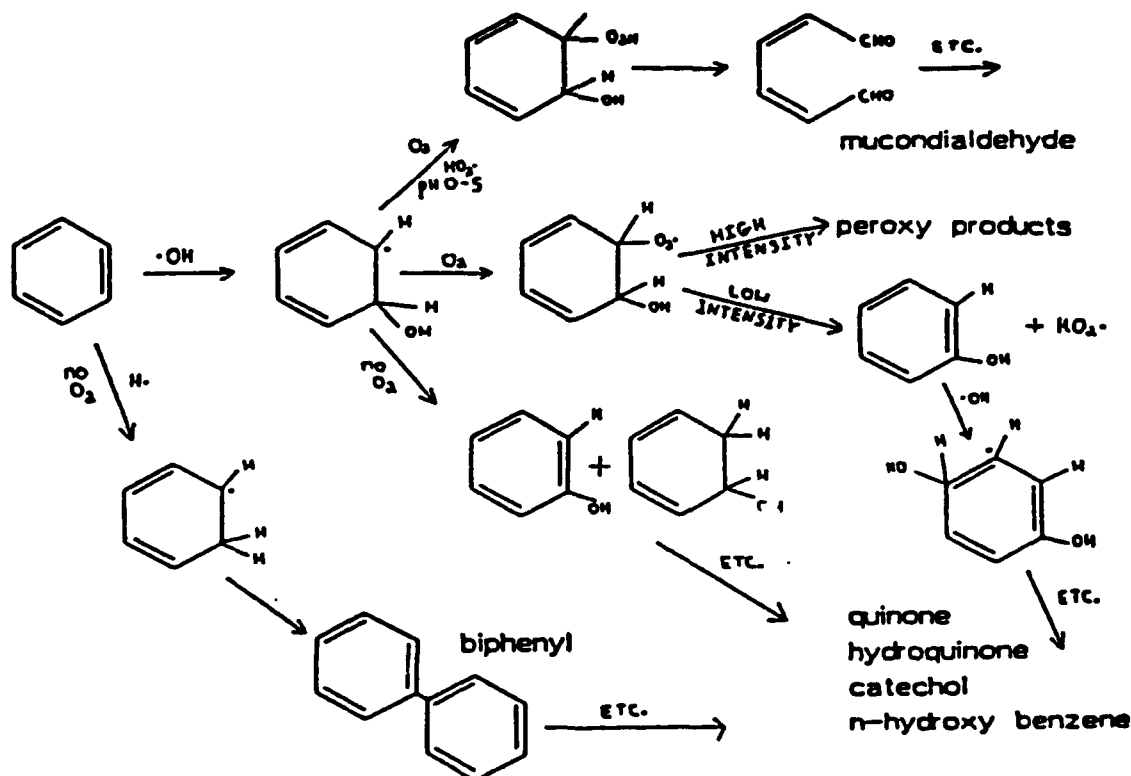


Figure 8.1: The possible benzene decomposition products are shown.

enough energy to continue on through the water, leaving collision "spurs" along their tracks as they strike other water molecules. Within the collision spurs are reactive species which can either combine with each other or diffuse out of the spurs into the bulk water.

Municipal waste streams consist of more than 99.9% water. The concentration of organic contaminants in industrial wastewater varies, with concentrations in the 0.1–100 ppm likely. In either case, direct interaction between electrons and solute molecules is negligible. Essentially all of the energy will be absorbed by the water, and since a 1.5 MeV beam electron will cause approximately 45,000 ionization events, solute molecules in water will interact with many water radiolysis products. Figure 8.1 shows the initial degradation products produced when benzene interacts with water radiolysis products. With continued irradiation, these initial daughter products are also destroyed.

Although various irradiation methods have been investigated,<sup>(8–11)</sup> the present high cost of electron beam accelerators has been a deterrent to its use. To date applications of electron beams to water treatment have all used electrostatic accelerators which generate continuous, low dose rate beams. In 1976 the first such system at the Deer Island Waste Treatment Plant in Boston was used to treat 120 gpm of liquid sludge at a dose of 400 krads.<sup>(10)</sup> More recently, a 1.5 MeV, 50 mA electron accelerator has been used to treat a 120 gpm waste flow at an experimental treatment plant in Miami, Florida.<sup>7</sup>

SRL has proposed the use of SNOMAD-IV induction accelerator technology for wastewater detoxification. This will provide a new opportunity because of its demonstrated reliability and low cost. Using this accelerator technology and novel, efficient treatment cell and window designs described in this proposal, a complete system could treat municipal wastewater at a 50 kRad dose for approximately \$0.06 per 1000 gallons or destroy 50 ppm concentration VOC in industrial wastewater (1 MRad dose) for about \$2.50 per 1000 gallons. The significantly higher capital cost (\$3M) of existing 200 kW electrostatic accelerators removes them from consideration for these treatment system applications. Induction linac technology can thus lead to a flexible, cost effective system for municipal and industrial wastewater treatment.

The major difference between SRLs linear induction accelerators and the present electrostatic accelerators is the fact that induction accelerators are repetitively pulsed with a low duty factor while the electrostatic accelerators are continuous wave (CW) machines. As a result of this difference the peak dose of the induction accelerators will be about 1000 times higher than that of the present electrostatic accelerators. So it is most important to establish the efficiency of decontamination of the wastewater by the induction accelerators.

The primary objectives of this ongoing research effort are (1) to demonstrate the effectiveness of pulsed electron beams in destroying trace organic contaminants at high dose rates, and (2) perform an economic analysis to determine the cost of decontaminating wastewater using SRLs all-solid-state linear induction accelerators. The linear induction accelerator will be flexible, the pulse repetition quickly adaptable to the wastewater flow, maintaining a constant dosage in the face of changing plant demand. The system will also be able to treat a wide variety of contaminants, including the organic contaminants investigated in the experimental portion of this effort.

High peak dose rate experiments are being conducted on the 0.5 MeV SNOMAD-IV injector. When the 1.0 MeV SNOMAD-IVB accelerator module is added to the beam line the experiments will be continued at higher electron beam energies. A foil window has been added to allow high dose rate ( $> 10^6$  R/sec) experiments using the model contaminants, with the goal of reducing the concentration of contaminants such as carbon tetrachloride, benzene, PCBs, toxic linear molecules and all toxic decomposition products from an initial concentration of 50 ppm down to less than 4 ppb.

The peak dose rates with a pulsed machine such as the SRL induction linac is three orders of magnitude larger than with continuous electrostatic machines. Dose rate will have an effect on the chemistry of the treatment process, and this effect is being investigated in this experiment. High dose rates result in high instantaneous concentrations of free radicals in solution. It has been shown that reactions which involve bimolecular termination of free radicals become more efficient as irradiation dose rate is increased.<sup>11</sup> The radical-radical recombinations between water

radiolysis primary radicals will be enhanced, but the reactions between the solutes and the radicals will be enhanced also.

A primary goal for these initial experiments is to find the set of experimental conditions which will yield an optimally high rate of solute reaction without significant primary radical recombination. The effect of dose rate is also of interest because most previous full scale irradiation work was done using gamma ray facilities or continuous electron beam facilities. If at a given dose, the effect of increasing dose rate is to increase the efficiency of the bimolecular contamination destruction, the economics of a full scale system using pulsed electron beams will be favored. Both the dose and dose rate in our system can be easily varied; the former by adjusting the pulse repetition rate, and the latter by adjusting the electron beam current and beam focusing.

### 8.1 SO<sub>X</sub> and NO<sub>X</sub> Removal from Stack Gases

Long term pollution from stack gases resulting in acid rain has caused substantial damage to the environment, notably forests and lakes, in various regions of the United States. This pollution results from the combustion of coal and petrochemicals by electrical power generating plants and industrial manufacturing plants. Primary precursors to acid rain are sulfur dioxide (SO<sub>2</sub>) and nitrogen oxides (NO<sub>X</sub>) which are combustion products from these plants. The SO<sub>2</sub> and NO<sub>X</sub> react in the atmosphere to form sulfuric and nitric acid mists that eventually precipitate to earth as rain or snow. This problem is primarily related to the use of high-sulfur-content coal and restrains its use despite its being the most abundant, readily available energy source in the United States. So reducing the SO<sub>2</sub> and NO<sub>X</sub> emission from flue gas will allow use of abundant, high-sulphur coal resources, lower energy costs and decrease our dependence on foreign energy sources.

SO<sub>2</sub> control has used flue gas desulfurization scrubbers after combustion, coal cleaning, coal conversion and gasification to reduce the sulfur emissions with varying degrees of success. Fluidized bed combustors have been used to a limited extent where the sulfur reacts with the bed materials during combustion to reduce the SO<sub>2</sub> emissions. These techniques are expensive

and requires additional research to cost-effectively reduce the SO<sub>2</sub> emission. NO<sub>X</sub> controls for stationary sources and power plants have concentrated on combustion modifications. Wet lime and wet limestone selective catalytic reduction (SCR) have been employed for SO<sub>2</sub> and NO<sub>X</sub> reduction. These techniques are expensive for example it cost \$230 per kilowatt output from a power plant to reduce the combined SO<sub>2</sub>/NO<sub>X</sub> emissions to 90% for SO<sub>2</sub> and 70% for NO<sub>X</sub>.

A proven method for reducing the combined emission of SO<sub>2</sub> to 95% and NO<sub>X</sub> to 90% is the use of high energy electron beam irradiation. Unfortunately this method is also expensive and costs \$225 per kilowatt which is almost as high as the SCR method discussed above. The primary reason for the high cost of this method of reducing SO<sub>2</sub>/NO<sub>X</sub> emission is the high cost of the electron beams. In the last five years, Science Research Laboratory (SRL) has developed an extremely reliable electron beam technology that is a factor of ten times less expensive than the existing technology. Should SRLs electron beam technology prove to be as effective in reducing SO<sub>2</sub>/NO<sub>X</sub> emission from stack gases then the cost of the electron method for controlling SO<sub>2</sub>/NO<sub>X</sub> emissions will be reduced by 25-30% to \$180 per kilowatt. There are several additional advantages to SRLs revolutionary all-solid-state induction accelerator technology. These include: (a) a compact design resulting in reduced cost for shielding and easier access to the equipment. (b) The modular design enables one to scale the technology to large scale power plants (c) Low maintenance and simple computer controlled operation that significantly reduce the running costs of the facility.

## 8.2 Brief Review of Electron Beam De SO<sub>2</sub>/NO<sub>X</sub>

The EBARA electron beam removal process<sup>(1)</sup> for SO<sub>2</sub> and NO<sub>X</sub> is shown schematically in Fig 8.2. Flue gas at 100°C is cooled to 70°C in a spray cooler. The fine mist of water from the spray nozzles in the cooler is totally evaporated by heat exchange with the hot flue gas. Since the dewpoint of the gas is approximately 50°C, no water is retained as liquid in the cooler, thereby providing "dry-bottom" operation. Prior to entry into the process vessel, stoichiometric quantities of gaseous ammonia are injected into the flue gas. In the process vessel, the flue gas is irradiated by the electron beam creating free radicals. These free radicals readily react with

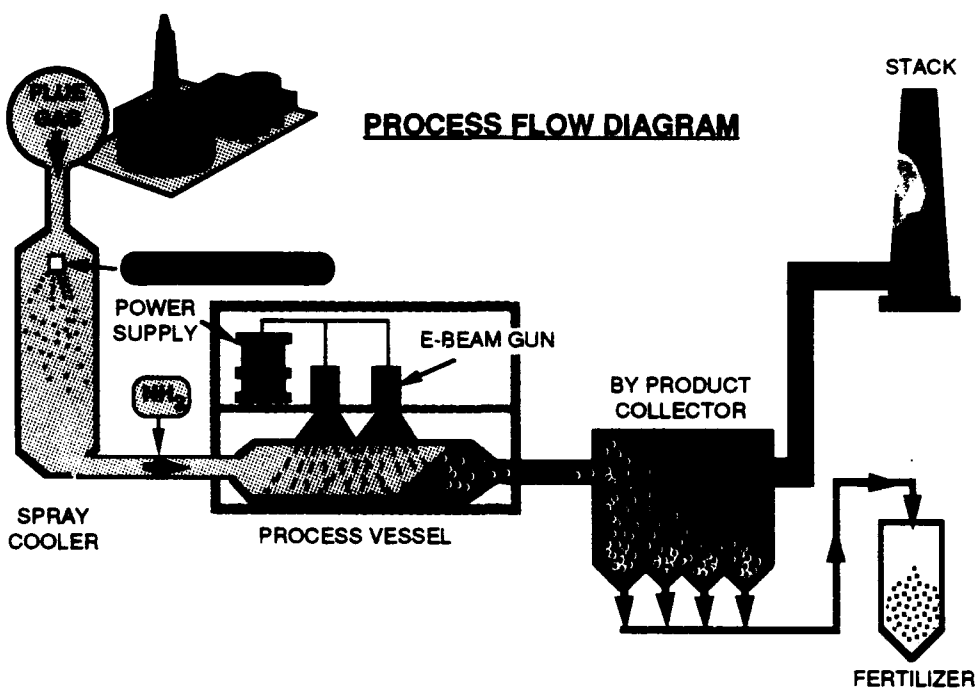


Figure 8.2: EBARA Electron Beam Process (simplified flow diagram)

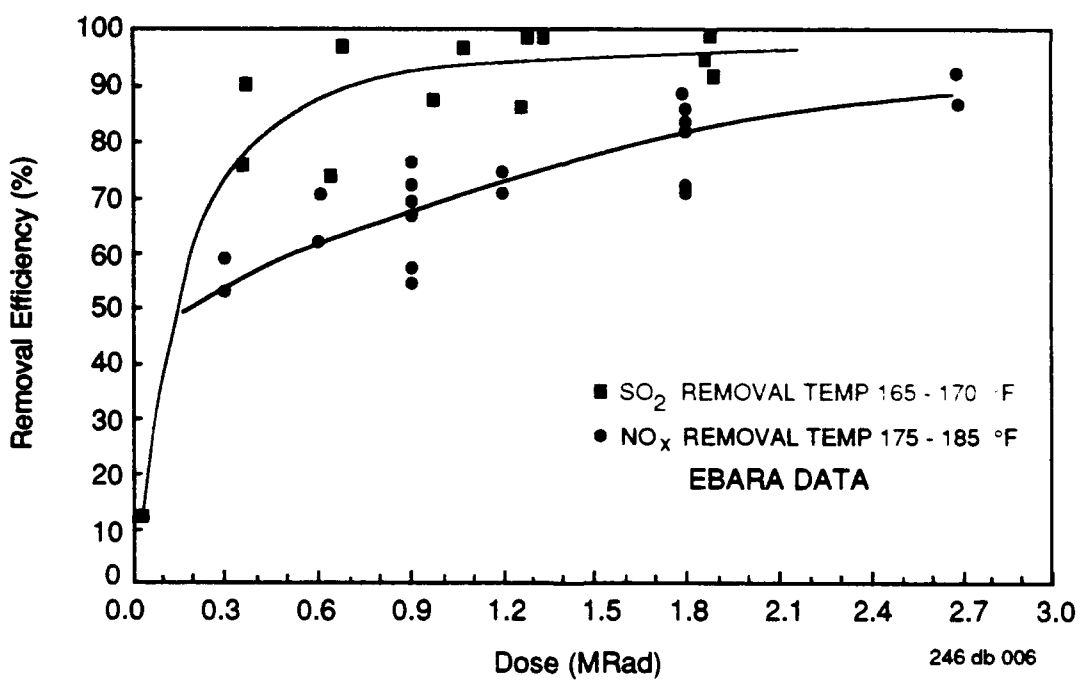


Figure 8.3: SO<sub>2</sub> and NO<sub>x</sub> Removal Efficiency versus Dose at Process Vessel Outlet

SCIENCE RESEARCH LABORATORY

$\text{SO}_2$  and  $\text{NO}_X$  to form their acid counterparts which react with the ammonia to form ammonium sulfate and ammonium nitrate particulates. Before its release to the atmosphere via the stack, the flue gas passes through a by-product collector which precipitates and collects the ammonium sulfate and ammonium nitrate particulates. These particulates are automatically removed and transported to a by-product storage vessel for later off-site removal and use as fertilizer.

Electron beam flue gas treatment systems offer several major advantages including

- **Efficient Removal of Environmental Pollutants** As shown in Fig. 8.3, in the electron beam process, up to 90% of the  $\text{SO}_2$  and 70% of the  $\text{NO}_X$  are simultaneously removed from the flue gas under optimal flue gas temperature conditions (155-170°F) and with an electron beam dose of 1 MRad which corresponds to approximately 1% of the output from the power plant. Higher removal of  $\text{SO}_2$  and  $\text{NO}_X$  are of course possible at higher dose rates. These removal efficiencies exceed conventional removal methods currently in use which require separate processes to remove  $\text{SO}_2$  and  $\text{NO}_X$ . In addition, the simultaneous removal of  $\text{NO}_X$  and  $\text{SO}_2$  emissions actually increase  $\text{NO}_X$  removal efficiency indicating higher efficiencies for high-sulphur-content coal without reducing  $\text{SO}_2$  removal efficiencies as shown in Figure 8.4.
- **Ease of Operation** Since it consists of only a spray cooler, process vessel, by-product collector and fan, the EBARA electron-beam process is easy to operate. The process is fully automated thereby minimizing operating costs.
- **Dry Mode of Operation** Conventional flue-gas treatment processes are generally wet systems which generate waste water and wet refuse which require expensive recycle treatment and landfill. The electron-beam process is a dry process which does not generate secondary environmental pollutants and in fact yields a valuable by-product.
- **Fertilizer By-product** In the electron-beam process, the resultant by-product from the removal of  $\text{SO}_X$  and  $\text{NO}_X$  from flue gas is a fertilizer compound consisting of various percentages of ammonium sulfate and ammonium nitrate, depending on the composition of

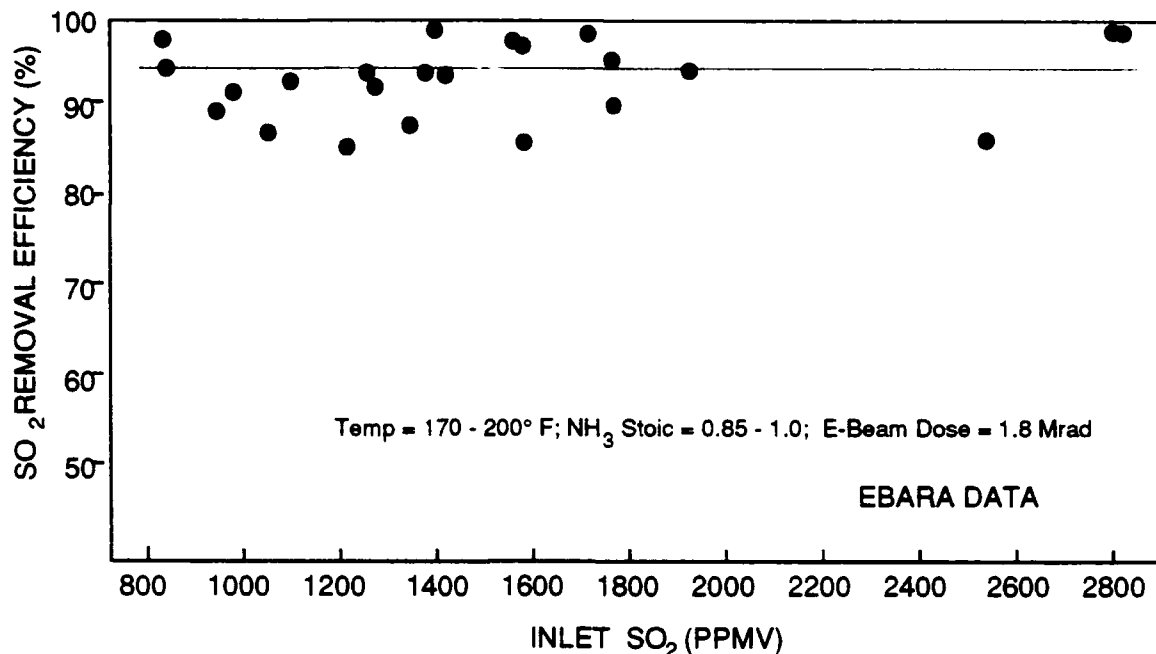


Figure 8.4a: SO<sub>2</sub> Removal Efficiency versus Inlet SO<sub>2</sub>

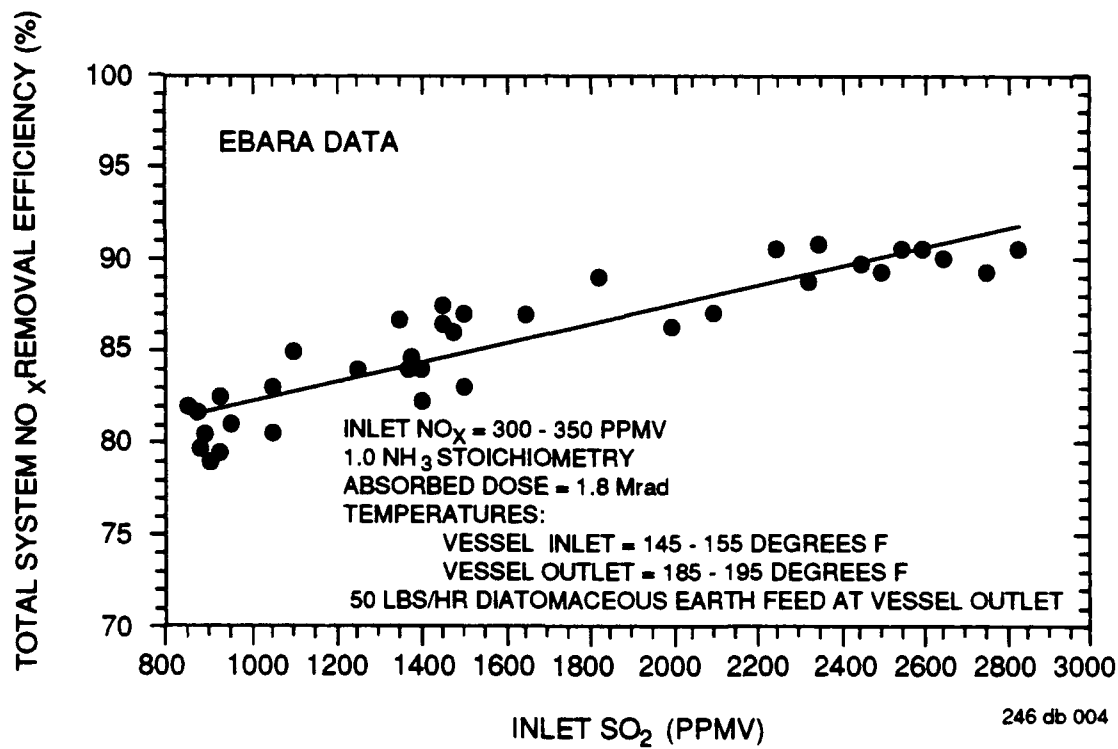


Figure 8.4b: NO<sub>x</sub> Removal Efficiency versus Inlet SO<sub>2</sub>

the fuel burned. Ammonium nitrate is the basic fertilizer for many agricultural products. Extensive testing conducted in the U.S. and Japan have demonstrated the effectiveness of this by-product as a fertilizer. Ammonium sulfate is required by land deficient in sulfur, generally located in the more arid regions of the world.

The two disadvantages of using currently available electrostatic accelerators are:

- **Capital cost** - capital costs of current electrostatic accelerator systems (>\$10/watt) are typically unaffordable for these applications.
- **Size** - Existing electrostatic accelerators are not compact and require large environmentally-controlled buildings which increase both capital and operating cost.

SRL has presented and discussed its all-solid-state electron beam technology with EBARA who has recently performed a detailed cost analysis for controlling the SO<sub>2</sub> and NO<sub>X</sub> emissions from stack gases using SRLs technology. EBARAs analysis predicts a 30% reduction in the capital cost of electron beam flue gas processing plants.\* As a result of these interactions between SRL and EBARA, EBARA will support efforts to commercialize SRLs accelerator technology.

The fact that SNOMAD-IV accelerator technology is much more compact than existing accelerator technology becomes clear from Fig. 8.5 which compares a scaled drawing of the all-solid-state induction accelerator with an existing electrostatic accelerator manufactured by Sumitomo Heavy Industries (Radiation Dynamics). Other electrostatic accelerators based on insulated core transformers are slightly more compact than the Dynamitron shown in Fig. 8.5 but still significantly larger than induction accelerators providing comparable power.

Efficient removal of SO<sub>2</sub> and NO<sub>X</sub> has been demonstrated by several groups<sup>(16-24)</sup> including The EBARA Environmental Corp.<sup>(15)</sup> These experiments which have been performed since the early 70's have demonstrated that SO<sub>2</sub> and NO<sub>X</sub> can be efficiently removed by high energy electron beam irradiation of stack gases.

When a high energy electron beam irradiates a gas target approximately half of the energy results in electron-ion pairs. During recombination of the electron-ion pairs, some of the gas

---

\* The EBARA letter is included at the end of this section.

### SRL INDUCTION ACCELERATOR

- 500 KV ELECTRON BEAM
- 300 KW AVERAGE POWER
- ACCELERATOR COST \$220K

- 500 KV ELECTRON BEAM
- 150 KW AVERAGE POWER
- ACCELERATOR COST \$1.5 M

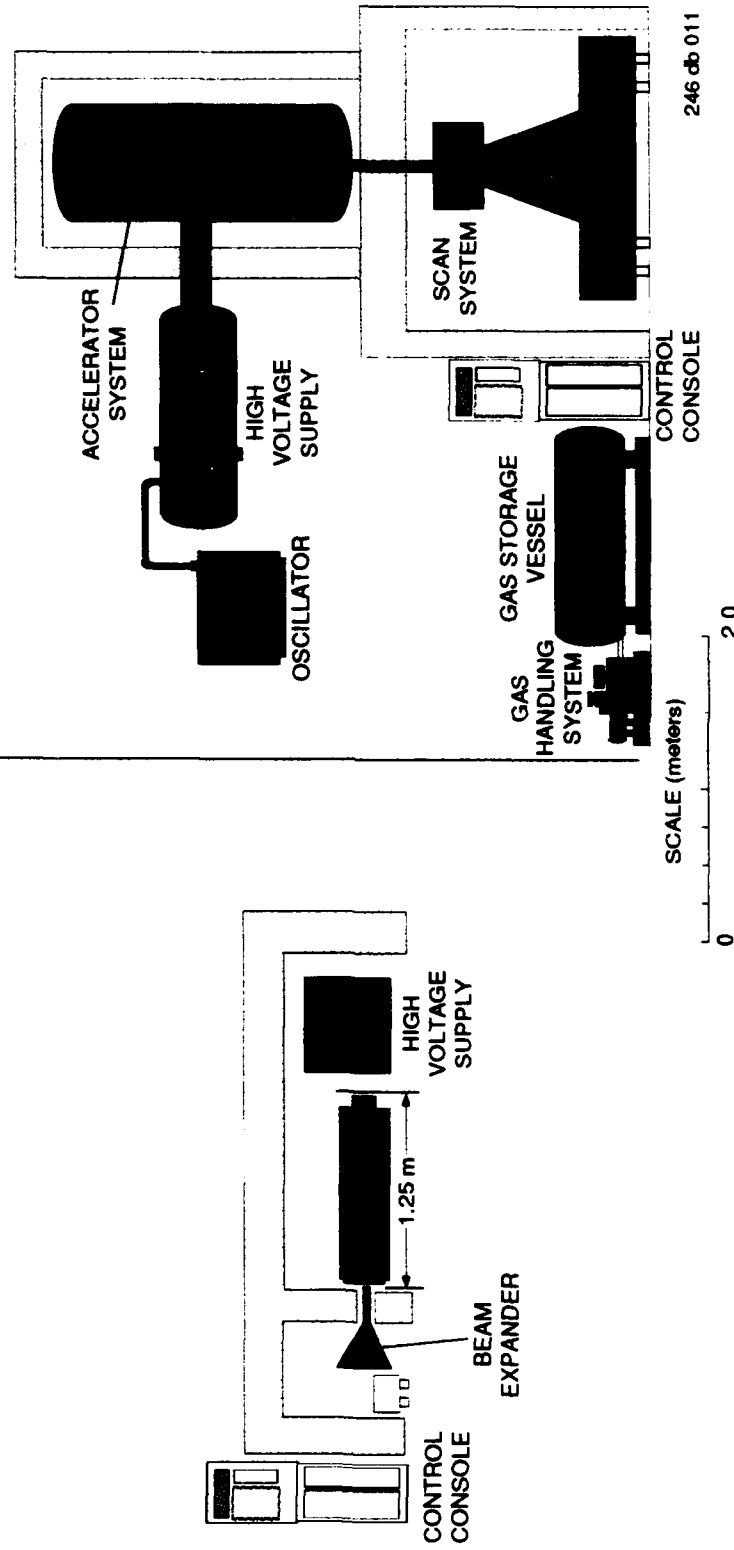


Figure 8.5: SRL compact induction accelerators deliver more power than NHV / EPS and dynamitron at one-tenth the cost.

dissociates resulting in atomic oxygen, nitrogen and OH radicals. The primary chemical reactions that generate the required active species for the oxidation and removal of the SO<sub>2</sub> and NO<sub>X</sub> are given in Table 8.2:

**Table 8.2**

Species		Product
H <sub>2</sub> O	→	OH + H
N <sub>2</sub>	→	2N
O <sub>2</sub>	→	2O
H <sub>2</sub> O	→	H <sub>2</sub> O <sup>+</sup> + e
N <sub>2</sub>	→	N <sub>2</sub> <sup>+</sup> + e
O <sub>2</sub>	→	O <sub>2</sub> <sup>+</sup> + e

Depending upon the composition of the flue gas, a number of reactions are likely to occur as a result of interaction with these radiological products; however, this process is primarily concerned with chemical reactions involving SO<sub>2</sub> and NO<sub>X</sub>. Based on known rate constants, the dominant reactions with these radiological products are shown in Table 8.3:

**Table 8.3**

Species		Product
SO <sub>2</sub> + 2OH	→	H <sub>2</sub> SO <sub>4</sub>
SO <sub>2</sub> + O	→	SO <sub>3</sub>
SO <sub>3</sub> + H <sub>2</sub> O	→	H <sub>2</sub> SO <sub>4</sub>
NO + OH	→	HNO <sub>2</sub> → NO <sub>2</sub> + NO + H <sub>2</sub> O
NO + O	→	NO <sub>2</sub>
NO <sub>2</sub> + O	→	NO <sub>3</sub>
NO <sub>2</sub> + OH	→	HNO <sub>3</sub>

The presence of ammonia (NH<sub>3</sub>) in the irradiated gases leads to the formation of ammonium salts from the sulfuric and nitric acids:

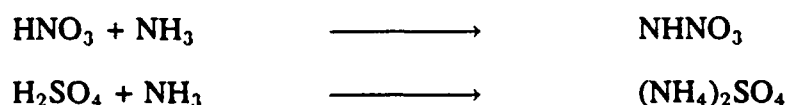


Figure 8.6 shows a simplified flow chart of the EBARA model which demonstrates these reaction mechanisms and their rate of change with respect to time. The flue gas enters at 140°C and is cooled by a water spray to 70°C. Before entering into the electron beam irradiated

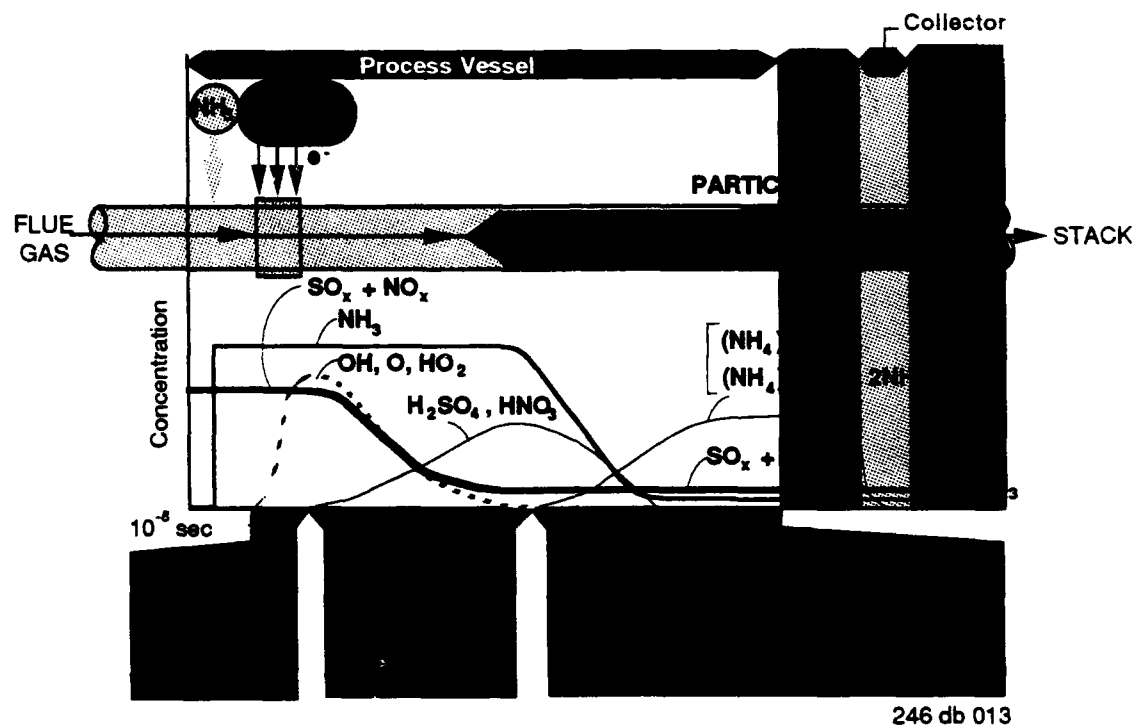


Figure 8.6: Model diagram of reaction mechanism

SCIENCE RESEARCH LABORATORY

volume, gaseous ammonia is injected into the flue. The  $\text{SO}_2$  is then converted into  $\text{H}_2\text{SO}_4$  and the  $\text{NO}_x$  into  $\text{HNO}_3$ . These conversions take place by reactions with atomic oxygen, radicals and ultimately by dissolving  $\text{SO}_3$  and  $\text{NO}_2$  in water. The specific chemical reactions are given in Table 8.3. From Fig. 8.6 one sees that the lifetime of the OH and O are of order  $10^{-5}$  sec. Induction accelerators are designed to operate at pulse repetition rates of  $10^4$  pps and if necessary it can be extended to  $2 \times 10^4$  pps. The effective duty factor, which is just the product of the duty factor and the lifetime of the OH radicals and atomic oxygen, is 10% for the pulse repetition rate of  $10^4$  pps and 20% at  $2 \times 10^4$  pps.

## References

1. L.C. Levaillant and C.L. Gallien, Radiat. Phys. Chem. 14, 309 (1979).
2. A. Farhataziz and M.A.J. Rodgers, eds. Radiation Chemistry: Principles and Applications, VCH, NY. (1987).
3. J.G. Trump, E.W. Merrill and K.A. Wright, "Disinfection of Sewage Wastewater and Sludge by Electron Treatment," Radiat. Phys. Chem. 24, 55 (1984).
4. E.W. Merrill, et. al., "Destruction of Trace Toxic Compounds in Water and Sludge by Ionizing Radiation," Amer. Inst. Chem. Eng. Sym. 74, 245 (1977).
5. A.K. Pikaev, Pulse Radiolysis of Water and Aqueous Solutions, Ind. Univ. Press (1967) 141-145.
6. S.W. Tay and E.W. Merrill, "Water purification by Electron Irradiation in the Presence of Polymers," NSF Final Report ECE-8612487 (1987).
7. C.N. Kurucz, T.D. Waite, W.J. Cooper and M.G. Nickelsen, "Full Scale Electron Beam Treatment of Hazardous Wastes - Effectiveness and Costs", in Proc. 45th Ann. Purdue Ind. Waste Conf., W. Lafayette, Ind., (1990).
8. A.K. Pikaev and V.N. Shubin, "Radiation Treatment of Liquid Wastes," Radiat. Phys. Chem. 24, 77 (1984).
9. A. Sakumoro and T. Miyata, "Treatment of Waste Water by a Combined Technique of Radiation and Conventional Methods," Radiat. Phys. Chem. 24 55 (1984).
10. M.R. Cleland, R.A. Fernald and S.R. Maloof, "Electron Beam Process Design for Treatment of Wastes and Economic Feasibility," Rad. Phys. Chem. 24, 179 (1984).
11. K.A. Dennison, "Radiation Cross-Linked Poly(ethylene Oxide) Hydrogel Membranes," Ph.D. thesis, M.I.T. (1986).
12. D.E. Savage and E.W. Merrill, "Destruction of Benzene in Water by Electron Irradiation in the Presence of Polymer," Proc. Conf. Amer. Inst. Chem. Eng., (1990).

13. J.P. Moran, "Design Basis for an Excimer Laser Master Oscillator Flow System," SDIO High Energy Laser Conf., Boulder, CO. (1987).
14. R.C. Gumerman, B.E. Burris and S.P. Hansen, Small Water System Treatment Costs, Pollution Tech. Review No. 136, Noyes Data Corp., N.J. (1986).
- 15) Norman W. Frank and Shinichi Hirano, 4<sup>th</sup> Symposium on Integrated Environmental Control, Washington, DC, March 2-4, (1988).
- 16) N. Suzuki, K. Nishimura, O. Tokunaga and M. Washino, J. Nucl. Sci. Technol. 16, 278 (1979).
- 17) R. Slater, "Computer Modeling of Electron Beam Initiated Removal of SO<sub>2</sub> and NO", Final Technical Report to Ebara International Corp, Subcontract No. EV-AB-84.
- 18) Helfritch, Dennis J. and Feldman, Paul L., "A Pilot Scale Study of Electron Beam Removal of SO<sub>2</sub> and NO<sub>X</sub> from Flue Gas", Agreement No. DE-FC22-83PC15079, U.S. Department of Energy, Pittsburgh Energy Technology Center, September 1985.
- 19) Wittig, S., Studzinski, W., Spiegel, G. and Jordan, S., "EBDS-Studie", LAFI-Bericht Nr. 381, 1983.
- 20) Fuchs, P., Roth, B., Schwing, U., Angle, H. and Gottstein, J., "Removal of SO<sub>2</sub> and NO<sub>X</sub> by the Electron Beam Process". Presented at the 6th International Meeting on Radiation Processing, Ontario, Canada, May 31 - June 5, 1987.
- 21) Person, C.P., Ham, D.O. and Boni, A.A., (1985), "Final Report for a Unified Projection of the Performance and Economics of Radiation-Initiated NO<sub>X</sub>/SO<sub>X</sub> Emission Control Technologies", Contract No. DE-AC22-840C70259, U.S. Department of Energy, Pittsburgh Energy Technology Center, Pittsburgh, PA.
- 22) Paur, H.R. and Jordan S., "Aerosol Formation in the Electron Beam Dry Scrubbing Process (ES-Verfahren)", presented at the 6th International Meeting on Radiation Processing, Ontario, Canada, May 31 - June 5, 1987.
- 23) Rothenberg, S.J., Dahl, A.R., Barr, E.B. and Wolff, R.K., "Generation, Behavior and Toxicity of Ammonium Sulfite Aerosols", Journal of Air Pollution Control Association, Vol. 36, No. 1, pp. 55-59 (1986).
- 24) McKnight, R.A., Antonetti, J.O. and Mattick, D., "A Utility View of the Ebara E-Beam NO<sub>X</sub>/SO<sub>X</sub> Removal Process", presented at the Acid Rain Conference in Washington, D.C., U.S.A., 1985.



## EBARA ENVIRONMENTAL CORPORATION

Hempfield Industrial Park, R.D. #6 - Box 516, Greensburg, PA 15601

Phone (412) 832-1200 Fax (412) 838-0279

January 8, 1991

Jonah Jacob  
Science Research Laboratory, Inc.  
15 Ward Street  
Somerville, MA 02143

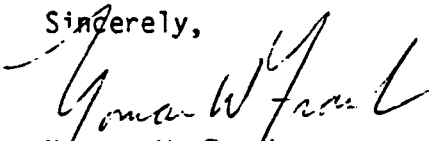
Dear Jonah,

We reviewed the proposed design of your accelerator in relationship to our SO<sub>2</sub> and NO<sub>x</sub> removal process. The SNOMAD-IV 0.5 MeV accelerator module is a compact system that would lend itself to our process and minimize capital costs for a full size plant. We feel that the further development of this module would be extremely helpful to the process, which would then help reduce pollutants from flue gases.

We made a cost estimate using your information and determined the compact modules would reduce the capital cost of our process by 22 to 26%. These are significant savings which would be attractive to utility users in their plans to reduce emissions.

We would appreciate being kept informed of your developments and wish you success in your endeavors. If at any time we can assist you, or furnish additional information, please feel free to call upon us.

Sincerely,



Norman W. Frank  
President

NWF:tlh

## SECTION 9

### SOLID STATE ULTRA-WIDEBAND SOURCES

#### 9.1 Introduction

Perhaps there is no more exciting outcome from the ferrite research we have been conducting than the adaptation of this technology to Ultra-Wideband pulse generators. The initial experiments that were performed under this contract lead us to believe that pulse generators could be constructed which were compact, reliable and capable of gigawatt output power at multi-kilohertz repetition rate. These pulse generators would be capable of generating pulses with subnanosecond risetimes and pulse widths of no more than a few nanoseconds. Pulse generators of this description had never before even been considered let alone fabricated and delivered.

The initial results from our research into ferrite principles was presented to DARPA. It was explained that we believed that this might lead to a new technology of great benefit to the services. As it turned out, the US Army Missile Command had previously inquired of DARPA whether or not there was a technology that might lead to an ability such as the one described above. Further research was funded and in the following section we describe two of the descendants of the initial breadboard pulse sources delivered to the US Army. These pulsers are denoted SLS-I and SLS-II (Shock Line System I & II) and have been delivered to the US Army installed in a specially customized Chevrolet cargo van.

The SLS-I (Shock Line System-I) is the larger and more powerful of two all-solid-state, Ultra-Wideband pulse generators available from Science Research Laboratory (SRL). The per pulse stored input energy for SLS-I is 9.2 Joules, but energy reclaimed by the energy recovery system reduces the input requirement to  $\approx$ 7 Joules. The output pulse energy is  $\approx$ 1.88 Joules in the form of a 0.825 GW, 2.3 nanosecond pulse. The maximum PRF capability is dependent on the charging technique and prime power source. SLS-I is designed to operate from a Lead-Acid, sealed, Gell Cell battery bank via an IGBT based Charge Module.

The maximum average operating PRF (Pulse Repetition Frequency) for SLS-I is 500 Hz. At this rate the 31 Amp-Hr, 540 Volt battery bank will provide continuous operation for more than 4 hours between charges. Each battery bank is equipped with a 3 kW charging supply which will provide 500 Hz operating capability indefinitely provided an external power source is available.

The SLS-I charging and energy storage system are designed to also provide a burst capability. The maximum operating PRF is 10 kHz but at this rate the run time duration must be limited to of order 3 seconds. Of course, longer run times are available at lower PRFs (e.g. 6 seconds at 5 kHz, 30 seconds at 1 kHz, etc.) as long as the average PRF is maintained below 500 Hz.

SLS-II (Shock Line System - II) is the smaller and more versatile of the two systems. The per pulse stored input energy for SLS-I is 2.26 Joules but energy reclaimed by the energy recovery system reduces the input requirement to  $\approx$ 1.6 Joules. The output pulse energy is  $\approx$ .36 Joules in the form of a 0.140 GW, 2.5 nanosecond pulse. The maximum peak operating PRF is 10 kHz as with SLS-I but the maximum average PRF of SLS-II is 1000 Hz and SLS-II can be run at 1000 Hz for more than 8 hrs off the standard 31 Amp-Hr. battery bank between charges. The drawback of the cheaper, lighter, SLS-II shock line system is that with its lower output energy it must be moved 2.5 time closer to the target to achieve the same field levels as SLS-I using the same antenna.

Each Ultra-Wideband source comes complete with its own control and charging system. It is therefore possible to run as many sources in tandem as desired as long as each source is supplied with its own antenna feed. It is a bit more difficult to operate individual sources in parallel as the output jitter is of order 2-3 nanoseconds, making it difficult to superimpose the output pulses which are of equivalent duration.

We will continue on with a more in depth description of the SLS-I and SLS-II, but we have supplied a simplified schematic representing the equivalent circuit of an electromagnetic shock line system in Fig. 9.1.

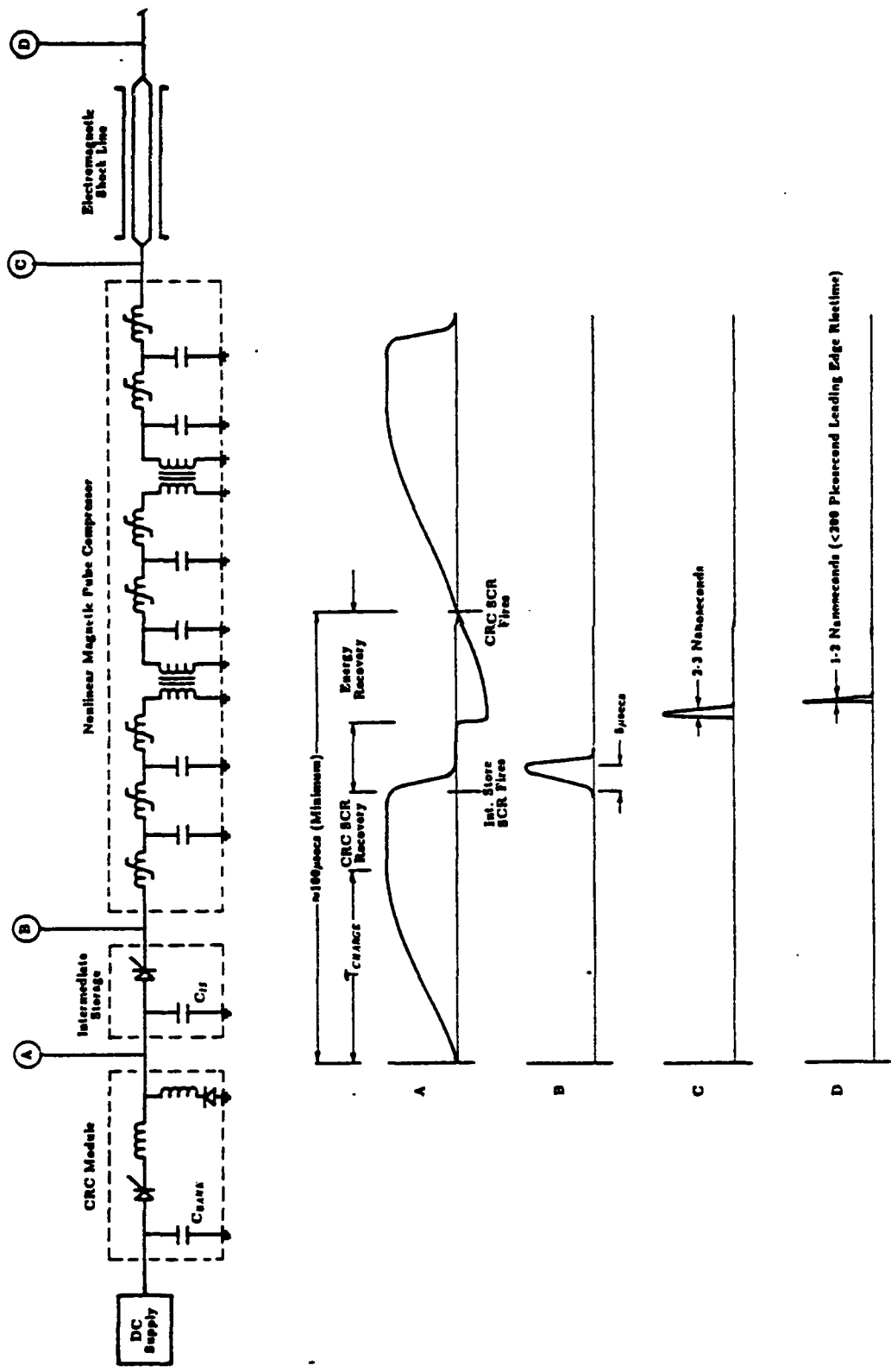


Figure 9.1: Simplified Schematic of Typical, All-Solid-State, Electromagnetic Shock Line System

## 9.2 SLS-I

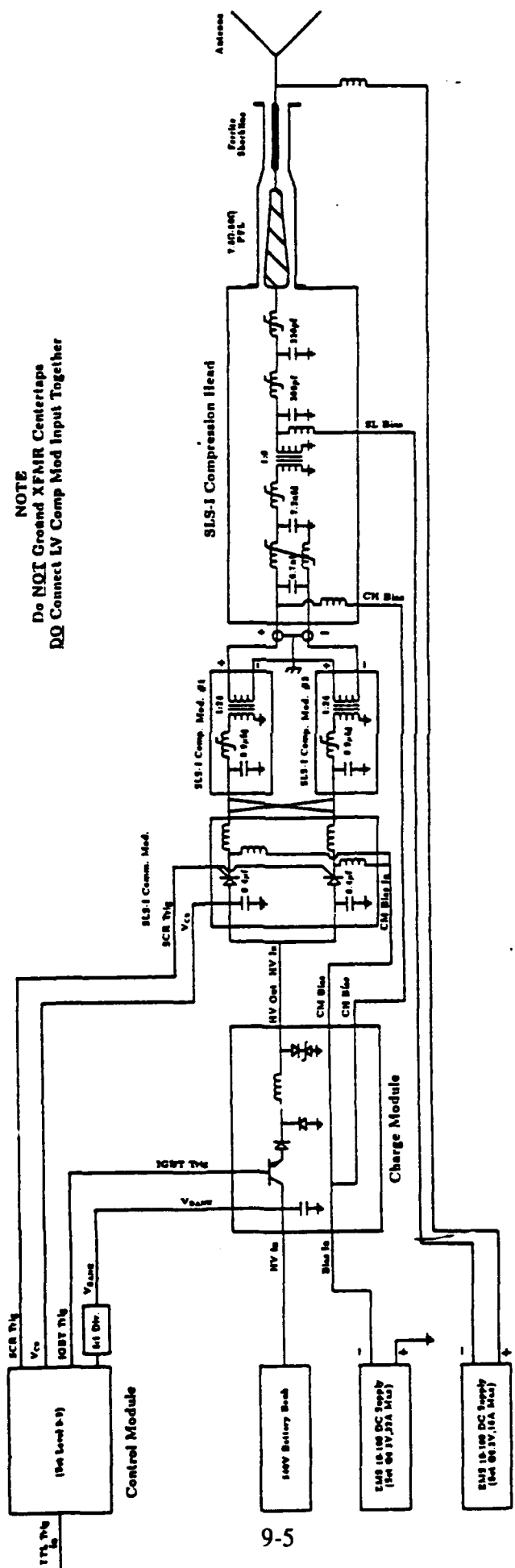
In this section we provide a more in depth description of the SLS-I shock line system. SLS-I is comprised of the following items:

- (1) Battery based prime power system with 3 kW charging supply.
- (2) IGBT/SCR GATE DRIVER Control Module or SSLAM SCR DRIVER Control Module
- (3) IGBT based Charge Module or SCR based Charge Module.
- (4) SCR Commutator Module
- (5) LV Compression Module #1
- (6) LV Compression Module #2
- (7) Nonlinear Magnetic Compression Head
- (8) EMS 10-100 Bias supply for the Comp. Hd. and Comm. Mod. bias
- (9) EMS 10-100 Bias supply for the Shock Line bias
- (10) Recirculating closed loop cooling system

A simple wiring diagram is provided (Fig. 9.2) to illustrate the required connections. All connection points are labelled and the appropriate cables will be provided. Items 2 through 7 must be closely colocated during operation, while the battery bank, bias supplies and cooler can be placed at a convenient distance. A photograph of the SLS-I shock line system minus batteries, bias supplies and cooler appears in Fig. 9.3.

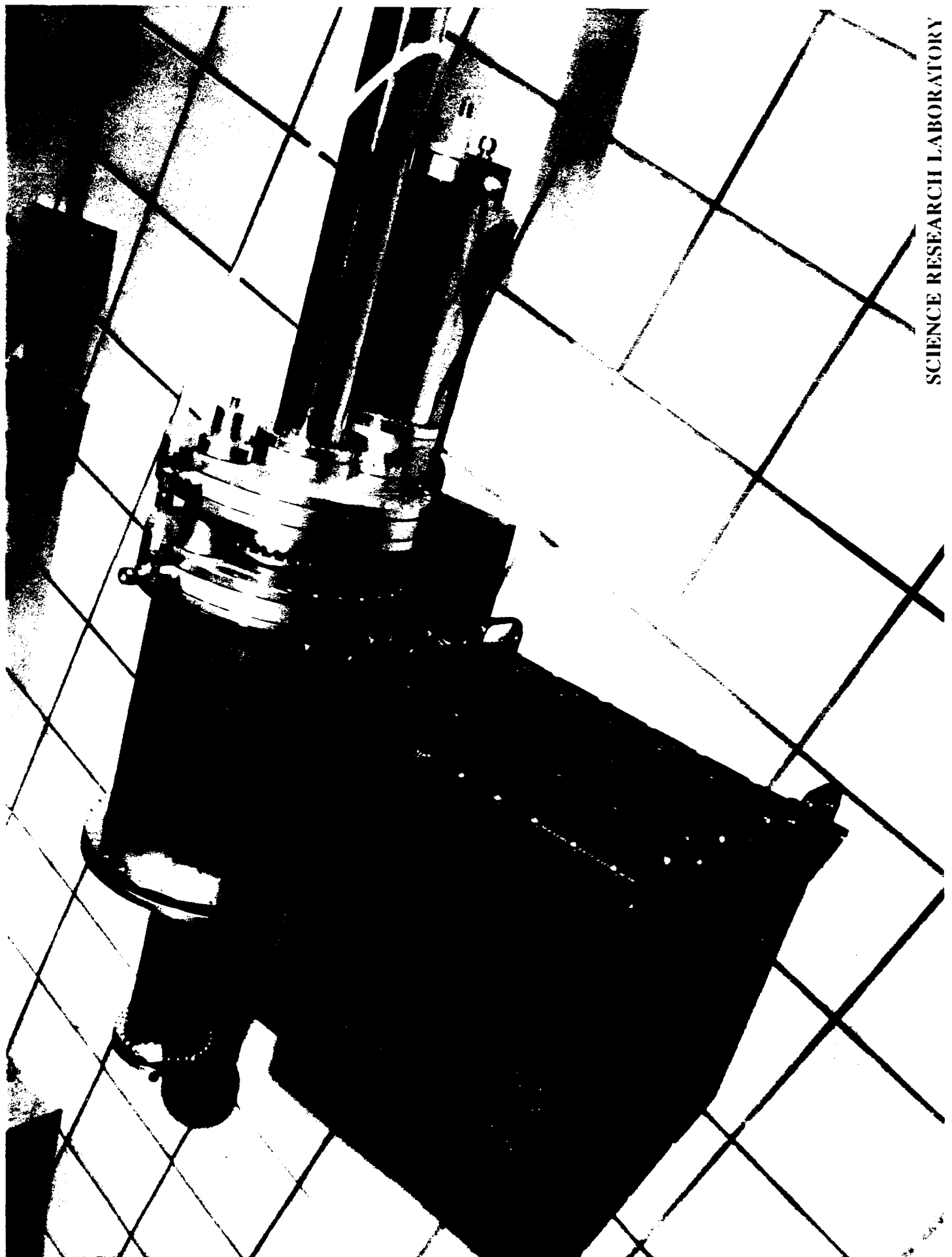
The Control Module contains all of the digital and analog circuitry required to control the operation of the SLS-I shock line system. It accepts a TTL level input signal from a customer supplied pulse generator as an indication to generate an output pulse. The power level of this output pulse can be adjusted through either the 10 turn potentiometer on the front panel or by supplying an external reference (0-5 volts). The Control Module takes the responsibility of controlling both the charging and discharging the Intermediate Storage capacitors. It controls the IGBT based Charge Module during the charging phase and supplies the SCR triggers which discharge the Intermediate Storage capacitors into the nonlinear magnetic compression chain. During both of these operations it monitors voltage and current levels throughout the system and

Figure 9.2: SLS-I Simplified Equivalent Circuit



SCIENCE RESEARCH LABORATORY

Figure 9.3: SLS-I Shock Line System



assures that all components are operating within acceptable limits.

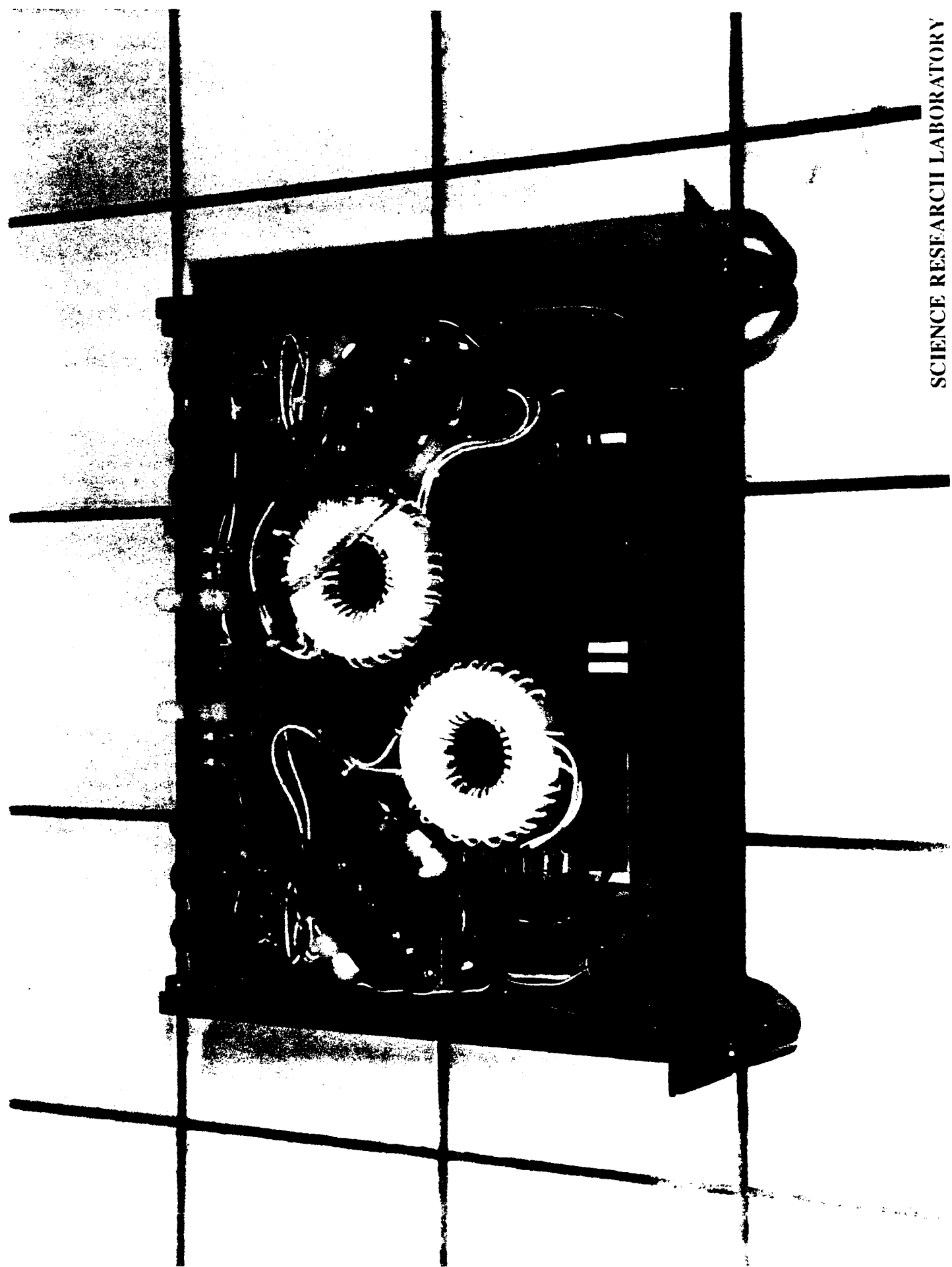
The IGBT charge module supplies the per pulse energy to a single SCR Commutation Module (Fig. 9.4). Two main commutator SCRs are housed in the SCR Commutator Module. The output from one SCR is on the left hand, back side of this chassis while the other resides on the right. Jumper cables from the SCR Commutator Module to the two LV Compression Modules are connected so that each SCR provides one half the input to each LV Compression Module. Each SCR is connected to an individual  $8.4\mu\text{fd}$ . Intermediate Storage capacitor bank. All capacitors are low loss polypropylene inverter capacitors with a floating foil design for improved reliability. Litz wire charging inductors limit the  $\text{dI/dt}$  after the SCRs are triggered and result in the energy being transferred from the Intermediate Storage capacitors to the Low Voltage Compression Modules in  $8.5\mu\text{secs}$ .

There are two Low Voltage Compression Modules (Fig. 9.5) in the SLS-I system. Each module contains a single stage of nonlinear magnetic compression and an induction style step-up transformer. Each module is designed to store half of the pulse energy and to temporally compress this energy from the  $8.5\mu\text{secs}$ . charge duration to the 650 nanosecond duration output pulse. After the compression occurs, an induction style transformer located in each module provides a voltage step-up from the 985 volt input to an output level of  $\approx 17$  kV. The transformers in the LV Compression Modules have a floating output. One LV Compression Module is designed to deliver a negative output while the other produces a positive output.

The outputs from the two Low Voltage Compression Modules power the SLS-I HV compression module. Inside the oil cooled, HV Compression Module are 4 stages of nonlinear magnetic pulse compression and a 1:6 induction style step-up transformer (Figs. 9.6 and 9.7). The  $\pm 17$  kV, 650 nanosecond duration input pulse is compressed into an 80 kV, 10.7 kA (850 Megawatt) pulse with a duration of 2.5 nanoseconds (Fig. 9.8). Following the final compression, the pulse energy is transmitted into a tapered transmission line with an input impedance of  $7.5\Omega\text{s}$  and an output impedance of  $50\Omega\text{s}$ . The  $\approx 200$  kV output from the tapered transmission line passes through an electromagnetic shockline before exiting to the antenna. The final transmitted

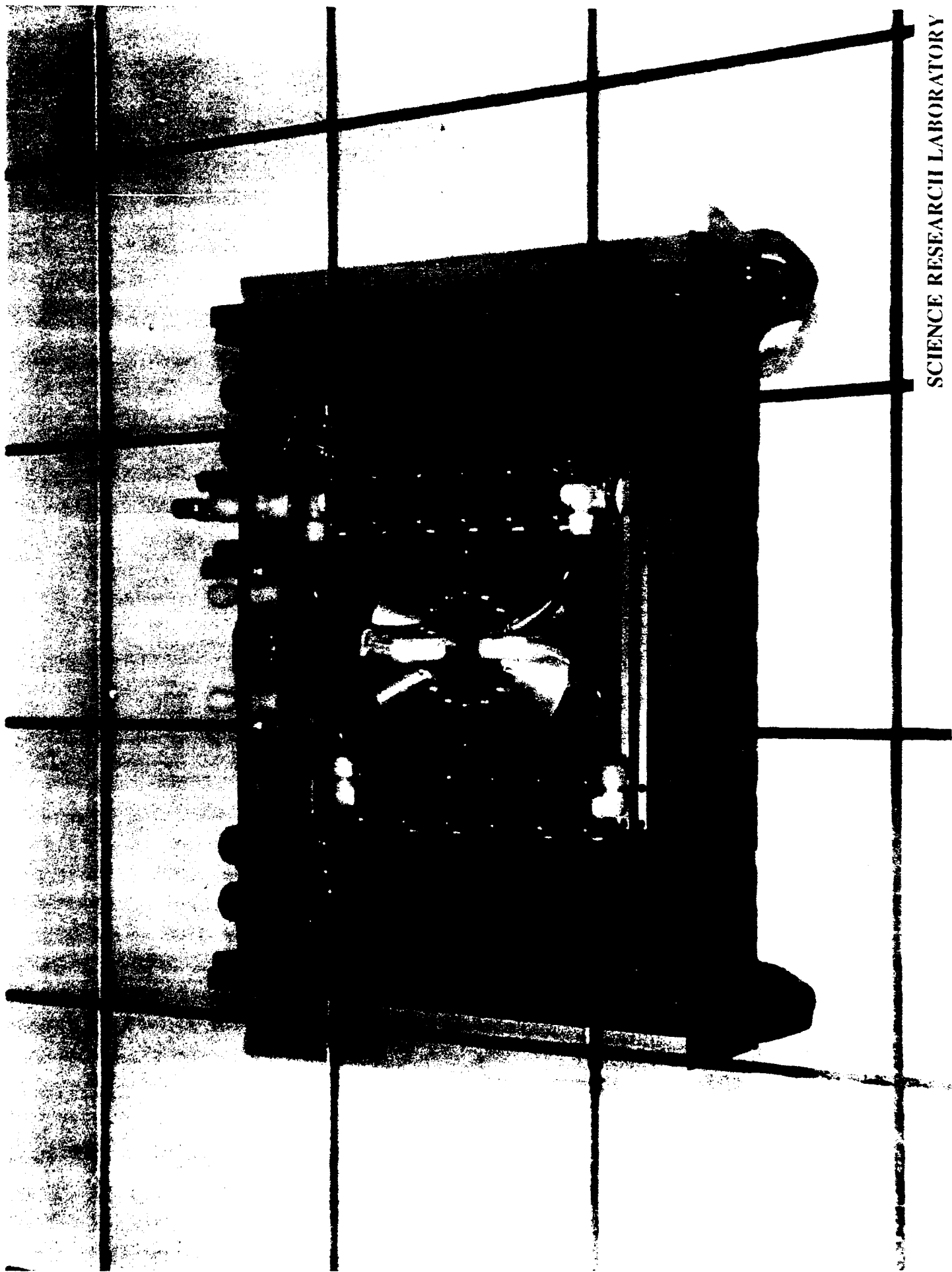
SCIENCE RESEARCH LABORATORY

Figure 9.4: SLS-I, SCR Commutation Module



SCIENCE RESEARCH LABORATORY

Figure 9.5: SLS-II, LV Compression Module



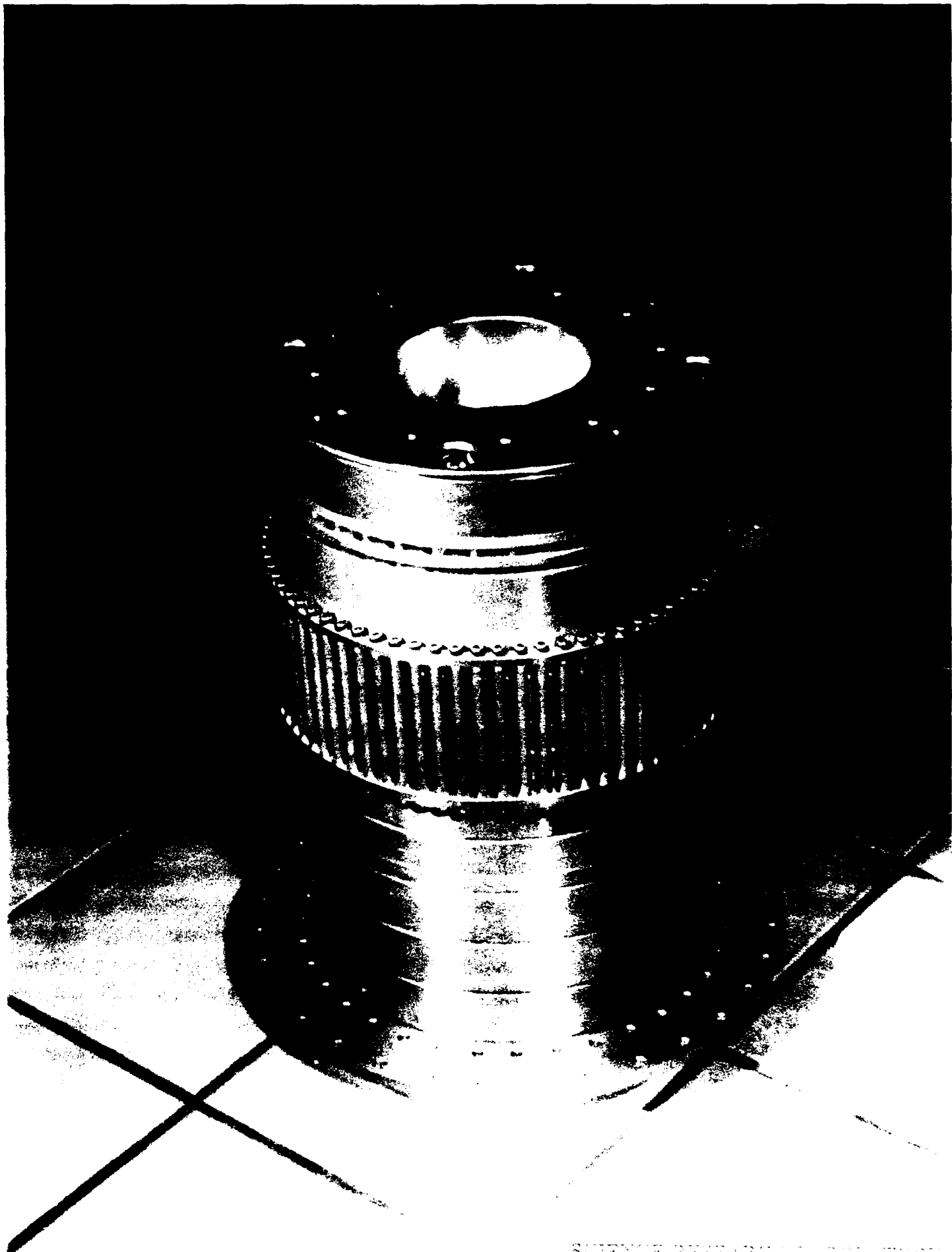
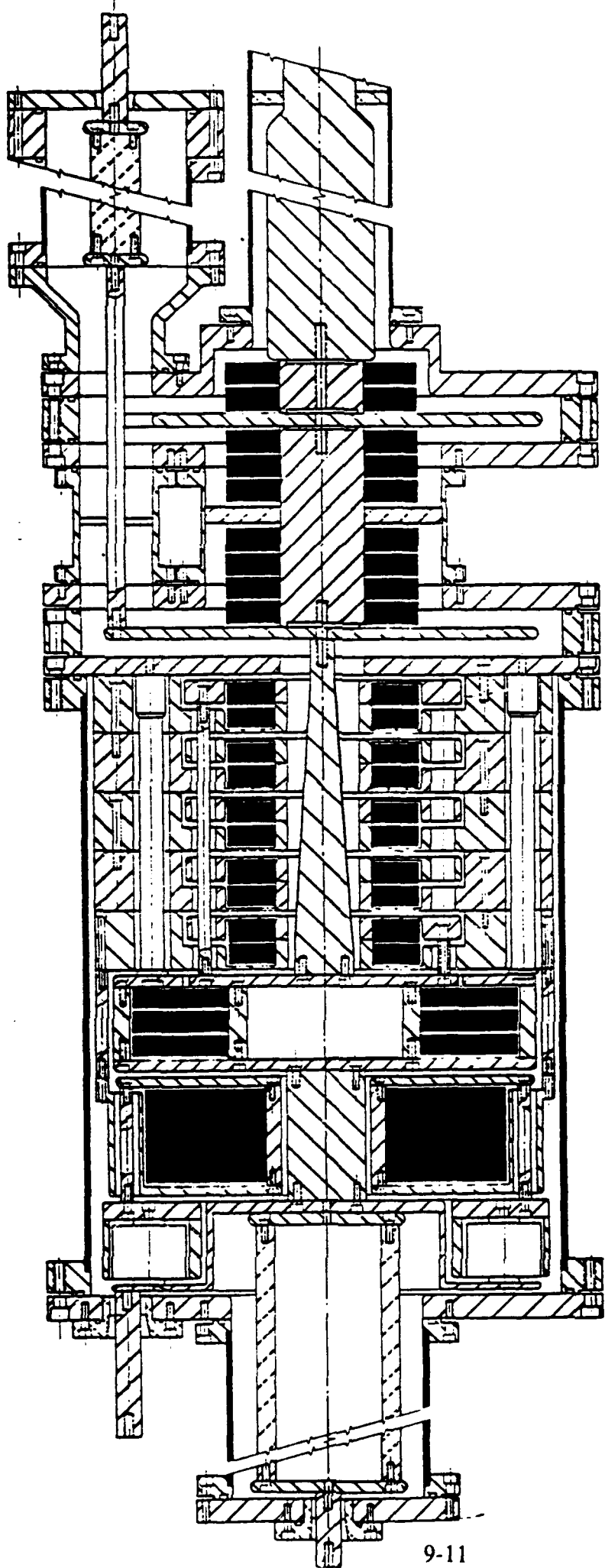


Figure 9.6: SLS-I RV Compression Module

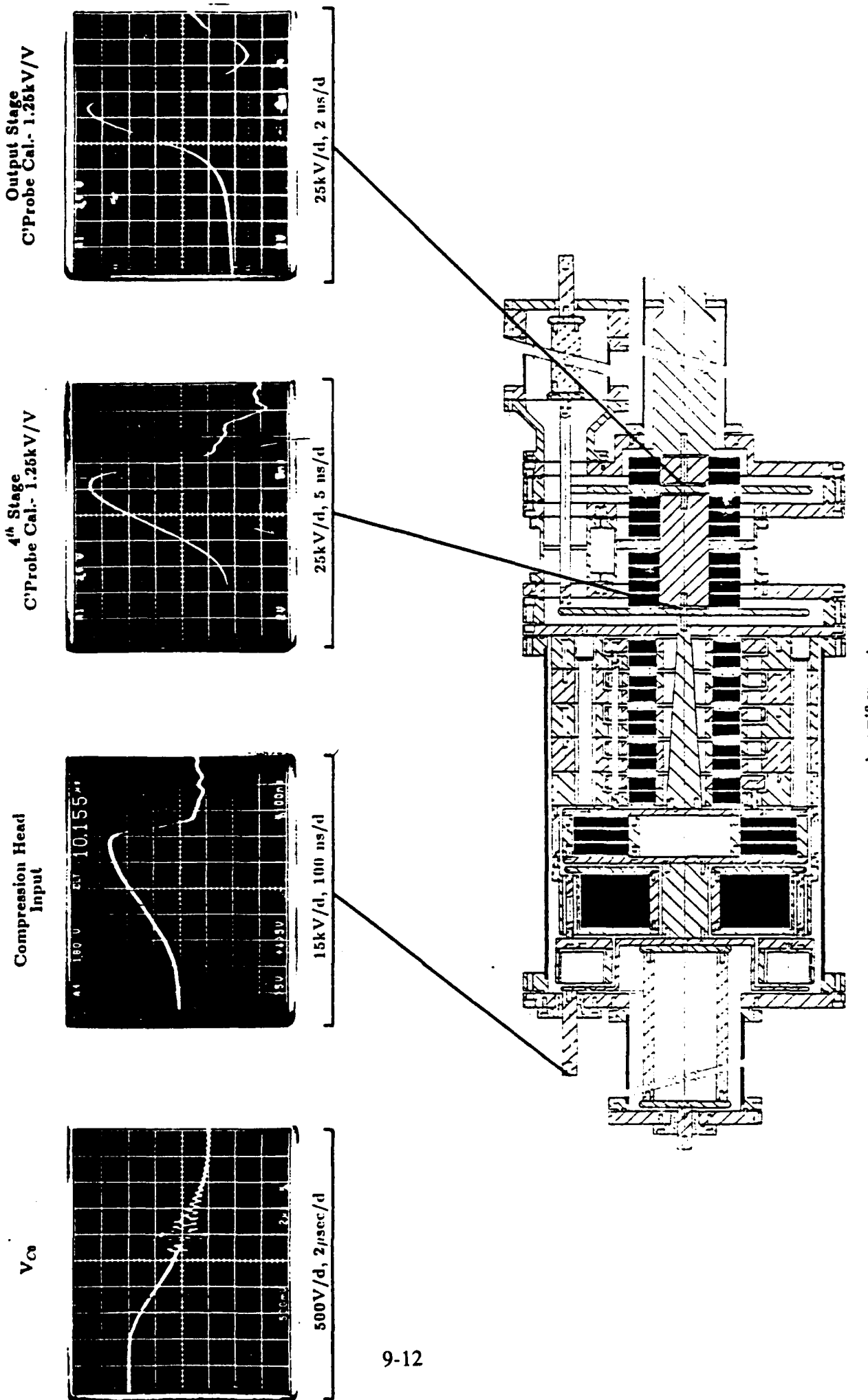
— 10 cm —

Figure 9.7: Cross Section of SLS-I HV Compression Module



SCIENCE RESEARCH LABORATORY

Figure 9.8: Operation of SLS-I



waveshape (Fig. 9.9) is a pulse of less than 2 nanoseconds in duration with a risetime of  $\approx$ 200 picoseconds.

The performance of SLS-I is further documented in Table 9.1.

### 9.3 Summary of SLS-I Operating Parameters

The SLS-I shock line system is designed to deliver a 200 kV amplitude, 2 nanosecond duration, 200 picosecond risetime pulse into a  $50\Omega$  load. The maximum average PRF is 500 Hz but a burst capability allows SLS-I to be operated at a peak PRF of up to 10,000 Hz. The maximum runtime duration at 10 kHz is 3 seconds. This limitation on runtime is not imposed by the battery based prime power system which stores sufficient energy for more than 7,000,000 pulses. The limitations on maximum average PRF and runtime duration at 10,000 Hz extend from the temperature rise in the final stages of nonlinear magnetic pulse compression network and the electromagnetic shock line.

The efficiency of a nonlinear magnetic compression stage is highly dependant on the operating time. Eddy current losses in tape wound cores and spin-damping losses in ferrite both increase linearly as the saturation time is reduced. In tape wound cores eddy current losses become the dominant loss mechanism at saturation times less than  $100\mu$ secs, while for most ferrites spin-damping losses become dominant at saturation time scales less than 100 nanoseconds.

For SLS-I, experimentation has shown that the front end components involved in producing the 34 kV, 650 nanosecond input to the HV Compression Module can all be operated in excess of 7 kHz average. The Metglas based 1<sup>st</sup> stage of the HV Compression Module which compresses the pulse from 650 nanoseconds to 44 nanoseconds will operate at an average PRF exceeding 3.5 kHz. The ferrite based 2<sup>nd</sup> stage which provides temporal pulse compression from 44 nanoseconds to 15 nanoseconds is limited to an average PRF of  $\approx$ 5 kHz. The ferrite based 3<sup>rd</sup> stage is required to saturate in  $\approx$  15 nanoseconds resulting in a three fold increase in loss per unit volume over the previous stage and a maximum average PRF of  $\approx$  2 kHz. The 4<sup>th</sup> stage is also ferrite but the 4 nanosecond saturation time drives the losses up to over 2000 Joules/meter<sup>3</sup> and forces a ceiling on the maximum average PRF of 500 Hz. The shock line ferrites are carefully

Transmitted Waveshape from SNOMAD-X (SLS-I Breadboard) and a TEM horn

Antenna Voltage - 200 kV peak

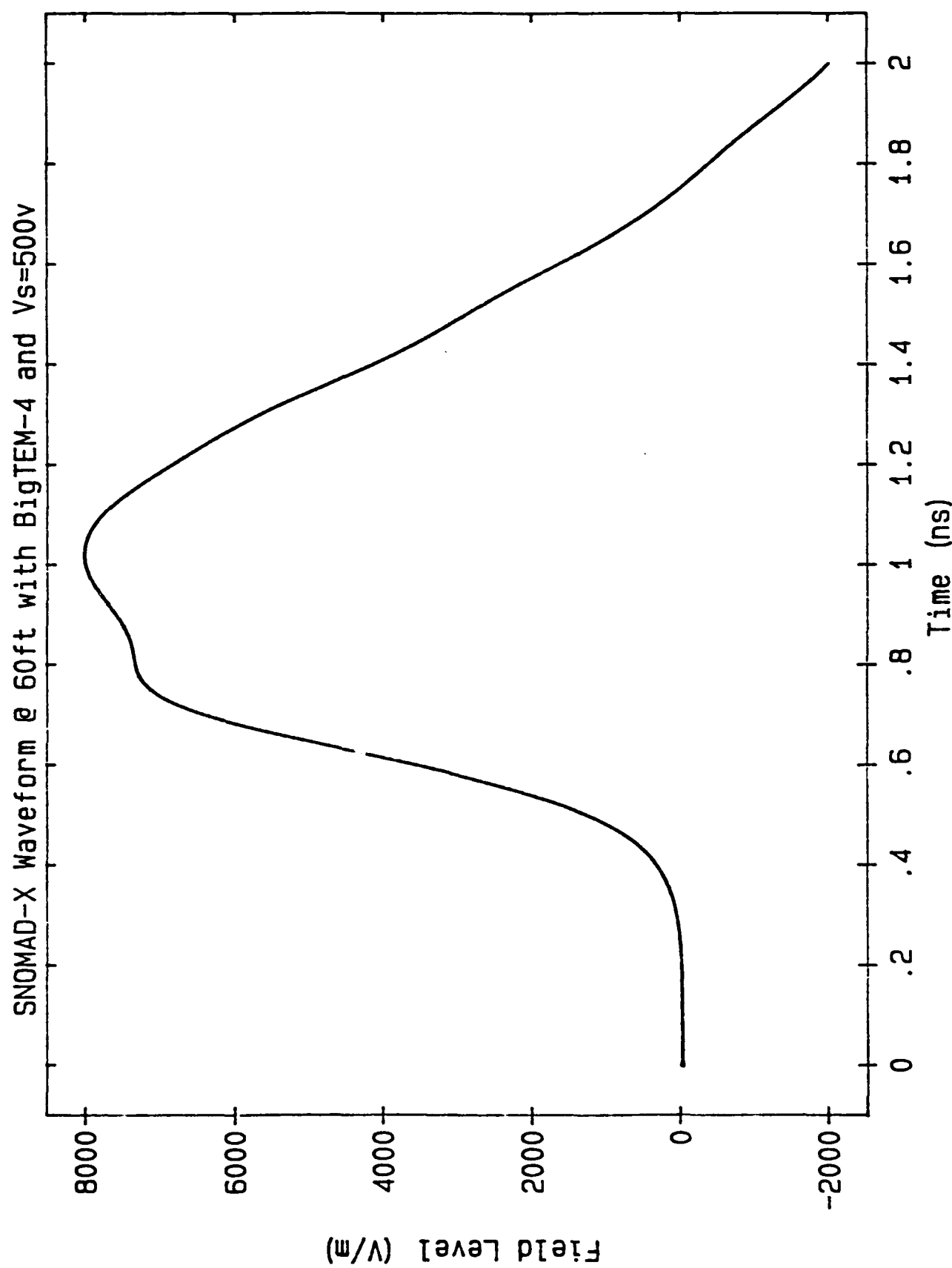


Figure 9.9: Typical Transmitted Output Pulse

**Table 9.1: SLS-I Preliminary Specifications**

**Input Power Requirements:**

Energy/pulse	9.216 joules
PRF	10 kHz
Power	92.16 KW
Voltage	600 volt
Current	153 Amps

**Intermediate Storage**

Capacitance	16.72 $\mu$ fd
Voltage	1,050 volts
Energy	9.216 joules
Stored charge	$17.55 \times 10^{-3}$ Coulombs
$\tau$ discharge	$\leq 8.5 \mu$ sec
I peak	$2.92 \times 10^3$ Amp
dI/dt	$1.08 \times 10^3$ A/ $\mu$ sec
dI/dt per device	540 A/ $\mu$ sec (1 $\times$ R355 West Code)
Commutation losses	$\sim .58$ joules

**1<sup>st</sup> Stage**

Capacitance	17.8 $\mu$ fd
Voltage	985 volts
Energy	8.636 joules
Core Type	.6 Mil $\times$ 2605 SC
# Turns	1
Core geometry	$2 \times 3.00"$ ID $\times$ 5.5" OD $\times$ 2" Wide
$\int V \cdot dt$	$\sim 4.33 \times 10^{-3}$ Vsecs
Lsat	$6.66/2$ nh + $1.64/2$ nh (STRAY) = $8.30/2$ nh
$\tau$ discharge	650 nsecs
Losses	$\sim 1.0$ joules (.60 cores, .4 caps)
Core volume	$2 \times 5.47 \times 10^{-4} \text{ m}^3$ , $2 \times 2.734$ kg

**Transformer**

Core Type	2605S3A
# Turns (PRIM)	1/2X1/12
# Turns(sec)	2
Losses	$\leq 1.0$ joules
Peak stress	26 kV/cm at 18. kV (.375" dia. Rod in .775" dia. hole)
Core geometry	$12 \times .875"$ ID $\times$ 1.75" OD $\times$ 1.0" wide
Output Energy	6.63 joules

**Output**

Capacitance	6.72 nfd
Voltage	$\approx 44.4$ kV
Energy	6.63 joules
Energy Lost	2.6 joules
Efficiency	72% joules
$\tau$ discharge	$\sim 650$ nsecs

**Table 9.1: SLS-I Compression Module (Continued)**

**1<sup>st</sup> Stage**

Capacitance	6.72 nfd
Voltage	34 kv
Energy In	6.63 joules
Energy Out	3.88 joules
Core Type	2605-SC
# Turns	2
Core geometry	$1 \times 2.5'' \text{ ID} \times 7.5'' \text{ OD} \times 2.0'' \text{ Wide}$
$\int V \cdot dt$	$\sim 14.2 \times 10^{-3} \text{ Vsecs}$
Lsat	50 nh
$\tau$ discharge	44 nsecs
Losses	$\sim 2.75$ joules
% Total Loss	$\sim 30\%$

**2<sup>nd</sup> Stage**

Capacitance	7.2 nfd
Voltage	30.641 kv
Energy In	3.88 joules
Energy Out	3.38 joules
Core Type	CN-20
# Turns	1
Core geometry	$3 \times 4.0'' \text{ ID} \times 8.0'' \text{ OD} \times 0.5'' \text{ Wide}$
$\int V \cdot dt$	$\sim 1.0 \times 10^{-3} \text{ Vsecs}$
Lsat	5.5 nh
$\tau$ discharge	15 nsecs
% Total Loss	$\sim 5.42\%$
Losses	$\sim .5$ joules

**1:6 Transformer**

Core Type	CMD-5005 Ferrite
# Turns (PRIM)	1/6
# Turns(sec)	1
Losses	$\leq .5$ joules
% Total Loss	$\sim 5.42\%$

**3<sup>rd</sup> Stage**

Capacitance	300 pf
Voltage	126 kV
Energy In	2.88 joules
Energy Out	2.38 joules
Core type	CMD-5005 Ferrite
Core Geom.	$7 \times 1.75'' \text{ ID} \times 4.0'' \text{ OD} \times 1/2'' \text{ w}$
$\int V \cdot dt$	1 Turn $\times 2.419 \text{ Vmsecs/Turn} =$ $224 \text{ kV}^* (15 \text{ nsecs}/2)$
LSAT	22 nh
$\tau$ discharge	4.17 nsecs
Losses	$\sim .5$ joules
% Total Loss	$\sim 5.42\%$

**Table 9.1: SLS-I Compression Module (Continued)**

<b>4<sup>th</sup> Stage</b>	Capacitance	200 pf
	Voltage	137 kV
	Energy In	2.38 joules
	Energy Out	1.88 joules
	Core type	CMD-5005 Ferrite
	Core Geom.	$2 \times 1.75'' \text{ ID} \times 4.0'' \text{ OD} \times 1/2'' \text{ w}$
	$\int V \cdot dt$	1 Turn $\times .51 \text{ Vmsecs/Turn} =$ 194 kV* (4.17 nsecs/2)
	LSAT	5.5 nh
	$\tau_{\text{discharge}}$	2.5 nsecs into 10Ωs
	Losses	~ .5 joules
	% Total Loss	~ 5.42%
<b>Output</b>	PFL Impedance	7.56Ωs
	Output Impedance	5.5Ωs
	Voltage In Line	79 kV
	Est. Volt. Out	287 kV (100Ωs)
	Peak Power Out	.825 Gw.

tailored so as not to further limit the average PRF. High saturation flux ferrites at the beginning of the line see a slower saturation time than the low flux ferrites at the end. The  $M_0$  of a ferrite is chosen to match its position in the line so that it can handle the same average PRF as the output stage of the pulse compression chain.

The maximum runtime duration during burst operation at up to 10 kHz PRF is set by a combination of the ferrite losses which at time scales less than 100 nanosecond saturation given approximately as

$$\text{Energy Lost/cm}^3 = \frac{M_0^2(\text{Gauss}) \cdot 2 \cdot 10^{-7} \text{ Joules/cm}^3}{\tau_{SAT}(\text{noseconds})}$$

and the specific heat of 0.75 Joules/ $^{\circ}\text{C}\cdot\text{cm}^3$ . The compression ferrites in SLS-I have an  $M_0 \approx 200$  gauss. The  $M_0$  of the electromagnetic shock line ferrites vary from 120 gauss at the beginning of the line to 20 gauss at the end of the line.

Extended performance of the SLS-I shock line system in terms of either average PRF or burst duration could be accomplished to some extent by further reducing the  $M_0$  of the ferrites used in the final stages of compression and in the shock line. Unfortunately the core volume requirements increase inversely as the square of  $M_0$ . Therefore the efficiency would remain the same but the pulser would get larger and the run time durations and average PRF would also increase as the inverse square of the ferrite  $M_0$ . While this could be done there has been no incentive in the past. The existing customers who make use of these systems have habitually used runtimes of 2 to 3 seconds followed by a delay of order 1 minute. This habit was formed by the operating limitations exhibited by all other commercially available UWB sources.

Cooling of the SLS-I shock line system is accomplished through the use of a 3 kW closed cycle coolant system. Two coolants are available which both provide the necessary dielectric and cooling properties. Standard HV transformer oil is more commonly used but a synthetic hydrocarbon manufactured by Castrol Inc under the title of Brayco 889 provides somewhat improved heat transfer and is generally more acceptable in terms of flammability and environmental compatibility. The minimum flow rate in either case is 4 liters per minute.

#### **9.4 SLS-II**

In this section we provide a brief description of SLS-II. SLS-II (Shock Line System - II) is small, lightweight, highly portable Ultra-Wide-Band source. It is comprised of the following items:

- (1) Battery based prime power system.
- (2) IGBT/SCR GATE DRIVER Control Module
- (3) IGBT based Charge Module
- (4) SCR Commutator Module
- (5) Nonlinear Magnetic Compression Head
- (6) EMS 10-100 Bias supply for the Comp. Hd. and Comm. Mod. bias
- (7) EMS 10-100 Bias supply for the Shock Line bias
- (8) Closed cycle coolant system

A simple wiring diagram of SLS-II is provided (Fig. 9.10) in order to illustrate the required connections. All connection points are labelled and the appropriate cables have been provided. A photograph of SLS-II minus the battery bank, bias supplies and cooler appears in Fig. 9.11.

A single 3" high X 13" deep rackmountable chassis combines the functions of SCR commutation, low voltage compression and initial voltage step-up. The output from this SCR commutation module delivers 19 kV, 400 nanosecond duration pulse to the input of the nonlinear magnetic compression head.

The final compression stage in the nonlinear magnetic compression head (Fig. 9.12) delivers a 177 Megawatt, 2.5 nanosecond duration pulse into the  $12\Omega$  input of a tapered impedance transmission line (Fig. 9.13). This transmission line supplies up to 90 kV to the  $50\Omega$  input of an electromagnetic shock line where the risetime of the output pulse is reduced to less than 200 picoseconds. The final waveshape transmitted from the antenna appears as shown in Fig. 9.14.

A summary of the performance specifications relating to SLS-II are supplied in Table 9.2.

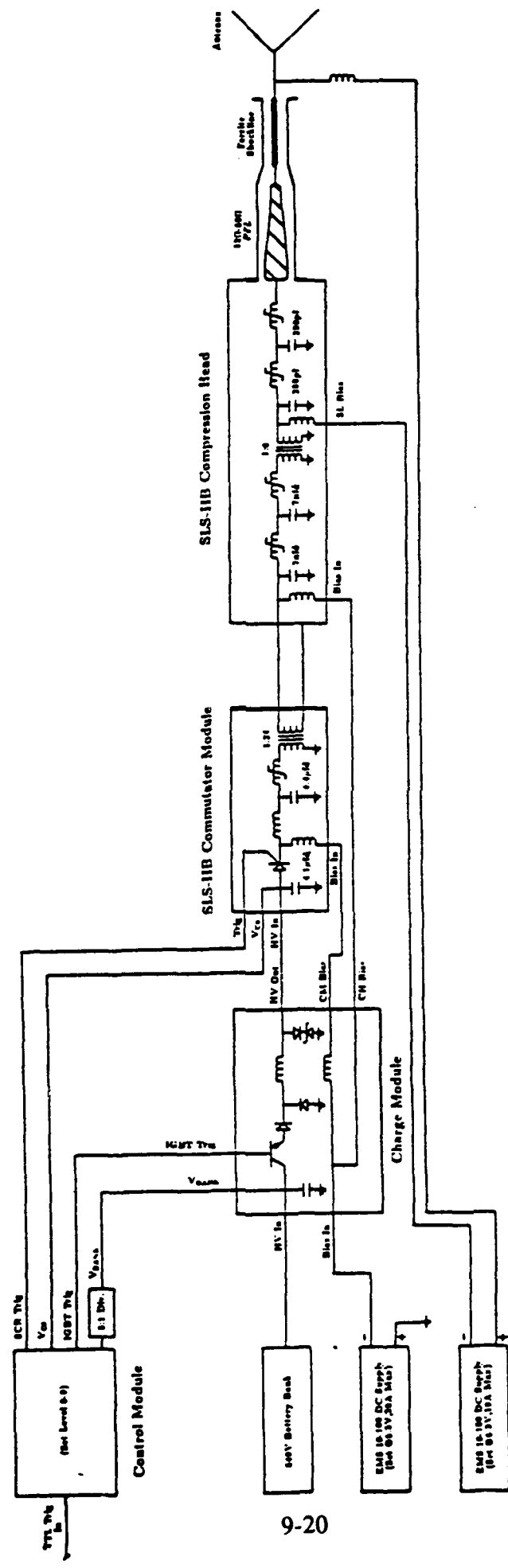


**Figure 9.10:** Simplified Schematic of SLS-II



9-21

Figure 9.11: SLS-II

SCIENCE RESEARCH LABORATORY

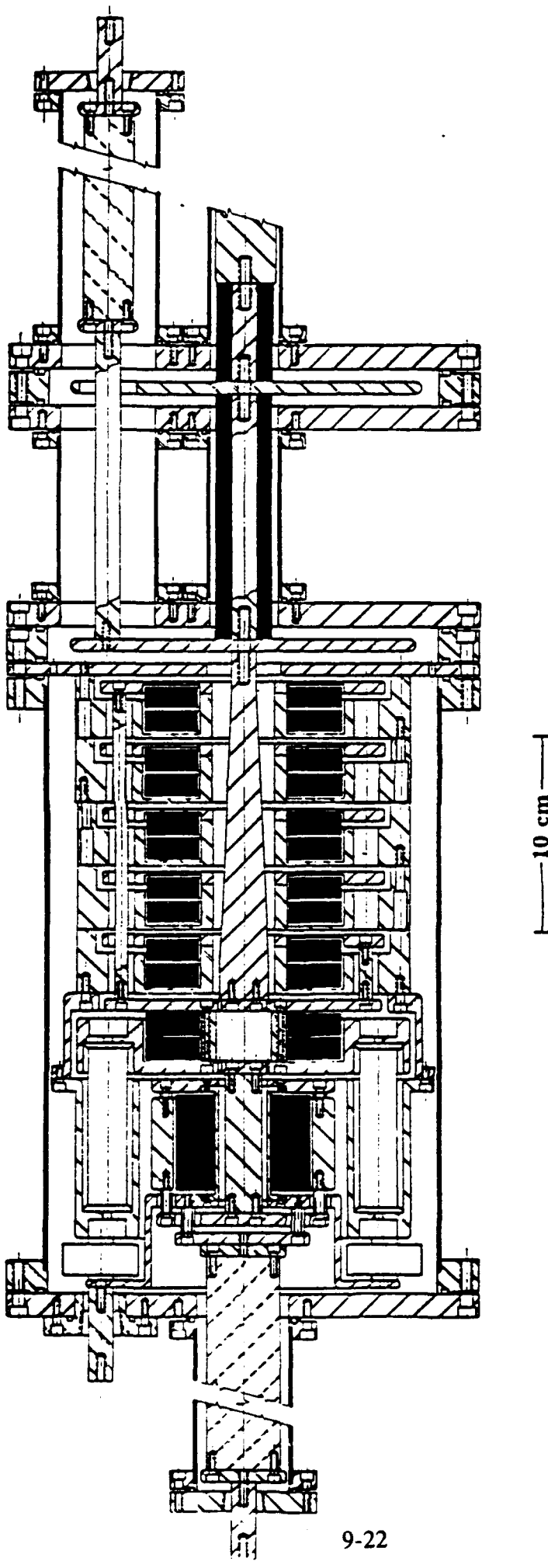


Figure 9.12: Nonlinear Magnetic Compression Head

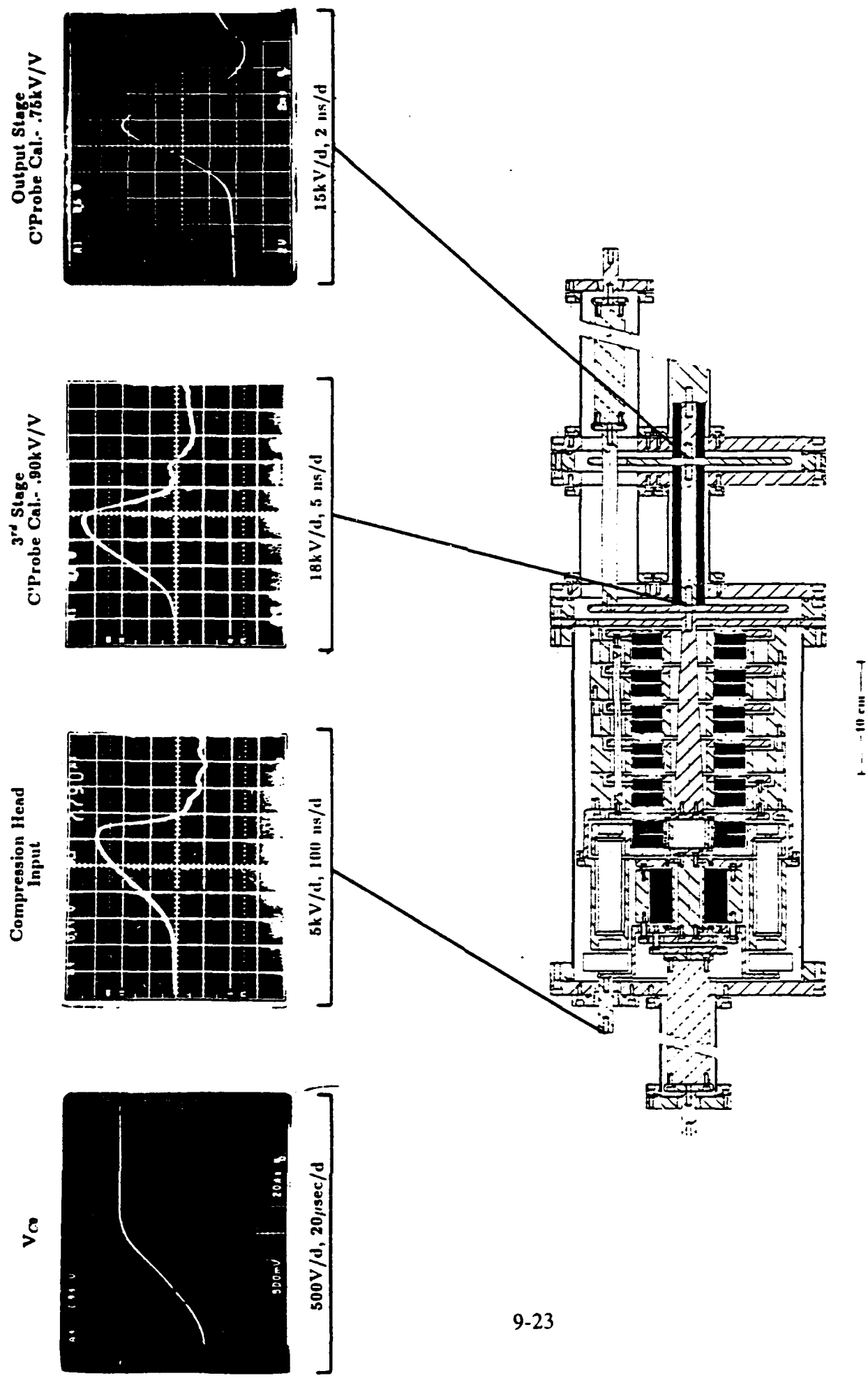


Figure 9.13: Operation of SLS-II

Transmitted Waveshape from SLS-II and a TEM horn

Antenna Voltage - 100 kV peak

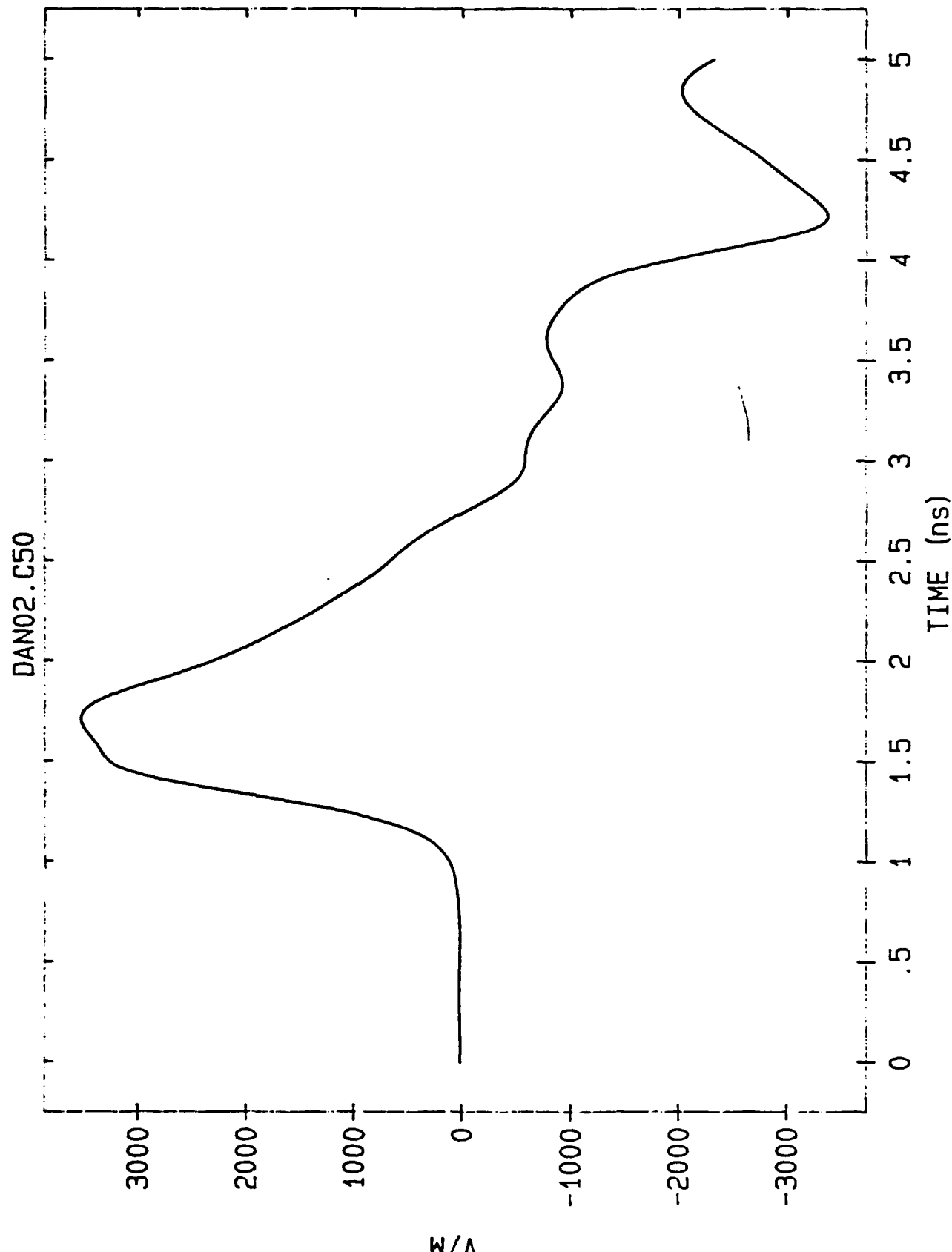


Figure 9.14: Output Pulse of SLS-II

**Table 9.2: SLS-IIIB Performance Specifications**

**Input Power Requirements:**

Energy/pulse	2.26 joules
PRF	10 kHz
Power	22.6 KW
Voltage	600 volt
Current	37.66 Amps

**Intermediate Storage**

Capacitance	4.1 $\mu$ fd
Voltage	1,050 volts
Energy	2.26 joules
Stored charge	$4.305 \times 10^{-3}$ Coulombs
$\tau$ discharge	$\leq 5.5$ $\mu$ sec
I peak	$1.23 \times 10^3$ Amp
dI/dt	$.7035 \times 10^3$ A/ $\mu$ sec
$I_T$ (RMS)	324 Amps
dI/dt per device	704 A/ $\mu$ sec (1 $\times$ R355 West Code)
Commutation losses	$\sim .26$ joules

**1<sup>st</sup> Stage**

Capacitance	4.4 $\mu$ fd
Voltage	953 volts
Energy	2.00 joules
Core Type	.6 Mil $\times$ 2605 SC
# Turns	1
Core geometry	$1 \times 2.25"$ ID $\times 3.75"$ OD $\times 2"$ Wide
$\int V \cdot dt$	$\sim 2.6 \times 10^{-3}$ Vsecs
Lsat	$5.36 nh + 1.64 nh$ (STRAY) = 7 nh
$\tau$ discharge	380 nsecs
Losses	$\sim .5$ joules (.30 cores, .2 caps)
Core volume	$2.316 \times 10^{-4} m^3$ , 1.39 kg

**Transformer**

Core Type	2605S3A
# Turns (PRIM)	1/12
# Turns(sec)	2
Losses	$\leq .24$ joules
Peak stress	26 kV/cm at 18. kV (.375" dia. Rod in .775 " dia. hole)
Core geometry	$12 \times .875"$ ID $\times 1.75"$ OD $\times 1.0"$ wide

**Table 9.2: SLS-IIIB Performance Specifications (Continued)**

**1<sup>st</sup> Stage**

Capacitance	7 nfd
Voltage	19 kV
Energy	.126 joules
Core Type	.6 Mil x 2605 SC
# Turns	2
Core geometry	1 x 1.125" ID x 2.75" OD x 2" Wide
$\int V \cdot dt$	$\sim 4.18 \times 10^{-3}$ Vsecs
Lsat	$38.43 \text{ nh} + 1.6 \text{ nh (STRAY)} = 40 \text{ nh}$
$\tau$ discharge	37 nsecs
Losses	$\sim .48 \text{ joules (.4 cores, .08 caps)}$

**2<sup>nd</sup> Stage**

Capacitance	7 nfd
Voltage	15 kV
Energy	.78 joules
Core Type	CN-20 Ferrite
# Turns	1
Core geometry	2 x 1.75" ID x 4.00" OD x 1/2" Wide
$\int V \cdot dt$	$\sim 4.0 \times 10^{-4}$ Vsecs
Lsat	$3.46 \text{ nh} + .54 \text{ nh (STRAY)} = 4 \text{ nh}$
$\tau$ discharge	17 nsecs
Losses	$\sim .1 \text{ joules (.06 cores, .04 caps)}$

**Transformer**

Core Type	CMD-5005 Ferrite
# Turns (PRIM)	1/6
# Turns(sec)	1
Losses	$\leq .08 \text{ joules}$
Core geometry	5 x 1.75" ID x 4.00" OD x 1.0" wide

**3<sup>rd</sup> Stage**

Capacitance	266 pfd
Voltage	60 kV
Energy	.60 joules
Core type	CMD-5005 Ferrite
Core Geom.	.50" ID x 1.10" OD x 5.1" w $(9.633 \times 10^{-4} \text{ M}^2)$
$\int V \cdot dt$	1 Turn x .493 Vmsecs/Turn = 60 kV* (15 nanosecs/2) (.5 Tesla)
LSAT	$27 \text{ nh} + 5 \text{ nh stray} \simeq 32 \text{ nh}$
$\tau$ discharge	6 nsecs
Losses	$\sim .12 \text{ joules}$

**Table 9.2: SLS-IIB Performance Specifications (Continued)**

**Output Stage**

Capacitance	200 pfd
Voltage	60 kV
Energy	.48 joules
Core type	CMD-5005 Ferrite
Core Geom.	.50" ID x 1.10" OD x 1.8" w ( $3.4 \times 10^{-4} M^2$ )
$\int V \cdot dt$	1 Turn x .174 Vmsecs/Turn = 60 kV* (6 nanosecs/2) (.5 Tesla) 9.566 nh + 2.48 nh stray $\simeq$ 12 nh
LSAT	1.6 nsecs E-fold (12 $\Omega$ )
$\tau_{\text{discharge}}$	Losses $\sim$ .12 joules
Peak Power Out	$\sim$ 177 MW
Peak Voltage Out	$\sim$ 90 kV (50 $\Omega$ )

## APPENDIX 1

### INTRODUCTION TO ELECTROMAGNETIC SHOCK LINES

The generation of subnanosecond, multi-gigawatt pulses is beyond the current state-of-the-art using modern pulsed power techniques. Gas and liquid discharge switches, even if they were sufficiently reliable, are limited to the production of pulses a few nanoseconds in duration. We will also show in the following report that even state-of-the-art nonlinear magnetic compression circuits are limited by ferrimagnetic material properties to similar pulse lengths.

In the late 1950s, Soviet scientists confronted with this problem envisioned a new concept for the production of extremely short pulses. The electromagnetic shock line has a simple analog to nonlinear acoustic phenomena experienced by anyone who has ever felt a sonic boom. In air, the velocity of sound is proportional to the square root of the derivative of the pressure with respect to the density of the medium. The relationship between pressure and density is nonlinear as pressure is approximately proportional to the density to the power of 1.4. As the intensity of sound increases, so does its velocity. Large displacements in air lead to nonlinear gas flow and the velocity of the crest will exceed the velocity of the trough. The wave front is distorted in much the same way as an ocean wave approaching the shore. The front of the wave continues to steepen as it propagates.

Investigations into the electromagnetic analog of the sonic shock wave began in the Soviet Union. Certainly electromagnetic nonlinearities exist in ferrimagnetic materials. In ferrites, the permeability depends on the field intensity and the velocity of electromagnetic radiation in the medium is proportional to the inverse square root of the permeability. The first theoretical study was carried out by Dr. V. L. German in 1953 and later refined by Dr. I. G. Katayev in 1958. Experimental research confirming the existence of electromagnetic shock waves was first conducted in the early 1960s. These initial experiments were published in the international literature but little information has appeared in recent literature. The initial experiments were quite successful with pulses shorter than 200 psec being generated.

While it may still lack experimental confirmation, in the following analyses we will show that pulses with risetimes as short as 30 picoseconds can be generated using ferrite-loaded coaxial transmission lines. The dominant RF spectral component of a 60 picosecond pulse is centered at 8 GHz. Differentiation of such a pulse, accomplished automatically by most short pulse antenna concepts, could yield spectral components centered at even higher frequencies.

It should be emphasized that electromagnetic shock lines shorten the pulse at the expense of energy. The leading edge is simply eroded away and that energy is lost or reflected back to the source. There is no power multiplication in a shock line. The output peak power level is approximately equal to the input power level. The electromagnetic shock line represents a pulse shaping technique, and as it only shapes the leading edges, short pulses with a sharp leading and trailing edge can only be produced by combining two pulses with sharp leading edges and opposite polarities which are temporally shifted. This can be accomplished either with a shorting stub attached to the output of a single shock line or by combining the output of two shocklines

of opposite polarity. In either case the output power level can at best be 1/2 the input power level.

In summary electromagnetic shock lines provide a mechanism for shaping a long pulse into a much shorter pulse but do not increase the peak power level. The frequency content of these pulses can be increased at high frequencies by decreasing the rise and fall time of the pulse. The low frequency spectrum can be tailored by adjusting the overall pulse length. In order to make effective use of this technology, a pulse of the desired output power level must be supplied to the line by an appropriate pulse generator. The closer the appearance of the input pulse to the desired output pulse, the more efficient the overall process will be. In practice we employ advanced nonlinear magnetic pulse compression technology to produce as short an input pulse as can be efficiently produced ( $\approx 2$  nsec duration). We then employ electromagnetic shock lines in order to reduce the risetime to less than 200 psecs. The first experiments have concentrated on producing output pulses with these extremely short risetimes at moderate power levels ( $\approx 1$  Gigawatt). Combining these short risetime pulses to produce a short duration pulse will reduce this output power level to of order 1/2 Gigawatt. Output powers of this level do not represent the limit of this technology by any means, but these parameters were chosen as a reasonable operating regime for a cost effective, first proof-of-principle experiment.

### 1.1 Theory of Electromagnetic Shock Lines

Later in this report we will discuss the loss mechanisms in ferrite and document the increasing losses with increasing  $dB/dt$ . We will find that at very short saturation times, the time dependent loss mechanism can best be described by

$$\frac{dM}{dt} \approx \lambda H \left( 1 - \frac{M^2}{M_0^2} \right) \quad (1)$$

where  $M_0/\lambda$  is known as the switching coefficient. This time dependent loss mechanism limits the minimum pulse length efficiently achievable through nonlinear magnetic pulse compression to approximately 1 nanosecond. It also limits the minimum risetime achievable with an electromagnetic shock line but, rather than 1 nanosecond, this limit will be proven to be less than 30 picoseconds.

We begin our analyses by examining the fields at the shock head, paying close attention to the dispersive properties of the ferrite. Although shock lines can be constructed which make use of other nonlinear media such as ferroelectric materials, here we will confine our attention to shock lines which employ the nonlinear behavior of ferrite.

The applied field in a coaxial transmission line is given as

$$H(\text{oersteads}) = \frac{2I(\text{statamps})}{cr} = \frac{0.4I(\text{amperes})}{d} \quad (2)$$

The magnetic induction is given by

$$B = \mu_0 H + 4\pi M \quad (3)$$

and we will define the relative permeability at the shock head as

$$\mu_{sh} = 1 + \frac{4\pi M}{H} = 1 + \frac{8kM_0}{H} \quad (4)$$

where

$$k = \frac{\pi(S_f - S_i)H}{L_0 I} \quad (5)$$

Here  $S_f$  is the ferrite cross-section per unit length of the line,  $S_i$  is the cross-section per unit length of the ferrite which is already saturated in the direction of the wave field, and  $L_0$  is the inductance per unit length of the line with the ferrite saturated.

Behind the shock head  $S_i = S_f$  and  $\mu_{sh} = 1$ . In this case the velocity of electromagnetic radiation in the line is given by

$$v_0 = \frac{1}{(L_0 C_0)^{1/2}} \quad (6)$$

where  $C_0$  is the capacitance per unit length. The velocity of the shock head is given by

$$v_{sh} = \frac{v_0}{\mu_{sh}^{1/2}} \quad (7)$$

The impedance of the line at the shock head is given by

$$Z_{sh} = V_{sh}/I_{sh} = Z_0 \cdot \mu_{sh}^{1/2} \quad (8)$$

where  $Z_0 = (L_0/C_0)^{1/2}$  is the impedance of the fully saturated line behind the shock head.

At the shock head the electromagnetic energy per unit length is given by

$$E_0 = 1/2C_0 V_{sh}^2 + 1/2L_0 I_{sh}^2 \quad (9)$$

and therefore the energy dissipated per unit length of the line in forming the shock head is given by

$$E_{lost} = 1/2L_0 I_{sh}^2 (\mu_{sh} - 1) \quad (10)$$

Some of this energy is dissipated in the ferrite and the remainder is reflected back toward the input of the pulsed power source. It is important to note that so long as  $\mu_{sh} > 1$ , the body of the pulse travels faster than the head. The pulse is constantly being eaten away at the leading edge as illustrated in Fig. 1.1.

The current ( $I_{sh}$ ) at the front of the shock head must be sufficient to charge the capacitance of the line to the shock head voltage ( $V_{sh}$ ) at a rate corresponding to the velocity of propagation, i.e.

$$I_{sh} = v_{sh} \cdot C_0 V_{sh} \quad (11)$$

Also, from Faraday's Law

$$V_{sh} = v_{sh} \left( \frac{\Phi_f}{l} - \frac{\Phi_i}{l} \right) \quad (12)$$

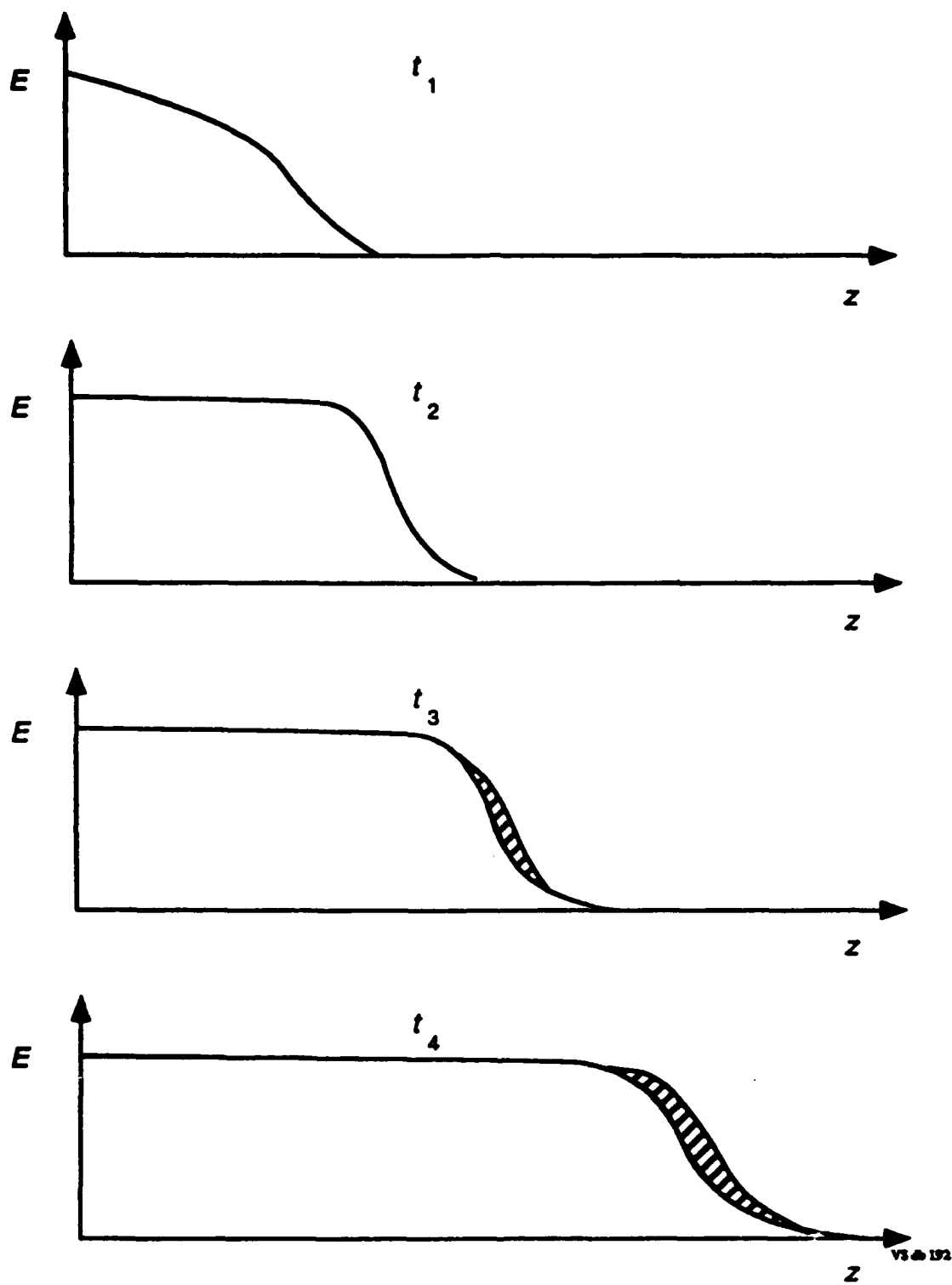


**Figure 1.1:** Mechanism by which a shock wave is set up owing to the nonlinear nature of the permeability and/or permittivity of a medium

where  $\Phi_i/l$  and  $\Phi_f/l$  are equal to  $\frac{\int B \cdot da}{l}$  before and after the passage of the shock wave. At any point along the line,

$$\frac{\Phi}{l} = L_0 I - 4\pi [S_f \cdot M - S_i \cdot (M - M_0)] \quad (13)$$

Combining Eqs. 11 and 12 for any position along the shock head we find

$$I_{sh} = V_{sh}^2 C_0 \left( \frac{\Phi}{l} - \frac{\Phi_i}{l} \right) \quad (14)$$

where  $\Phi_i/l$  can be written as

$$\frac{\Phi_i}{l} = -4\pi(2S_i - S_f)M_0 \quad (15)$$

if the line has been fully reset in front of the shock head. Combining Eqs. 13 and 15

$$\frac{\Phi}{l} - \frac{\Phi_i}{l} = L_0 I - 4\pi(S_f - S_i)(M_0 + M) \quad (16)$$

and

$$I = v_{sh}^2 C_0 [L_0 I - 4\pi(S_f - S_i)(M_0 + M)] \quad (17)$$

Substituting  $C_0 L_0 = 1/v_0^2$  yields

$$I = \left( \frac{v_{sh}}{v_0} \right)^2 I - v_{sh}^2 C_0 (S_f - S_i)(M_0 + M) \quad (18)$$

or

$$I = \frac{4\pi}{(1 - (\frac{v_{sh}}{v_0})^2)} (S_f - S_i) v_{sh}^2 C_0 (M_0 + M) \quad (19)$$

Now remembering that

$$\frac{dM}{dt} \approx \lambda H \left[ 1 - \left( \frac{M}{M_0} \right)^2 \right]$$

and following Katayev by introducing the variable

$$y = \arctan(M/M_0) \quad (20)$$

and using Eqs. 2,6,7,8, and 19, we find

$$\frac{dy}{dt} = \frac{\lambda H_0}{M_0} \frac{1}{1 + e^{-2y}} \quad (21)$$

Integration yields

$$y - \frac{1}{2}e^{-2y} = \frac{\lambda H_0}{M_0} t \quad (22)$$

and

$$I = \frac{M_0 I_0}{H_0 \lambda} \frac{dy}{dt} \quad (23)$$

from which it can be shown that

$$I = \frac{I_0}{1 + e^{-2y}} \quad (24)$$

The graph of  $I(t)$  provided in Fig. 1.2 indicates that the risetime of  $I(t)$  from a level of  $0.1I_0$  to  $0.9I_0$  is given by

$$\tau_{sh} = \frac{6.7M_0}{\lambda H_0} \quad (25)$$

where once again  $H_0$  is the peak of the magnetic field and  $M_0/\lambda$  is the switching coefficient.

The coefficient  $\lambda$  is sometimes known as the relaxation frequency and has units of  $\text{sec}^{-1}$ . It is determined by the crystal structure and is essentially constant for all cubic ferrites. It can best be understood as the frequency at which  $\bar{\mu}_r - 1$  goes to unity, where  $\bar{\mu}_r$  is defined as

$$\bar{\mu}_r = 1 + \frac{4\pi M_0}{H} \quad (26)$$

If we write  $H_0 = \alpha H_{max}$  where  $H_{max} = \frac{4\pi M_0}{\mu_0}$  is defined as the magnetic field required to saturate the ferrite when  $\bar{\mu}_r = 2$ , then we can rewrite Eq. 25 in an approximate form as

$$\tau_{sh} = \frac{6.7(\bar{\mu}_r - 1)}{\alpha 4\pi \lambda} \approx \frac{1}{2\alpha \lambda} \quad (27)$$

Equation 27 imparts intuitive insight into our expression for  $\tau_{sh}$ . It can quite simply be interpreted as saying that when the spins are flipped at the relaxation frequency, the relative permeability begins to approach unity. Once the relative permeability goes to unity, the velocity of the shock head equals the main body of the pulse and the shock line can no longer function. An approximate form of Eq. 25 could have been intuitively derived simply on the basis of this interpretation and the more rigorous analyses avoided. The value of this relaxation frequency is the same for all Zn-Ni ferrites and is approximately given by

$$\lambda \approx 1.12 \cdot 10^{10} \text{ Hz.}$$

while

$$M_0 \approx 200 \text{ gauss}$$

We see from Eq. 25 that the risetime at the head of the shock wave depends only on the switching coefficient of the ferrite and the peak magnetic field. In theory this magnetic field could be raised to an arbitrary level at a given current by reducing the diameter of the shock line. A decrease in shock line diameter by a factor  $\alpha$  would result in a risetime reduction by the same factor. In practice this can only be continued until the electric fields generated in the ferrite exceed the breakdown strength of the ferrite. If we simply filled a coaxial line with ferrite and kept the electric field a factor of two below the breakdown strength of the ferrite, we would find that the minimum risetime would be of order 200 psecs. If, however, we surrounded the ferrite with a low permittivity material with a much higher breakdown strength than the ferrite itself (e.g. oil or fluorinert), the electric field in the ferrite corresponding to a given magnetic field is substantially reduced and risetimes shorter than 30 psec are achievable.

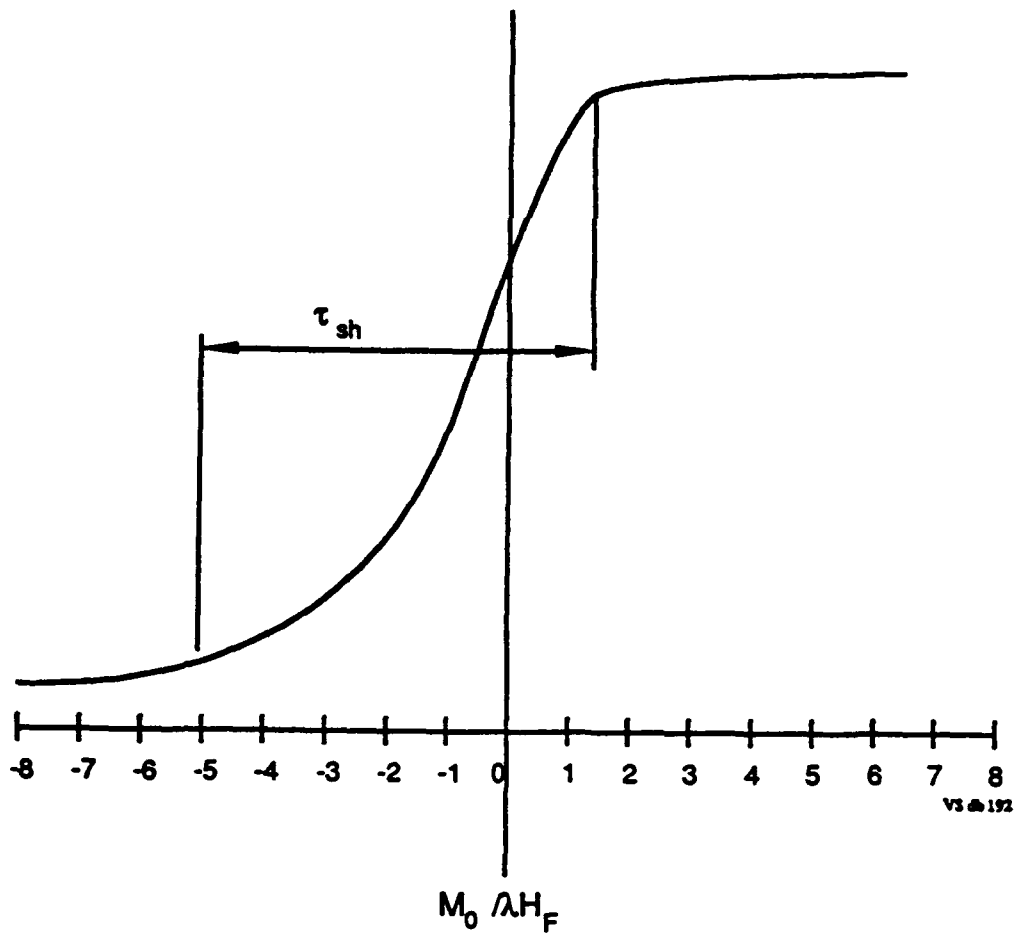


Figure 1.2: Structure of the front of a shock wave

The required length of the ferrite shock line depends only on the initial pulse risetime and  $\mu_{sh}$  since the velocity of the shock head was shown to be simply given as  $v_{sh} = v_0/\mu_{sh}^{1/2}$ . Therefore the required line length in terms of the initial pulse risetime  $\tau_{int}$  is simply

$$\text{Length} = \frac{\tau_{int} v_0}{\mu_{sh}^{1/2} - 1} \quad (26)$$

In this section we have discussed the basic fundamentals of ferrite shock line operation. In the following section we will attempt to derive detailed design criteria.

## 1.2 Detailed Design of a Ferrite Shock Line

In the preceding section we arrived at an expression for the risetime at the shock head which depended inversely in the peak magnetic field in the wave. This field was limited by the geometry of the line and the breakdown electric field in the ferrite. Filling the outer sections of the line with low permittivity materials was suggested as a means for increasing the magnetic field without increasing the electric field in the ferrite. The shock line pictured in Fig. 1.3 illustrates this design concept.

The impedance of the line in Fig. 1.3 is given by

$$\rho_0 = \frac{60}{\epsilon_{eff}^{1/2}} \cdot \ln \frac{D}{a} \quad (1)$$

once the ferrite is saturated in the direction of the wave field.  $\epsilon_{eff}$  is given by

$$\epsilon_{eff} = \frac{\epsilon_D \epsilon_F \ln \frac{D}{a}}{\epsilon_D \ln \frac{d}{a} + \epsilon_F \ln \frac{D}{d}} \quad (2)$$

where  $\epsilon_D$  and  $\epsilon_F$  are the permittivities of the dielectric and ferrite layers respectively.

The electric field in the ferrite is given by

$$E = \frac{V_{sh}}{a} \frac{\epsilon_D}{\epsilon_D \ln \frac{d}{a} + \epsilon_F \ln \frac{D}{d}} \quad (3)$$

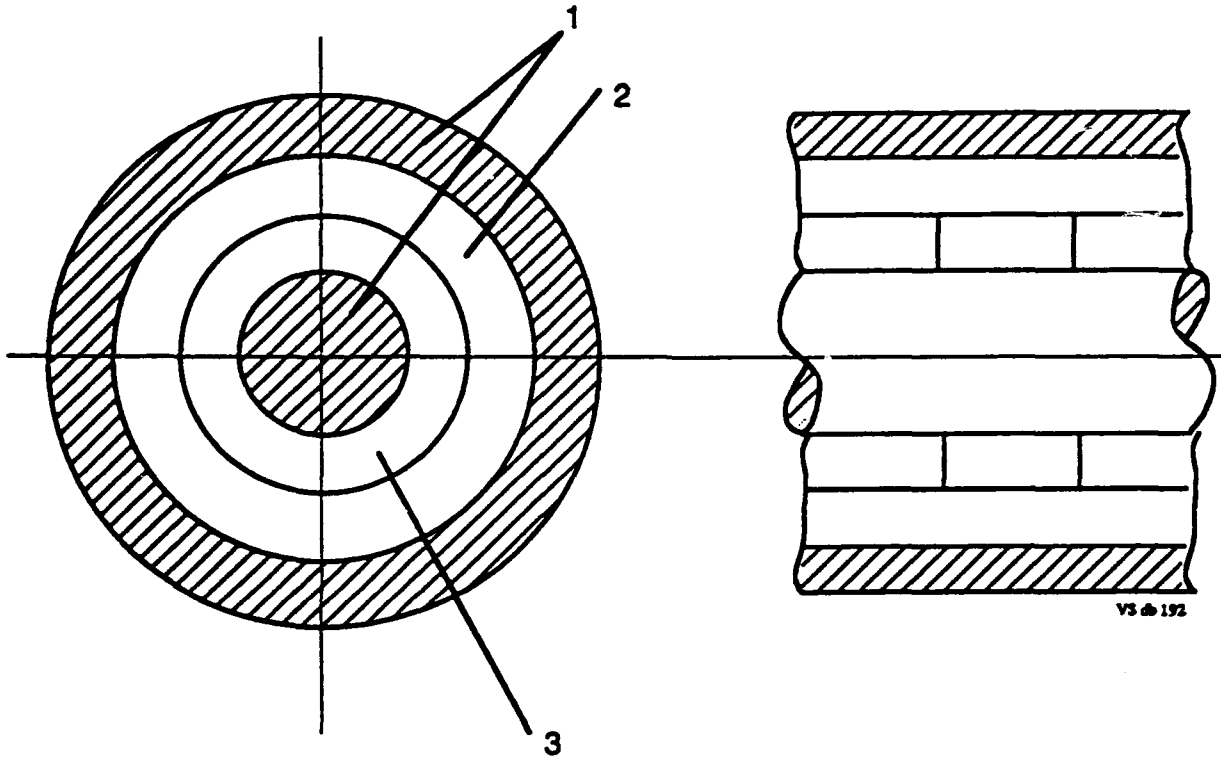
This electric field is constrained to be less than  $E_F$  where  $E_F$  is defined as 1/2 the breakdown electric field strength of the ferrite ( $E_F \approx 10^5 V/cm$ ).

Let  $H_F$  be defined as the magnetic field in the ferrite when  $E = E_F$ .

$$H_F = \frac{0.4 I_{sh}}{a} \quad (4)$$

At the shock head, the relative permeability of the ferrite is given by  $\mu_{sh}$  and the impedance of the line is therefore given by

$$\rho_{sh} = \frac{60}{\epsilon_F^{1/2}} \frac{T_F}{\sigma} \left( 1 + \frac{8\pi M_0}{H_F} \sigma \right)^{1/2} \cdot \left[ \left( 1 - \frac{\epsilon_F}{\epsilon_D} \right) \sigma + \frac{\epsilon_F}{\epsilon_D} \right]^{1/2} \quad (5)$$



- 1 - Internal and external conductors
- 2 - Dielectric layer
- 3 - Ferrite layer consisting of rings  
threaded over the inner conductor

Figure 1.3: Coaxial pulse shaping line

where  $T_F = \ln \frac{d}{a}$ ,  $T_D = \ln \frac{D}{a}$  and  $\sigma = \frac{T_F}{T_F + T_D}$

At the limit of the ferrite dielectric strength,  $E = E_F$

$$H_F = 0.4 \frac{T_F}{\sigma} \left[ \frac{\epsilon_F}{\epsilon_D} + \left( 1 - \frac{\epsilon_F}{\epsilon_D} \sigma \right) \right] \frac{E_F}{\rho_{sh}} \quad (6)$$

or

$$H_F = 4\pi M_0 \sigma \left[ \left( 1 + 2.8 \cdot 10^{-6} \epsilon_F \left( \frac{E_F}{\pi M_0 \sigma} \right)^2 \left( \frac{\epsilon_F}{\epsilon_D} + \left( 1 - \frac{\epsilon_F}{\epsilon_D} \right) \sigma \right) \right)^{1/2} - 1 \right] \quad (7)$$

We will assume the use of a ZnNi ferrite for which  $d/a=4/3$ ,  $\epsilon_F = 14$ ,  $E_F = 10^5$  V/cm, and  $M_0 = 200$  gauss. We will use mineral oil as the second dielectric with  $\epsilon_D = 2.7$ . We can then rewrite Eqs. 5 and 7 as

$$\frac{H_F}{4\pi M_0} = \sigma \left( \left( 1 + \frac{1}{\sigma^2} (5.185 - 4.185\sigma) \right)^{1/2} - 1 \right) \quad (8)$$

and

$$\rho_{sh} = \frac{4.602}{\sigma} \left[ 1 + 2\sigma \left( \frac{4\pi M_0}{H_F} \right) \right]^{1/2} (5.185 - 4.185\sigma)^{1/2} \quad (9)$$

A plot of  $H_F/4\pi M_0$  versus  $\sigma$  is provided in Fig. 1.4 while  $\rho_0$  and  $\rho_{sh}$  are plotted as a function of  $\sigma$  in Fig. 1.5. In Fig. 1.6 we plot  $\tau_{sh}$  as a function of  $\sigma$  based on a relaxation frequency  $\lambda = 1.12 \cdot 10^{10}$  Hz. The minimum shock head risetime varies from 115 picoseconds with  $\sigma = 1$  (the shock line completely full of ferrite) to 21 picoseconds as  $\sigma$  approaches 0 (most of the line filled with oil).

The value for  $\mu_{sh}$  is simply given by

$$\mu_{sh} = \frac{\rho_{sh}}{\rho_0} \quad (10)$$

At the interface between the saturated and unsaturated sections of the line there is an impedance mismatch given by  $\rho_{sh}/\rho_0$  and this mismatch causes the reflection of some of the energy. It is easy to show that

$$\frac{I_0}{I_{sh}} = \frac{1}{2} \left( 1 + \frac{\rho_{sh}}{\rho_0} \right) \quad (11)$$

$$\frac{V_0}{V_{sh}} = \frac{1}{2} \left( 1 + \frac{\rho_0}{\rho_{sh}} \right) \quad (12)$$

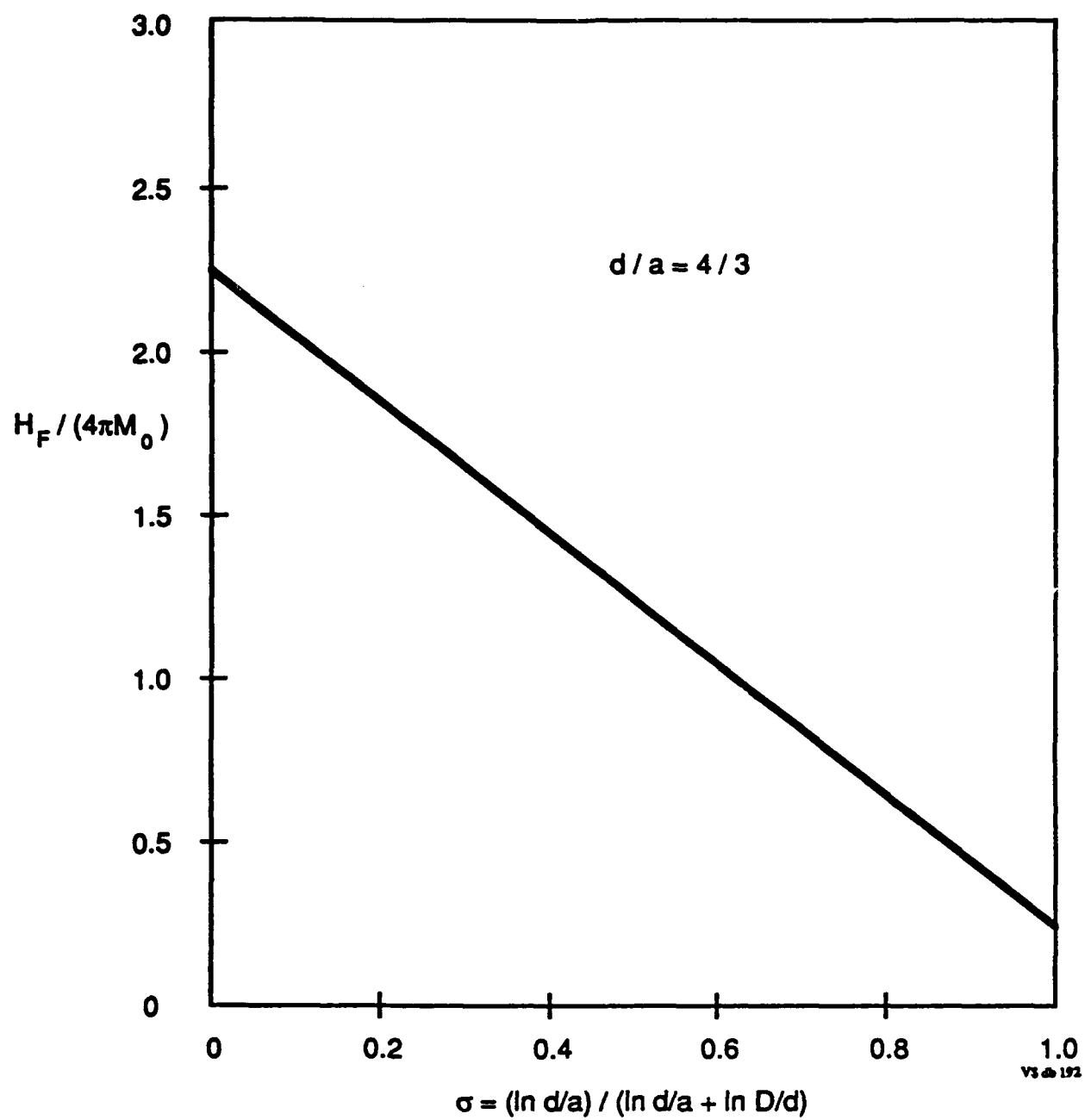
and therefore

$$\frac{Power_{in}}{Power_{out}} = \frac{1}{4} \left( 1 + \frac{\rho_{sh}}{\rho_0} \right) \left( 1 + \frac{\rho_0}{\rho_{sh}} \right) \quad (13)$$

The outer diameter of the line is simply given by

$$\ln \frac{D}{d} = \left( \frac{1}{\sigma} - 1 \right) \ln \frac{d}{a} \quad (14)$$

where we assigned a value of 4/3 to  $d/a$  and the value for  $a$  is determined from the expression  $H_F = 0.4I_{sh}/a$ .



$$\sigma = (\ln d/a) / (\ln d/a + \ln D/d)$$

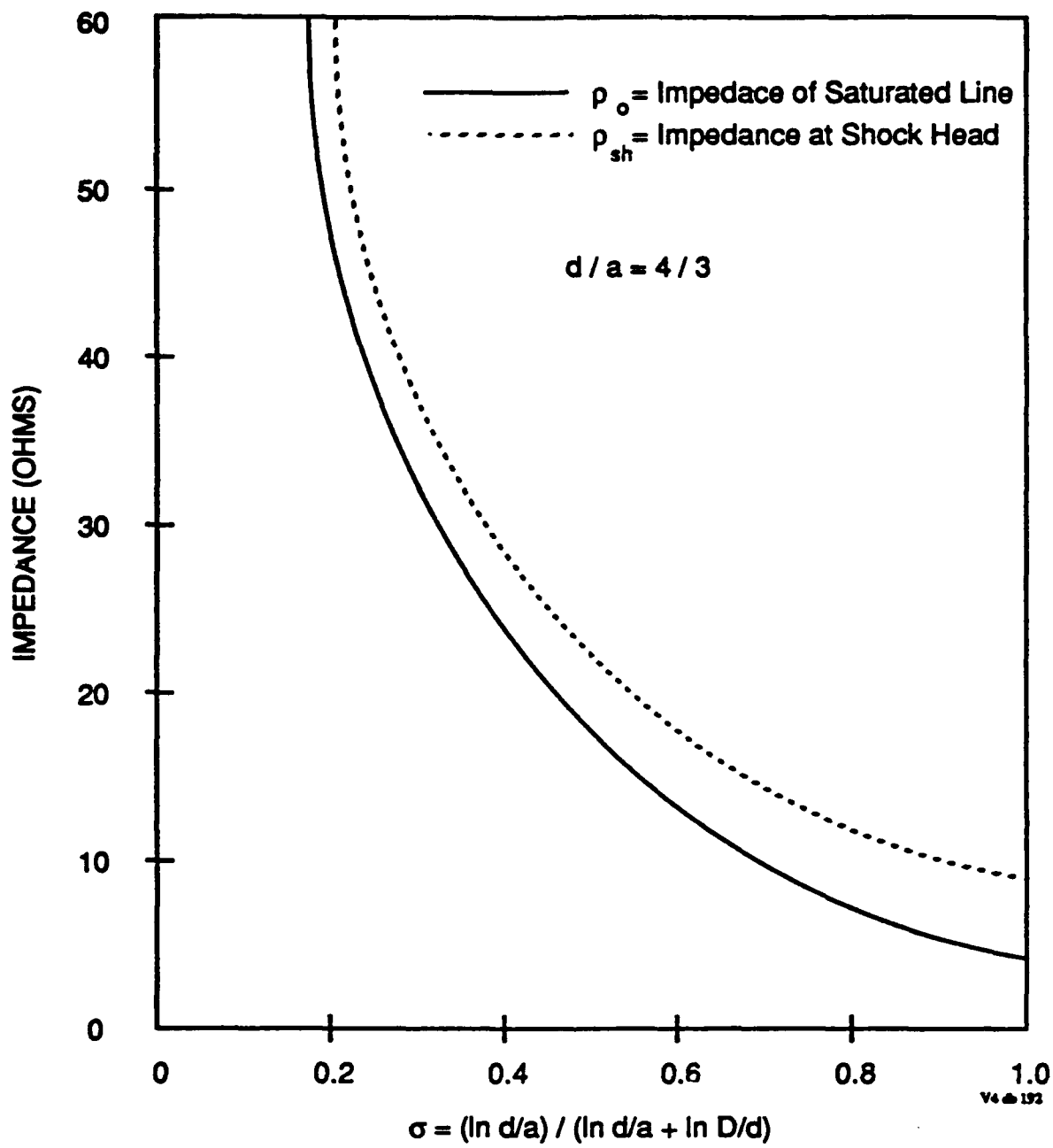
d = Ferrite Outer Diameter

a = Line Inner Diameter

D = Line Outer Diameter

$$\epsilon_F = 14, \epsilon_D = 2.7, E_F = 10^5 \text{ V/cm}, \text{ and } M_0 = 200 \text{ gauss}$$

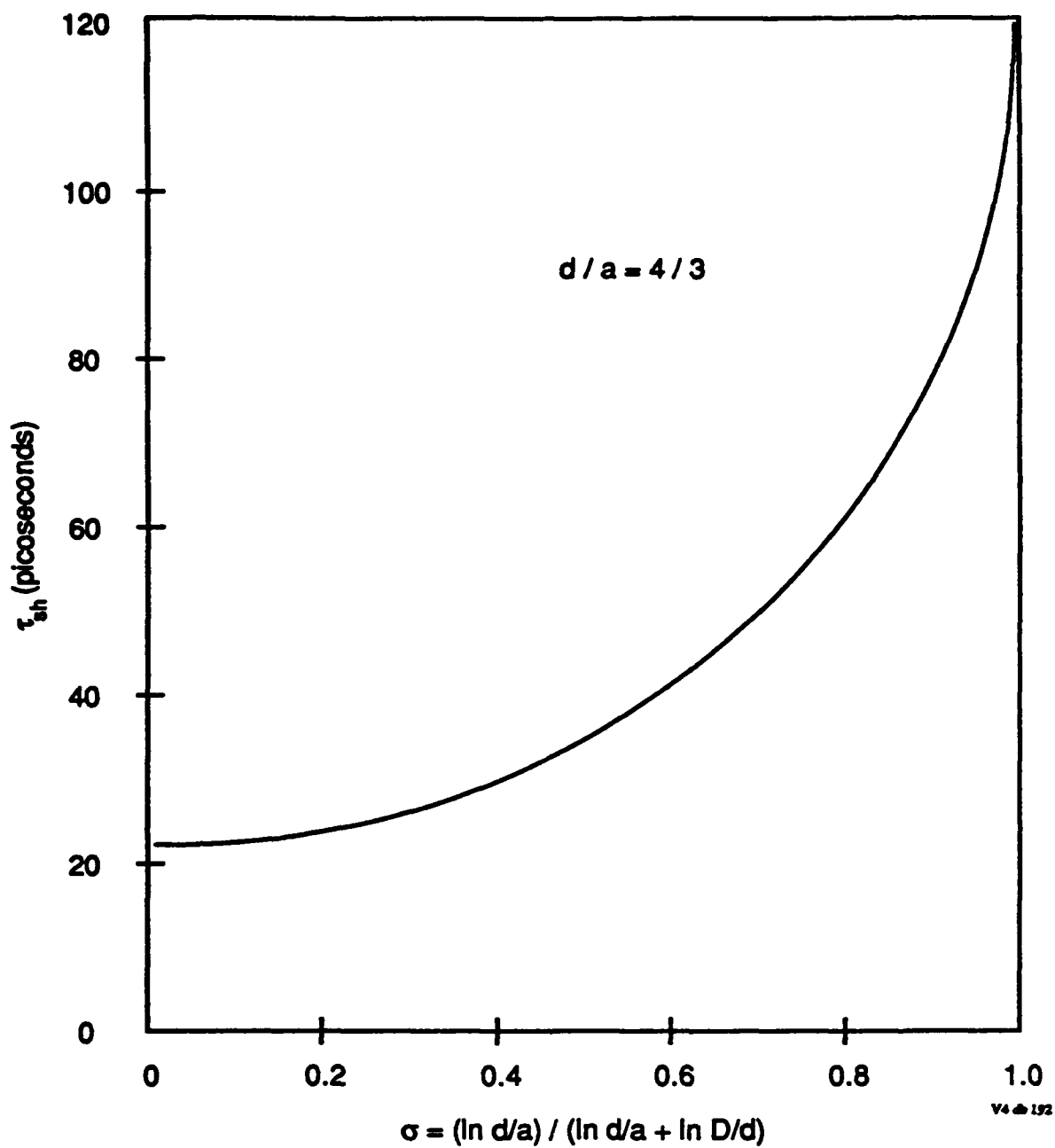
Figure 1.4:  $H_F / (4\pi M_0)$  versus  $\sigma$



$d$  = Ferrite Outer Diameter  
 $a$  = Line Inner Diameter  
 $D$  = Line Outer Diameter

$\epsilon_F = 14$ ,  $\epsilon_D = 2.7$ ,  $E_F = 10^5$  V/cm, and  $M_0 = 200$  gauss

Figure 1.5: Shock line impedance versus  $\sigma$



$d$  = Ferrite Outer Diameter  
 $a$  = Line Inner Diameter  
 $D$  = Line Outer Diameter

$\epsilon_F = 14$ ,  $\epsilon_D = 2.7$ ,  $E_F = 10^5$  V/cm, and  $M_0 = 200$  gauss

Figure 1.6: Risetime of output pulse versus  $\sigma$

In this section we have derived the basic design rules. In the following section we will discuss the specific design used in our first experiment.

### 1.3 SNOMAD-V Shock Line Design

Based on the preceding analyses, we were now in a position to design a shock line matched to the SNOMAD-V pulser. We will assume  $\sigma = 0.4$  which according to Fig. 1.5 yields a  $\rho_0 = 21.55\Omega$  and  $\rho_{sh} = 26.64\Omega$ .

Attaching 4 parallel lines with this impedance to the output of SNOMAD-V driver provides an excellent impedance match. With these parameters we can expect an output risetime of  $\approx 30$  picoseconds into 4 parallel  $27\Omega$  loads or 8 parallel  $54\Omega$  loads as will be the case here. At the nominal 150 kV output voltage of SNOMAD-V, each line will be driven with  $I_0 \approx 7kA$ . From Eq. 11 we find  $I_{sh} \approx 6.26kA$ . The output voltage from the shock lines will be  $\approx 165$  kV and the output power is approximately equal to the input power.

Referring to Fig. 1.4 we see that  $H_F/4\pi M_0 = 1.516$  and since  $M_0 = 200$  gauss,  $H_F = 3,810$  Oersteads. Remembering that  $H_F = 0.4I_{sh}/a$ , we find  $a \approx 0.66cm$  and since  $d/a=4/3$   $d \approx 0.88cm$ . From Eq. 14 we find that the outer diameter of the line is 1.355 cm, and returning to Eq. 2 we find the  $\epsilon_{eff} \approx 4$  and therefore  $v_0 = c/2$ . The required length of each shock line to erode a 1.35 nsec input risetime away is  $\approx 86cm$ .

The experiments proved that the electric field stress levels were too high for reliable operation at 10 kHz PRF. We modified the design in such a way that H was reduced to of order 1,000 Oersteads with a comparable reduction in the electric fields. The output risetime rose to  $\approx 150$  picoseconds which is close to the predicted value. More information on the present state of the art in electromagnetic shock line sources is presented in the main body of the report.

### 1.4 Creating a Rectangular Pulse

A ferrite shock line by itself will not produce a rectangular pulse; instead, it produces a pulse with a very fast risetime. In order to produce a rectangular pulse, two equal amplitude pulses with opposite polarities must be formed and recombined with the desired temporal shift (Fig. 1.7).

One mechanism for accomplishing this is to use a shorting stub arranged as shown in Fig. 1.8. In this figure, Line II which is short-circuited at the far end is chosen to have an electrical length one half the duration of the desired output pulse. Line I represents the electromagnetic shock line from which the wavefront-steepened pulse emerges and Line III is the transmission line connected to the load. The impedances are chosen so that half of the pulse energy emerging from Line I travels directly to the load and the other half travels down Line II reflecting with opposite polarity from the short at the far end and canceling the wave in Line II when it arrives back at the junction. In order to avoid losing more than half of the pulse energy, Line II can be ferrite loaded so that it initially appears as a much higher impedance.

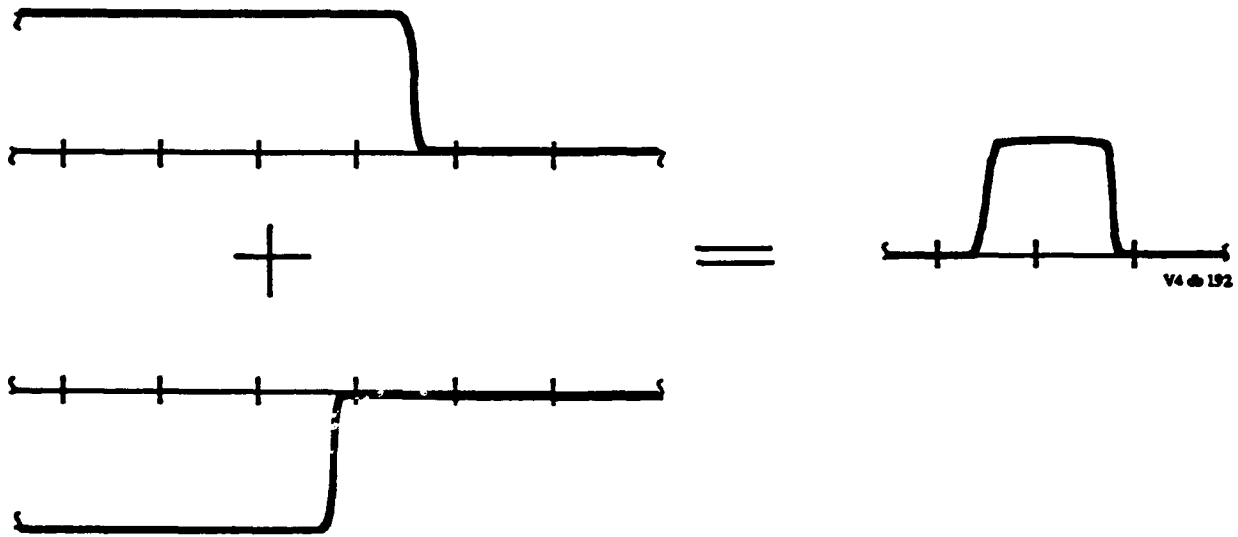
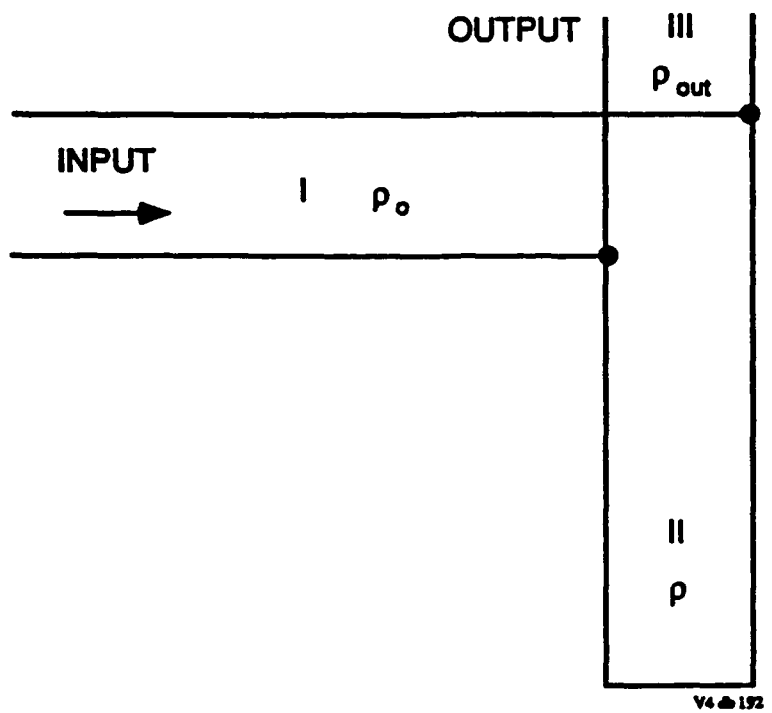


Figure 1.7: Technique for forming a rectangular pulse



V4 192

- I - Shaping line
- II - Short circuited section of transmission line
- III - Transmission line leading to the load

**Figure 1.8 :** System for shaping a rectangular pulse by a short-circuited section of transmission line

## APPENDIX 2

### NONLINEAR MAGNETIC MATERIAL SELECTION

It is important to understand when it is advantageous to use ferrite rather than metglass or Ni-Fe tapes. In this section we will compare the attributes of ferrites with those of metglass and Ni-Fe tapes. The first stage compression reactor step-up transformer and (sometimes) the second stage compression reactor are designed around metglass cores. This is the last stage in the compression chain where metglass can be employed if efficiency is an important consideration. Metglass is composed of a mixture of silicon and iron which is mixed while liquefied and then rapidly quenched so that it remains amorphous. The resistivity of this alloy is three times that of most ferro-magnetic materials. However, at saturation times much less than  $10^{-6}$  seconds, the losses begin to scale inversely with the saturation time as eddy currents become the dominant loss mechanism (see Fig. 2.1).

The figures in this section can either be found in the contract #140 final report or are included with this report.

Metglass, a mixture of silicon and steel possesses the magnetic properties of steel (i.e.  $\Delta B \sim 36$  kg,  $H_c \sim 0.05$  Oe,  $\mu_r \approx 10,000$ ) but affords much higher resistivities ( $\rho \sim 130 \mu\Omega\text{-cm}$ ) because of its glass-containing atomic structure. Unfortunately it has a rough surface texture resulting in inherent packing factors of only 0.8 and the addition of interlaminar insulation further reduces this to  $\sim 0.7$  in a wound core. Interlaminar insulation can be avoided if the material can be vapor deposited with a very thin layer of MgO or SiO<sub>2</sub>. The inherent 0.8 packing factor associated with roughness can be improved upon by hot rolling the metglass. These techniques are aimed at the objective of achieving an overall packing factor of 0.8.

Even with a packing factor of only 0.7 (compared to almost unity with ferrite), when the inherent  $\Delta B_s \leq 3.1$  Tesla of metglass is compared to  $\Delta B_s \leq 0.65$  Tesla of Zn<sub>.60</sub> Ni<sub>.40</sub> ferrite (core volume depends inversely on  $\Delta B_s$ <sup>2</sup>), metglass is preferred when eddy current losses are not a problem. As the saturation times get shorter and eddy current losses increase, removing the waste heat from the interlaminar core structure becomes very difficult. Manganese zinc ferrites would seem a logical choice to span the gap between metglass and Zn<sub>.60</sub> Ni<sub>.40</sub> ferrite, but geometric resonances encountered in the large cores required at this pulse energy eliminate it from consideration. Other iron alloys such as 50-50 Ni-Fe have been tested but suffer from the same heat removal problems as metglass. The higher conductivity of these alloys requires them to be thinner and this results in a greater expense and a lower net packing factor. It is hoped that advances in coating technology will improve the situation in the future.

The time dependent losses in ferro-magnetic ribbons are typically explained in terms of a saturation wave which encircles the tape and proceeds toward the center at a rate which is linearly dependent on the applied voltage. Ignoring the fact that domain wall locations are initially pinned to impurity sites, the H-field required to change the state of magnetization of a

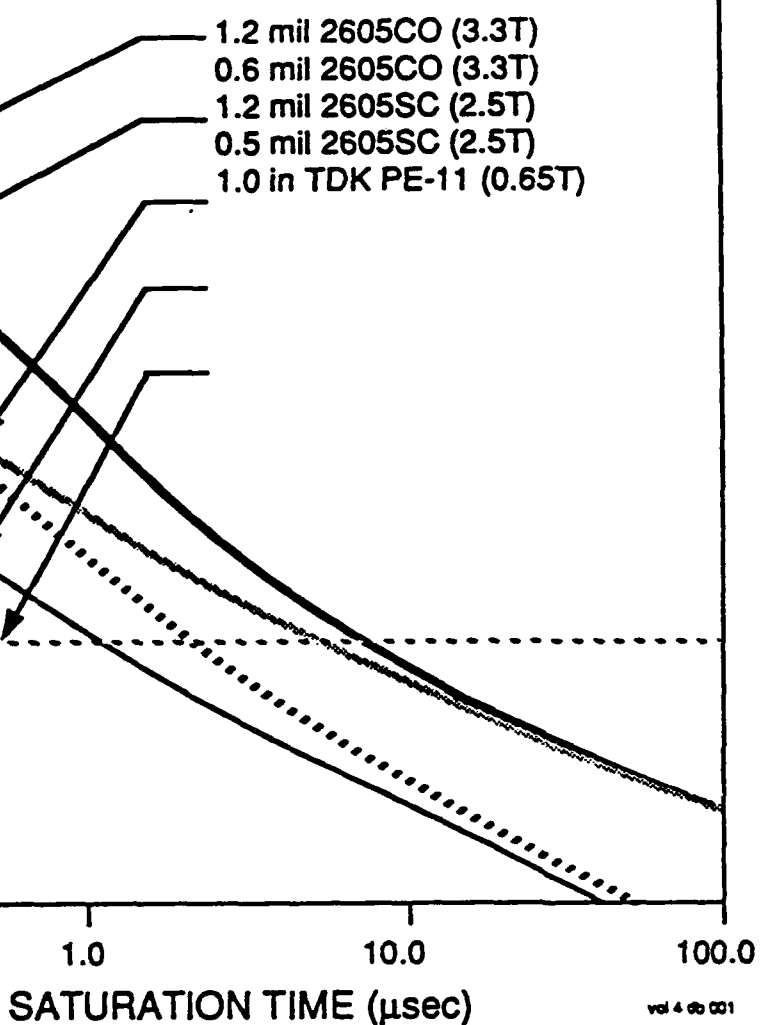


Figure 2.1: Estimated core loss versus saturation time

1, d is the sample  
 during saturation is

preferred domain  
 dependent losses  
 create a much more  
 segmented by graphs

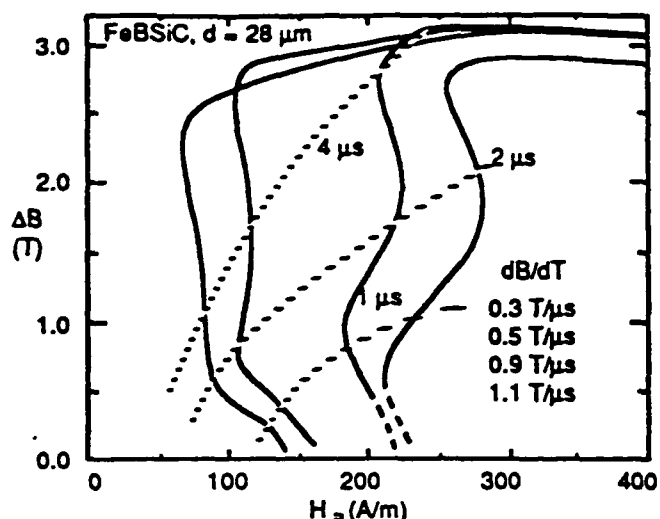
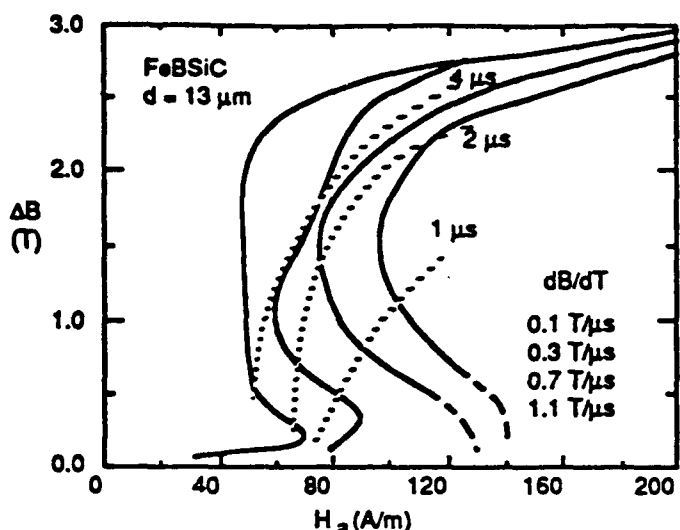
ice normalized by  
 es and then ferrite

erial choice. The  
 es for adequately  
 d metglass is the  
 with  $\geq 100$  nsec

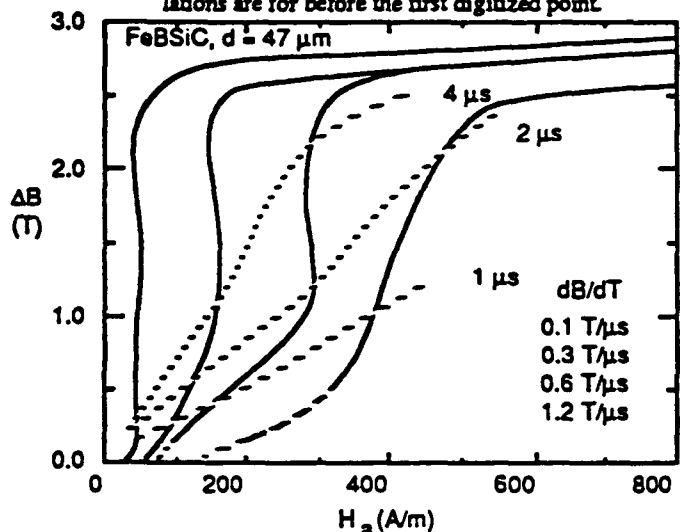
ed in Fig.s 2.3 -  
 tions driven from  
 from 5.0  $\mu$ secs. to  
 iceable. It should  
 ectly proportional  
 tglass tapes with

nted in Figs. 2.9  
 1 more consistent  
 . Ni-Fe tapes are

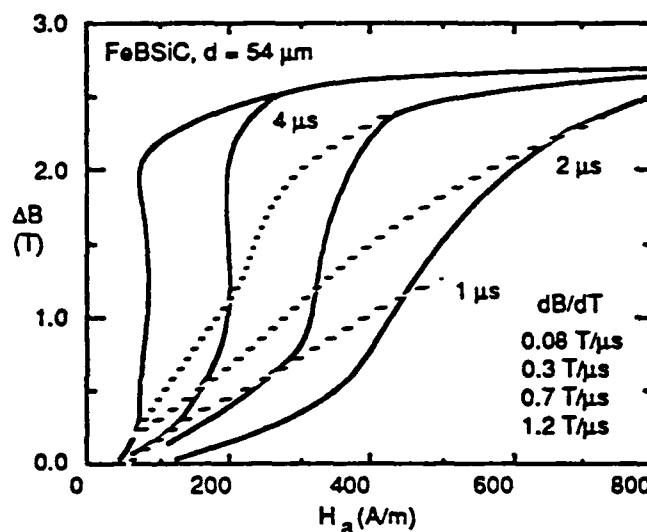
e analogy to the  
 s an electrically-  
 ure similar to the  
 n the electron in  
 nponents consist  
 oles which make  
 the alignment of



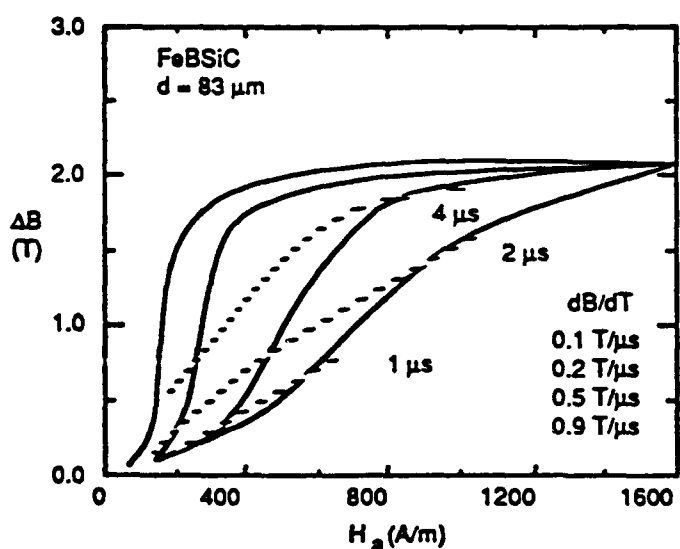
Dynamic magnetization and pulse permeability curves for 13  $\mu\text{m}$  FeBSiC ribbon. Dashed extrapolations are for before the first digitized point.



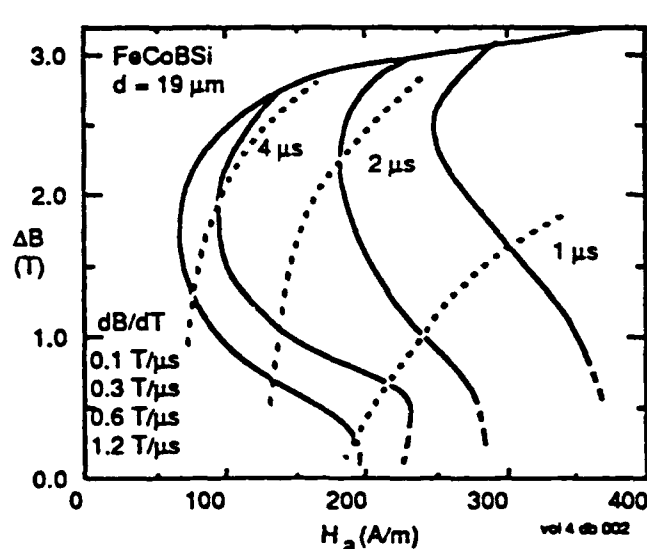
Dynamic magnetization and pulse permeability curves for 47  $\mu\text{m}$  FeBSiC ribbon.



Dynamic magnetization and pulse permeability curves for 54  $\mu\text{m}$  FeBSiC ribbon.



Dynamic magnetization and pulse permeability curves for 83  $\mu\text{m}$  FeBSiC ribbon.



Dynamic magnetization and pulse permeability curves for 19  $\mu\text{m}$  FeCoBSi ribbon.

Figure 2.2: Time dependent ferrite loss measurements

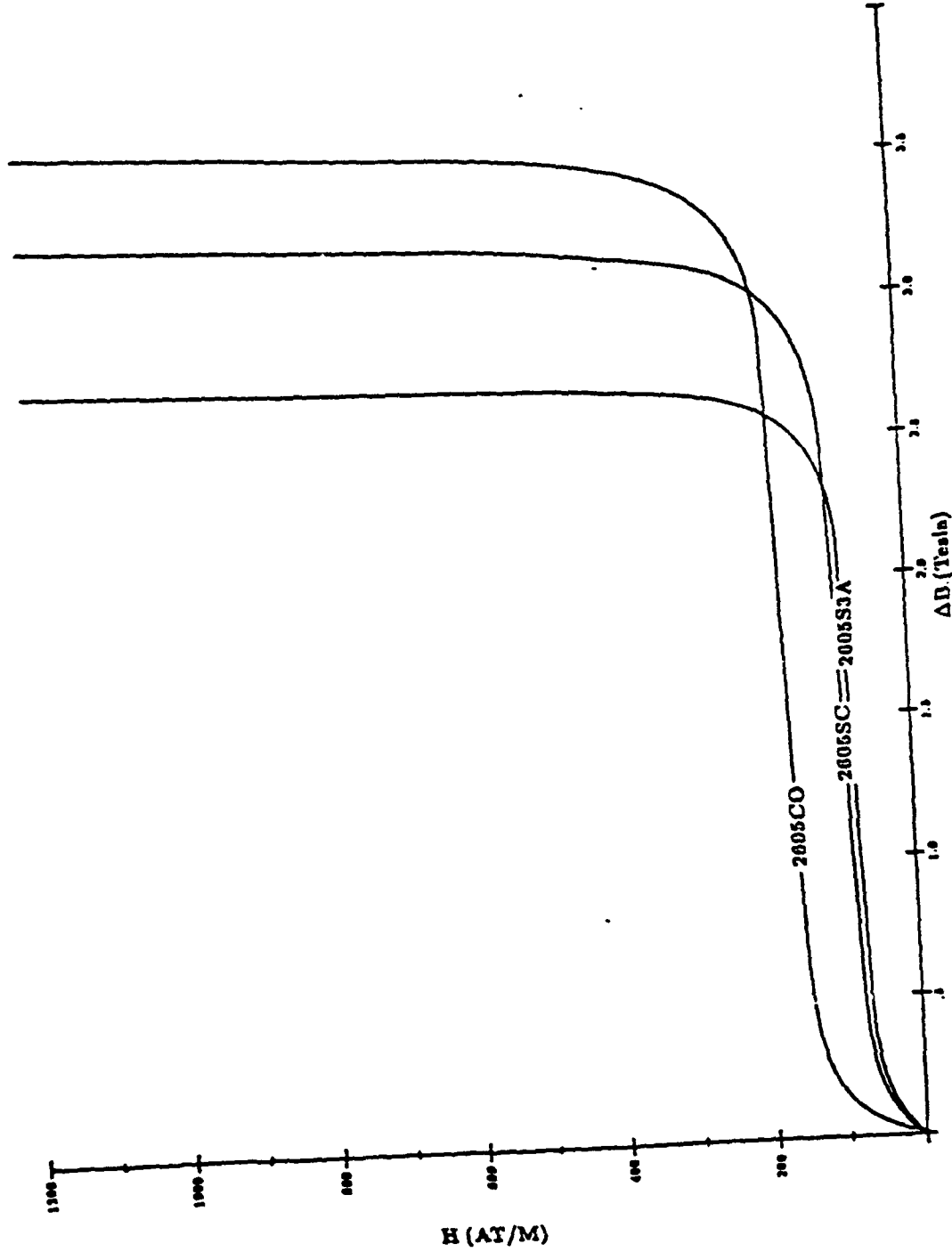


Figure 2.3: 5.0  $\mu$ sec Saturation Time

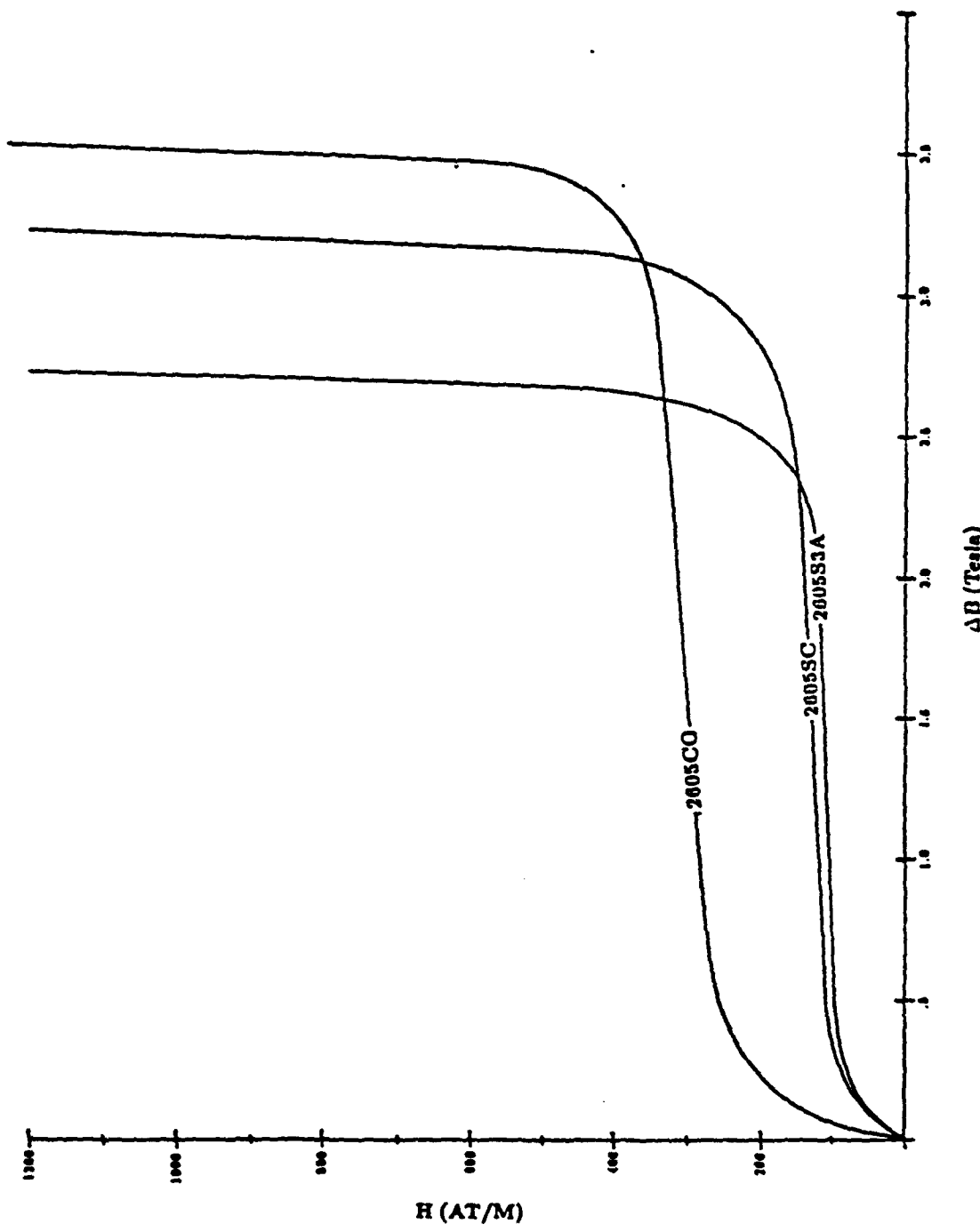


Figure 2.4: 3.0  $\mu$ sec Saturation Time

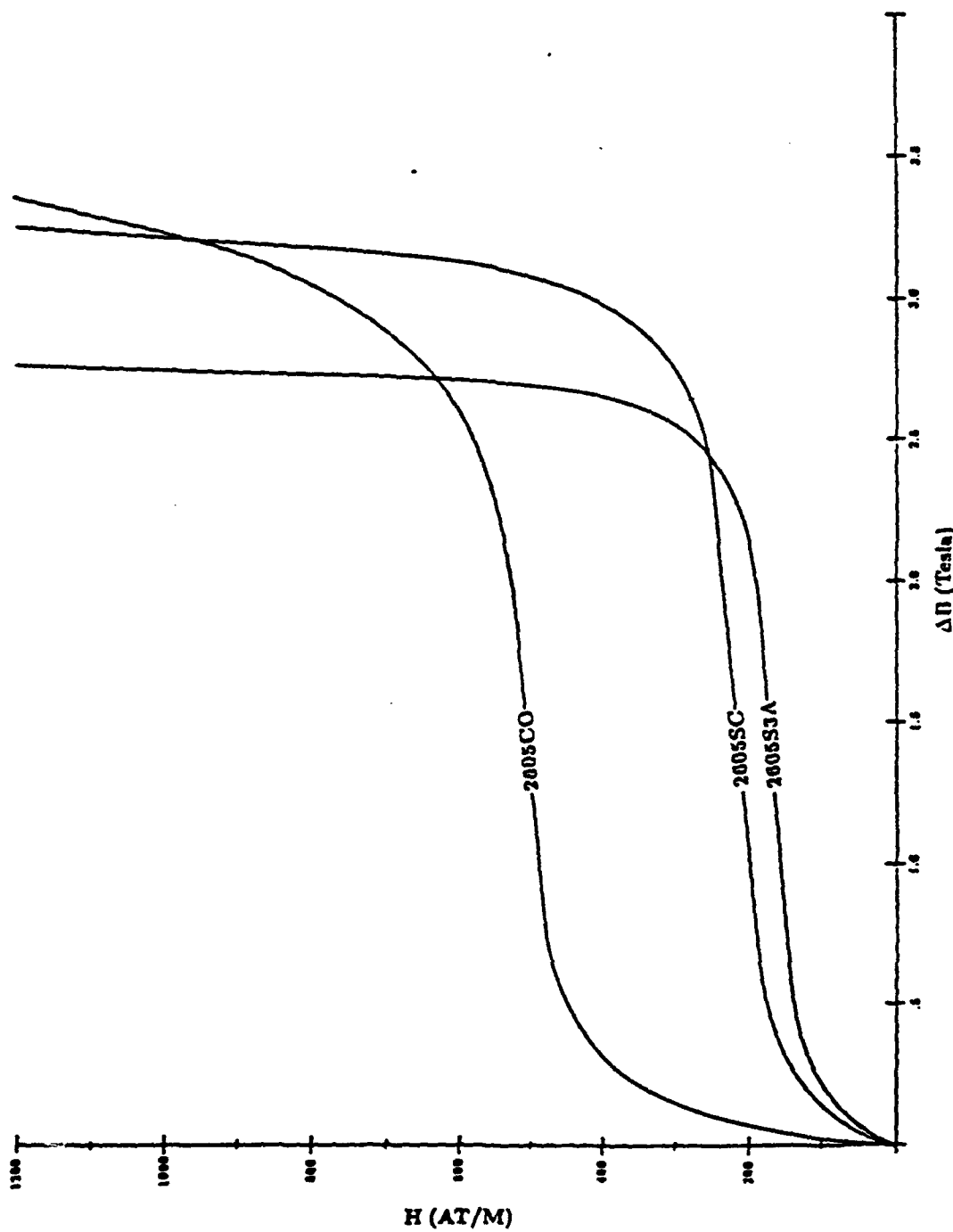


Figure 2.5: 1.5  $\mu$ sec Saturation Time

SCIENCE RESEARCH LABORATORY

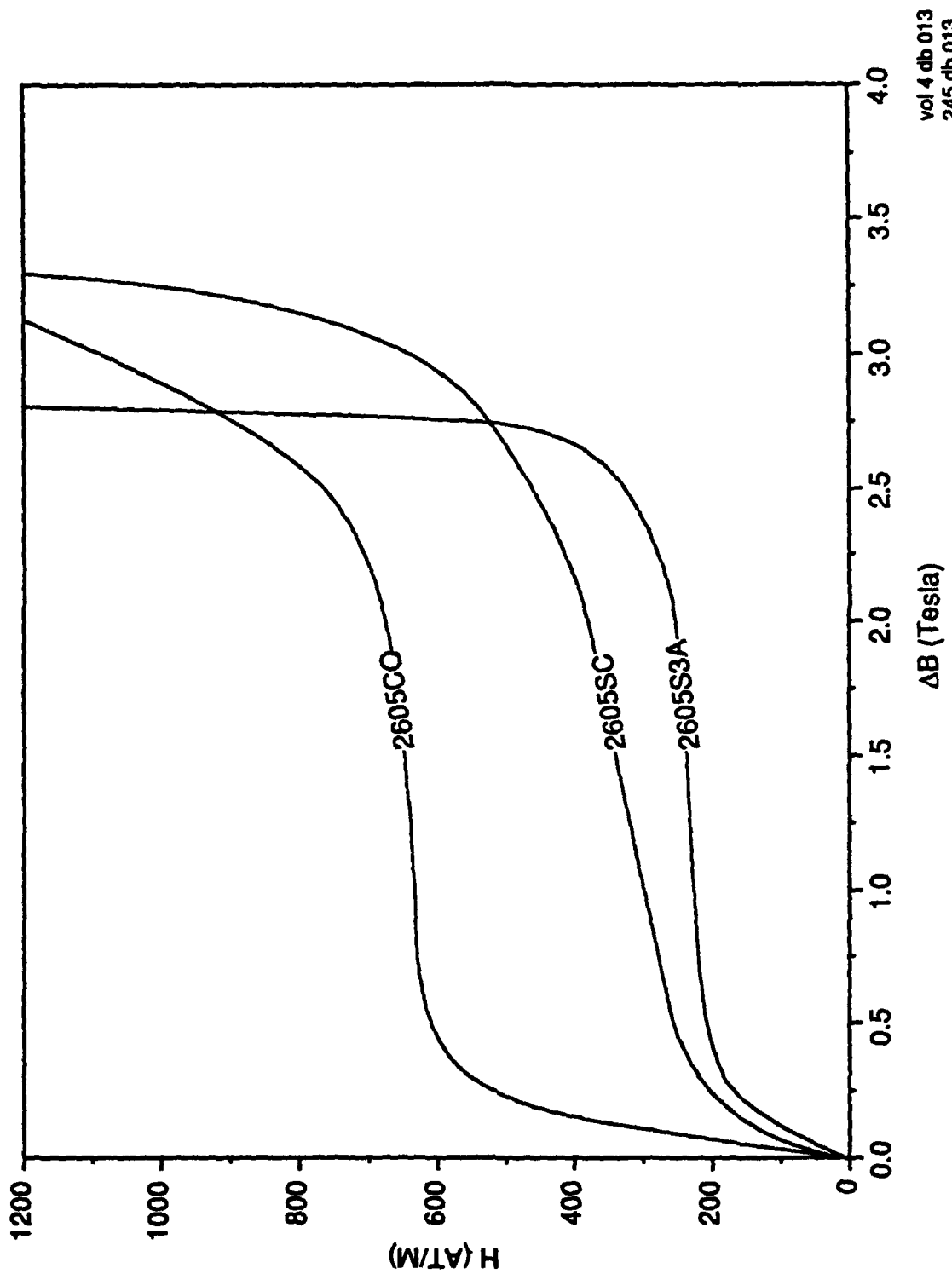


Figure 2.6: 1.2  $\mu$ sec Saturation Time

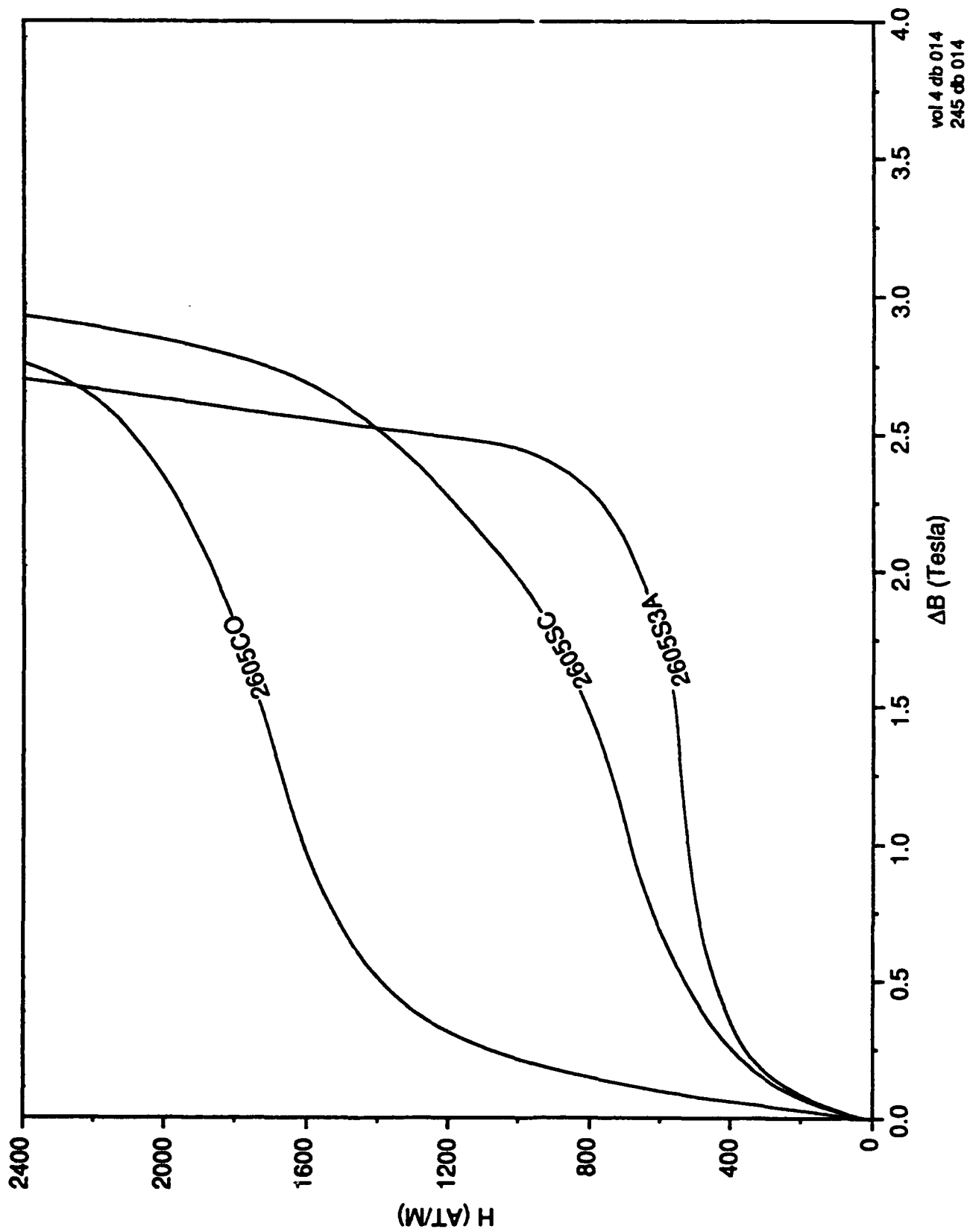


Figure 2.7: 0.5  $\mu$ sec Saturation Time

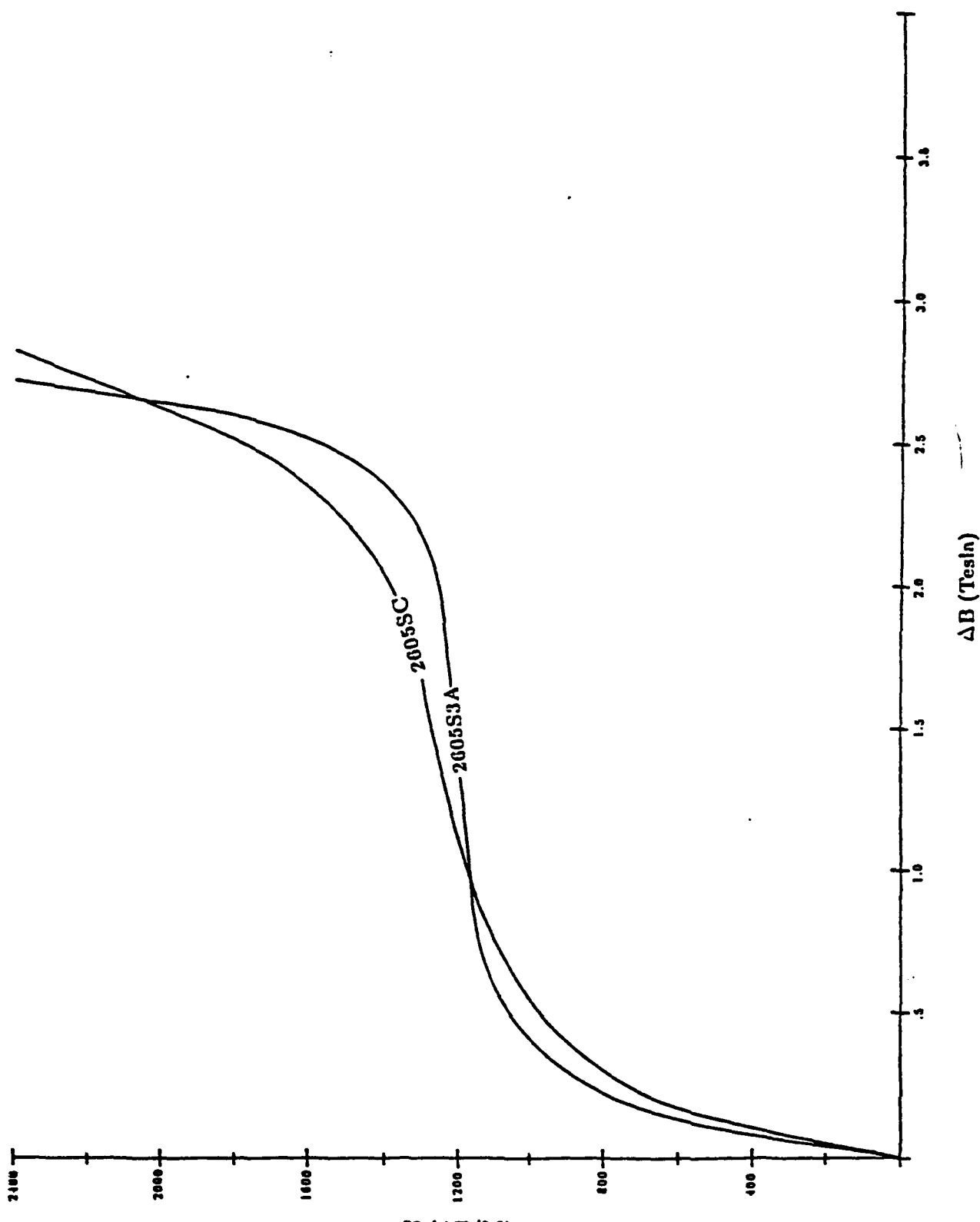


Figure 2.8: 0.25  $\mu$ sec Saturation Time

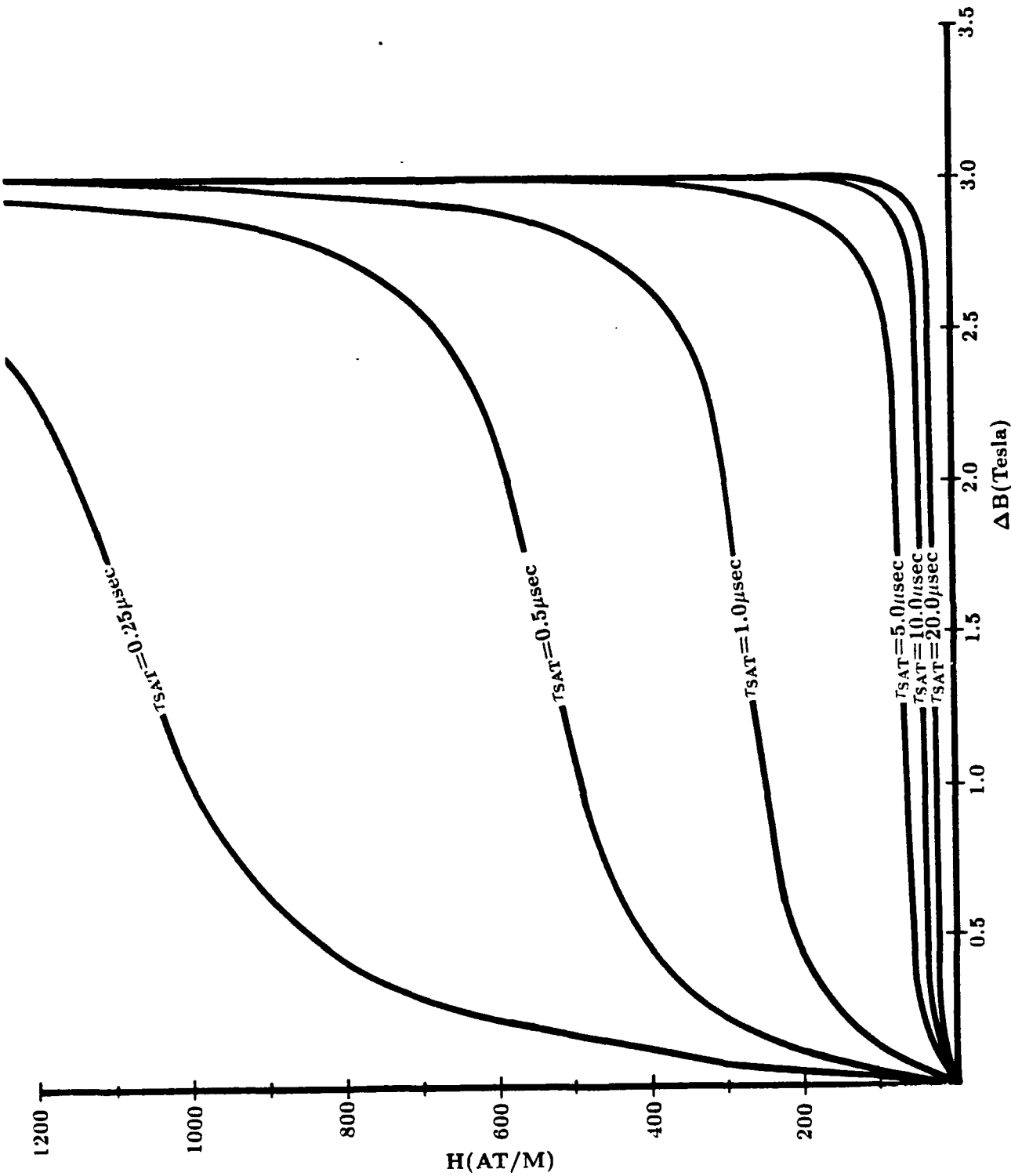
2-10



Figure 2.9: 1.2 mil 50-50 Ni-Fe Tape

SCIENCE RESEARCH LABORATORY

Figure 2.10: 0.6 mil 50-50 Ni-Fe Tape



these dipoles. When the external fields are applied perpendicular to the internal fields they exert a thrust or torque on the spinning electrons.

In the case of a spinning top (Fig. 2.11) application of a force perpendicular to the axis of spin will initiate precession. The precession frequency  $\omega_0$  depends on the angular momentum of the top and the gravitational force  $Mg$  acting on the center of mass of the top. The gravitational torque is

$$T = MgL \sin \theta$$

where  $\theta$  is the angle of inclination and  $L$  is the distance from the pivot point to the center of mass. The angular momentum vector will maintain a constant angle  $\theta$  with the vertical and the top will precess about the vertical axis with an angular velocity

$$\frac{d\phi}{dt} = \omega_0 = \frac{T}{p \sin \theta}$$

The spinning electron can be treated as a spinning top where the forces of gravity are replaced by the magnetic forces. In the case of a spinning electron the angular momentum and magnetic moment are parallel vectors with absolute values of  $p$  and  $\mu_e$ . The gyromagnetic ratio is defined as

$$\gamma = -\mu_e/p = ge/2mc$$

where  $e$  is the electronic charge,  $m$  the electron mass,  $c$  the velocity of light and  $g$  is the Lande g-factor and is approximately equal to 2. The torque on the electron from a constant magnetic field is simply

$$T = \mu_e H \sin(\theta)$$

By comparison with the above result for a spinning top, it is obvious that the precessional frequency is simply given as

$$\omega_0 = \gamma H$$

Here the magnetic field  $H$  is the actual magnetic field seen by the electron and represents the vector sum of both the internal and applied external fields.

In the case of microwave circulators, a very large external field is applied which dominates the internal fields. In this case the resonance line width is very narrow and occurs at a frequency of thousands of megahertz. In the cases where the internal field dominates, the resonance occurs at much lower frequencies and the linewidth is quite broad as the internal domain structure is by definition nonisotropic and is randomly oriented with respect to the applied field. The internal field arises from the alignment of individual spinning electrons into domains and is given by

$$H_{int} = M_{sat}/\mu - 1$$

If the alignment is truly random, then a simple vector sum will result in an average field given as

$$H_{int} = 2/3M_{sat}/\mu - 1$$

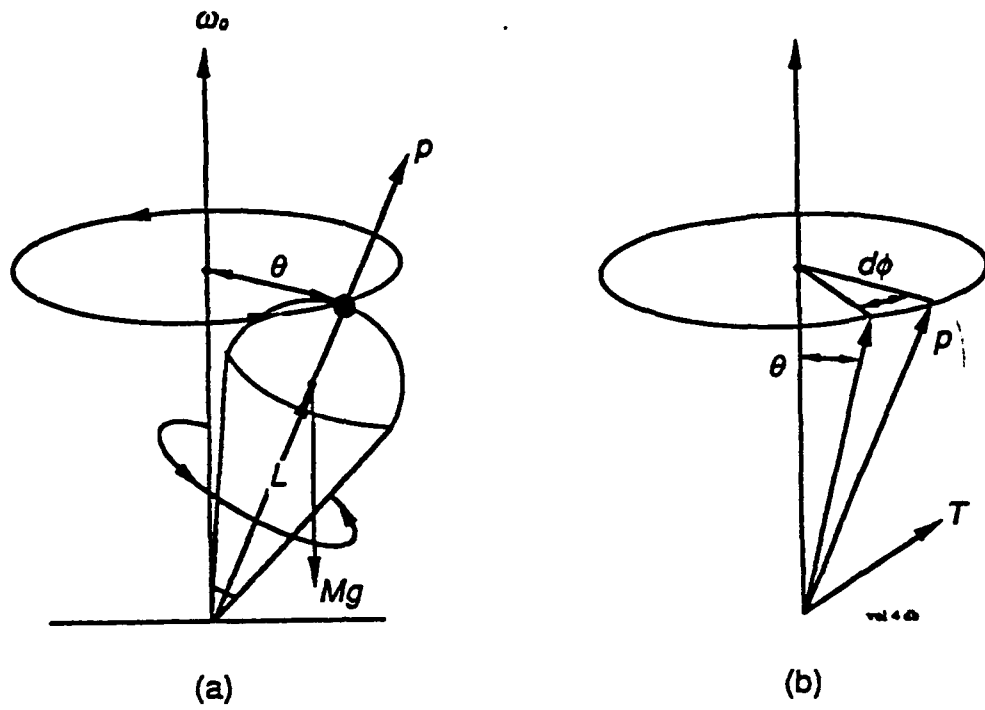


**Figure 2.11:** Processional motion of a spinning symmetrical top in a gravitational field. The precession of the rigid body at frequency  $\omega_o$  is shown schematically in (a), and the angular momentum and torque vectors are shown in (b).

Therefore, as related above, the resonant frequency in the absence of an externally applied field is given by:

$$\nu_{res} = \frac{\gamma \cdot M_{sat}}{3 \cdot \pi \cdot (\mu_i - 1)}$$

where:

$\gamma$  = gyromagnetic ratio ( $\sim 0.22 \times 10^6$ )

$M_{sat}$  = Saturation magnetization ( $2.5 \rightarrow 3.5 \times 10^5$  A/M)

$\mu_i$  = Initial permeability as  $\nu \rightarrow 0$ .

It is now obvious that the resonant frequency of a material can be easily shifted through a variety of measures. Application of an external bias field parallel to the applied time dependent field will increase the resonant frequency. Annealing a toroidal ferrite in the presence of a strong toroidal field can increase the ferromagnetic resonant frequency by a factor of 1.5. Reduction of the permeability will also increase the resonant frequency. This can be accomplished through the introduction of an air gap in the toroid or through a change in composition.

In zinc-nickel ferrites, the initial permeability and therefore the ferrimagnetic resonant frequency can be varied simply by reducing the zinc content and replacing it with additional nickel. An example of this behavior is shown in a plot of the real part of the initial permeability versus frequency for ferrites of various compositions (Fig. 2.12). These ferrites are manufactured by Ceramic Magnetics Corporation and the compositions  $(Zn_{45} Ni_{55})$ ,  $(Zn_{30} Ni_{70})$ ,  $(Zn_{15} \cdot Ni_{85})$ ,  $(Ni_{1.0}) \cdot Fe_2O_4$  correspond to C2025, C2050, C2075, N40 respectively. Also available from this manufacturer are the compositions  $(Zn_{54} Ni_{46})$ ,  $(Zn_{60} Ni_{40})$ ,  $(Zn_{65} Ni_{35}) \cdot Fe_2O_4$  corresponding to C2010, CN20, and CMD5005 respectively.

It is also critical to note that as the initial permeability drops, the Curie temperature increases. This can be understood by realizing that as the permeability drops, the energy required to change magnetic states increases and therefore the random thermal energy required to disrupt the state also increases.

The frequency dependence of ferrite losses has best been modeled by Landau and Lifshitz. They have proposed that the losses be modeled as

$$\frac{d\vec{M}}{dt} = \gamma(\vec{M} \times \vec{H}) - \lambda \left( \frac{\vec{M} \times (\vec{M} \times \vec{H})}{M_0^2} - \vec{H} \right)$$

In this equation,  $\gamma$  is the gyromagnetic ratio and  $\lambda$  is the relaxation frequency. This model describes the motion of a spinning top in a viscous medium. The term multiplied by  $\gamma$  represents the DC anisotropy and the term multiplied by  $\lambda$  is the viscous damping. The first term represents the precessional motion of the magnetization. This motion as in the case of a spinning top is perpendicular to the direction of both  $\vec{H}$  and  $\vec{M}$ . The second term signifies a damping force acting on the precessional motion. In the case where the second term dominates, this equation

## C2025, C2050, C2075, N40 High Frequency Nickel-Zinc Ferrites

This group of materials was specifically engineered to give high flexibility in accommodating requirements to 400 MHz. Our engineering department will work with you on your particular needs to determine which if these ferrites is best for you.

### Typical Magnetic Characteristics

	C2025	C2050	C2075	N40
INITIAL PERMEABILITY, <1 MHz	175	100	35	15
MAXIMUM PERMEABILITY	1100	390	150	50
MAXIMUM FLUX DENSITY, 'gaus	3500	3400	2700	1600
REMANENT FLUX DENSITY, 'gaus	2600	2400	1800	700
COERCIVE FORCE, 'cerstad	1.5	3.0	7.0	7.5
CURIE TEMPERATURE, °C	270	340	420	510
dc VOLUME RESISTIVITY, ohm-cm @ 40 cerstad applied field strength	$10^6$	$10^7$	$10^8$	$10^{10}$

### Initial Permeability Versus Frequency

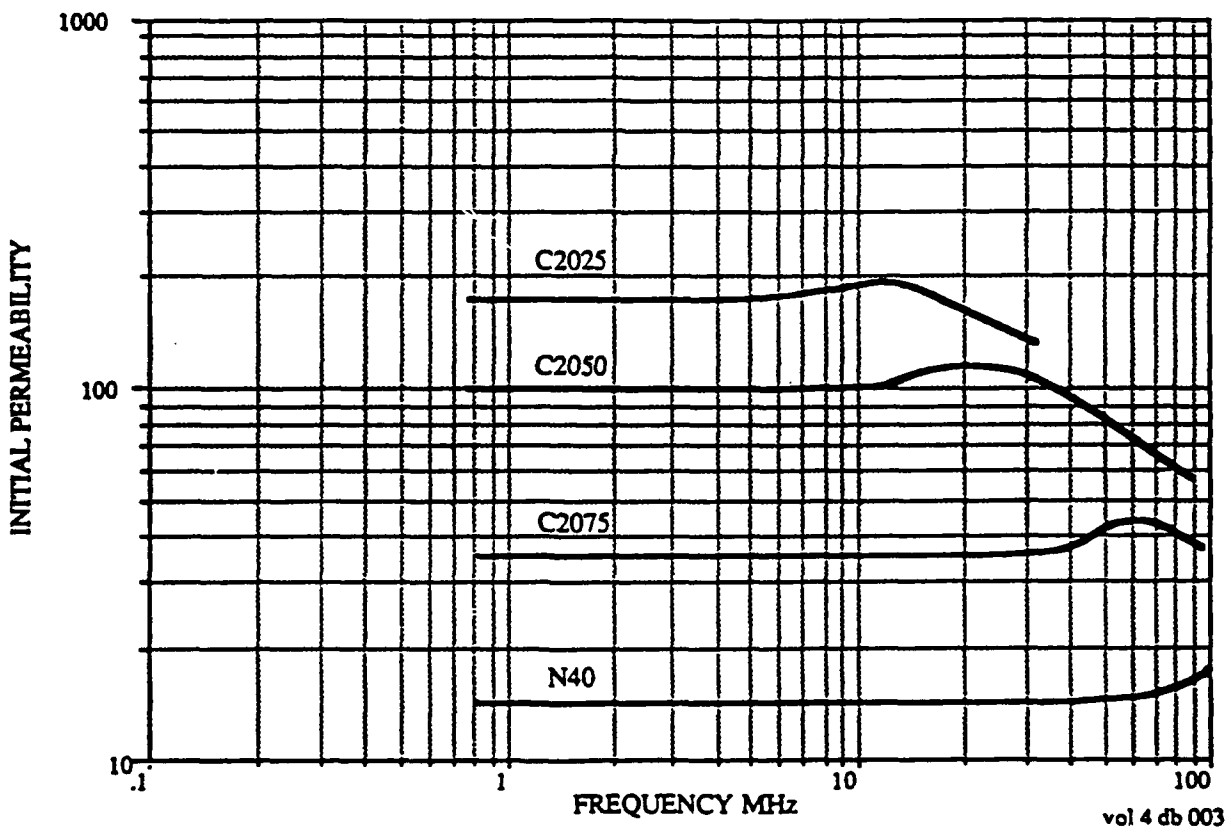


Figure 2.12: High frequency nickel-zinc ferrite permeability

can be rewritten as

$$\frac{dM}{dt} \approx \lambda H \left( 1 - \frac{M^2}{M_0^2} \right)$$

The value for  $\lambda$  can be derived from the frequency dependence of the initial permeability. For large displacements around the demagnetized state let us assume

$$\left( 1 - \frac{M^2}{M_0^2} \right) \approx 1/2$$

We will also assume the motion is oscillatory in which case

$$\frac{dM}{dt} = i\omega M \approx \frac{\lambda H}{2}$$

and since

$$\mu_r = 1 + \frac{4\pi M}{H}$$
$$\frac{\omega(\mu_r - 1)}{4\pi} = \frac{\nu}{2}(\mu_r - 1) \approx \frac{\lambda}{2}$$

In other words  $\lambda$  is the frequency at which  $(\mu_r - 1)$  approaches unity. It might be expected that because the crystal structures are identical, the value of  $\lambda$  would be similar between various ZnNi ferrite compositions. Indeed examination of Fig. 2.13 allows one to draw the conclusion that  $\lambda$  is almost identical between the various compositions and is equal to  $\sim 10^{10}$  Hz.

### Dielectric Properties

Ferrites are semiconductors with resistivities ranging from  $10 \Omega\text{-cm}$  to  $10^8 \Omega\text{-cm}$  at room temperature. The relative dielectric permittivity ranges from 10 to as high as 100,000. The dielectric permittivity along with its frequency dependence are extremely important parameters in electromagnetic shock line design as the ferrite forms the transmission line medium.

Ferrite is a polycrystalline material consisting of semiconducting grains surrounded by thin boundaries with much higher resistivity. The grain boundaries are typically composed of insoluble materials which diffuse into the grain boundaries during sintering. They are typically nonmagnetic and are occasionally added intentionally. Calcium Oxide and Silicon Dioxide are examples of materials which are sometimes added by the manufacturer to increase the low frequency resistivity. One example of such a material is Ceramic Magnetics MN8CX. This ferrite is a manganese-zinc ferrite with an artificially high DC resistivity of  $10,000 \Omega\text{-cm}$ . As we will see below, such additions are of little practical significance at high frequencies at which the large capacitance of these grain boundaries shunts the high resistivity, exposing the inherent resistivity of the crystallites.

If we define  $\alpha$  as the ratio of the boundary layer thickness to thickness of the average crystallite, then we can predict the dielectric behavior of the ferrite based on the experimentally determined conditions that  $\alpha \ll 1$ ,  $\epsilon_{\text{crystallite}} \approx \epsilon_{\text{boundary}}$ , and  $\alpha\rho_{\text{boundary}} \gg \rho_{\text{crystallite}}$ . Therefore at low frequencies the impedance of the crystallite is negligible compared with the

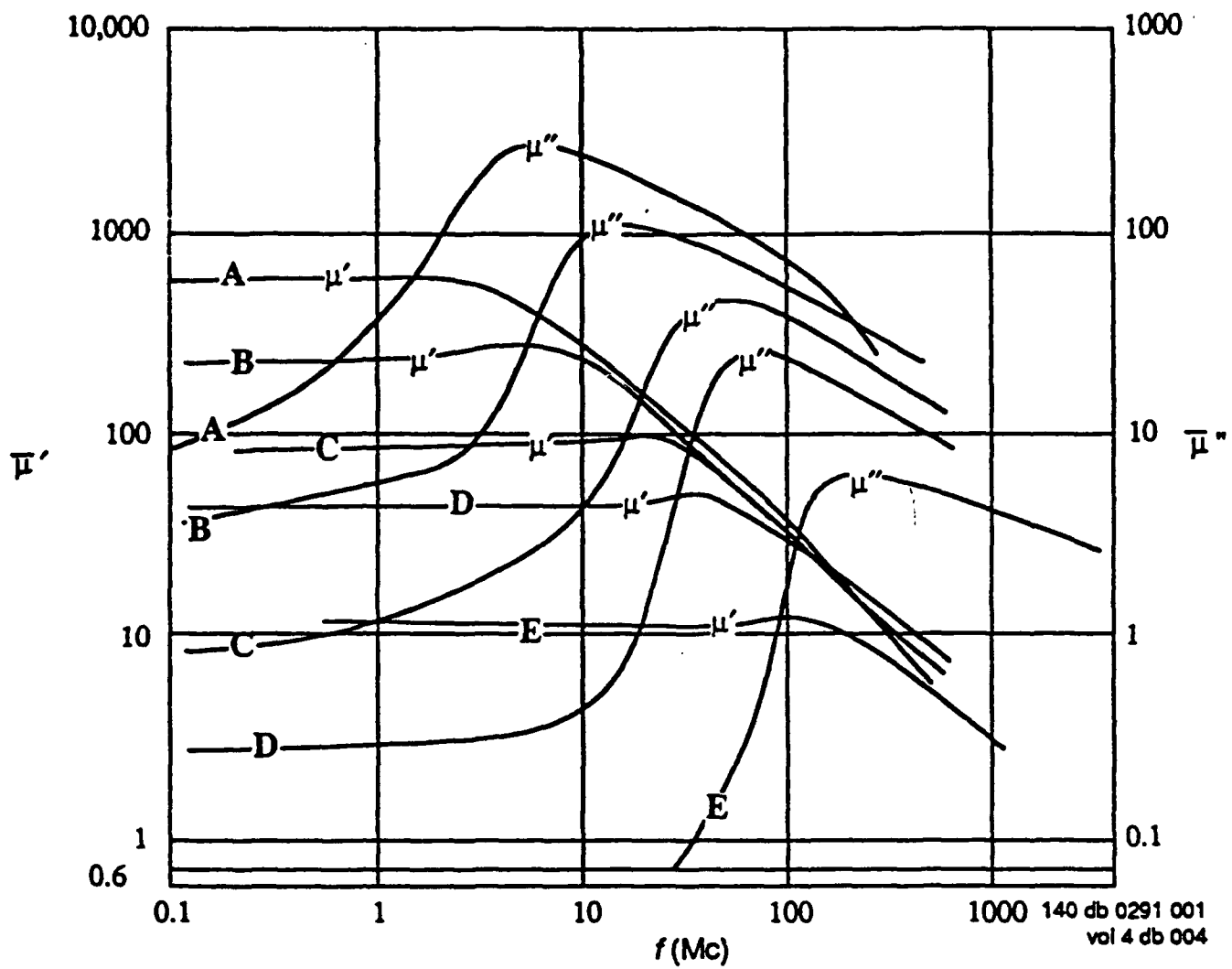


Figure 2.13: Frequency dependence of real and imaginary parts of the initial permeability for polycrystalline NiZn ferrite. (compositional ratio NiO:ZnO = (A) 17.5:33.2, (B) 24.9:24.9, (C) 31.7:16.5, (D) 39.0:9.4, (E) 48.2:0.7, remaining part  $\text{Fe}_2\text{O}_3$ ) (Gorter).

impedance of the boundary layers and the resistivity is approximately given as  $\alpha\rho_{\text{boundary}}$  and the permittivity approaches  $\epsilon_{\text{boundary}}/\alpha$ .

At high frequencies the boundary layer capacitance is short-circuited by the high boundary layer capacitance and the dielectric permittivity and resistivity approach that of the crystallites. The relaxation frequency is defined as  $1/2\pi\tau$  where  $\tau$  is the characteristic decay time of the junction capacitance. The relaxation frequency is given by

$$f_r = \frac{1}{2\pi\epsilon_0} \frac{\frac{1}{\rho_{\text{crystallite}}} + \frac{1}{\rho_{\text{boundary}}}}{\epsilon_{\text{crystallite}} + \epsilon_{\text{boundary}}/\alpha}$$

Experimentally-measured curves of both permittivity and resistivity as a function of frequency for two different zinc-nickel compositions are presented in Fig. 2.14. These compositions labeled B1 and 4B1 are produced by Phillips and correspond to  $(\text{Zn}_{60} \text{ Ni}_{40})$  and  $(\text{Zn}_{50} \text{ Ni}_{50}) \cdot \text{Fe}_2\text{O}_4$  respectively.

The eddy current power loss density is simply given as

$$P = \frac{(\omega B_0 d)^2}{\rho\beta}$$

where  $\rho$  is the resistivity,  $d$  is the characteristic dimension and  $\beta$  is the geometric factor. For a toroid,  $d$  is the width of the toroid and  $\beta = 24$ . For a sphere,  $d$  is the diameter and  $\beta = 80$ . The eddy current losses can also be characterized as a contribution to the loss angle given as

$$\tan(\delta_r) = \frac{\omega\mu\mu_0 d^2}{2\rho\beta}$$

The resistivity and permittivity are also temperature dependent. This effect is documented by the measurements presented in Fig. 2.15 of the same two compositions. These measurements were taken at 1 MHz but the slopes of the curves are similar at differing frequencies.

The curves indicate that for Zn-Ni compositions, the resistivity never will drop below  $10^4$   $\Omega\text{-cm}$ . This resistivity is  $10^8$  times higher than the resistivity of metglass. The eddy current losses in a 1 inch thick Zn-Ni toroid are equivalent to the losses in a 0.1 mil metglass tape for the same flux excursion. In Mn-Zn ferrites, the eddy current losses cannot be neglected as they approach  $10 \Omega\text{-cm}$  in the frequency range we are interested in. This means that a 1 inch thick Mn-Zn ferrite toroid will exhibit eddy current losses equivalent to 3 mil thick metglass tape undergoing the same flux excursion. In addition the Mn-Zn ferrites exhibit a large dielectric constant. Electromagnetic radiation propagates through the material at only a few centimeters per microsecond. This allows fairly small structures to be resonant in the frequency ranges of interest. If the entire ferrite toroid forms a single resonant structure, the loss tangent approaches unity.

### Ferrite Sample Measurements

Sample ferrites were tested which spanned the range of applicable compositions. These ferrites were manufactured by Ceramic Magnetics Corporation and the compositions purchased

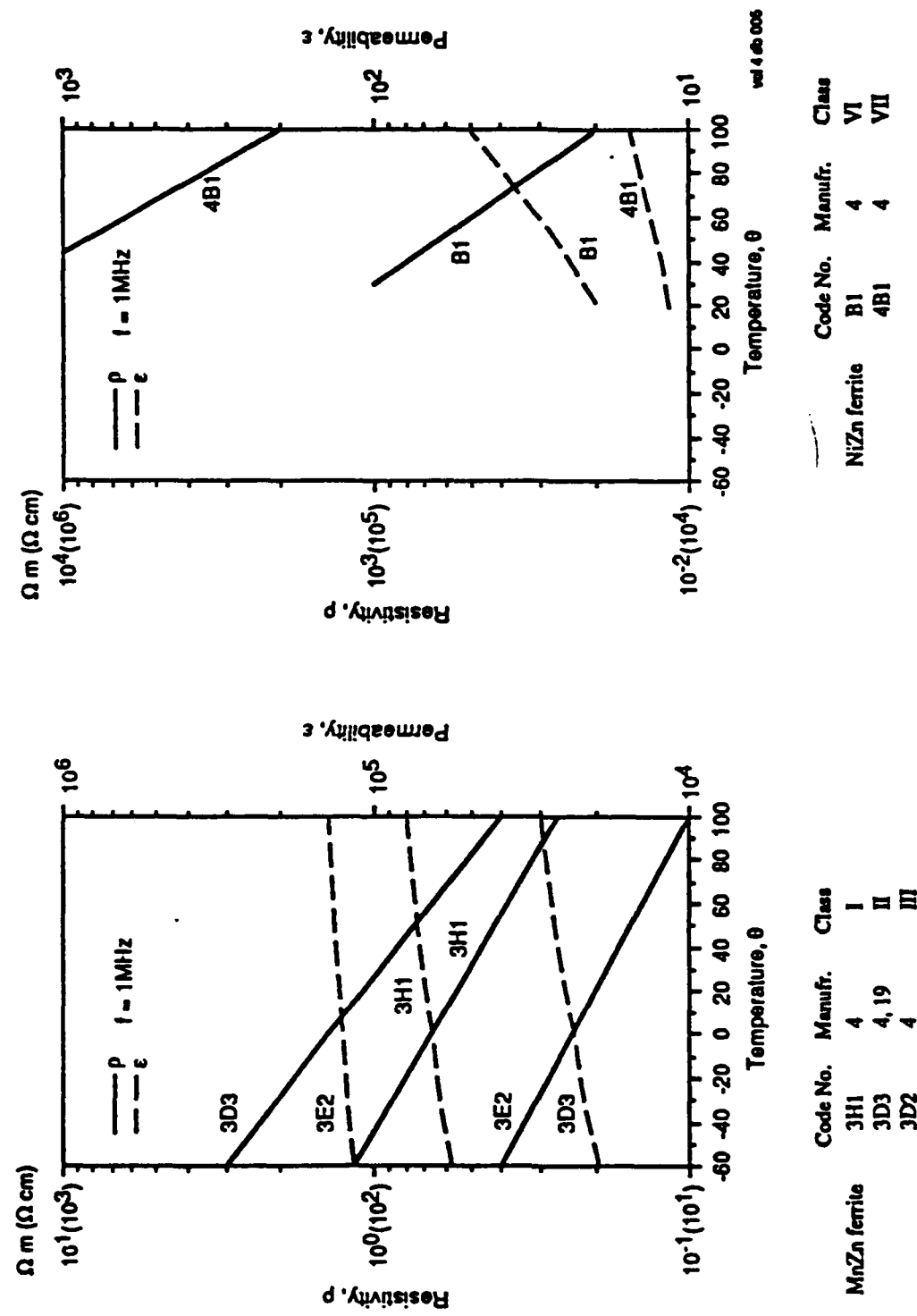


Figure 2.14: Resistivity of various ferrites as a function of temperature

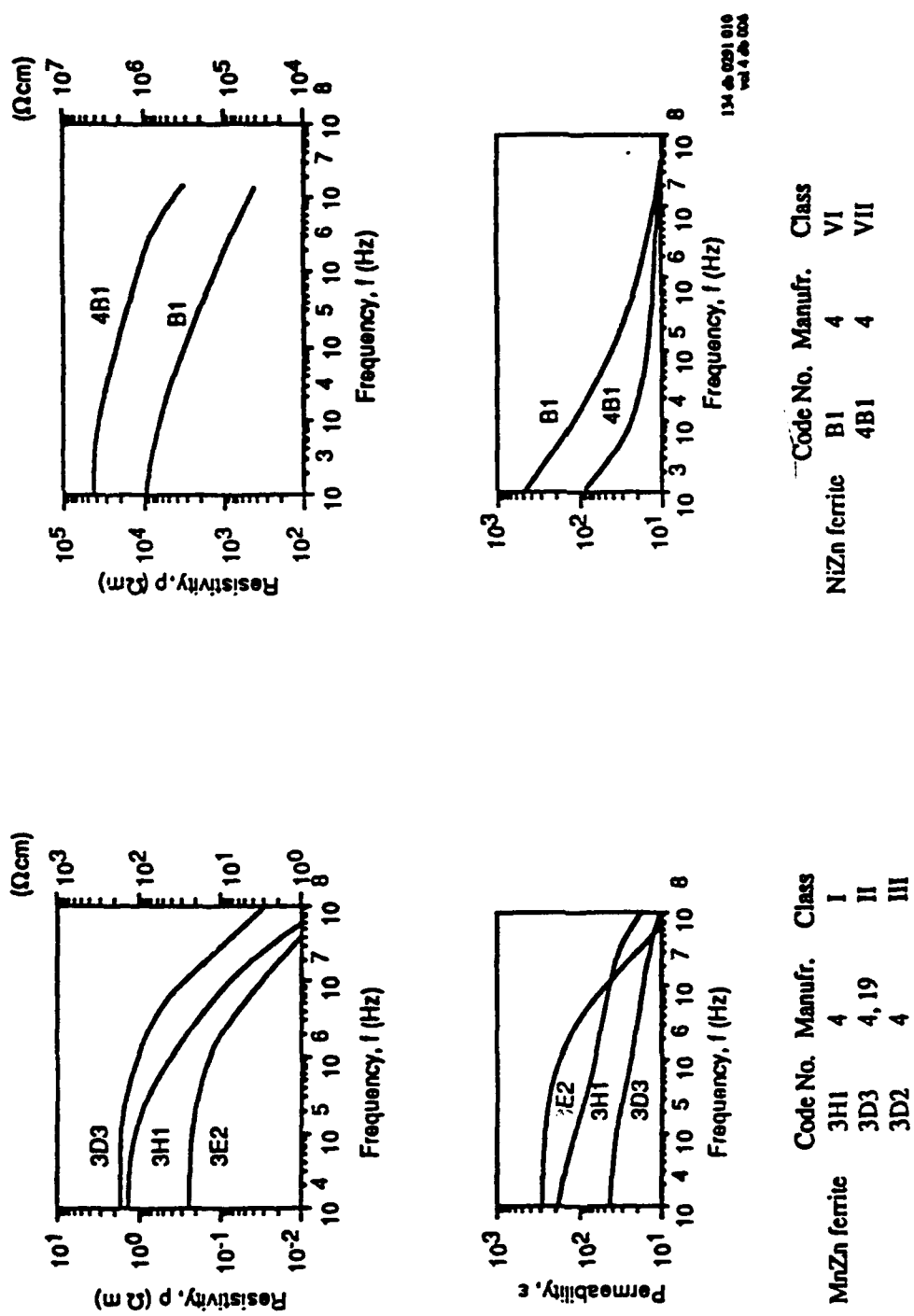


Figure 2.15: Resistivity and permeability of various ferrites as a function of frequency

-  $(Zn_{65} Ni_{35})$ ,  $(Zn_{60} Ni_{40})$ ,  $(Zn_{54} Ni_{46})$ ,  $(Zn_{45} Ni_{55})$ ,  $(Zn_{30} Ni_{70})$ ,  $(Zn_{15} \cdot Ni_{85})$ ,  $(Ni_{1.0}) \cdot Fe_2O_4$  - correspond to CMD-5005, CN20, C2010, C2025, C2050, C2075, N40 respectively. Preliminary evaluation eliminated both C2075 and N40 from consideration.

A simplified schematic of the test stand used to evaluate these samples is presented in Fig. 2.16. Samples were reset slowly and then rapidly cycled from  $-B_r$  to  $B_s$ . Minor loops were not measured as they are not of interest in the applications we are considering where all of the available flux excursion in the ferrite is typically required. The saturation time-scales which could be measured range from 50ns to 500ns. At saturation times longer than 500ns, metal tape wound cores will outperform any available ferrite. At saturation times shorter than 50ns the test stand did not have sufficient drive power. The experimental results are presented in Figs. 2.17-2.20.

The energy dissipated in the ferrite as the flux swings from  $-B_r$  to  $B_s$  is plotted as a function of saturation time in Fig. I.21. The units are Joules/Meter<sup>3</sup> versus saturation time in nanoseconds.

If the ferrite is employed as a saturable reactor in a nonlinear magnetic compressor, then the volume of core required is linearly dependent on the square of the available flux swing. Simply because a candidate material exhibits a lower loss per unit volume does not mean it is the best choice as the core material. The best technique to identify the optimum core material in a saturable reactor is to plot energy loss per meter<sup>3</sup> per Tesla<sup>2</sup>. This plot appears in Fig. 2.22.

In high repetition rate applications, temperature rise can be an issue. As the temperature rises, the available flux swing is reduced until at the Curie temperature the available  $\Delta B$  goes to zero. The higher the Curie temperature for a given composition, the more power can be dissipated in a given size sample with a specified surface temperature. In a case where the ferrite surface is anchored to a temperature of 50°C, the plot in Fig. 2.23 gives an indication of the maximum repetition rate at which a given composition can be operated. Here the energy loss per cycle is divided by the maximum allowable temperature rise. The lower a curve lies on this plot, the higher the usable repetition rate.

Even though the permeability of various ferrite compositions all approach the same value as the saturation time approaches zero, there are some applications which can benefit by a ferrite composition exhibiting a reduced  $\Delta B$ . As an example, the optimum ferrite for use in an electromagnetic shock line is the ferrite which saturates at the minimize H field at a given time scale. Therefore if the permeability is to be a constant independent of composition, the composition which will yield the minimum risetime in a shock line application is that which exhibits the minimum  $\Delta B$ . TTVG-800 and G-350 are two examples of reduced  $\Delta B$  ferrites which are available from microwave ferrite suppliers such as Trans-Tech. The saturation flux of TTVG- 800 is 1/3 that of CMD-5005 while G-350 exhibits less than 1/6 the  $\Delta B$  of CMD-5005. This is further illustrated in Fig.2-24 where coercive force is plotted against saturation time. At time scales of order 1 nanosecond or less the output risetime of an electromagnetic shock line will scale linearly with the exhibited  $\Delta B$ .

In Fig.2.25 we plot the energy lost per cubic meter of magnetic material as a function of material and saturation time. As it turns out the saturation losses of ferrite scale linearly with

2-23

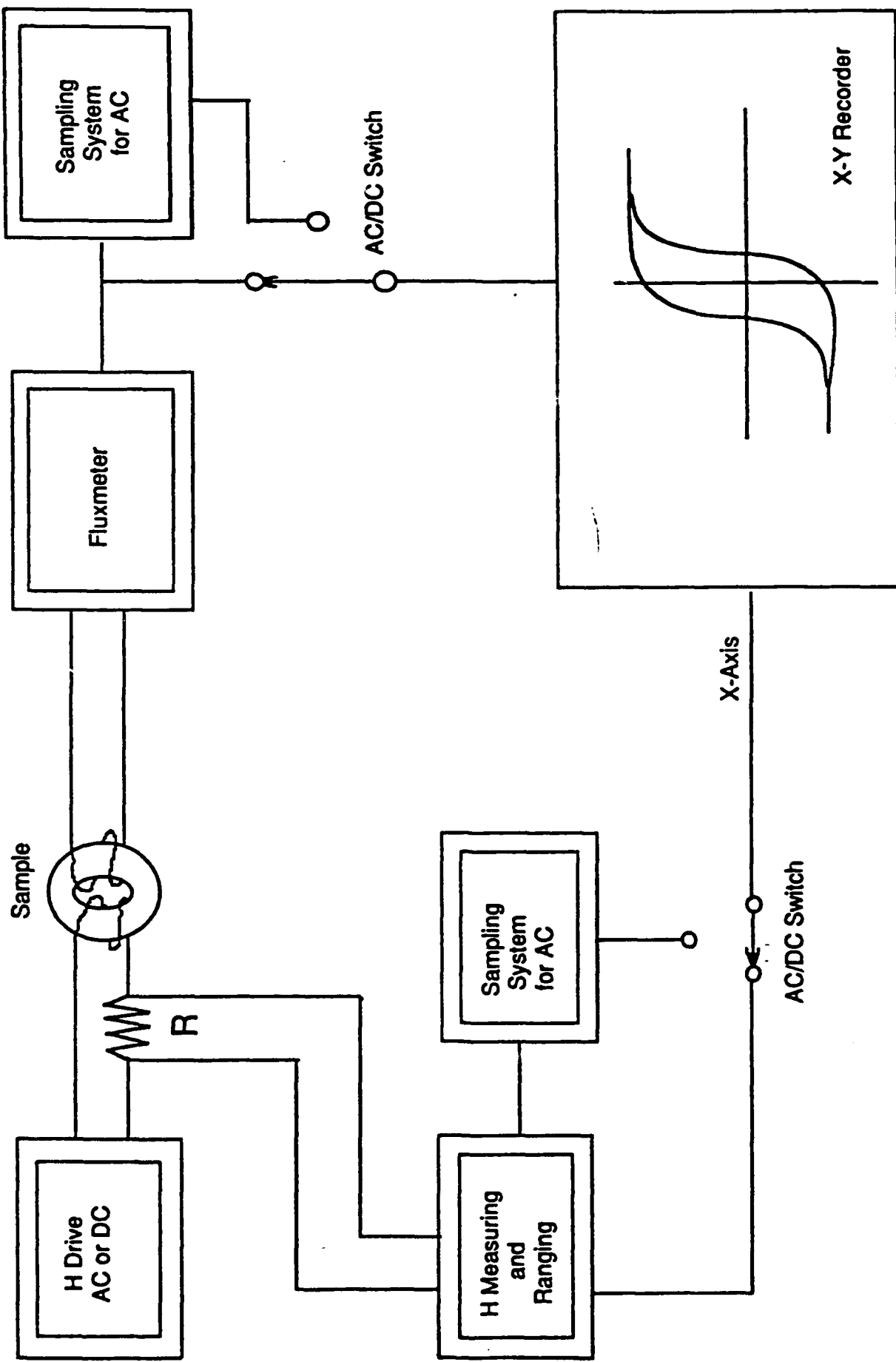


Figure 2.16: B-H loop measurements

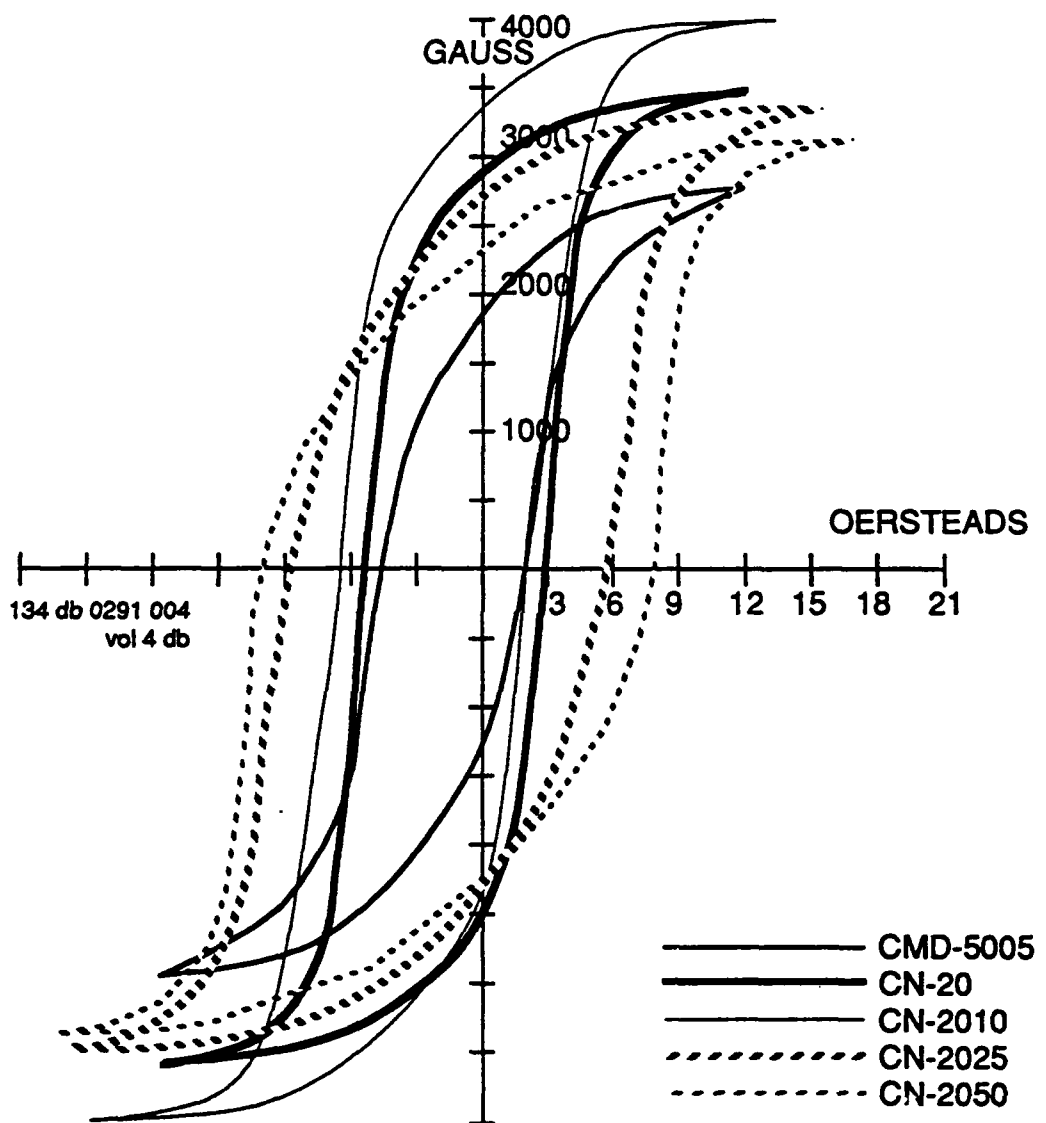


Figure 2.17: Hysteresis curves measured at  $\tau_{sat} = 500$  ns

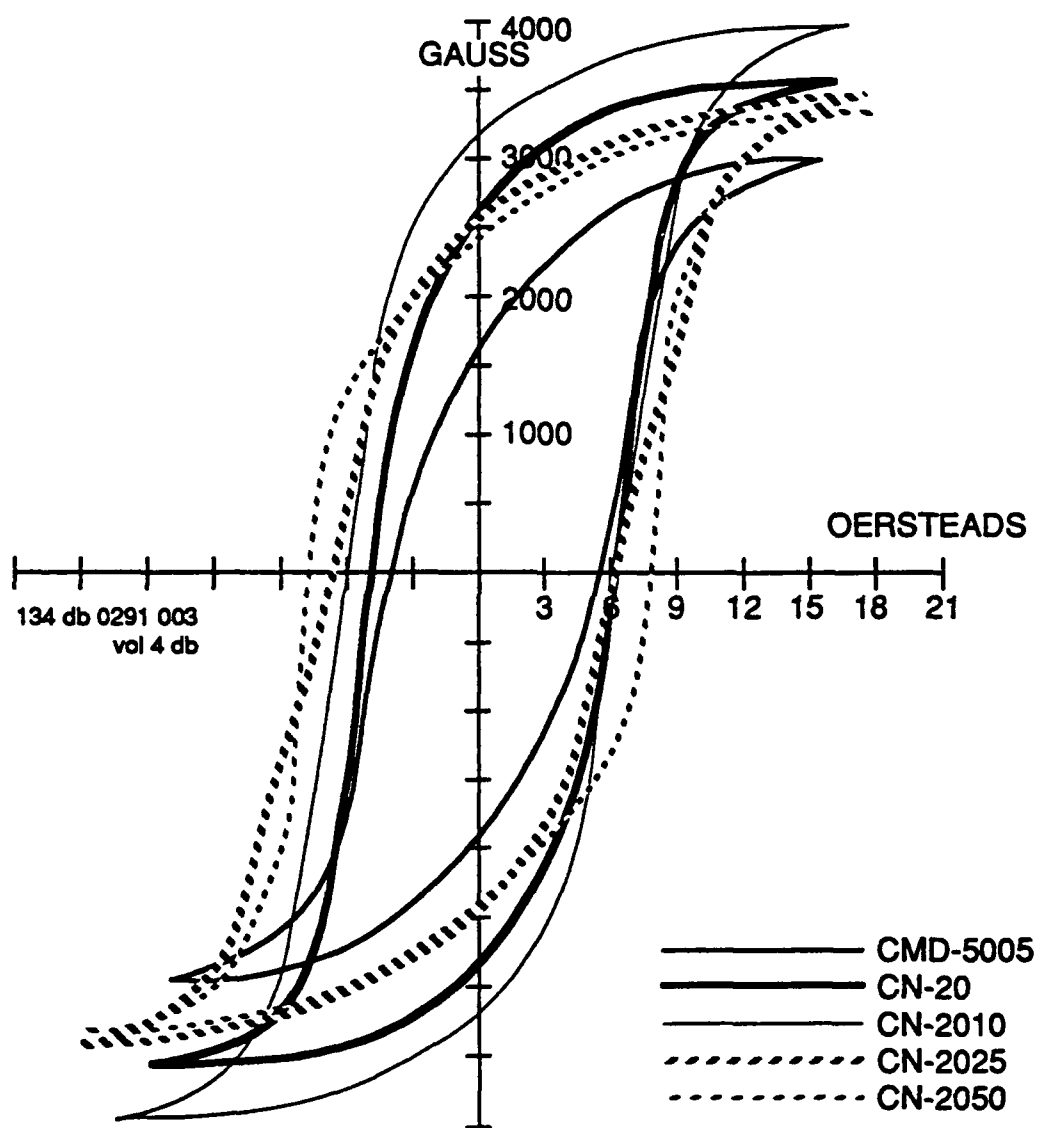


Figure 2.18: Hysteresis curves measured at  $\tau_{sat} = 250$  ns

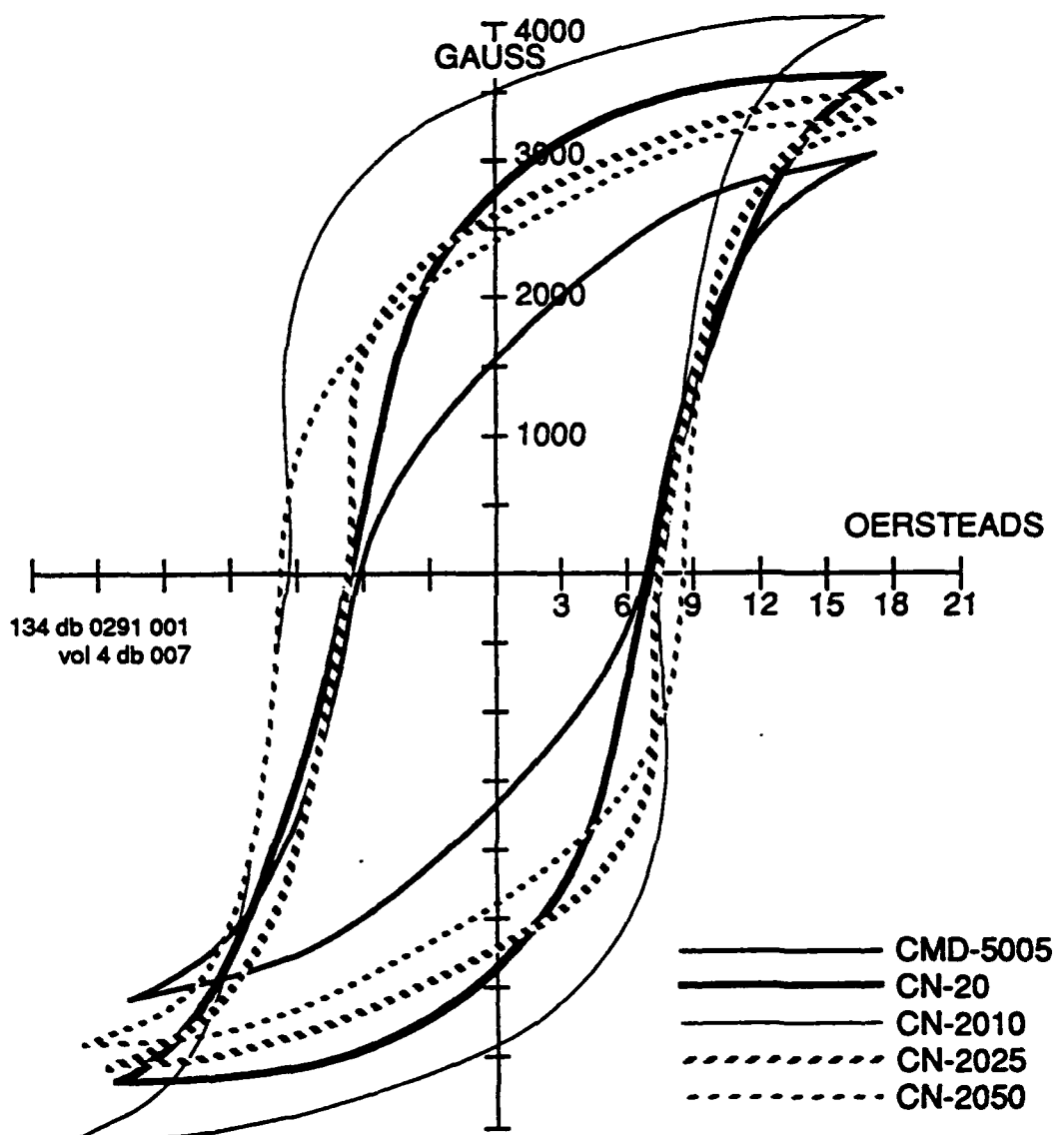


Figure 2.19: Hysteresis curves measured at  $\tau_{sat} = 100$  ns

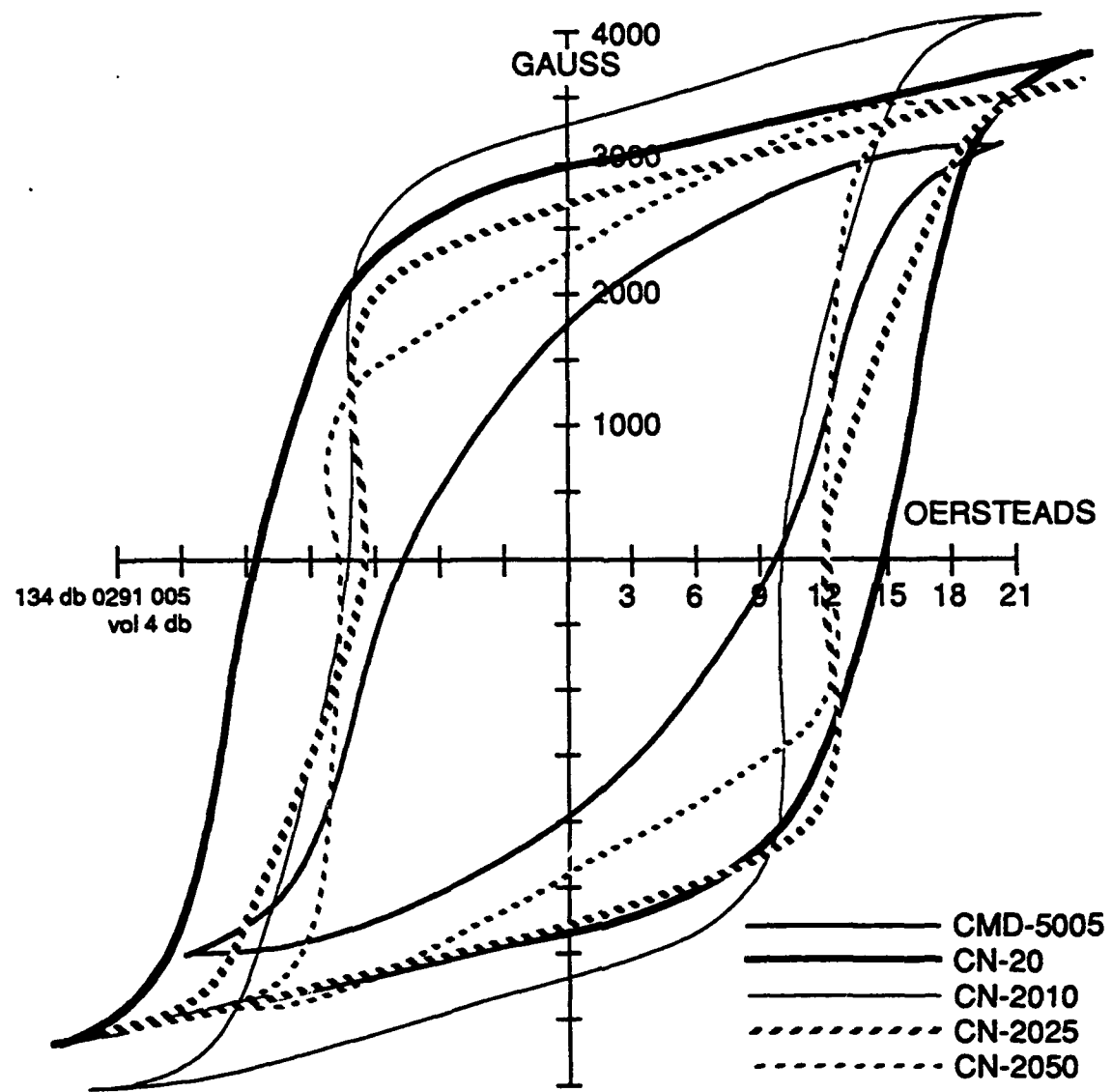


Figure 2.20: Hysteresis curves measured at  $\tau_{sat} = 50$  ns

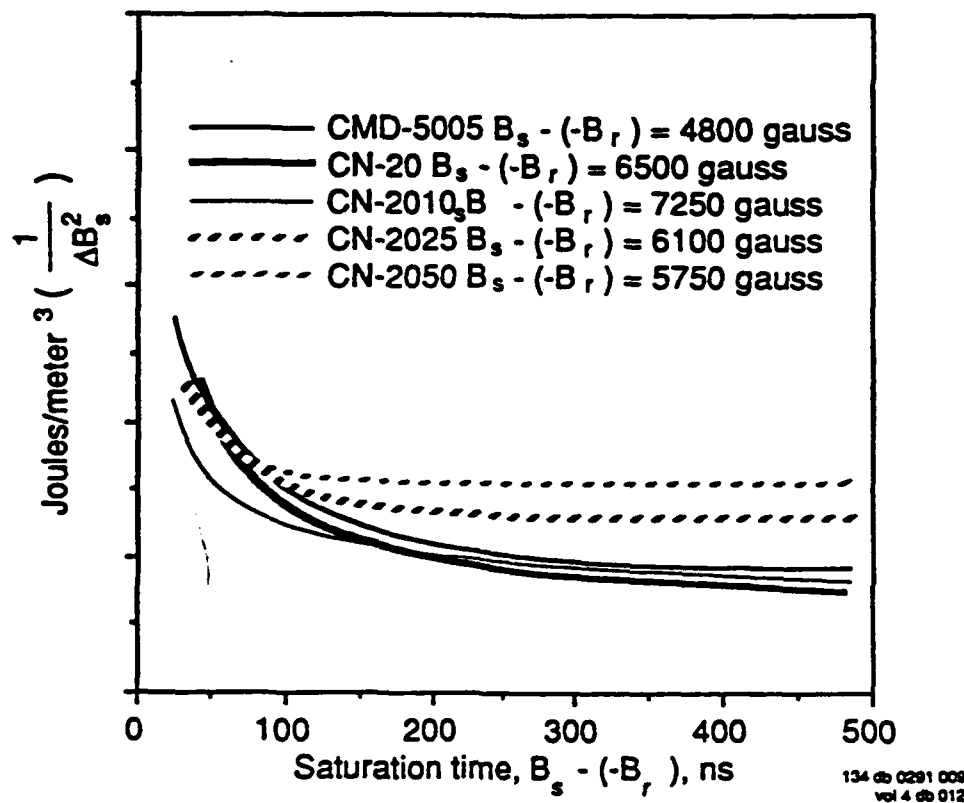


Figure 2.21: Normalized energy dissipated in various ferrite materials as a function of saturation time.

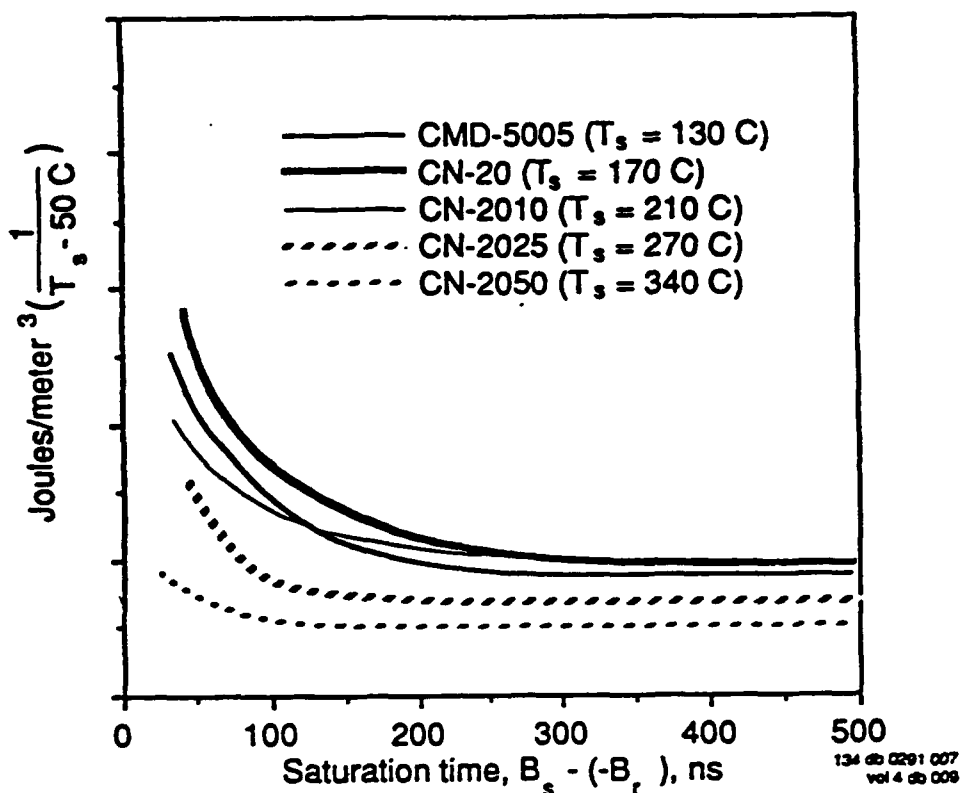


Figure 2.22: Data for maximum temperature rise allowable in various ferrite materials

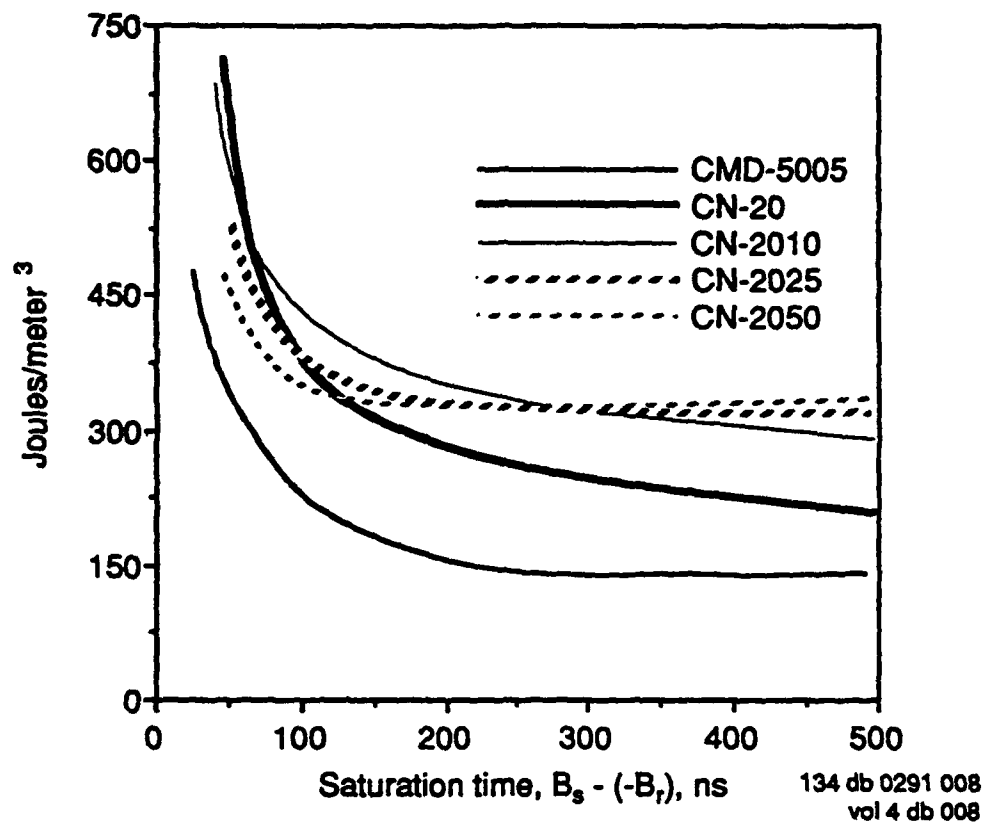
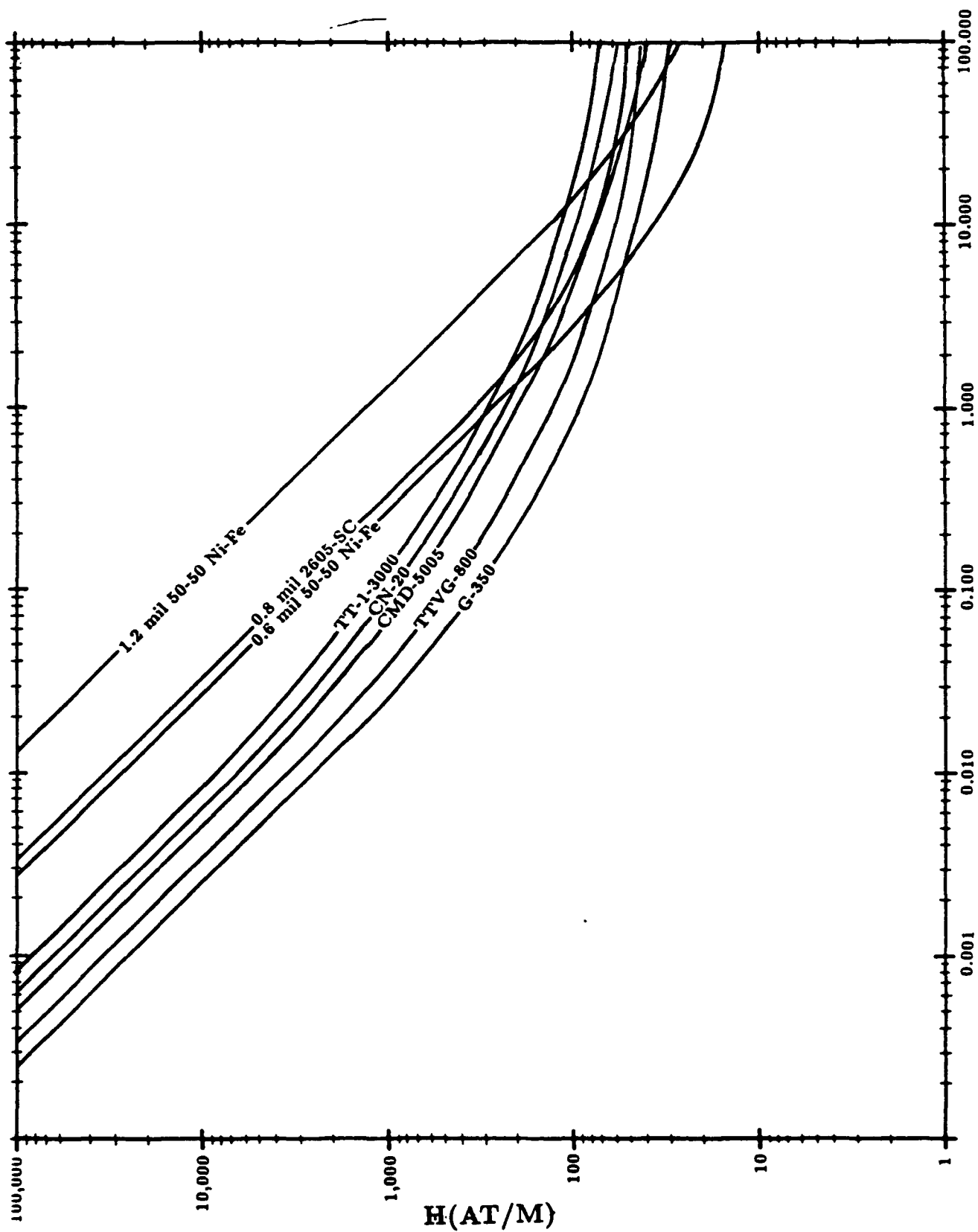


Figure 2.23 Energy dissipated in ferrite materials as a function of saturation time.

Figure 2.24: Square Wave Saturation Time ( $\mu$ sec)

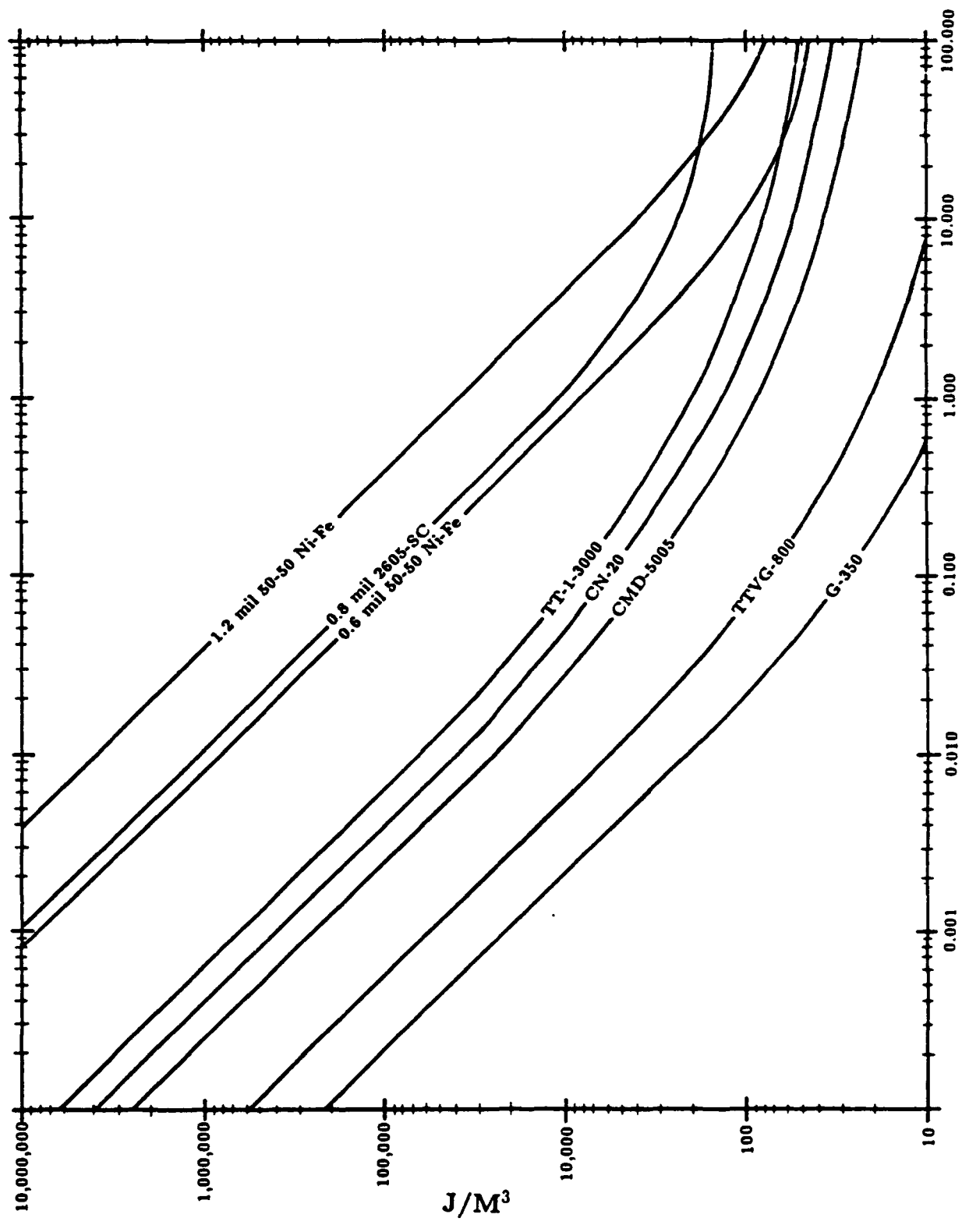


Figure 2.25: Square Wave Saturation Time ( $\mu$ sec)

the inverse of saturation time due to spin resonance damping while the metal tapes show the same temporal behavior but for a different reason. In the case of metal tapes the losses at short saturation times become dominated by eddy current losses which also scale inversely linear with saturation time.

An important figure of merit for the design of nonlinear magnetic pulse compressors is the quantity %Energy Lost/Gain<sup>2</sup> plotted as function of material and saturation time in Fig.2.26. The core volume required to achieve a given temporal compression factor with a stage of magnetic compression scales linearly as the square of the gain and inversely as the square of the available flux swing (packing factor X  $\Delta B$ ). The predicted efficiency can be readily derived from Fig.2.26 by simply choosing the optimum material, desired gain and saturation time.

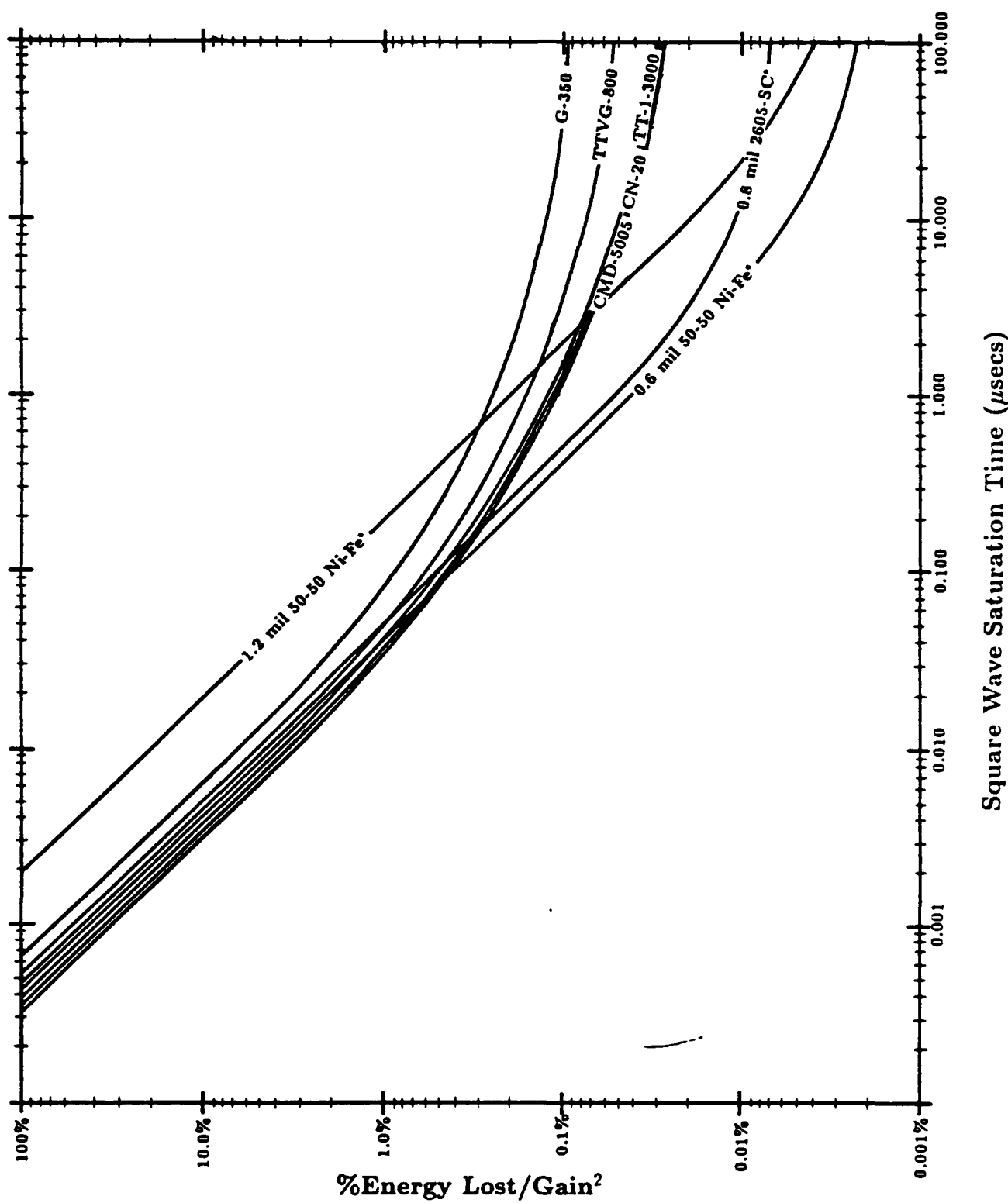


Figure 2.26: • Packing Factor = 0.7 Assumed, Unity Packing Factor Assumed for all Ferrites

## APPENDIX 3

### SCR SELECTION

Understanding the loss mechanisms in SCRs is important in establishing the operating limitations for these devices. If a simple model is assumed where the usable area of the device is a function of the time interval between triggering ( $t = 0$ ) and device turn-on ( $t = t_0$ ), then for an interdigitized gate structure the active area would be given by

$$A(t) = A_0 \cdot \frac{t}{t_0} \quad t < t_0$$

$$A(t) = A_0 \quad t > t_0$$

For a center-fire gate structure the time dependence of the conducting area should be

$$A(t) = A_0 \cdot \left( \frac{t}{t_0} \right)^2 \quad t < t_0$$

$$A(t) = A_0 \quad t > t_0$$

where  $A_0$  is the total junction area and  $A(t)$  is the time dependent region which is fully conductive.

The energy dissipated per pulse will be given by

$$\text{Energy} = \int_0^\tau I^2(t) \cdot R(t) dt$$

where  $\tau$  is the pulse length and  $R(t)$  is the time-varying resistance of the junction. According to this simple model

$$R(t) = R_0 \cdot \frac{A_0}{A(t)}$$

If a current waveform having a sinusoidal time dependence is assumed, then for  $t_0 \ll \tau$

$$\text{Energy Loss} = I_0^2 R_0 \cdot \left( \frac{\pi^2 t_0^3}{6\tau^2} + \frac{\tau}{2} \right) \quad A(t) = A_0 \left( \frac{t}{t_0} \right)$$

$$\text{Energy Loss} = I_0^2 R_0 \cdot \left( \frac{2\pi^2 t_0^3}{3\tau^2} + \frac{\tau}{2} \right) \quad A(t) = A_0 \left( \frac{t}{t_0} \right)^2$$

We can therefore define a predicted dynamic resistance given by

$$R(\tau) = R_0 \left[ 1 + \text{const} \cdot \left( \frac{t_0}{\tau} \right)^3 \right]$$

This predicted energy loss does not adequately describe the experienced time-dependent behavior of SCRs. Immediately following turn-on ( $< 1 \mu\text{sec}$ ), this time dependence may be

present, but use of a saturable magnetic assist limits the peak current during this interval to such a low value that little energy is dissipated. Analyses of experimentally-measured time dependent losses in such circuits indicates a behavior given approximately by

$$R = R_0 \left[ 1 + \frac{\text{const}}{I_0} \cdot \left( \frac{dI}{dt} \right) \right]$$

This would indicate that to first order the actual device turn-on losses are not adequately described by a model where the conduction area is time dependent but rather by a model in which the whole device requires time to react to changing currents. This suggests that so long as the limiting  $dI/dt$  is not exceeded (which might result in excessive voltage drops followed by electrical breakdown), the energy absorbed due to rising conduction currents is most likely distributed throughout the device.

It appears that the diffusion of minority carriers across the junction is the dominant loss mechanism. This means that even after an SCR has been conducting low level current indefinitely,  $dI/dt$  losses will still be associated with an increase in current. This mechanism also explains why the reverse recovered charge during turn-off is such a strong function of the  $dI/dt$ . Saturable inductors to limit turn-on currents will only help if they reduce the current during the first microsecond or so when the conduction area is still expanding.

It is also easy to explain why the voltage drop across the device increases faster than linearly with  $dI/dt$  for pulse lengths approaching the carrier lifetime. Rapid fluctuations in the current cause rapid carrier concentration variations at the junction with very little effect on the concentrations far from the junction. This results in a decrease in the effective diffusion capacitance. For sinusoidal waveforms it can be shown that the effective junction diffusion capacitance defined as  $C_d = dQ/dV$  is given by

$$C_d = (1/2)\tau(dI/dV) \quad \omega\tau \ll 1$$

$$C_d = \left( \frac{\tau}{2\omega} \right)^{1/2} (dI/dV) \quad \omega\tau \gg 1$$

After reviewing the test data accumulated in an intensive effort by Ed Cook at LLNL, it appeared redundant to establish our own SCR test stand. Instead, candidate devices whose performance had been thoroughly documented were installed at different times into the modified SNOMAD-I driver. Performance data was collected under actual operating conditions with SNOMAD-I driving a copper vapor laser at full power. Since devices with different case and wafer sizes were tested, in some cases several devices ( $\leq 4$ ) were installed in an isolated parallel fashion.

The wide variation in performance indicated in the manufacturers specifications is somewhat deceiving. The maximum RMS current is predominantly determined by the wafer area while the peak operating voltage is determined by the wafer thickness. The recovery times are determined primarily by the carrier lifetime and the junction diffusion capacitance. The recovery times can be decreased by decreasing the carrier lifetime but at the expense of slightly increased conduction losses.

In summary all of the devices are based on silicon, use similar doping levels, and have similar gate interdigititation levels. All the manufacturers listed sell SCRs with similar operating voltages, RMS current levels, and dI/dt capability. Choosing a device with a lower RMS current rating will require the designer to parallel several devices. The selection of an appropriate SCR is straightforward and, for a given operating envelope, if the appropriate device from one manufacturer fails, it is likely that an equivalent device from any of the other manufacturers will be at least stressed very close to its limit in the same socket.

## APPENDIX 4

### CAPACITOR SELECTION

As reliability and performance continues to improve, components which initially could be neglected begin to impact the overall reliability. Capacitors are a good example of this phenomenon. Present requirements for low loss operation a 10 kHz reliably and continuously for years eliminates most energy storage media. Mylar, the most common storage medium for pulsed power applications at low duty factors, must be eliminated because of its high loss tangent. Polycarbonate and reconstituted mica also are unusable for this reason.

Aluminized polypropylene with interleaved aluminum foil conductors fully extended appears to be the best dielectric material for the low voltage front end. Strontium titanate ceramic capacitors demonstrate a similar loss tangent and would be used in the front end of the pulser if fabrication in thin sheets were not so difficult. They are an excellent choice at voltages in excess of 20 kV where they can be fabricated as disks.

Candidate polypropylene capacitors are available from several manufacturers. Rhoderstein, WIMA, ByCap, GE, Sprague, and Maxwell are examples. WIMA presents a product line which extends to 2 kV operating voltage and is suitable for operation at CW repetition rates in excess of 100 kHz. Strontium titanate capacitors are only available from TDK and Murriata-Erie. TDK is the most common supplier and manufactures devices in the range of 20-50 kV. Parameters for the various candidate dielectric materials appear in Table 4.1.

The loss tangent of capacitors is also a strong function of the charge and discharge time. The best choice for a capacitor operating at 1.0  $\mu$ sec time scales is not necessarily still the best choice at 10 nanosecond charge or discharge times. In most cases the losses will continue to increase as the charging time is reduced until the loss tangent approaches unity and the capacitor becomes a resistor. This time scale is simply determined by multiplying the ESR (Equivalent Series Resistance) by the capacitance value. The result is an RC time which represents the ultimate high frequency limit of this capacitor. This time scale is usually independent of the size of the individual capacitor and depends primarily on the dielectric media and construction technique. This is further documented in Table 4.2. Here the ESR was measured for an extensive collection of capacitors. It is easily noticeable that the limiting charge time ( $ESR \cdot C$ ) is relatively independent of capacitance and primarily dependent on capacitor type.

**Table 4.1: The Essential Characteristics of the Plastic Film Dielectrics Used**

Physical characteristics of the film	Polyester	Polycarbonate	Polypropylene	SrTiO <sub>2</sub>	Reconstituted Mica
Dielectric constant 1 kHz/23 °C	3.3 (positive as temp. rises)	2.8 (largely constant over temp. range)	2.2 (negative as temp. rises)	~ 5000	
Dielectric loss factor tan δ/23 °C	1 kHz 10 kHz 100 kHz 1 MHz	5 × 10 <sup>-3</sup> 11 × 10 <sup>-3</sup> 18 × 10 <sup>-3</sup> 20 × 10 <sup>-3</sup>	1.5 × 10 <sup>-3</sup> 5 × 10 <sup>-3</sup> 10 × 10 <sup>-3</sup> 10 × 10 <sup>-3</sup>	1 × 10 <sup>-4</sup> 1 × 10 <sup>-4</sup> 1 × 10 <sup>-4</sup> 1 × 10 <sup>-3</sup>	< 0.1 %
Specific volume resistance Ω x cm/23 °C		10 <sup>18</sup>	2 × 10 <sup>17</sup>	6 × 10 <sup>18</sup>	> 10 <sup>12</sup>
Dielectric strength in V/μm at 23 °C		580 V.	535 V.	650 V.	> 10
Preferred temperature range	-55....+ 100 °C	-55....+ 100 °C	-55....+ 85 °C	-30....+ 85 °C	-65....+ 125 °C
Dielectric absorption in % at 23 °C	0.20...0.25	0.12...0.25	0.05...0.10	< 0.1 %	0.5 %
Energy Density	12.7 kJ/m <sup>3</sup>	9.5 kJ/m <sup>3</sup>	5.4 kJ/m <sup>3</sup>	15 kJ/m <sup>3</sup>	15 kJ/m <sup>3</sup>

430000  
Vol 4 Ed 10

**Table 4-2: Capacitor Performance Specifications**

Capacitor Type	ESR
RHOED. 100pf 1600V FKP	150 mΩ
RHOED. 220pf 1600V FKP	60 mΩ
RHOED. 680pf 1600V FKP	35 mΩ
ROYAL MICA .01μfd 5000V MKP	54 mΩ
RHOED. .01μfd 400V MKP	58.5 mΩ
SPRAG .022μfd 1600V MKP	39 mΩ
RHOED .047μfd 2000V MKP	47 mΩ
MALLORY .05μfd 1600V FKP	31.5 mΩ
RHOED. .1μfd 600V MKP	30.5 mΩ
BYCAP .1μfd 1000V FKP	17 mΩ
RHOED .1μfd 1600V FKP	21 mΩ
WIMA .1μfd 1600V FKP	20 mΩ
RHOED .1μfd 2000V FKP AXIAL LEAD	24 mΩ
WIMA .1μfd 2000V MKP	40 mΩ
ROYAL MICA .125μfd 1000V	22.5 mΩ
WIMA .15μfd 1250V FKP	15 mΩ
RHOED .22μfd 160V MKP	22.5 mΩ
RHOED .22μfd 1600V MKP	25 mΩ
RHOED .22μfd 1000V FKP AXIAL	22.5 mΩ
WIMA .22μfd 1250V MKP	12 mΩ
WIMA .22μfd 1000V MKP	28 mΩ
BYCAP .25μfd 1000V FKP	14.3 mΩ
BYCAP .5μfd 1000V FKP	9.3 mΩ
BYCAP 1.0μfd 1000V FKP	8.3 mΩ
STANLEY R.M. 1.0μfd 1000V	13 mΩ
WIMA 1.5μfd 400V MKP	9 mΩ
SPRAG 2.0μfd 200V MKP	26 mΩ
RHOED. 2.2μfd 400V MKT	19 mΩ
SPRAG 2.5μfd 200V MKP	20.5 mΩ
SPRAG 3.0μfd 200V MKP	17.5 mΩ

**Table 4-2: Capacitor Performance Specifications (Continued)**

BAR. TIT. 50pf 6kv	9300 mΩ
BAR. TIT. 100pf 6kv	7500 mΩ
BAR. TIT. 480pf 6kv	1600 mΩ
COND PROD 200pf 30kv	465 mΩ
TDK 560pf 50kV	820 mΩ
TDK 1000pf 50kV	500 mΩ
TDK 1400pf 20kV	358 mΩ
TDK 1700pf 30kV	311 mΩ
TDK 1700pf 50kV	318 mΩ
TDK 2500pf 20kV	231 mΩ
MUR ER 2700pf 30kV	266 mΩ
KD STRON. TIT. 10,000pf 7.5kV	172 mΩ

## APPENDIX 5

### TRANSFORMER DESIGN

The high performance transformer design used in all of the nonlinear magnetic pulse compressors is an advanced hybrid transformer developed by SRL. This transformer combines the advantages of conventional multiple turn transformers with the unique properties of an induction accelerator. This makes pulse transformers with extremely low leakage inductance and high step-up ratios a reality.

In conventional magnetic pulse compressor design, transformers are frequently interleaved with compression stages. When the operating impedance becomes difficult to handle, a transformer is used to change the value to an optimum impedance. This avoids compression reactors with thousands of turns or a fractional turn. In high performance magnetic switches which operate on submicrosecond time scales, these transformers must be carefully designed as continuous transmission lines. Great care is taken to both confine the leakage magnetic fields and simultaneously to avoid breakdown level electric fields.

Step-up transformers can be constructed by either using multiple secondary turns, using fractional numbers of primary turns, or any combination thereof. At first, the concept of fractional primary turns may seem somewhat foreign but it is the basis of all induction linacs where forcing the electron beam to make several secondary turns would be very difficult.

An equivalent circuit for a transformer using a fractional turn primary appears in Fig. 5.1. A simplified cross-sectional view appears in Fig. 5.2. Here multiple primary windings are all fed in parallel while the secondary is a single turn formed by the series connection of the same windings. The equivalent circuit for the more conventional multiple secondary turn transformer appears in Fig. 5.3, while a simplified cross-section is shown in Fig. 5.4. Here a single high permeability core is used for isolation and the secondary makes multiple passes around the core adding on the primary voltage with each pass.

In the case of either transformer it is extremely important to understand where currents are flowing and in which regions the magnetic fields are confined. An example is presented in Fig. 5.5. Here the regions occupied by the magnetic fields has been shaded. We will assume that the permeability of the magnetic core is infinite and therefore the shunt inductance is infinite and no net current flows around the core. In order for the currents to exactly cancel, the ratios of the currents in the primary and secondary are equal to the ratio of the number of turns. This can be understood more intuitively by thinking of the primary transmission line as feeding into the secondary transmission lines all in parallel.

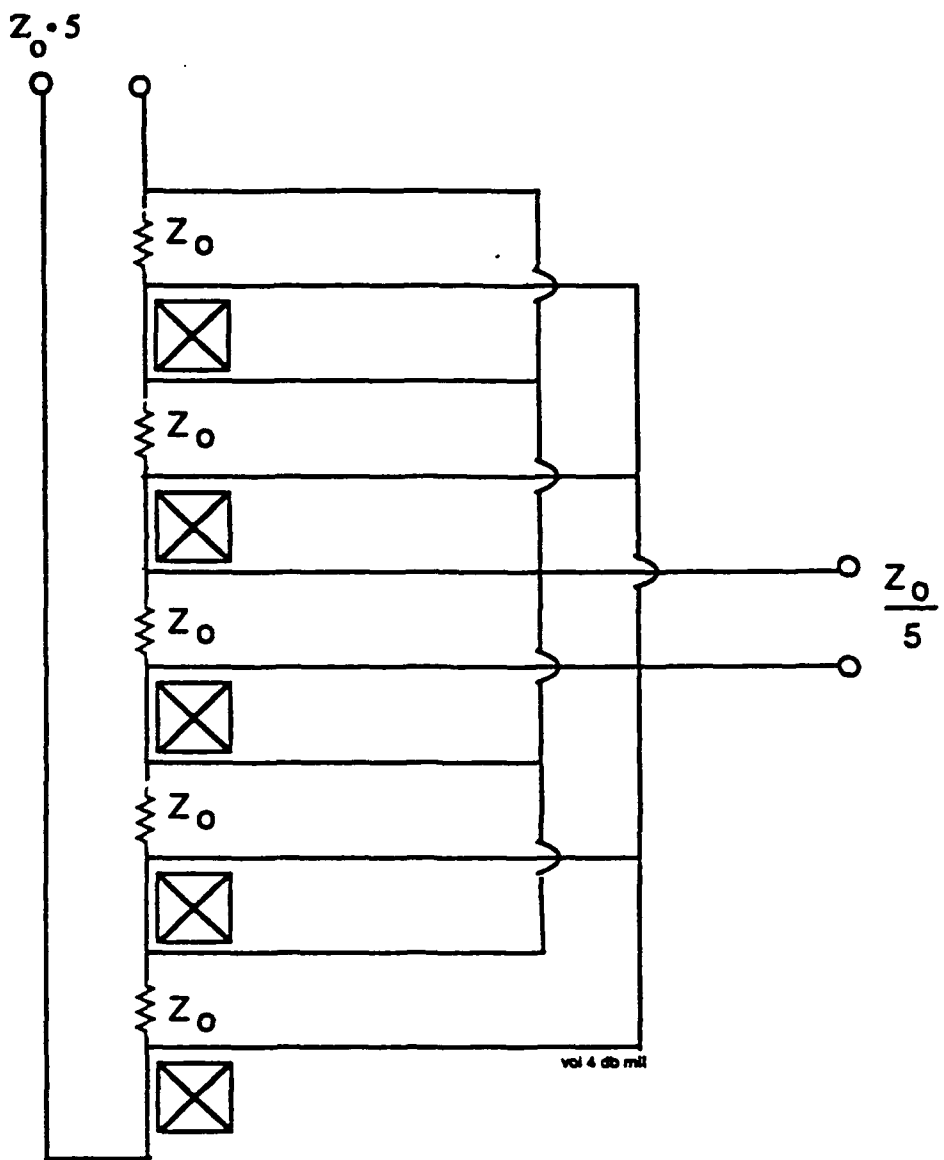


Figure 5.1: Equivalent circuit of induction style transformer

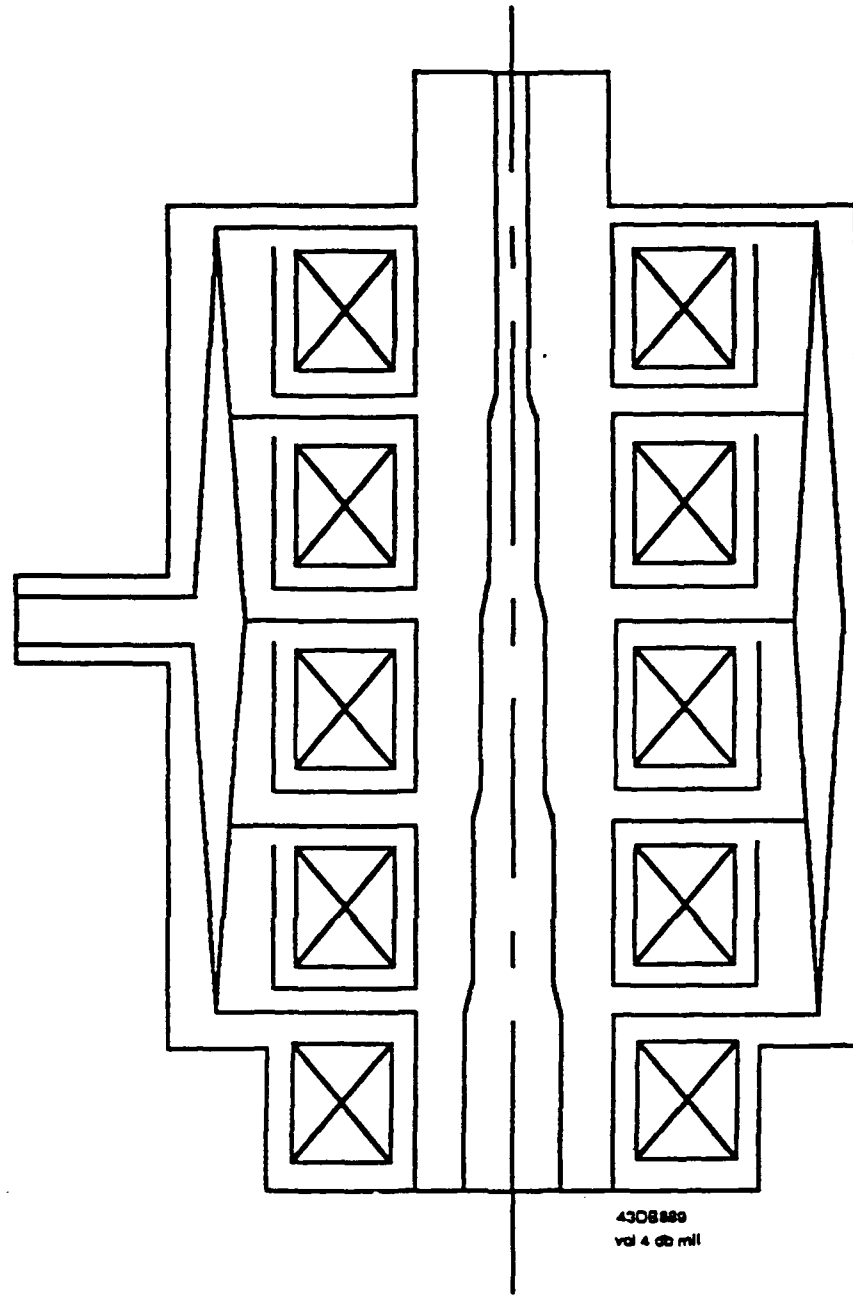


Figure 5.2: Simplified fractional turn primary transformer

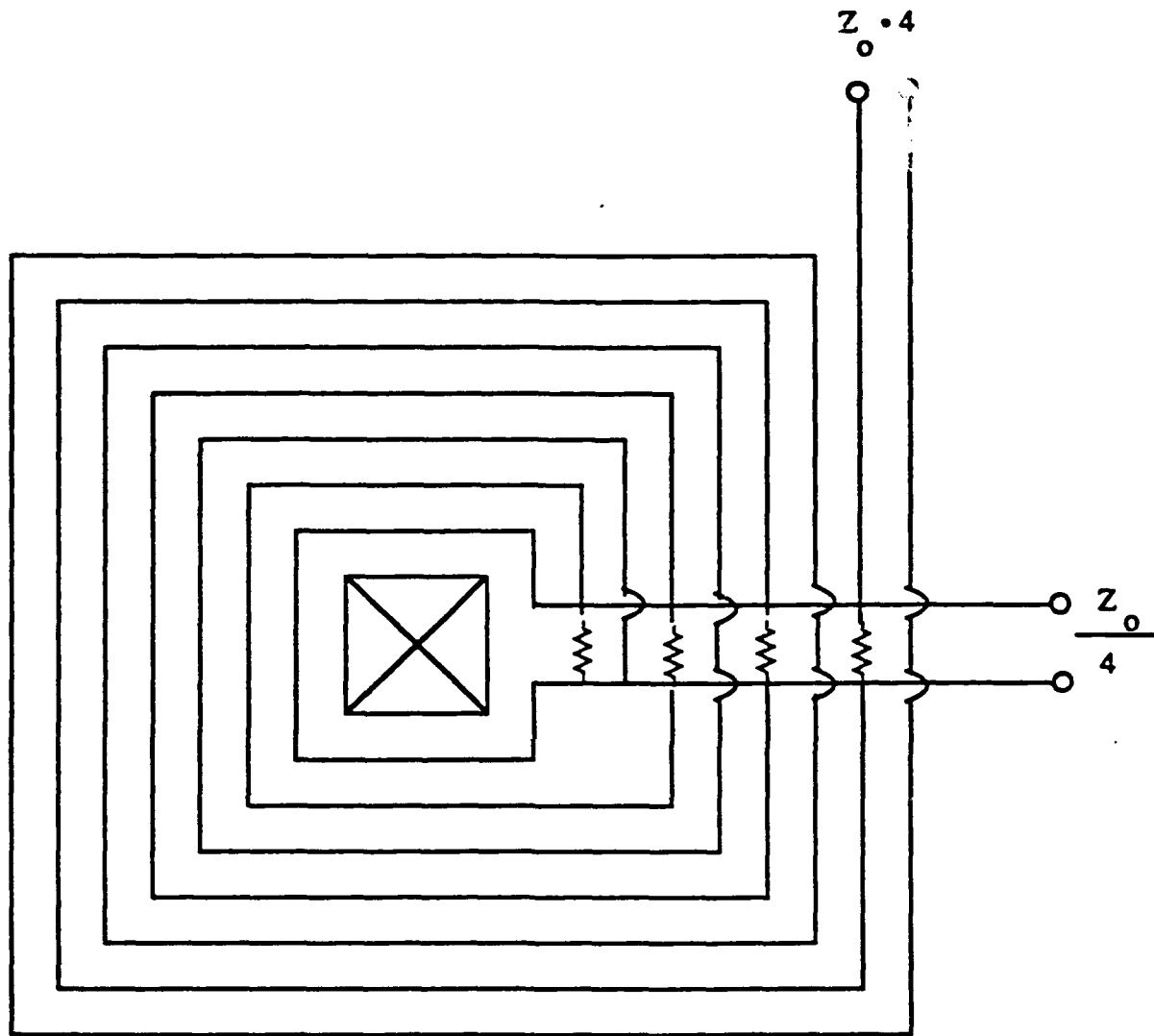


Figure 5.3: Equivalent circuit of multiple turn secondary transformer

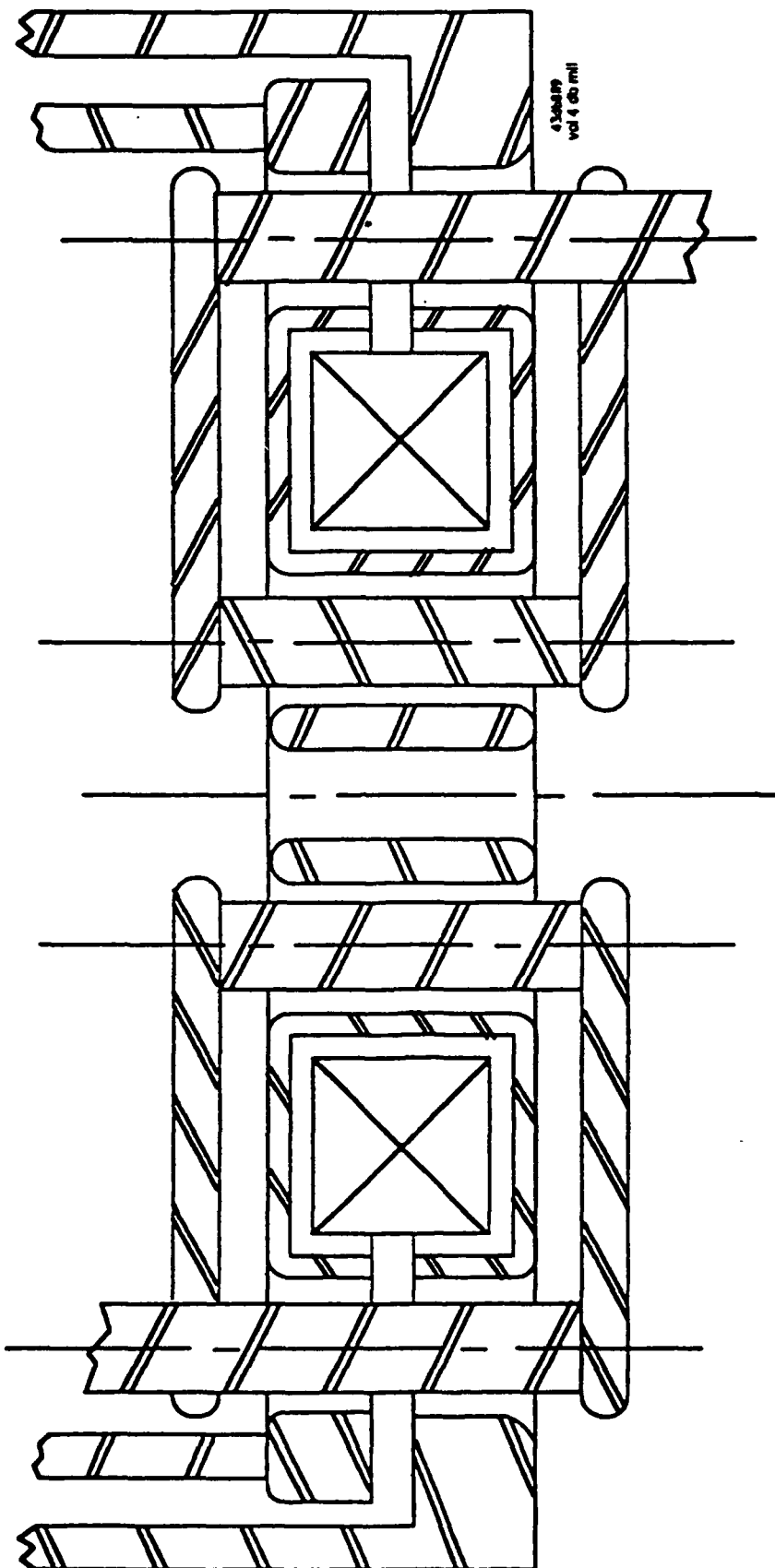


Figure 5.4: Simplified multiple turn secondary transformer

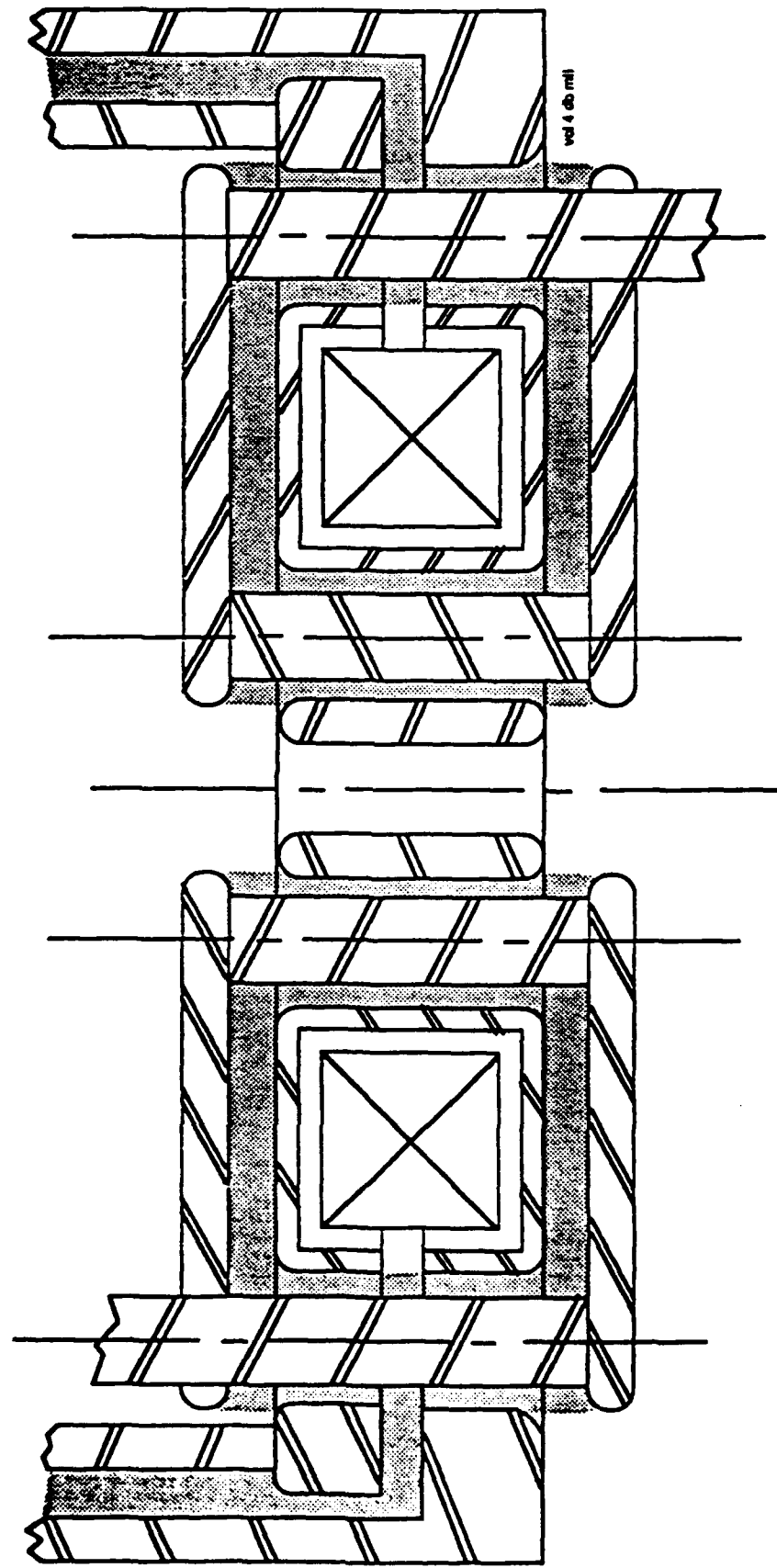


Figure 5.5: Simplified multiple turn secondary transformer with volume occupied by leakage field shown shaded

## APPENDIX 6

### NONLINEAR MAGNETIC COMPRESSORS

The concept of using saturable reactors as a basis of high power pulse generators is not a new concept and certainly not invented by the authors, but there have been few recent applications of this technology. Perhaps the authors rather than inventing this idea have helped to find it a home.

The use of saturable reactors for high power pulse generation was first described by Melville in 1951. At that time output powers levels as high as a megawatt were being sought for Radar applications. There were no SCRs at the time and thyratrons were rapidly developed to the point where they could deliver these power levels routinely and the idea of nonlinear magnetic pulse compression simply disappeared. The development of induction linear accelerators and discharge lasers requiring gigawatts of input power revived this old technology.

The basic principle underlying nonlinear magnetic driver operation involves using a saturable core as an inductor in a resonant circuit. The circuit is designed to allow the core of the next stage to saturate before a significant fraction of the energy stored in the capacitors of the previous stage is transferred. This nonlinear saturation phenomenon shifts the resonant frequency of this resonant circuit by the square root of the permeability shift as the core saturates. These stages are typically cascaded (Fig. 6.1) and energy is coupled faster and faster from one stage to the next. These circuits are efficient at transferring power in both directions since they act not only to upshift the frequency in the forward direction thereby providing temporal compression, but also downshift the frequency of a voltage pulse as it cascades back up the chain in the reverse direction. The energy which reflects from the mismatched load can be saved and applied to the next pulse.

In the remainder of the section we present a more quantitative description of the compression chain operation. The analyses is based on saturable inductors with toroidal geometries, and for the sake of clarity several simplifying approximations have been introduced. All circuit components will be assumed lossless and all extraneous inductances ignored. Also the expression for saturated inductance will assume that the area enclosed by the turns is simply the core cross-sectional area, while in practice the packing factor must be properly calculated.

Saturation of an inductor occurs when the magnetic field in the inductor core reaches the saturation magnetization. This assumes of course that the core material is ferri- or ferromagnetic material. Saturation is measurable as a large incremental change in the material permeability.

According to Maxwell,

$$\int E \cdot dl = V_L = N \frac{\partial \Phi}{\partial t} = NA \frac{\partial B}{\partial t}$$

$$\int V_L dt = NA \Delta B$$

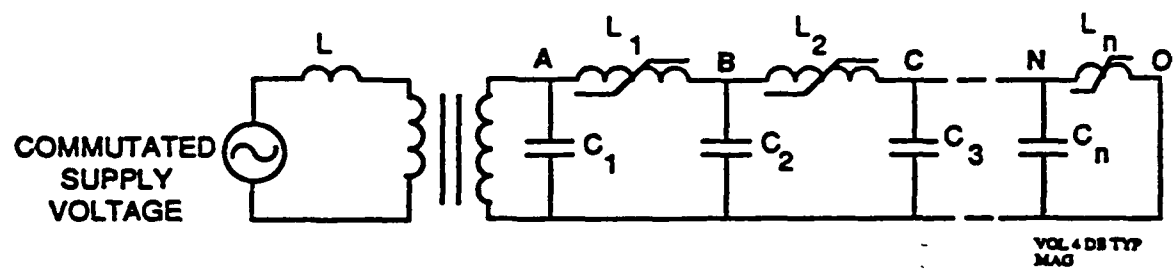
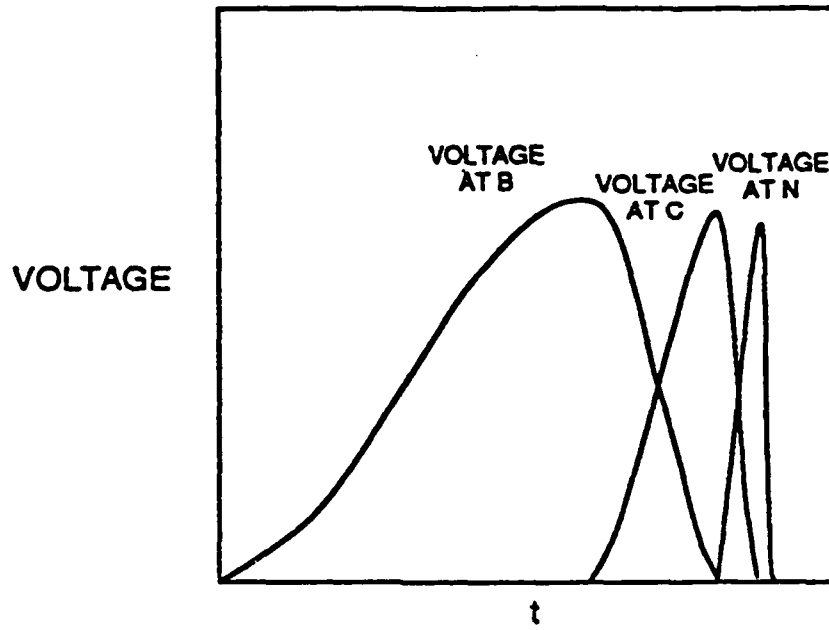


**Figure 6.1: Typical magnetic switch operation**

and if the core has been reset

$$\int_0^{\tau_{sat}} V_L dt = NA(-(-B_r) + B_s) = NA\Delta B,$$

where N is the number of turns around the core, A is the area of the core, and  $B_r$  ( $B_s$ ) the remanent (saturating) magnetic field.

If we make all of the capacitance values in the compression chain equal to  $C_0$ , then for a capacitor preceded in the chain by  $L_{n-1}$  and followed by  $L_n$  the time required to charge the next capacitor in line after inductor  $L_{n-1}$  saturates is given by

$$\tau_{charge}^{C_n} = \tau_{discharge}^{C_{n-1}} = \pi \left( L_{n-1}^{sat} \cdot \frac{C_{n-1} C_n}{C_{n-1} + C_n} \right)^{1/2} = \pi \left( \frac{L_{n-1}^{sat} \cdot C_0}{2} \right)^{1/2}$$

The time required to charge capacitor  $C_n$  should be designed to be approximately equal to the time to reach  $B_{sat}$  in inductor  $L_n$ . Therefore

$$\tau_{sat}^{L_n} \approx \tau_{charge}^{C_n} = \frac{\Delta B_s N_n A_n}{\bar{V}_c}$$

Ideally

$$\bar{V}_c = V_{C_0} \int_0^{\pi/\omega} \frac{(1 - \cos \omega t)}{2} dt = \frac{V_{C_0}}{2}$$

therefore

$$\tau_{charge}^{C_n} \approx \frac{2\Delta B_s}{V_{C_0}} N_n A_n$$

where  $V_{C_0}$  is the peak charge voltage of capacitor  $C_n$ . After inductor  $L_n$  saturates we find:

$$L_n = \frac{\mu_n^{sat}}{2} w_n N_n^2 \ln \left( \frac{R_{0_n}}{R_{i_n}} \right) \approx \frac{\mu_n^{sat} N_n^2 A_n}{2\pi R} \approx \frac{\mu_n^{sat} N_n^2 A_n}{\text{volume}}$$

Where  $w_n$  is the axial width of the toroid  $R_{0_n}$  ( $R_{i_n}$ ) the core outer (inner) radius. It also follows that if the core saturates at the peak of the charging waveform then

$$L_{n-1}^{sat} = \frac{2}{C_0} \left( \frac{2\Delta B_s N_n A_n}{\pi^2 \bar{V}_c} \right)^2$$

and

$$\frac{L_n^{sat}}{L_{n-1}^{sat}} \approx \frac{\mu_n^{sat} \pi^2}{\text{volume}_n} \cdot \frac{(\frac{C_0}{2} \bar{V}_c^2)}{4\Delta B_s^2} \approx \frac{\text{energy}}{\text{volume}_n} \left( \frac{\mu_n^{sat} \pi^2}{4\Delta B_s^2} \right)$$

since

$$\text{gain} = \frac{\tau_{charge}^{C_n}}{\tau_{charge}^{C_{n+1}}} = \left( \frac{L_n^{sat}}{L_{n+1}^{sat}} \right)^{1/2}$$

The core volume requirement to produce a given temporal compression and corresponding energy gain is given by

$$\text{volume}_n = \text{gain}^2 \cdot \text{energy} \left( \frac{\mu_n^{sat} \pi^2}{4 \Delta B_s^2} \right)$$

In practice not all of the fields are confined to the core and if we define the packing factor pf to be the ratio of the inductance calculated by assuming all of the magnetic field energy is stored in an ideal saturated toroid to the actual measured saturated inductance then our core volume requirement can be rewritten as

$$\text{volume} = \text{gain}^2 \cdot \text{Pulse Energy} \cdot \left( \frac{\mu_0 \cdot \pi^2}{4 \cdot (\Delta B_s \cdot pf)^2} \right)$$

The packing factor is defined as

$$pf = \frac{\int_{V_f} H^2 dv}{\int_{\text{all space}} H^2 dv}$$

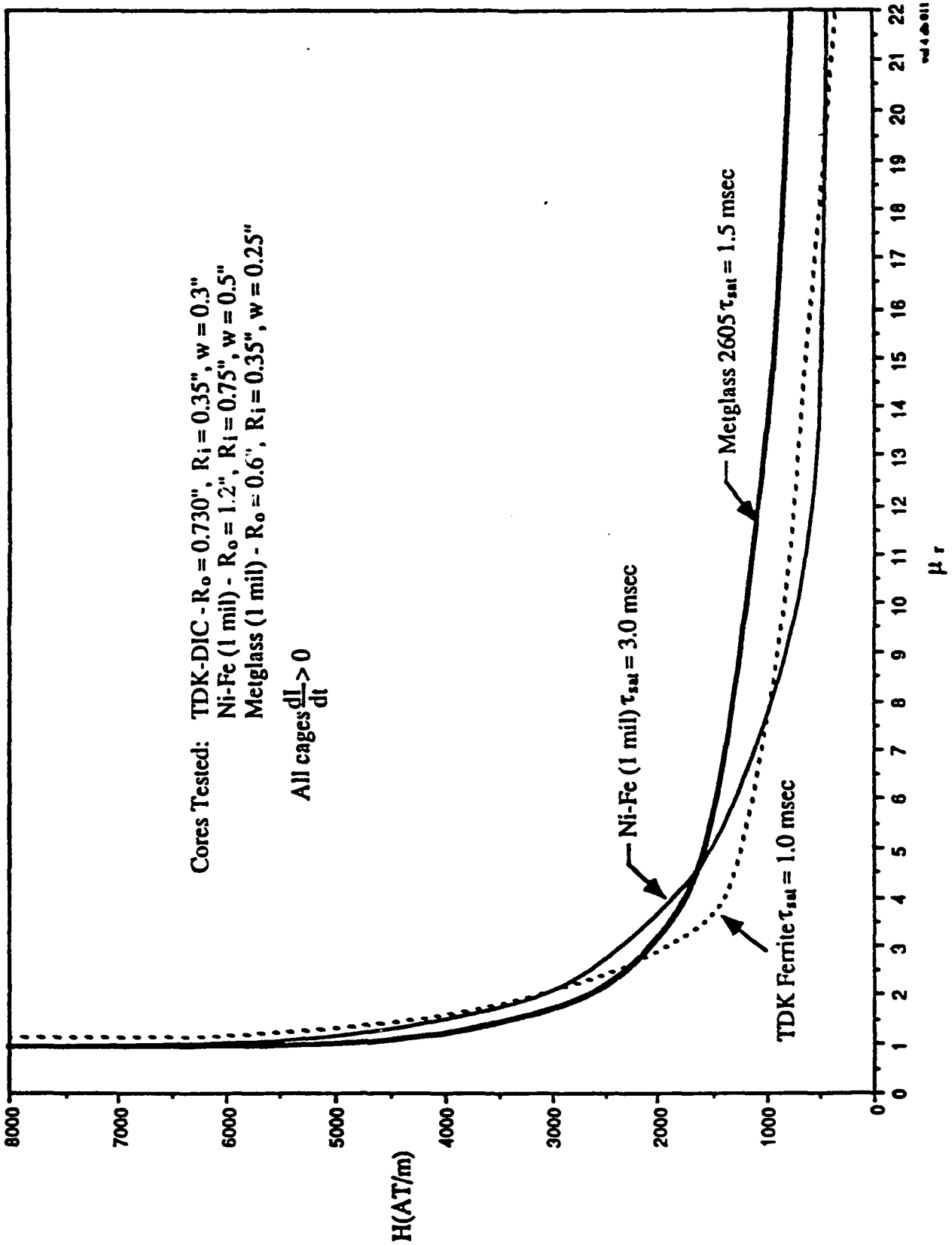
where  $V_f$  is the actual volume occupied by the ferri- (ferro) magnetic core material excluding all interlaminar insulation and voids. Optimization of this packing factor is crucial in magnetic switch design and is accomplished by enclosing the core in a tightly fitting conducting housing. The multiple turns are formed as coaxial transmission lines which pass through this housing. Circulating currents set up in this housing exclude the magnetic flux and contain it in the desired volumes.

With the saturable material completely enclosed in conducting coaxial housings, the voltage per turn associated with the  $dB/dt$  of the core appears across a single narrow gap on the outside diameter of each housing. Connecting the coaxial transmission lines in the inner and outer housings with radial transmission lines across the top and bottom of the core completes the turns. The impedances of these transmission lines are adjusted so that

$$Z_{LINE} \approx \sqrt{\frac{2 \cdot L_{sat}}{C}}$$

while simultaneously every effort is made to minimize  $L_{sat} \cdot C$  which is proportional to the square of the pulse length. Here  $L_{sat}$  and  $C$  refer to the saturated inductance of the reactor and the value of the storage capacitance respectively.

It is important in the design of a compression stage that a minimum of excess core volume is employed as the losses are linearly proportional to the core volume. In a properly designed core  $\mu_n^{sat}$  is close to  $\mu_0$  and a curve is provided in Fig. 6.2 for the purpose of fine tuning a design.



6-5

Figure 6.2

## APPENDIX 7

### COMMAND RESONANT CHARGE SYSTEMS

Command Resonant Charge (CRC) systems are a common interface between any repetitive pulse power system and a DC supply. The job of a CRC is to deliver a preset quantity of energy to the intermediate storage units between pulses. The CRC provides a technique for pulse charging without the 50% energy loss associated with resistance charging. In its simplest form the CRC appears as shown in Fig. 7.1.

If we assume switch  $S_2$  is open and  $V_{C_0}=0$  at time  $t=0$ , then when switch  $S_1$  closes  $C_0$  charges to  $V_{C_0}(t=\tau_{charge}) = V_{C_{BANK}} \cdot \frac{2C_{BANK}}{C_{BANK}+C_0}$  in a time given by  $t=\tau_{charge} = \pi \sqrt{L \cdot \frac{C_{BANK}C_0}{C_{BANK}+C_0}}$ . If  $C_{BANK}$  is much large than  $C_0$  then  $C_0$  is charged to a voltage almost twice that of the bank voltage.

If the power supply impedance is high then  $C_{BANK}$  may not recharge back to its original level during a burst of pulses but only between bursts. The voltage on  $C_{BANK}$  for the  $n^{th}$  pulse is given by

$$V_{BANK} \approx V_{BANK}(t_0) - n \cdot \frac{C_0 \overline{V_{C_0}(\text{charged})}}{C_{BANK}} + n\Delta t \frac{(V_{BANK} - V_{SUPPLY})}{R}$$

In burst mode applications  $R$  is typically very large in order that the DC power supply requirements can be scoped to handle the average load and not the peak load. This greatly reduces the cost of the DC supply. In the case that  $R$  is large then the capacitor bank voltage continuously sags from the first pulse to each successive pulse in a burst. The most common solution to this problem is a regulation scheme known as DeQueing. A simple CRC with DeQueing appears in Fig. 7.2.

Here we see that a third switch ( $S_3$ ) has been added to our previous CRC circuit. Closing  $S_3$  terminates the charge by shorting the charge inductor. Charge that would have been conducted to capacitor  $C_0$  simply flows in a loop around and through the charging inductor until the next charge pulse when this current adds to the current flowing through switch  $S_1$ . If a series of pulses all at a constant voltage level are desired then switch  $S_3$  is closed on each charging cycle at a preset voltage level which is less then the lowest voltage charge state in the series. In other words as all but one of the pulses would normally charge to a higher level then the lowest voltage pulse, each pulse except the lowest level one are clipped to a voltage equal to or less then the nominal charge voltage of the lowest voltage pulse in the series.

Normally this is accomplished by comparing the voltage on  $C_0$  with a preset reference level and closing switch  $S_3$  when this level is reached. The reference voltage is adjusted downward until all of the pulses in a series are clipped and at a common voltage level (Fig. 7.3).

The problem with this simple minded scheme is that a time delay will always exist between the time that  $C_0$  is sensed to have the desired voltage and when switch  $S_3$  is closed to halt the

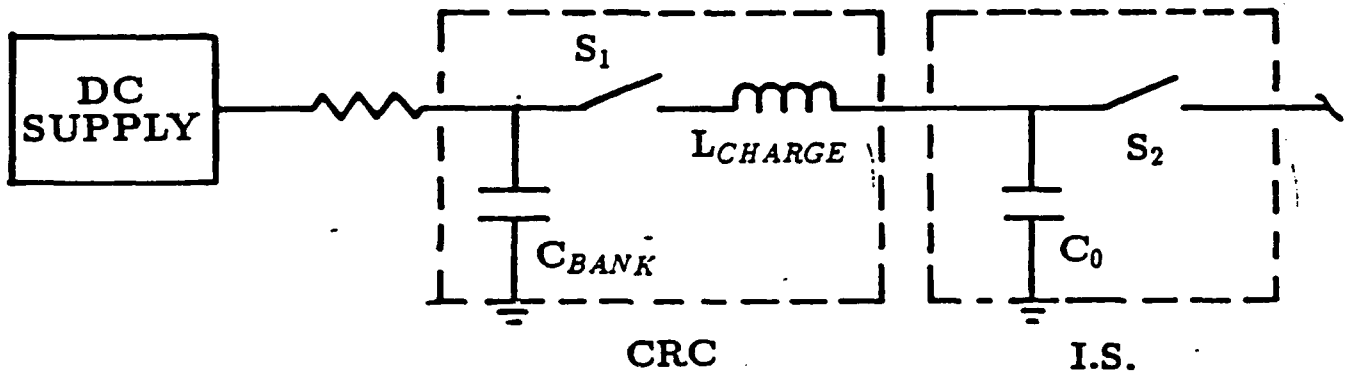


Figure 7.1: A CRC in its simplest form

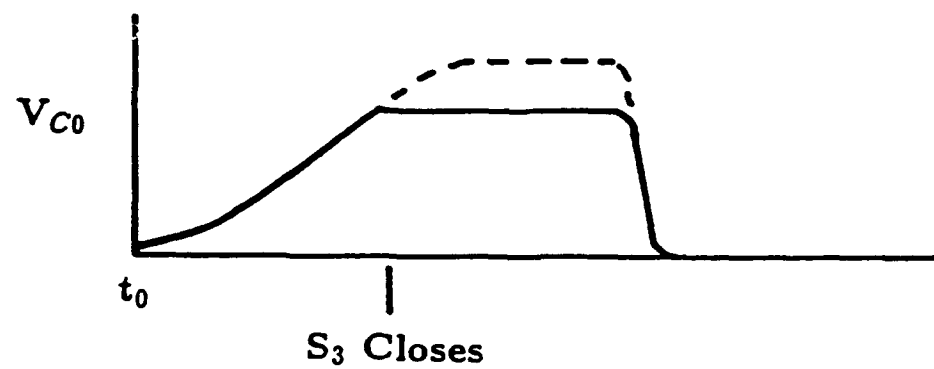
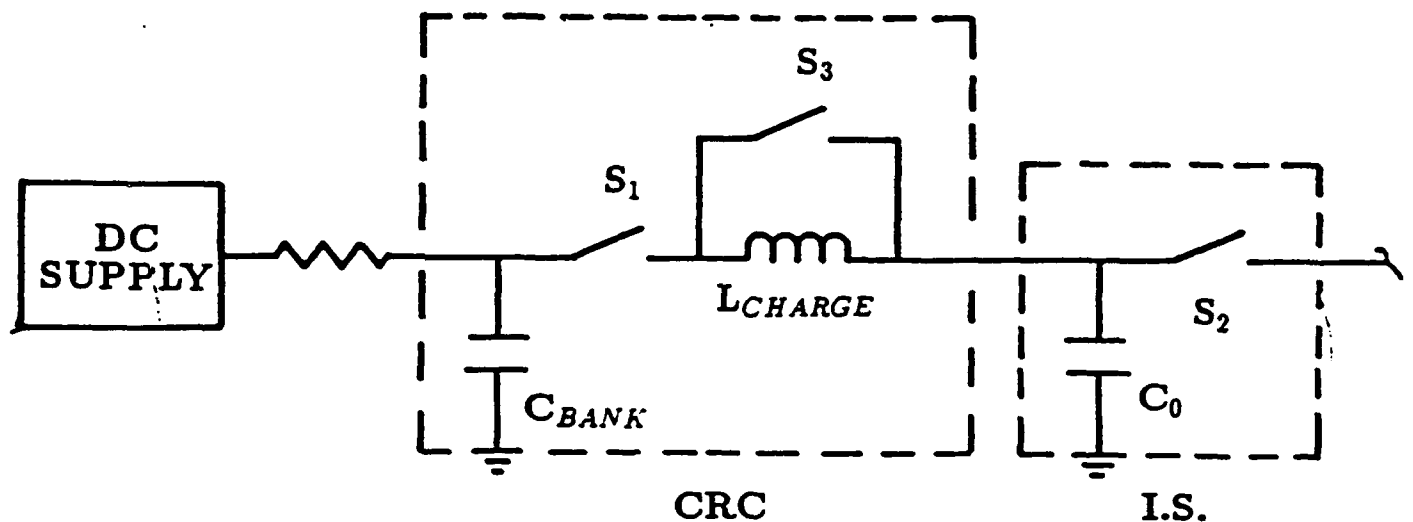


Figure 7.2: CRC with DeQue Regulation

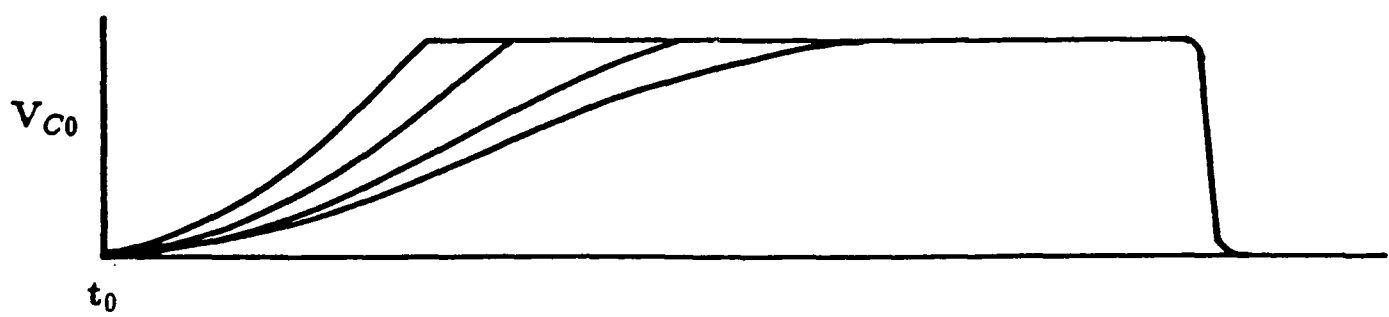
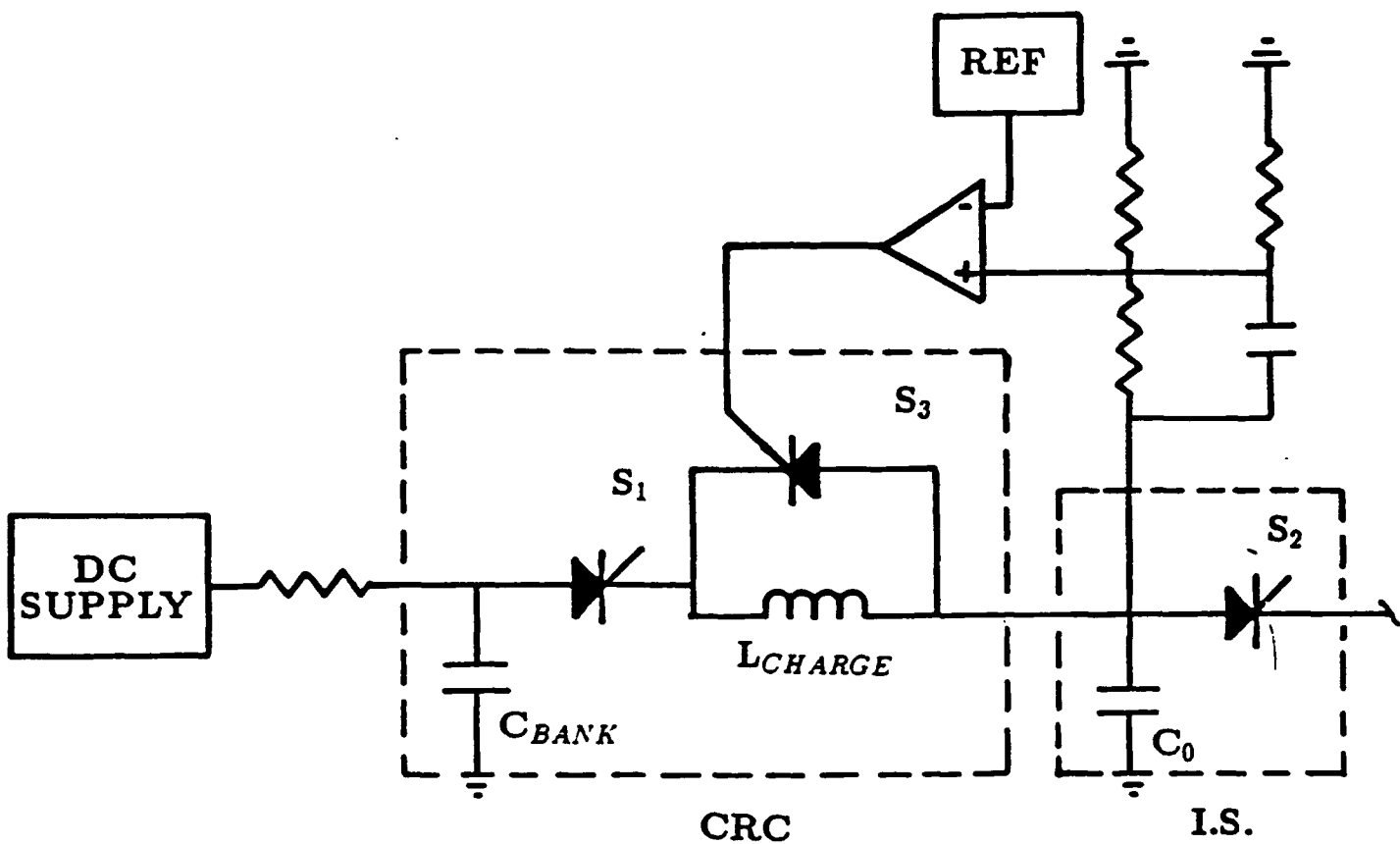


Figure 7.3: CRC with DeQue Regulation

charging cycle. Even if the time delay is the same for all pulses in the burst, the first derivatives (rate of charge) of  $V_{C_0}$  will vary between successive pulses and the amount of overshoot created by this time delay will depend on the unclipped voltage of each pulse. More explicitly, if  $t_0$  is the time that  $V_{C_0} = V_{REF}$ , then  $C_0$  will continue to charge for a time  $\Delta t$  required to sense this occurrence and close switch  $S_3$ . The voltage on capacitor  $C_0$  at time  $t_0 + \Delta t$  (Fig. 7.4) is given as

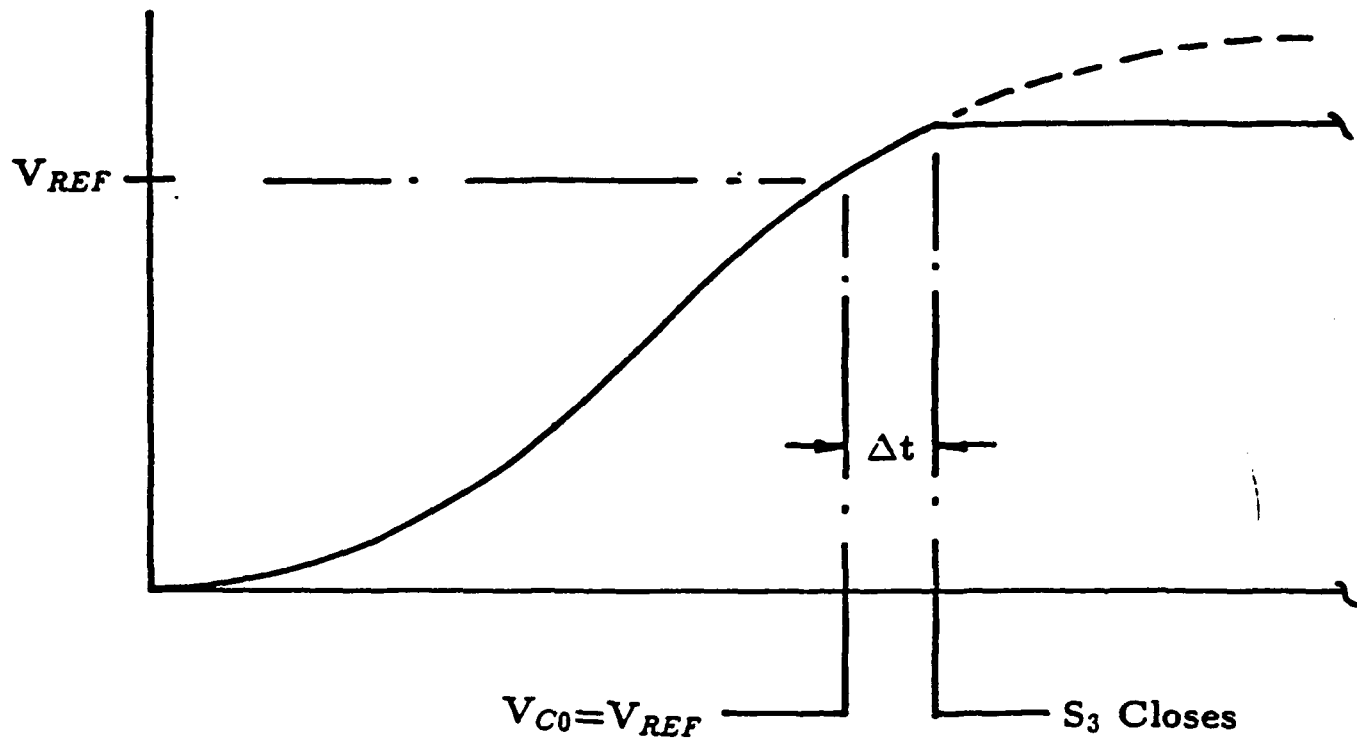
$$V_{C_0}(t_0 + \Delta t) = V_{C_0}(t_0)(= V_{REF}) + \frac{dV_{C_0}}{dt} \Delta t + 1/2 \frac{d^2V_{C_0}(t)}{dt^2} \Delta t^2 \dots$$

Now the quantity  $\frac{dV_{C_0}}{dt} = \frac{I_{CHARGE}}{C_0}$  and the charging current could be simply sensed by a current shunt either on the ground connection of the capacitor bank of  $C_0$  but it has been found simpler to built a derivative divider (simply a capacitor in series with a resistor) adjusted to add directly to the standard resistive divider output. As many derivatives can be taken as found desirable but usually one or two is enough. In spite of the simplicity of this simple error correction scheme many people are not aware of it and it is seldom used.

Another method of achieving voltage regulation while using a CRC is known as post-regulation (Fig. 7.5). The idea behind post-regulation is simple. The intermediate storage capacitor is allowed to charge to a voltage in excess to that which is desired. After the charging sequence is completed switch  $S_3$  is closed and  $C_0$  is drained until the desired voltage is achieved. Once this preset final voltage level is reached then switch  $S_3$  is opened. It is immediately obvious that in this case that an SCR would be an inappropriate switch since it cannot be reopened while conducting current. A switch such as a MOSFET would be required, but this not the only way to achieve regulation using this concept.

In the case that switch  $S_3$  is only a closing switch then this technique can still be applied but the closing of switch  $S_3$  must be properly timed. This is further illustrated in Fig. 7.6. Switch  $S_3$  is closed earlier when the initial charge state of  $C_0$  is higher. The earlier switch  $S_3$  is closed the more charge is drained from  $C_0$  through  $S_3$ . Switch  $S_3$  need not be an opening switch in this case and will recover after  $C_0$  is discharged through switch  $S_2$ .

Energy recovery is an important feature which should be added to all pulse charging and gatling gun systems. It is a rare situation indeed when all of the energy delivered at the output of a pulse generator is actually absorbed by the load. In the case of Magnetic Switches (Nonlinear Magnetic Pulse Compressors) energy reflected from a mismatched load travels back up the pulse compression chain and appears as a reversed voltage on  $C_0$ . The reflected energy will always appear in the form of a voltage opposite in polarity to the initial charge state of  $C_0$  independent of the sign of the mismatch. The reason for this is that once saturated, all nonlinear magnetic compression reactors act as diodes and will pass charge in only one direction, in this case the direction of the main pulse. If the sign of the reflected wave is the same polarity as the main drive pulse then the direction of these ferromagnetic diodes will reverse themselves after a preset time beginning with the stages closest to the load but when it reaches the transformer, transformer saturation will reverse the polarity and it will travel rapidly to the front of the chain.



$$V_{FINAL} = V_{C0}(t + \Delta t) = V(t_0) + \frac{dV}{dt} \Delta t + \frac{1}{2} \frac{d^2V}{dt^2} \Delta t^2 + \dots$$

Figure 7.4: Time Delay Induced Error in DeQue Regulation

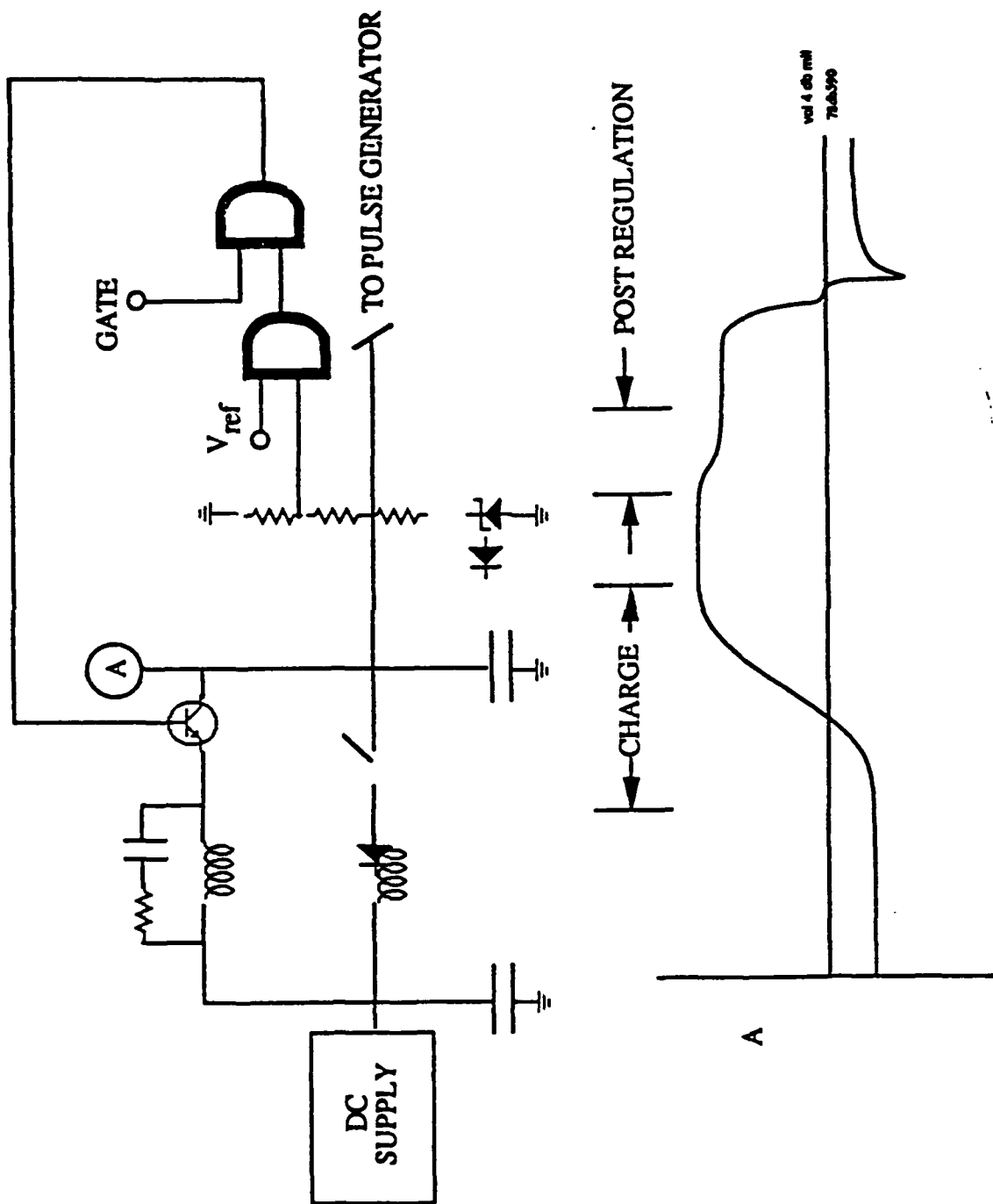


Figure 7.5: Post regulation circuit

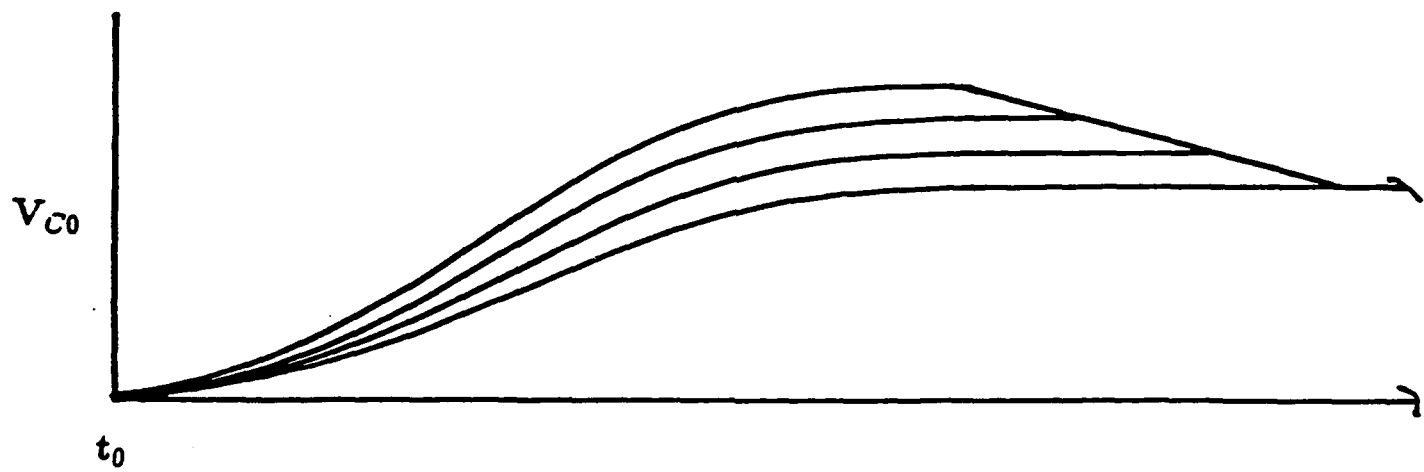
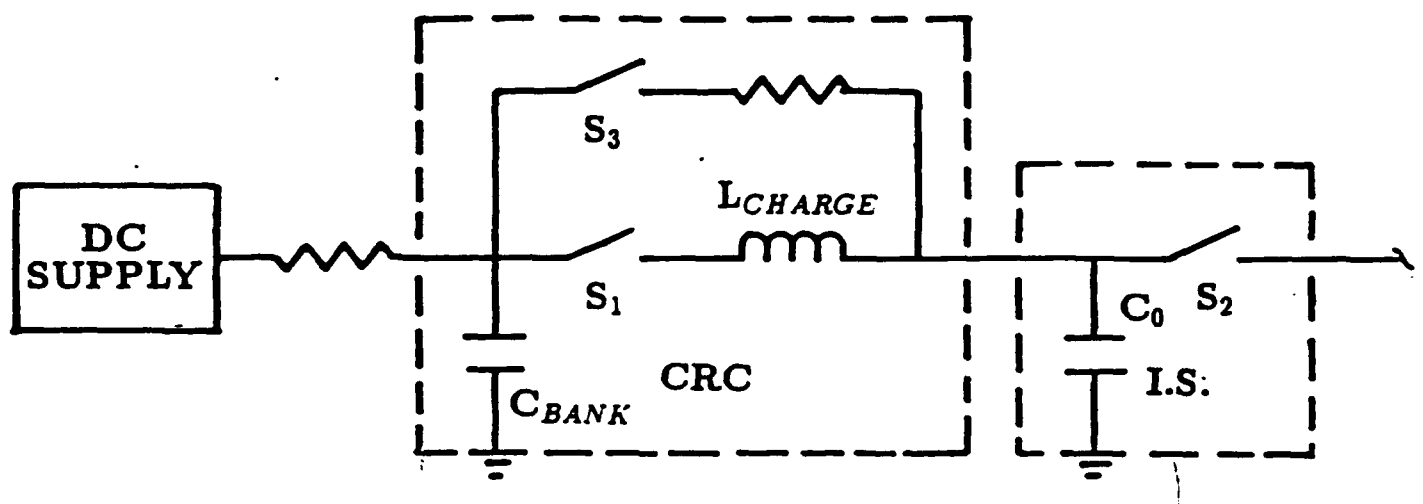


Figure 7.6: Simple Post Regulation Scheme

The energy recovery circuit is simple but care must be taken to avoid instabilities. The typical circuit is as shown in Fig. 7.7. When the recovered charge is recomputed into  $C_0$  by switch  $S_2$  which would still be conducting from the main discharge pulse, current begins to flow in inductor  $L_2$ . The series combination of  $L_2$  and  $C_0$  forms a resonant circuit. The resulting waveform on  $C_0$  is also depicted in Fig. 7.7, and after a period of time given approximately by  $t = \pi\sqrt{L_2 C_0}$  the polarity of  $C_0$  has been reversed and this energy will automatically reduce the energy required to recharge  $C_0$ .

The astute reader will immediately recognize a problem. If  $C_0$  begins not from zero but with some initial charge, then the final charge voltage will depend on the amount of recovered charge. Oddly enough the greater the recovered charge the lower will be the level of the next resonant charge. Specifically if when the command resonant charge cycle begins (switch  $S_1$  closes)  $C_0$  begins with a voltage  $V_0$  then the final unregulated charge voltage will simply be given as

$$V_{C_0}(t = \tau_{charge} = V_0 + 2(V_{BANK} - V_0) \left( \frac{C_{BANK}}{C_0 + C_{BANK}} \right)$$

In fact if  $V_0$  approaches  $V_{BANK}$  there will be no charge transferred at all. If  $V_0$  is the opposite polarity of  $V_{BANK}$  then things really get interesting. In this case  $C_0$  charges to a voltage higher than if  $C_0$  were initially set to zero voltage. In most cases a higher initial voltage on  $C_0$  will mean more energy in the reflection. Each successive pulse will increase in amplitude until there is usually a problem. This is further illustrated in Fig. 7.8.

In the case of negative feedback the charge state typically becomes bimodal, but in the case of positive feedback charge voltages can reach phenomenal levels determined primarily by the Q of the charging circuit. Initial experiments in this area proved that a charge voltage in excess of 500 volts could easily be reached with a power supply setting of only 20 volts.

The proper technique for employing energy recovery is to properly time the next charging cycle so that the feedback from energy recovery is neither negative or positive as shown in Fig. 7.9. Switch  $S_1$  (Charge switch) must be closed a preset interval after the closure of switch  $S_2$  (Discharge switch). At first this condition would appear to fix the PRF at some constant rate, but that is not the case. The reader's mental state must be altered to think in terms of discharging  $C_0$  and then charging rather than thinking the reverse. The discharge pulse rather than the charge pulse is the first event in generating a burst of pulses.  $C_0$  remains fully charged between bursts.

Energy recovery is essential for this application as efficiency is a real concern in these high average power systems.

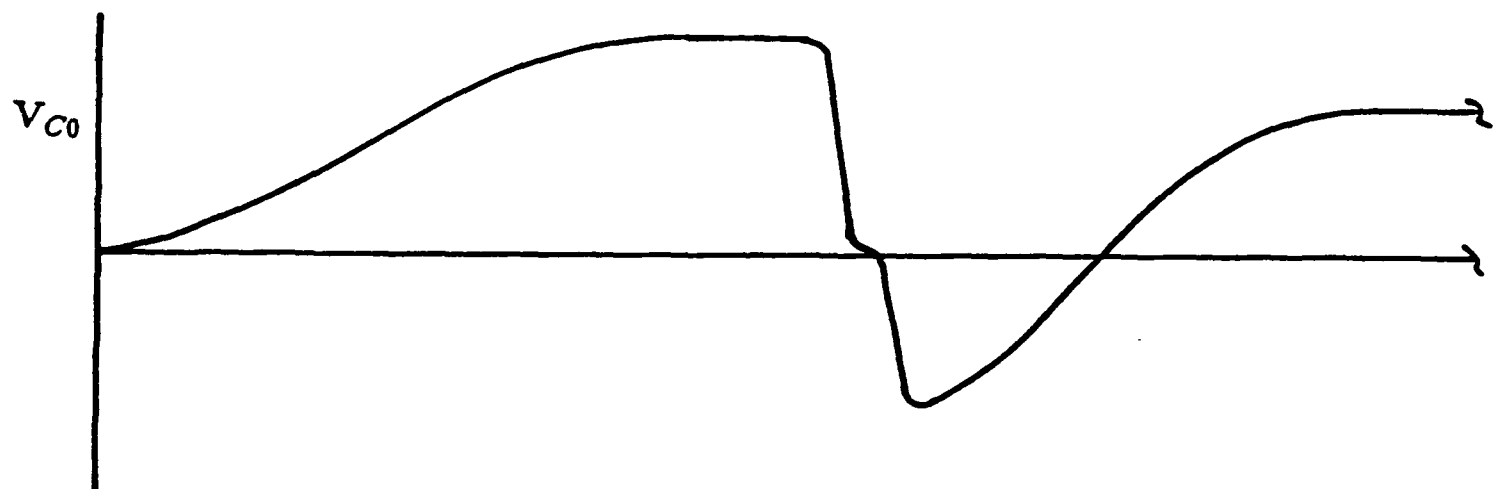
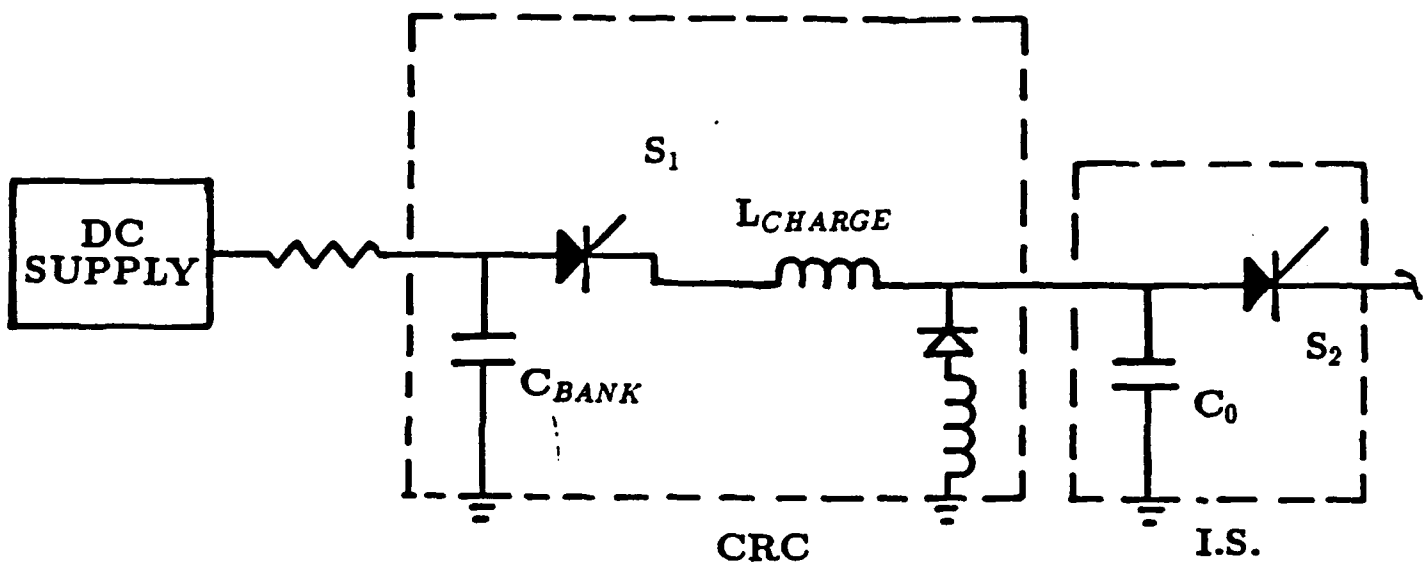


Figure 7.7: Simple Energy Recovery Scheme

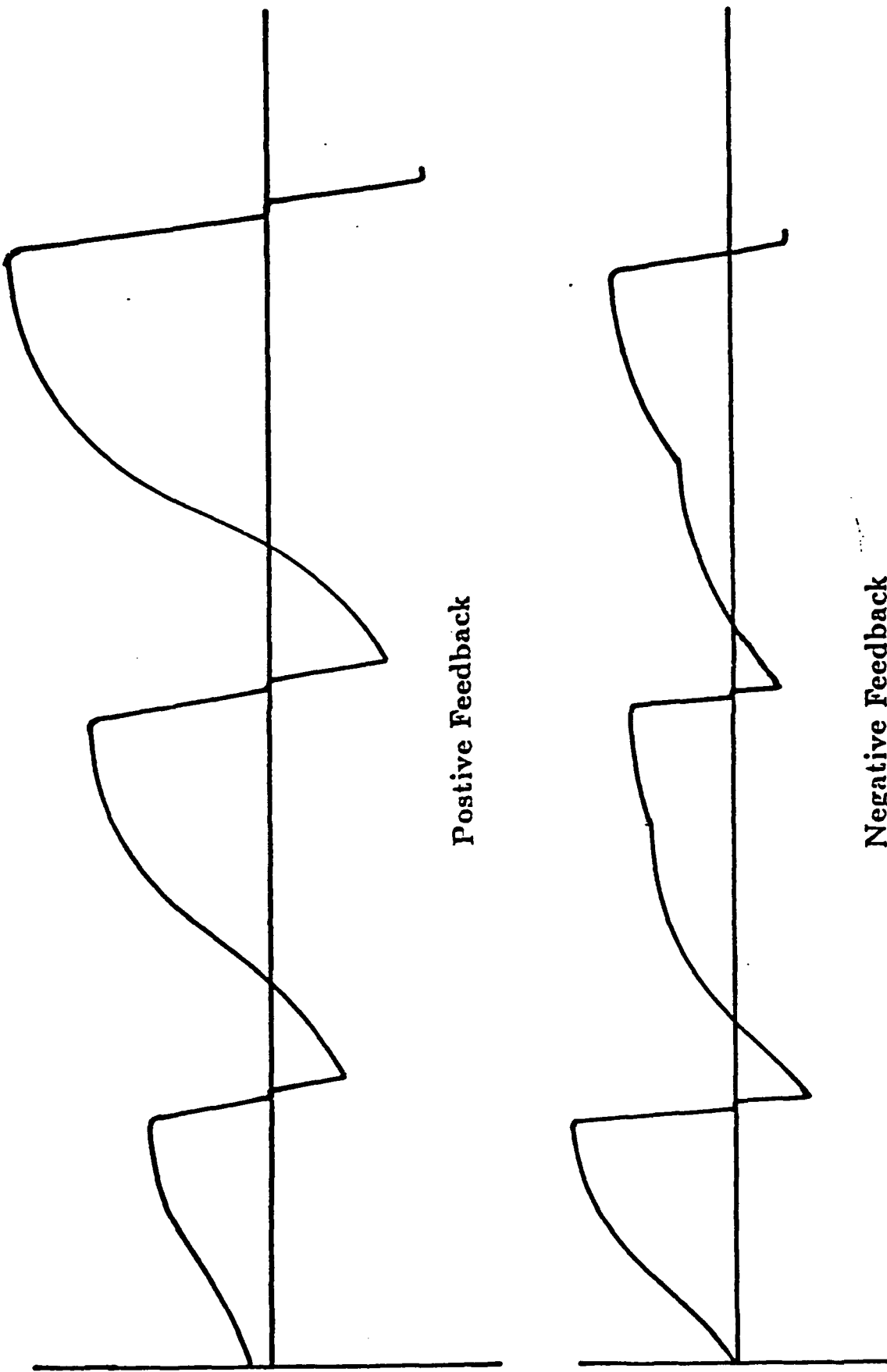


Figure 7.8: Effect of Timing on Energy Recovery Circuits

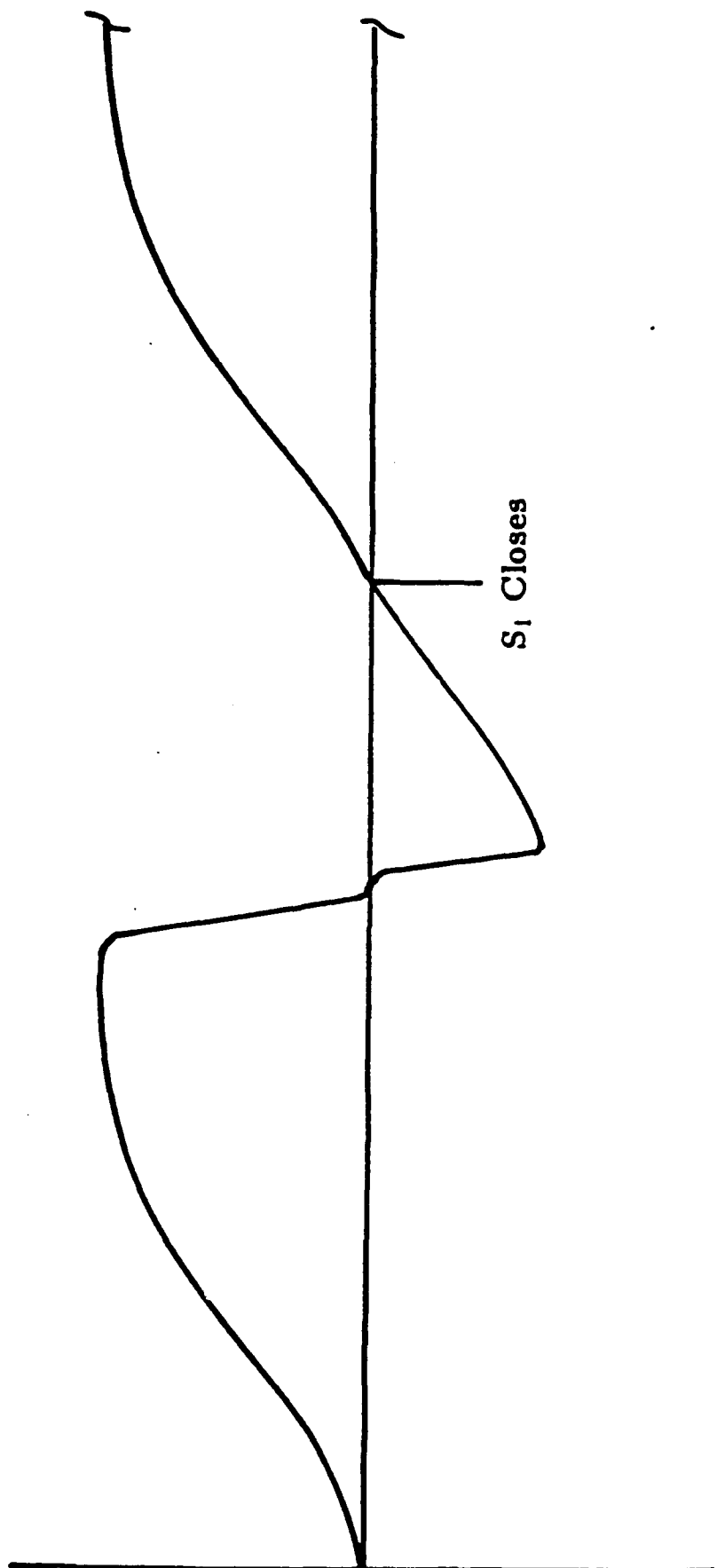


Figure 7.9: Properly Timed Energy Recovery Circuit with Zero Feedback

## APPENDIX 8

### THE SNOMAD SCR TRIGGER SYSTEM

The performance of the main commutator SCRs influences the design of the entire SSLAM modulator. In order for SCRs to function properly they must be provided with adequate trigger signals at the proper times. Indeed SCRs will fail if improperly triggered and experience has proven that any SCR failure in a SSLAM modulator can always be directly linked to a failure in the SCR trigger circuit. This understanding has resulted in an almost complete elimination of SCR failures. Providing proper SCR triggers at the correct times is the responsibility of the SSLAM SCR Driver in conjunction with the TRIGGER-I trigger circuit.

We will begin our discussion of the SNOMAD SCR trigger system with a description of the TRIGGER-I trigger circuit. A detailed schematic of this circuit can be found in Fig. 8.1. A section of the printed circuit board containing this circuit can be found in the SNOMAD modulator. This circuit assures that under almost all conditions the SCRs will receive sufficient trigger signal to turn on the entire junction. A partial trigger will only turn on some fraction of the junction resulting in almost certain device failure if the area turned on is smaller than required for the  $dI/dt$  to which the device is subjected.

The TRIGGER-I trigger circuit contains a trigger transformer which receives its input from two sources. The primary trigger source is the SNOMAD SCR Driver and this drives a 30 turn winding of the trigger transformer through a  $100 \Omega$  current limiting resistor. The SNOMAD SCR Driver also supplies a reverse bias to reset the transformer in between trigger pulses. A second winding on the trigger transformer is fed from energy stored in the  $0.1 \mu\text{fd}$ . snubber capacitor. This winding performs a regenerative function in that as the SCR begins to conduct, energy is fed into the gate via the auxiliary 60 turn winding. The more the SCR conducts, the more energy is fed into the gate until the SCR is fully turned on. The voltage appearing on this auxiliary winding also induces a voltage on the 30 turn winding used by the primary trigger source. This signal is transmitted to all of the main commutation SCRs, so as one SCR turns on all of the other SCRs are guaranteed to be turned on to share the load.

In summary the TRIGGER-I trigger circuit is the SCRs final line of defense against destructive partial triggers. TRIGGER-I's responsibility is to see that should an SCR begin to conduct, the SCR is turned on fully and all of the other SCRs are also turned on to share the load. It also performs the less challenging role of feeding charge through the SCR anode during the turn on phase and reducing  $dV/dt$  transients, as well as delivering the output of the SNOMAD SCR Driver to the SCR gate after transforming the impedance from  $\sim 100$  ohms to  $\sim 10$  ohms.

A picture of the SNOMAD SCR Driver appears in Fig. 8.2. The SNOMAD SCR Driver is housed in a 3 inch high by 15 inch deep standard rack mount chassis. It is a complete self contained unit including control logic, pulse amplifiers and power supplies. The SNOMAD SCR Driver requires only a single TTL level trigger pulse, 115 VAC, and voltage divider inputs to function. The voltage divider inputs allow the Driver chassis to monitor the voltage on the SNOMAD modulator power supply and Intermediate Storage capacitors. The SNOMAD SCR Driver

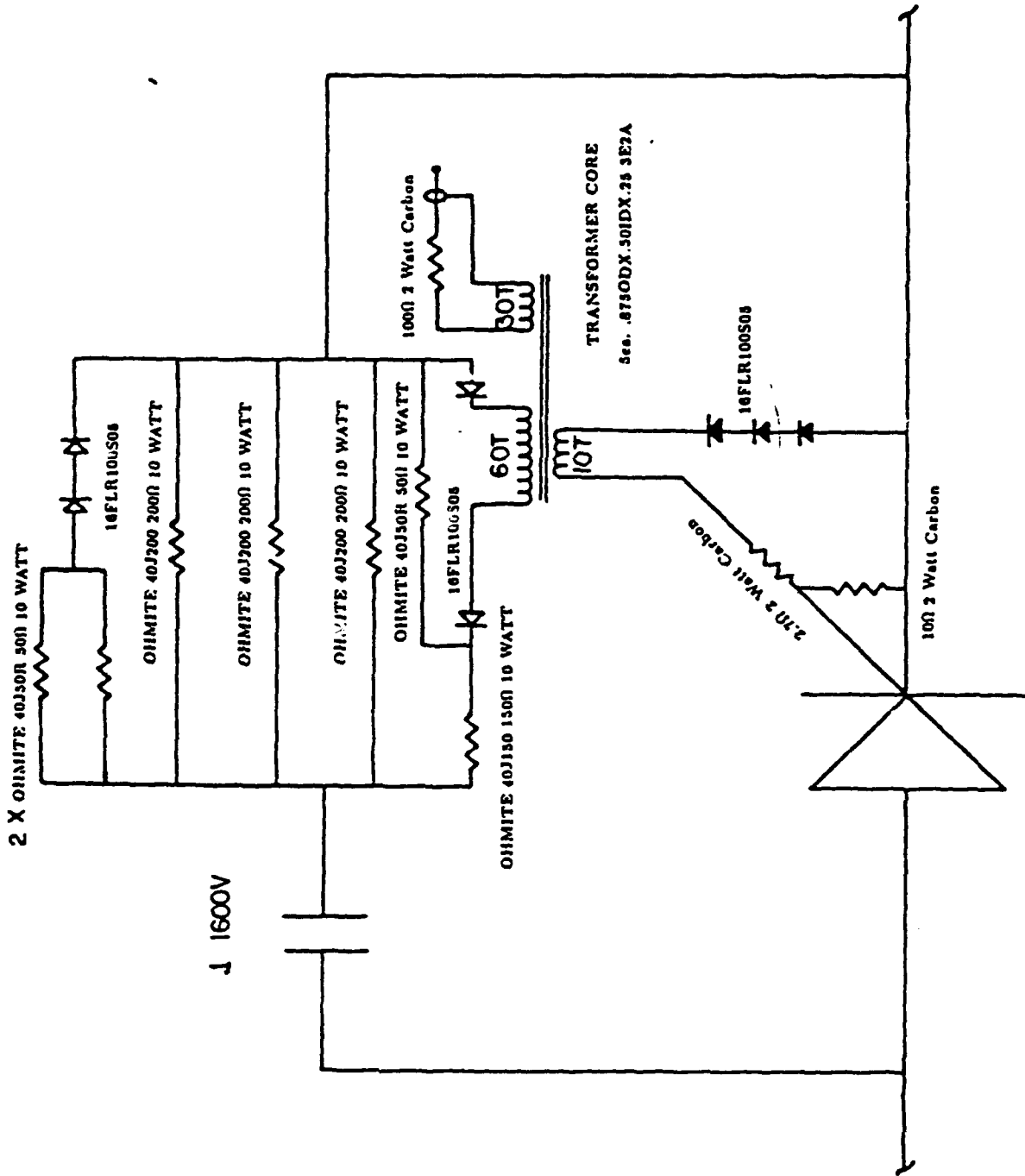
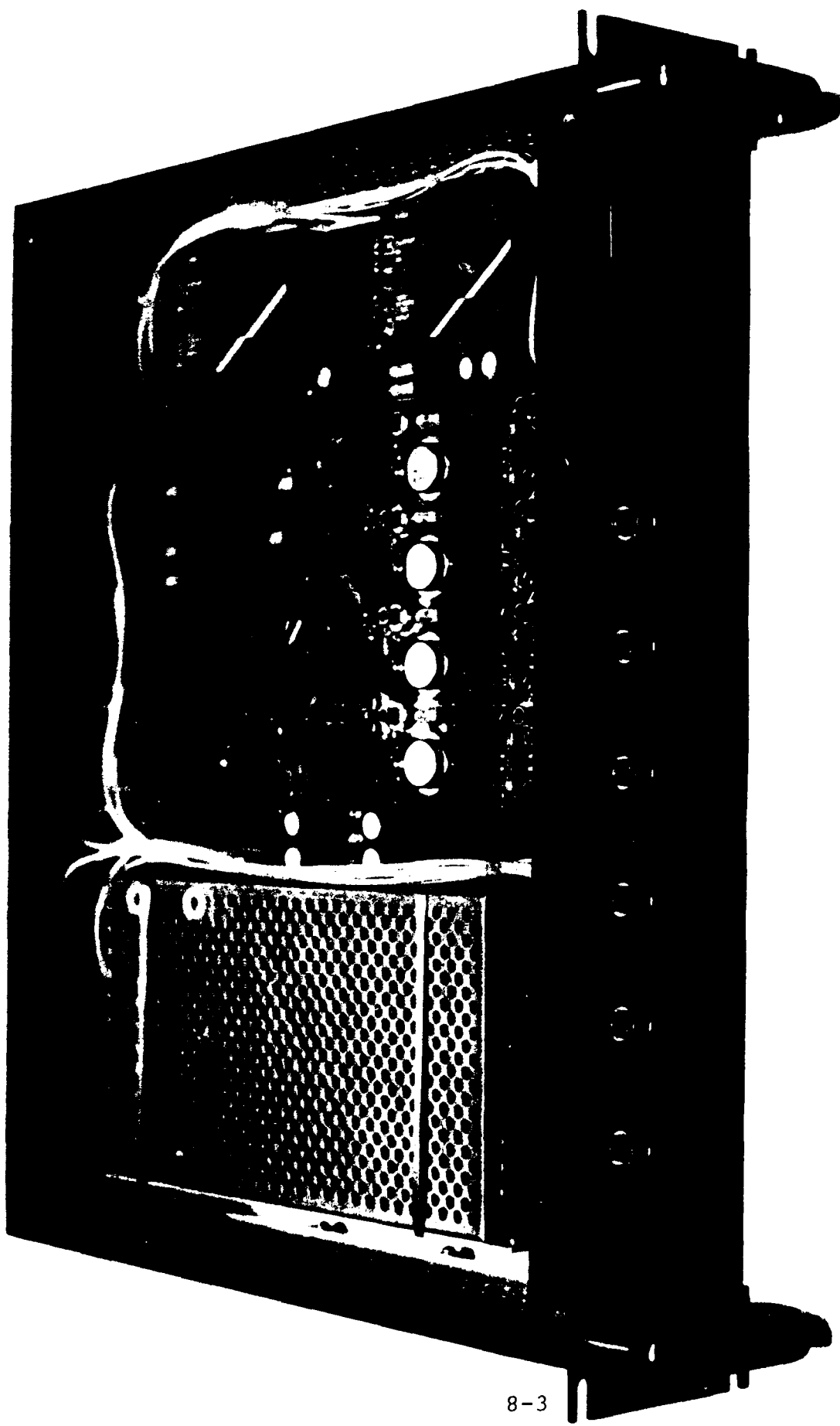


Figure 8.1: TRIGGER-I Snubber Board

SCIENCE RESEARCH LABORATORY

Figure 8.2



also accepts input from several photodiodes mounted at strategic locations inside the modulator enclosure. The SNOMAD SCR Driver will disable the modulator should the photodiodes indicate an arc, in the case of an overvoltage or undervoltage condition of the Intermediate Storage capacitors, or in the case of insufficient power supply voltage to assure proper functioning of the TRIGGER-I snubber boards. The SNOMAD SCR Driver logic circuit also determines the timing between the Command Resonant Charge (CRC) pulse and the triggering of the main commutator SCRs. It also assures that false input trigger signals to the chassis are ignored by locking out the TTL input trigger for a period of 220  $\mu$ secs after receiving each trigger input.

A simplified schematic of the SNOMAD SCR Driver logic circuits appears in Fig. 8.3. Referring to this schematic, sensoring inputs are carefully filtered and compared against adjustable references by high speed NE522 comparators. In case the photodiodes detect an arc or an overvoltage condition is sensed the driver is disabled for 0.1 seconds to allow breakdown products to disassociate. A series of five 74121's generate the timing sequence, and a set of three buffers provide information to the operating system regarding the modulator status. The SNOMAD SCR logic circuit provides two inputs to the output circuit. These two outputs are the properly timed trigger signals at TTL levels which control the CRC and Main SCR triggering. Referring to Fig. 8.4 which shows a simplified schematic of the SNOMAD SCR Driver output circuit, the output trigger signals from the logic circuit are buffered via 75452 peripheral line drivers. The outputs of the 75452's drive IRF-460 MOSFETS which generate the 150 VDC trigger signals via 1:2 isolation transformers. The IRF-460 MOSFETs are protected from transients by a saturable isolation inductor and a diode clipper circuit. A bias circuit is also tied to each MOSFET output to assure that the trigger transformers on the TRIGGER-I snubber board are properly reset between pulses.

Finally in Table 8.1 we provide a parts list for the SNOMAD SCR Driver chassis. Negatives for the printed circuit board, SRL-2650, on which all of the component mount are kept on file at SJS and made available to the DARPA for reproduction. Silkscreened instructions found on this printed circuit board make assembly straightforward. Silkscreened front and rear panels for the SNOMAD SCR Driver can also be purchased from this vendor.

In summary, The SNOMAD SCR Driver chassis in conjunction with the TRIGGER-I trigger circuit performs an invaluable role in the overall SNOMAD modulator system. They monitor the modulator status and control its functioning. They assure both the survival of the modulator and the SCRs.

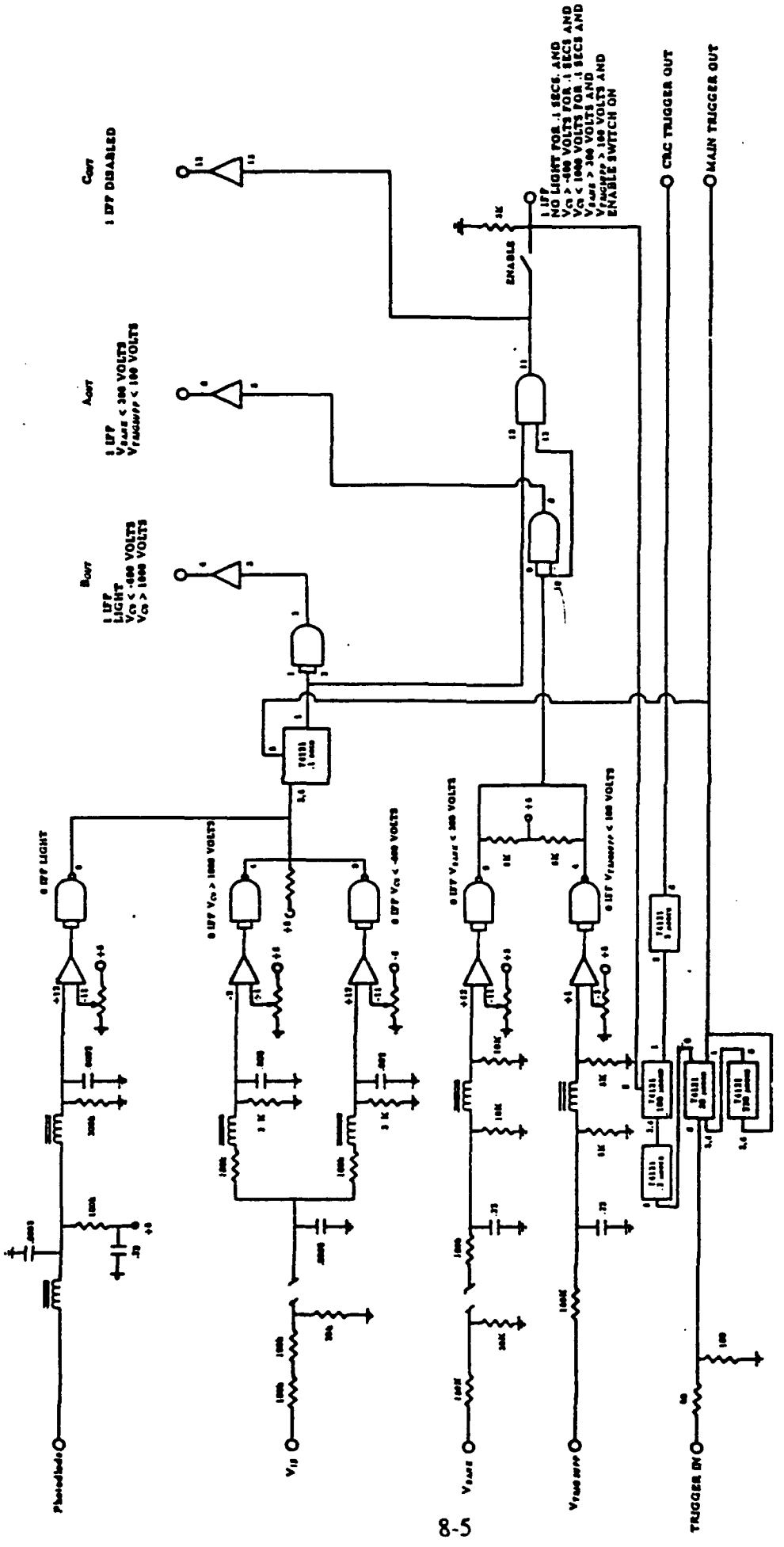


**Figure 8.3:** SSLAM SCR Driver Logic Circuit

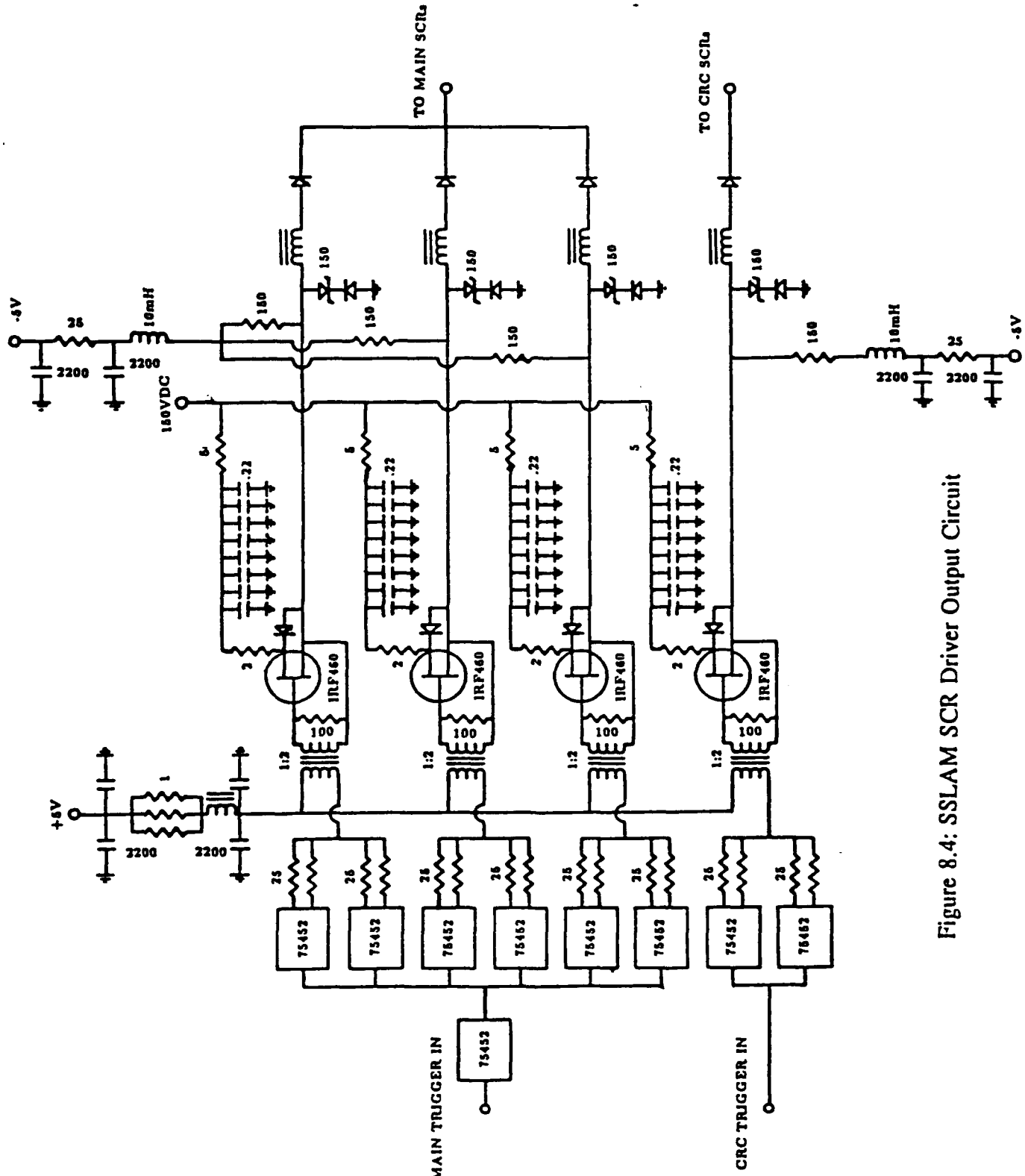


Figure 8.4: SSLAM SCR Driver Output Circuit

**TABLE 8-1: SSLAM SCR DRIVER COMPONENT LIST**

DESCRIPTION	VENDOR	QUANTITY
SRL-2650 PC BOARD	SJS	1 ea.
TECHMAR VCD-3H-13D-BF/H-BP-RFP-1:CBA.R-2:SC-3H-13D-B		1 ea.
FMP5-2K 5V,2A	KEPCO/TDK	2 ea.
NEW 44F1642 2200 $\mu$ fd,16V	MALLORY	7 ea.
NEW 59F316 50mH,65ma.	MILLER	4 ea.
NEW 15F2259 .5mH,2A.	MILLER	1 ea.
IR16FL100S05	IR	18 ea.
1N3015RB 200V Zener	MOTOROLA	32
IRF-460	IR	4
MKP-1845-.01,400V	RHOED.	8 ea.
MKP-1841 .22,160V	RHOED.	22 ea.
FKP-1 100pf,1600V	WIMA	1 ea.
FKP-1 680pf,1600V	WIMA	6 ea.
AUGAT 814-AG-10D	NEW 67F1801	10
AUGAT 808-AG-10D	NEW 67F1800	9
NEW 46F1439 SWITCH	2600H11E ARROW HART	1 ea
NEW 46F1858 SWITCH	2600HR11E ARROW HART	1 ea.
SN75452	TI	9
SN74121	TI	4
NE522	SIGNETICS	3
SN7408	TI	1
SN7404	TI	1

25Ω 1/2w CC	Allen-Bradley	16
50Ω 1/2w CC	Allen-Bradley	1
100Ω 1/2w CC	Allen-Bradley	6
200Ω 1/2w CC	Allen-Bradley	1
500Ω 1/2w CC	Allen-Bradley	1
3kΩ 1/2w CC	Allen-Bradley	2
5kΩ 1/2w CC	Allen-Bradley	5
6kΩ 1/2w CC	Allen-Bradley	1
10kΩ 1/2w CC	Allen-Bradley	3
30kΩ 1/2w CC	Allen-Bradley	1
40kΩ 1/2w CC	Allen-Bradley	1
100kΩ 1/2w CC	Allen-Bradley	2
150kΩ 1/2w CC	Allen-Bradley	1
200kΩ 1/2w CC	Allen-Bradley	1
1 MEGΩ 1/2w CC	Allen-Bradley	1
1Ω 3.25W	OHMITE 13F145	3
2Ω 3.25W	OHMITE 13F145	4
5Ω 3.25W	OHMITE 13F145	4
25Ω 3.25W	OHMITE 13F145	1
75Ω 3.25W	OHMITE 13F145	1
20kΩ 1/2w	NEWARK 81F1153 AB	5
.875ODX.5IDX.25 3E2A	846XT250 FERROXCUBE	4
.500ODX.375IDX.25 3E2A	768XT188 FERROXCUBE	4
.375ODX.187IDX.125 3E2A	266CT125 FERROXCUBE	4
RED # 24 AWG 600V TFE BELDEN		25ft
BLK # 24 AWG 600V TFE BELDEN		15ft
WHT # 24 AWG 600V TFE BELDEN		25ft

## APPENDIX 9

### INDUCTION CELL DESIGN

Both RF and induction linear accelerators are composed of multiple transmission line transformers. While these transmission lines are all driven in parallel as the electron beam passes through them, their voltages add energy to the electron beam in series. Isolation between the transmission lines is achieved by connecting them with a beam pipe which is below cutoff at the operating frequency for all modes except the  $\text{TEM}_{00}$ . The electron beam forms the inner conductor for this mode. Early Soviet literature describes RF accelerators as air core induction linacs.

If the accelerator is to be efficient, the losses in the transmission line must be negligible in comparison to the energy coupled into the electron beam. In other words, the effective impedance of the transmission line  $Z_{\text{eff}}$  must be large compared to  $V_{\text{LINE}}/I_{\text{BEAM}}$ . For an RF accelerator, the characteristic line impedance  $Z_{\text{LINE}}$  may be low, less than 100 ohms, but it is resonant and therefore the effective impedance becomes  $Z_{\text{eff}} = Z_{\text{LINE}} \cdot Q_L/2\pi$  (lowest order mode) where  $Q_L$  is the loaded  $Q$  of the resonant cavity.

Resonant RF structures also have the advantage that they provide a voltage step up over the drive voltage by a factor.

$$V_{\text{acc}} = V_{\text{driver}} \cdot Q_L^*/2\pi$$

where:

$$Q_L^{*-1} = Q_u^{-1} + Q_e^{-1} + Q_{\text{beamloading}}^{-1}$$

The disadvantage of resonant structures is that a cavity (shorted  $\lambda/2$  transmission line) is never simply resonant with a single mode and the wake functions of the electron beam have Fourier components which feed energy into all available modes. Some of these modes are spatially antisymmetric and act to steer the electrons into the beam pipe wall. This sets an upper limit to the total charge which can be accelerated during an RF cavity decay time ( $\tau = Q_L/\omega$ ).

An induction cell is non-resonant and if designed properly stores neither the drive fields nor the wake fields. This dramatically increases the practical operating current but also places constraints on the minimum efficient operating current. If the induction accelerator cell used vacuum as a transmission line medium, the maximum impedance in practice would be less than a few hundred ohms. In operating induction linacs which provide short pulses ( $\sim 50$  ns), this line is filled with ferrimagnetic material (ferrite); for long pulses ( $50 \text{ nsec} \leq \tau_p \leq 1 \mu\text{sec}$ ) ferromagnetic materials (e.g. Si-Fe, Metglass, Superpermalloy) are employed. Most high frequency ferrites have dielectric constants of order  $\epsilon_r = 10$  and permeabilities of order  $\mu_r = 1000$ . With ferrite as a medium, the characteristic transmission line impedance is increased over the vacuum value by a factor of  $(\mu_r/\epsilon_r)^{1/2} = 10$ , yielding effective shunt impedances as high as several thousand ohms. Also the use of ferrite shortens the length of the transmission line required to provide isolation at the desired drive pulse length. Since the group velocity,  $v_g = c/(\mu_r \epsilon_r)^{1/2} \simeq c/100$ , the transmission line is shorter than the vacuum equivalent by a factor of order 100. Some low

frequency RF accelerators employ ferrite solely for this purpose even though the line is resonant.

In summary the use of ferrite in the accelerator cell increases the practical micropulse length by a factor of 100 and the use of a non-resonant structure (induction linac) increases the maximum electron beam current by not storing wake fields. The penalty accompanying these advantages is centered on the fact that induction accelerators are incapable of efficiently accelerating very low current beams.

Design of an induction accelerator cell is relatively straightforward if these basic operating principles are kept in mind. The following rules must be observed. The variables discussed refer to those pictured in Fig. 9.1.

I. The length ( $h$ ) of the ferrite loaded transmission line is determined by the pulse length and the electrical characteristics of the ferrite.

$$2 \cdot h \geq \tau_p (\text{pulse length}) \cdot \text{velocity}$$
$$= \tau_p \cdot \frac{c}{\sqrt{\epsilon_r / \mu_r}} \approx \frac{\tau_p \cdot c}{100}$$

In practice, the best performance is achieved by setting  $h = \tau_p \cdot c/100$  or in other words setting the line length equal to a single transit time rather than a round trip time. This constraint arises because the ferrite properties are field dependent and the minimum ferrite volume is achieved by designing around a single transit time. Making  $h$  longer than a transit time is wasteful as the additional ferrite will never be seen by the pulse. Summarizing, for optimum performance:

$$h \approx \frac{\tau_p \cdot c}{(\epsilon_r / u_r)^{1/2}} \approx \frac{\tau_p \cdot c}{100}$$

II. The value for  $(R_o - R_i) = \Delta R$  is set by the drive voltage and the maximum flux swing of the ferrite. As the wave generated by the drive pulse is transmitted down the line, the creation of a saturation wave must be avoided or the impedance of the line will appear time dependent.

$$\text{Since : } \int E \cdot dl = - \frac{d}{dt} \int B \cdot da$$

if one assumes  $\mu$  is constant and  $B = \mu H$

then

$$B \leq B_{sat}.$$

Two extreme cases may be considered:

A) If  $B(r) = \text{const}$ , then

$$\text{Voltage} \leq \Delta B_s \cdot \Delta R \cdot v_g$$

B) If  $B(r) \propto 1/r$  and if no portion of the line is allowed to saturate

$$B(R_i) \leq B_{sat}$$

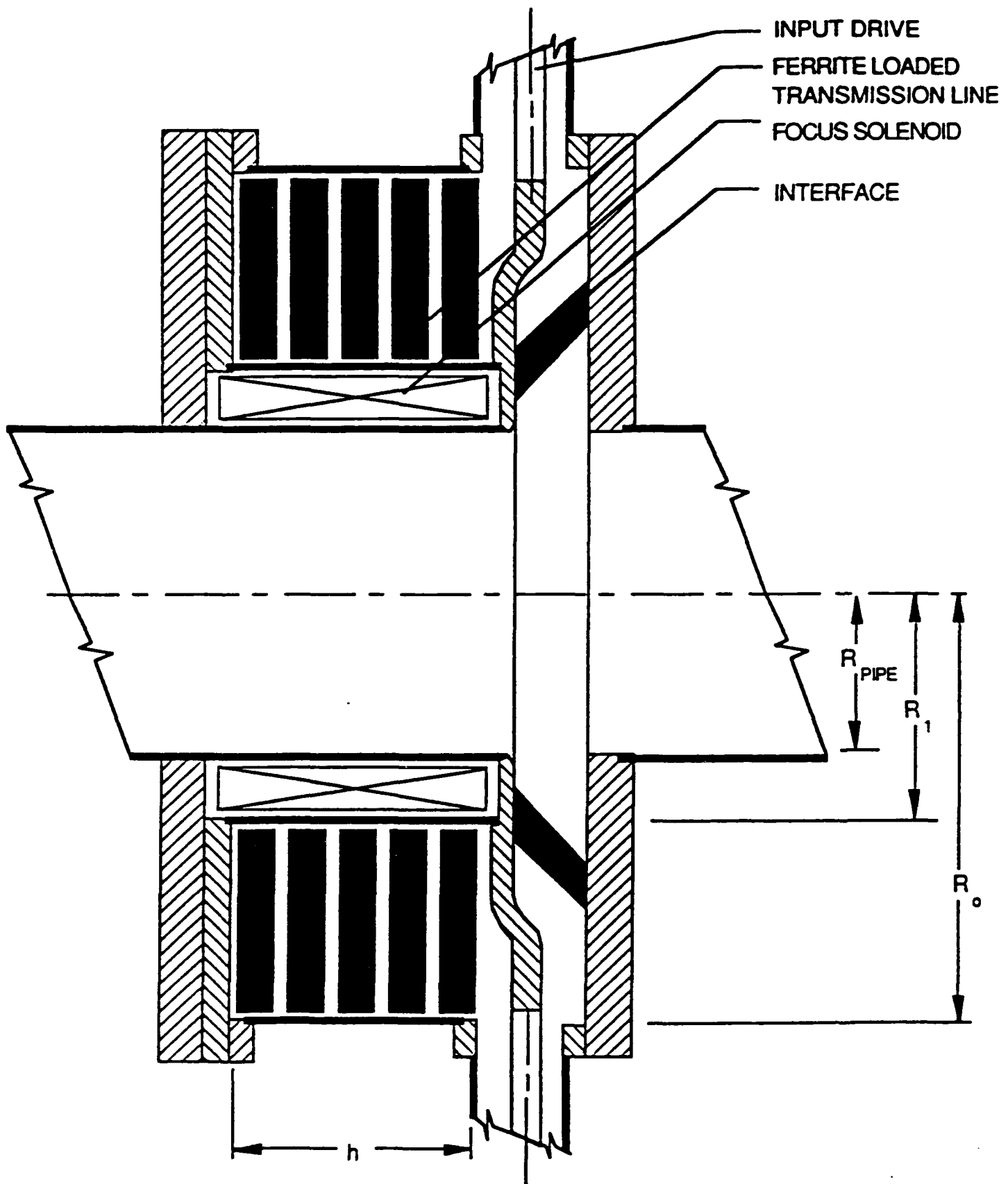


Figure 9.1: Simplified cross section of an induction accelerator cell

and

$$\text{Voltage} \leq \Delta B_s \cdot v_g \cdot R_i \cdot \ln(R_o/R_i)$$

In practice  $\mu$  is not a constant and is dependent on both  $dB/dt$  and  $H$ . This causes the real requirement to lie somewhere in between cases (A) and (B) so that  $B(r)\alpha r^{-\alpha}$ ,  $0 \leq \alpha \leq 1$ .

### III. Beam Pipe Radius - $R_{PIPE}$

Three competing requirements determine the optimum value for  $R_{PIPE}$ :

- (A) The growth of the beam break-up instability (BBI) is exponentially dependent on  $R_{PIPE}^{-2}$ . (i.e.  $A = A_0 \exp(I_{BEAM} \cdot V_{acc} \cdot \text{Const.}/B_{kg} R_{PIPE}^2 \cdot E_{gap})$ )
- (B) The impedance of the ferrite loaded transmission line decreases approximately linearly with  $R_{PIPE}^{-1}$ .
- (C) The weight of the accelerator increases as the square of  $R_{PIPE}$ .

In short the losses are increasing with  $R_{PIPE}$  linearly while the growth of BBI is decreasing exponentially as  $R_{PIPE}^2$ . It is essential in these designs to fully understand the dependence of the growth rate of the BBI on pipe diameter. In past designs, the pipe diameter has been undersized and has resulted in designs which were not compatible with full current operation. This applies to both RF and induction linear accelerators.

#### 9.1 Operating Voltage and Gradient

It has been shown above that the length of the accelerator is set by the choice of core material and pulse length. In addition the beam pipe radius is determined primarily by BBI considerations. It was also shown that the value of  $\ln R_o/R_i$  was determined by the core material and the individual gap drive voltage. Indeed once the drive voltage, current and pulse length are selected, then limiting values for the accelerator cell are uniquely determined.

The operating current, total accelerator voltage and pulse length are set by the application. This leaves the individual gap voltage the only unspecified parameter. We have shown above that the accelerator gradient is linearly proportional to the individual gap voltage. What we will show below is that while the coupling coefficient (the fraction of energy deposited in the beam versus the energy lost in the accelerator cores) is independent of gradient, the accelerator weight and cost becomes exponentially dependent on the gradient in the limit of large gradients. We will also show that for constant BBI gain, accelerator weight and cost in the limit becomes exponentially dependent on  $\sqrt{I_{beam}}$ .

The equivalent circuit for an induction linac is the same as that for all transformers.

One must bear in mind that while the number of secondary turns  $N_{sec}$  is unity, the number of primary turns is fractional given by

$$N_{prim} = \frac{1}{\# Acc\ cells}$$

$$Z_{out} = \frac{V_{acc}}{I_{beam}}$$

while  $Z_{in}$  the input drive impedance to the individual cells is given by

$$Z_{in} = \frac{V_{gap}}{I_{percell}}$$

The shunt impedance to ground is determined by the accelerator cell geometry and choice of core material. It is given by

$$Z_{shunt} = \frac{1}{2\pi} \sqrt{\frac{\mu}{\epsilon}} \ln R_o / R_i$$

Under the assumption that no ferrite is allowed to exceed a flux swing of  $\Delta B_s$ , and  $B(r) \propto 1/r$ , we saw that the accelerator gap voltage was given by

$$V_{gap} = \Delta B_s \cdot v_g \cdot R_i \ln R_o / R_i$$

where  $v_g = c/(\epsilon_r \mu_r)^{1/2}$  is the wave velocity in the ferrite,  $R_i(R_o)$  the inner (outer) radius of the ferrite core. The accelerator shunt impedance is then simply determined by the characteristic impedance of this ferrite loaded transmission line

$$\begin{aligned} Z_{SHUNT} &= Z_{LINE} = \frac{1}{2\pi} \sqrt{\frac{\mu}{\epsilon}} \ln \left( \frac{R_o}{R_i} \right) = \frac{1}{2\pi} \sqrt{\frac{\mu}{\epsilon}} \frac{V_{gap}}{v_g \cdot \Delta B_s \cdot R_i} \\ &= \frac{1}{2\pi} \mu \cdot \frac{V_{gap}}{\Delta B_s \cdot R_i} \end{aligned}$$

If the electron beam impedance is defined as

$$Z_{beam} = \frac{V_{gap}}{I_{BEAM}}$$

then the coupling coefficient (= energy coupled to the beam/the total energy incident on the accelerator cell) is given by

$$K = \frac{Z_{SHUNT}}{Z_{BEAM} + Z_{SHUNT}} = \frac{1}{\frac{2\pi \Delta B_s R_i}{\mu I_{BEAM}} + 1}$$

A plot of coupling coefficient versus ferrite core inner radius for several different beam currents appears in Fig. 9.2. Here we have assumed a ferrite with a  $\mu_r = 400$  and  $\epsilon_r = 12$ .

It should be noted that the coupling coefficient is independent of accelerator gradient but increases with increasing current and decreasing ferrite core inner radius.

The cost and weight of the accelerator structure is to first order linearly dependent on the core column.

$$\text{Core Volume} = \# \text{cells} \cdot \text{cell core length} \cdot \pi(R_o^2 - R_i^2) \quad (9.1)$$

and

$$V_{gap} = \frac{V_{acc}}{\# \text{cells}} = \Delta B_s \cdot v_g \cdot R_i \ln(R_o/R_i) \quad (9.2)$$

if  $B \propto 1/r$  and no ferrite is allowed to exceed a flux excursion of  $\Delta B_s$ . We can then rewrite Eq. (1) as

$$\text{Core Volume} = \frac{V_{acc}}{V_{gap}} \cdot v_g \cdot \tau_{pulse} \cdot \pi R_i^2 \exp\left(\frac{V_{gap} \cdot 2}{\Delta B_s \cdot v_g \cdot R_i}\right)^{-1} \quad (9.3)$$

where  $\tau_{pulse}$  is the pulse length. It should be noted that the minimum core volume (d core volume/d  $V_{gap} = 0$ ) is always achieved when  $V_{gap} = 0$ . Also for  $2 \cdot V_{gap}/\Delta B_s \cdot v_g \cdot R_i \ll 1$ , core volume is approximately independent of  $V_{gap}$  while for

$$\frac{2V_{gap}}{\Delta B_s \cdot v_g \cdot R_i} \gg 1$$

core volume becomes exponentially dependent on  $V_{gap}$ .

This becomes obvious upon careful examination of Fig. 9.3. Here we have assumed  $\mu_r = 400$ ,  $\epsilon_r = 12$ , and  $\tau_{pulse} = 50$  nsec. Referring to Eq. (3), it also appears that core volume is linearly dependent on  $\tau_{pulse}$ . The dependency on  $v_g = c/(\mu_r \cdot \epsilon_r)^{1/2}$  is somewhat more subtle. For small values of  $V_{gap}/R_i$  the core volume varies as  $1/\mu_r^{1/2}$  but as  $V_{gap}/R_i$  becomes large, core volume becomes exponentially dependent on  $\mu_r^{1/2}$ .

It is also obvious from Fig. 9.3 that the inner ferrite core radius dramatically impacts the accelerator weight at a given gradient. Referring to Fig. 9.2 the efficiency degrades rapidly as the ferrite inner radius is increased. This inner radius is determined primarily by the beam pipe radius and the thickness of the focusing solenoid. Arbitrary reduction of these parameters independently of the current will result in the onset of the Beam Break-up Instability which will drive the accelerator beam current into the walls.

The amplitude of the BBI oscillation throughout the accelerator is given by:

$$A = A_0 \exp\left(\frac{\text{const.} NIZ_\perp \omega}{B_{kg}}\right)$$

where

$$K = 1.16 \cdot 10^{-13} \text{ kg} \cdot \text{sec}/(\text{kamp} \cdot \text{ohm})$$

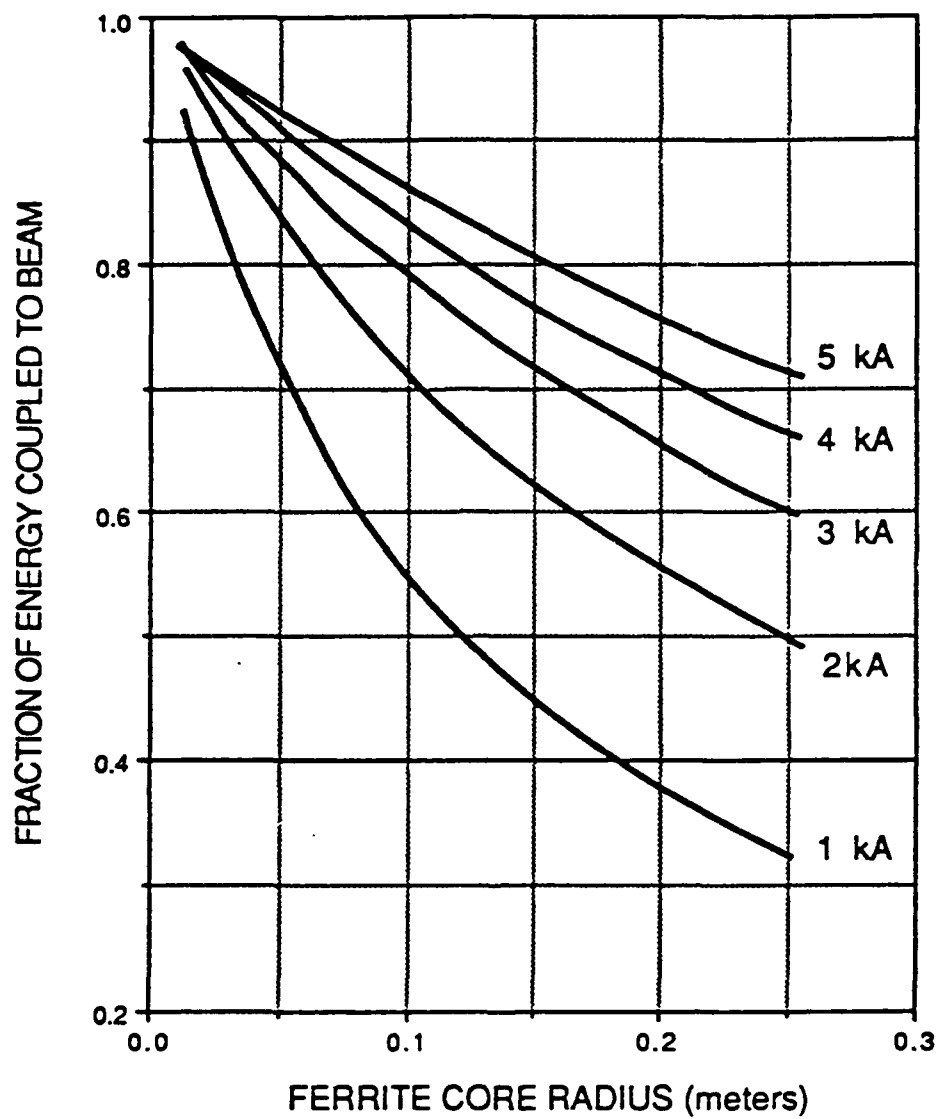


Figure 9.2: Coupling coefficient:

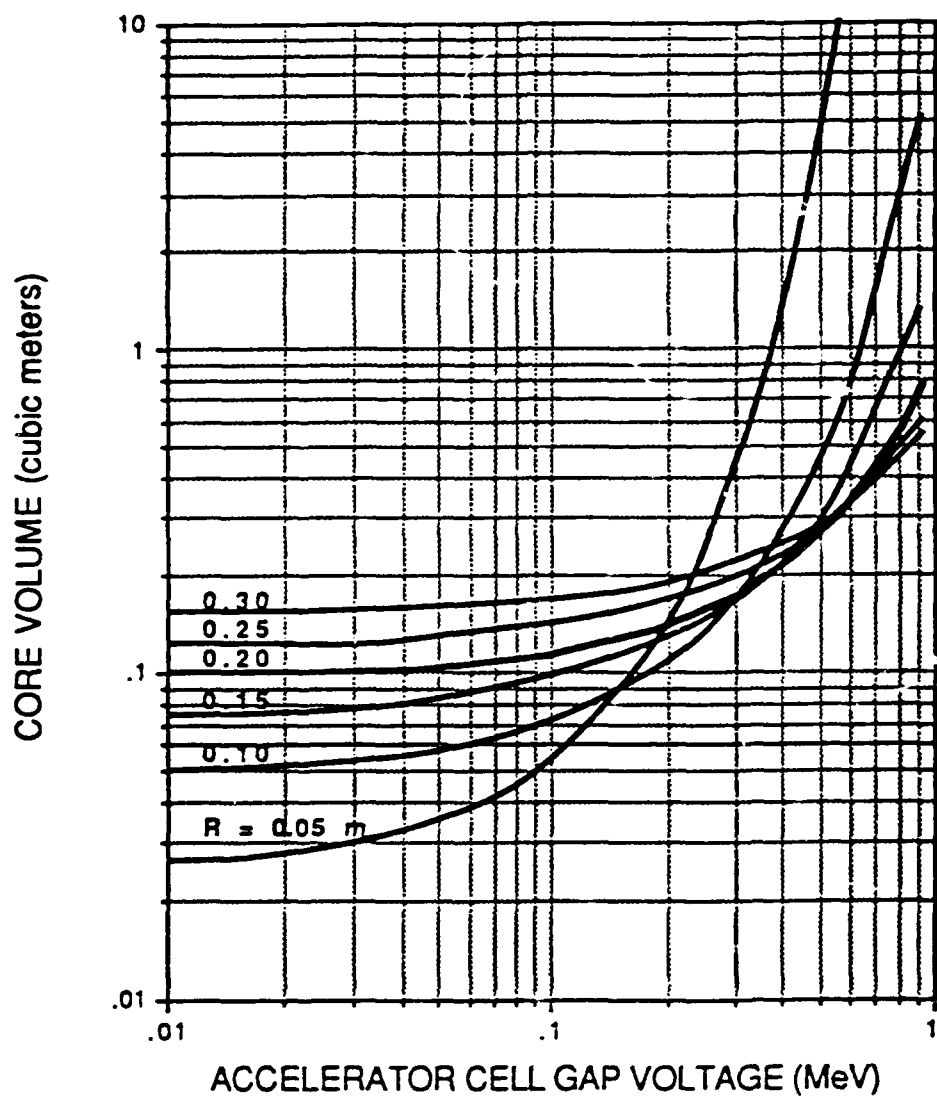


Figure 9.3 : Accelerator core volume per megavolt

AD-A256 779 FERRITE RESEARCH AIMED AT IMPROVING INDUCTION LINAC  
DRIVEN FEL PERFORMANCE PHASE 2(U) SCIENCE RESEARCH LAB  
INC SOMERVILLE MA D BIRX 15 OCT 92 SRL-13-F-1992

4/24

UNCLASSIFIED XB-DNR N00014-90-C-0165

NL

END  
FILMED  
DTIC

N = Number of accelerator gaps

$\omega$  = Mode frequency

I = Accelerator current

$B_{kg}$  = Focusing field

Substituting

$$NZ_{\perp} = N(Z_{\perp}/Q) \cdot Q = \frac{\text{const.}_1 \cdot Q \cdot V_{acc}}{E_{gap} \cdot R_{pipe}}$$

where

$V_{acc}$  = Accelerator voltage

$E_{gap}$  = Accelerator gap electric field stress

$R_{pipe}$  = Beam pipe radius provides the following equation for the BBI amplitude.

$$A = A_0 \exp \left( \text{const.} \cdot \frac{I \cdot V_{acc}}{B_{kg} R_{pipe}^2 \cdot E_{gap}} \right)$$

Therefore, the BBI amplitude depends exponentially on the inverse of the accelerator gap stress and the beam pipe radius squared.

In order to minimize both the beam pipe radius and the solenoid thickness ( $B_z$ ) while holding BBI gain constant at a given current and accelerating potential, the accelerator gap stress must be increased to as high a value as practicable. Unfortunately at the high duty factors required for most of these applications, exceeding the threshold where field emission in the gap occurs is not allowed. Understanding this limit is essential to optimizing the design.

The core volume become exponentially dependant on the inverse of  $\Delta B_s$ . This makes things somewhat complicated as the individual gap voltages and beam pipe inner radius must be determined before the optimum material can be selected. At this point we will attempt to document the ferrite properties and the optimum choice will be left for the engineer responsible for a specific accelerator cell design.

## APPENDIX 10

### BEAM BREAK-UP INSTABILITY AND THE GAP FIELD

The amplitude of the BBI oscillation throughout the accelerator is given by:

$$A = A_0 \exp \left( \frac{\text{const.} N Z_{\perp} \omega}{B_{kg}} \right)$$

where

$K = 1.16 \cdot 10^{-13}$  kg - sec/(kamp-ohm)

$N$  = Number of accelerator gaps

$\omega$  = Mode frequency

$I$  = Accelerator current

$B_{kg}$  = Focusing field

Substituting

$$N Z_{\perp} = N(Z_{\perp}/Q) \cdot Q = \frac{\text{const.}_1 \cdot Q \cdot V_{acc}}{E_{gap} \cdot R_{pipe}}$$

where

$V_{acc}$  = Accelerator voltage

$E_{gap}$  = Accelerator gap electric field stress

$R_{pipe}$  = Beam pipe radius provides the following equation for the BBI amplitude.

$$A = A_0 \exp \left( \text{const.} \cdot \frac{I \cdot V_{acc}}{B_{kg} R_{pipe}^2 \cdot E_{gap}} \right)$$

Therefore, the BBI amplitude depends exponentially on the inverse of the accelerator gap stress and the beam pipe radius squared.

In order to minimize both the beam pipe radius and the solenoid thickness ( $B_z$ ) while holding BBI gain constant at a given current and accelerating potential, the accelerator gap stress must be increased to as high a value as practicable. Unfortunately at the high duty factors required for most of these applications, exceeding the threshold where field emission in the gap occurs is not allowed. Understanding this limit is essential to optimizing the design.

An investigation of the limiting electric field stress as a function of various surface conditioning techniques has been undertaken. This study was aimed at both documenting maximum usable electric field levels as well as searching for new gap electrode processing techniques that

might extend these limits. The test stand which was employed to make the measurements is shown schematically in Fig. 10.1. This test stand consists primarily of a vacuum vessel equipped with high voltage feed through, movable anode and a diagnostic package capable of making sensitive temporal voltage, current and optical measurements. The normal operating base vacuum of  $1 \cdot 10^{-8}$  Torr insured that residual gas did not effect the experiments.

Electron emission from the surface under test was monitored by two techniques. A phosphor screen anode was monitored for light emission by a photomultiplier tube (PMT) and an open shutter Polaroid camera. In addition, a Rogowski current monitor measured the total cathode current. Optical emission from the phosphor anode foil was calibrated against the Rogowski current monitor. This technique allowed us to measure average emission currents as small as  $1 \text{ mA/cm}^2$ . The cathode test surface was fabricated from 304 stainless steel in the form of a "Chang" profile in order to minimize the effects of geometrical field enhancement on the measurements.

Various conditioning steps were performed on the test surfaces and the average field emission current densities were measured as a function of electric field stress and time. As a condition for determining the usable electric field stress levels, the surfaces were exposed to field stress levels at which full breakdown occurred; subsequently the field stress was reduced until a level was reached where zero measurable emission ( $< 1 \text{ ma/cm}^2$ ) was observed over an effective pulse length of approximately .5  $\mu\text{secs}$ .

The measured electric field as a function of surface conditioning are presented in Table 10-1. The date supports a composite of various theories for high voltage breakdown. The first two surface processing techniques were designed to differentiate between two widely proclaimed mechanisms for vacuum breakdown.

The first test surface was carefully prepared with special attention paid to eliminating dielectric occlusions. The 304 SS blank was dry machined to a  $\sqrt{125}$  (.000125)" RMS surface irregularities) surface finish.

No abrasives were used in connection with this process so as to eliminate dielectric occlusions as a breakdown mechanism. A  $\sqrt{125}$  surface is visibly rough and therefore if vacuum breakdown through whisker dominated field emission followed by whisker explosion is a valid process it should certainly be the primary breakdown mechanism for this surface.

For the second set of measurements the surface was carefully polished with abrasives including a final buffering with .2 micron levigated alumina. The resulting surface was a stunning mirror finish. No attempt was made to remove imbedded alumina powder other than washing and wiping the surface with kimwipes soaked in acetone.

The experimental results from these two tests would tend to indicate that both dielectric occlusions and whisker enhanced field emission are important considerations and neither can be neglected.

In the third processing technique the mechanically polished surface described above was electropolished. Sufficient material ( $\approx .5 \text{ mil}$ ) was removed to assure no abrasive residue

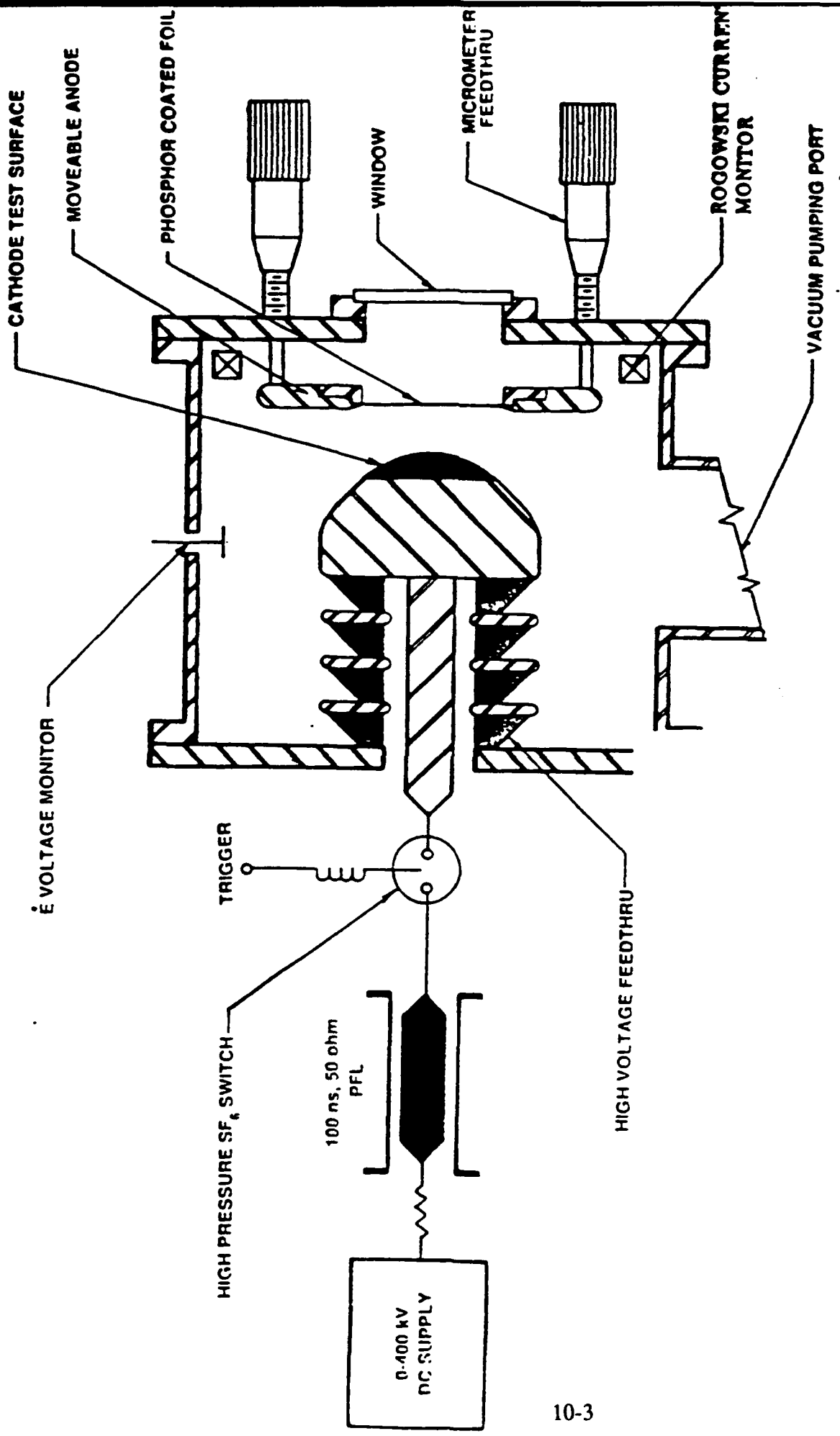


Figure 10.1: Simplified Schematic of High Voltage Cathode Test Stand

TABLE 10-1

# PRELIMINARY STUDIES STAINLESS FIELD EMISSION THRESHOLDS

- EXPERIMENTAL CONDITIONS

$< 1.10^{-7}$  TORR PRESSURE

NO BARIUM SOURCE PRESENT

CATHODE AT ROOM TEMPERATURE

CATHODE AREA ~ 100 cm<sup>2</sup>

- SURFACE CONDITION

$E_{MAX}^*$

$\sqrt[125]{ }$  MACHINED SURFACE                            75 kv/cm

MECHANICALLY POLISHED TO                            100 kv/cm  
MIRROR FINISH WITH .05  
MICRON ALUMINA GRIT

ELECTROPOLISHED                                    150 kv/cm

WET HYDROGEN FIRED 1 1/2 HRS.                    280 kv/cm  
(GREENED)

\* FIELD STRESS AT WHICH EMISSION BOTH REMAINS WELL BELOW  
.1 A/cm<sup>2</sup> OVER 100 ns AND REDUCED EMISSION WITH INCREASED  
SHOT NUMBER OCCURS.

remained. This surface probably corresponds to one of the best achievable uncoated surfaces and it would probably be impractical to rely upon reproducing it in large quantities. It should also be noted that electropolishing preferentially removes the steel atoms with respect to chromium. An electropolished stainless steel surface is primarily composed of chromium. This is important for the next processing step.

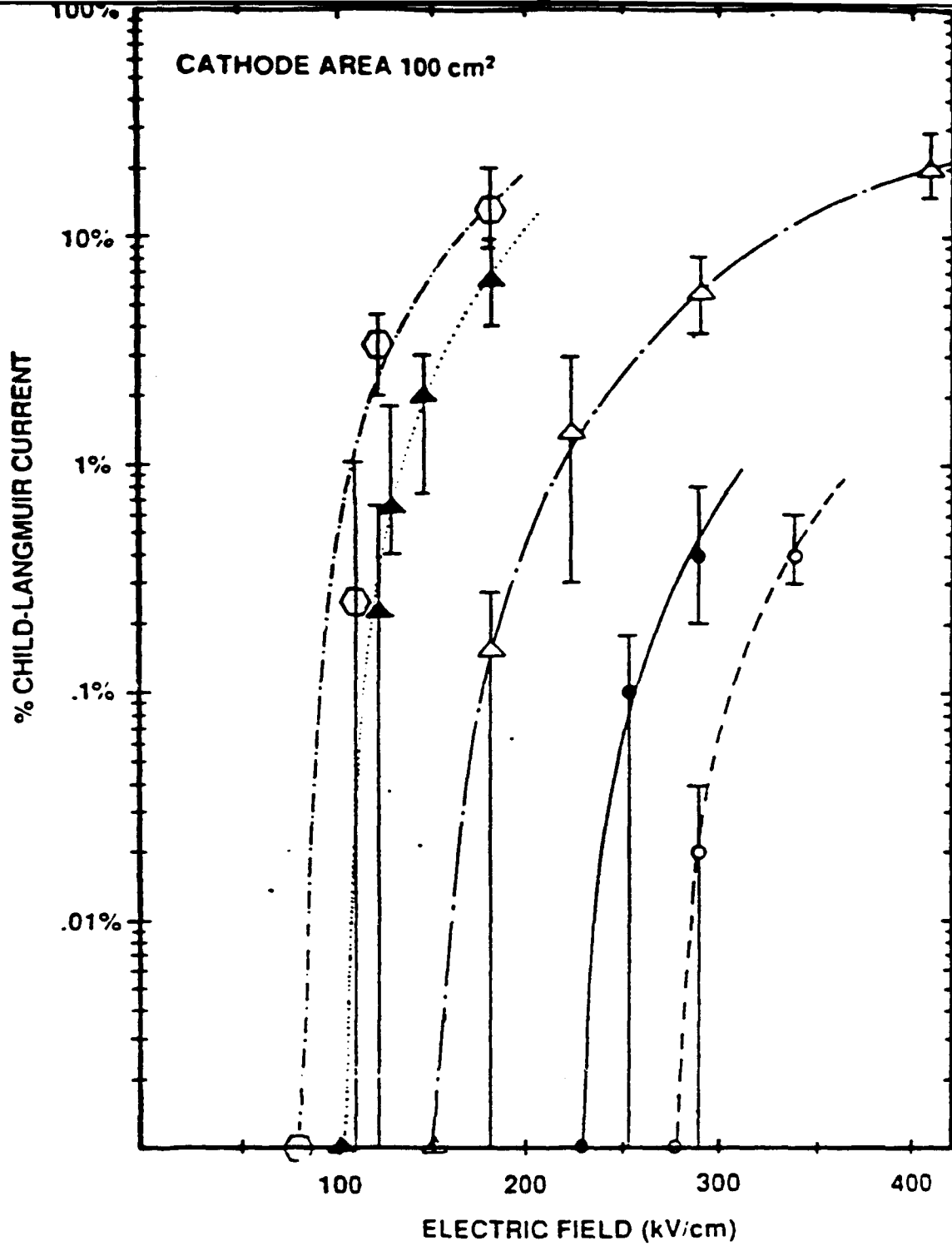
The fourth and final process was to heat the surface to 960° C for 1.5 hrs. in an atmosphere of H<sub>2</sub> saturated with water vapor. The effect of this procedure ("Greening") is to oxidize only the chromium which is the dominant constituent of the surface after electropolishing. The resulting surface of Cr<sub>2</sub>O<sub>3</sub> is a P type semiconductor with large amounts of oxygen vacancies. This high dielectric constant, partially conducting surface probably acts to minimize the net field enhancements of irregularities at the surface while actually reducing the average electric field at the stainless steel surface. The results appear analogous to that which has been measured for Al<sub>2</sub>O<sub>3</sub> coatings on aluminum vacuum surfaces.

Because the condition of < 1 mA/cm<sup>2</sup> emission is not the conventional criteria used to classify vacuum breakdown, we also provide curves of average emission current versus time in Figs. 10.2 through 10.5.

The results (Figs. 10.2-10.5) indicate that operation at electric field levels up to 300 kV/cm may be possible. Previous induction linacs have been designed around peak stresses of ~ 150 kV/cm which is probably reasonable since little surface conditioning was attempted. It was also found that simple mechanical polishing of a surface does not yield much benefit. Dielectric occlusions (imbedded polishing compound) which can lead to large electric field enhancements are probably responsible for this result. These enhancement factors can be just as significant and detrimental as the emission sites found on an unpolished surface.

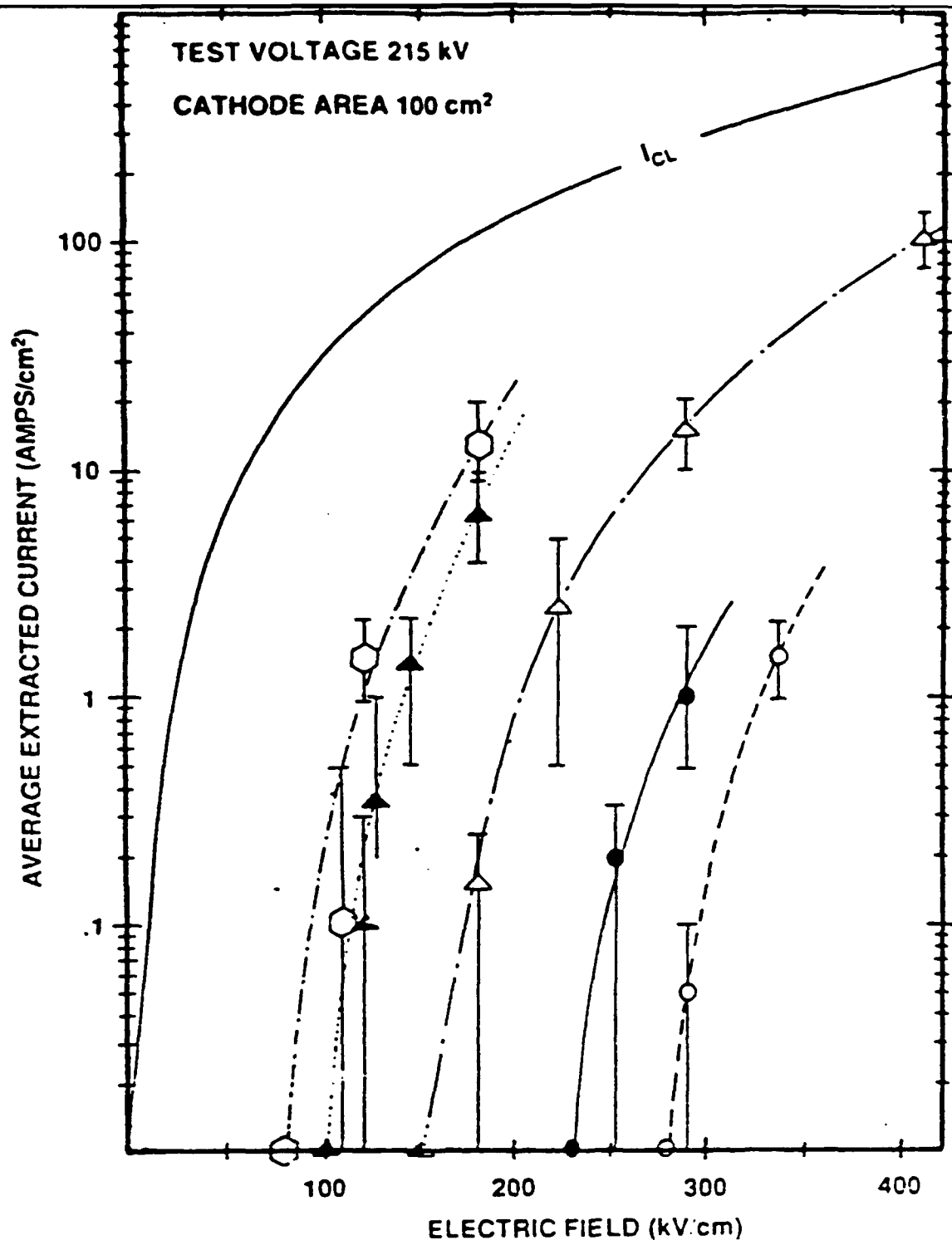
Electropolishing will remove most of these impurities and therefore helps considerably. Unfortunately electropolishing also exposes basic impurities found in the stainless steel such as carbon particles. A process known as "Greening" (firing an electropolished stainless steel surface in wet hydrogen for ~ 1 hour at 950°C) improves the situation considerably. Electropolishing etches away the iron atoms leaving a surface primarily composed on metallic chromium. The "Greening" process leaves the remaining iron in the metallic state but oxidizes this chromium surface forming O<sup>-</sup> doped Cr<sub>2</sub>O<sub>3</sub> and Cr<sup>+</sup> doped Cr<sub>2</sub>O<sub>3</sub>. The resulting high permittivity semiconducting coating tends to shield high permittivity occlusions eliminating the enhancement factor. As mentioned above the field stress achievable on these surfaces exceed 300 kV/cm with greening. Similar field stress levels have been achieved on anodized aluminum surfaces probably for similar reasons.

Care must be taken when employing coated surfaces. A breakdown involving an arc can reduce the surface breakdown field back to levels between 100 and 200 kV/cm. These coatings can be used to advantage if reasonable safety factors are employed and several vacuum tube manufacturers (e.g. EG&G, Varian) have actually marketed devices operating at ~ 200 kV/cm.

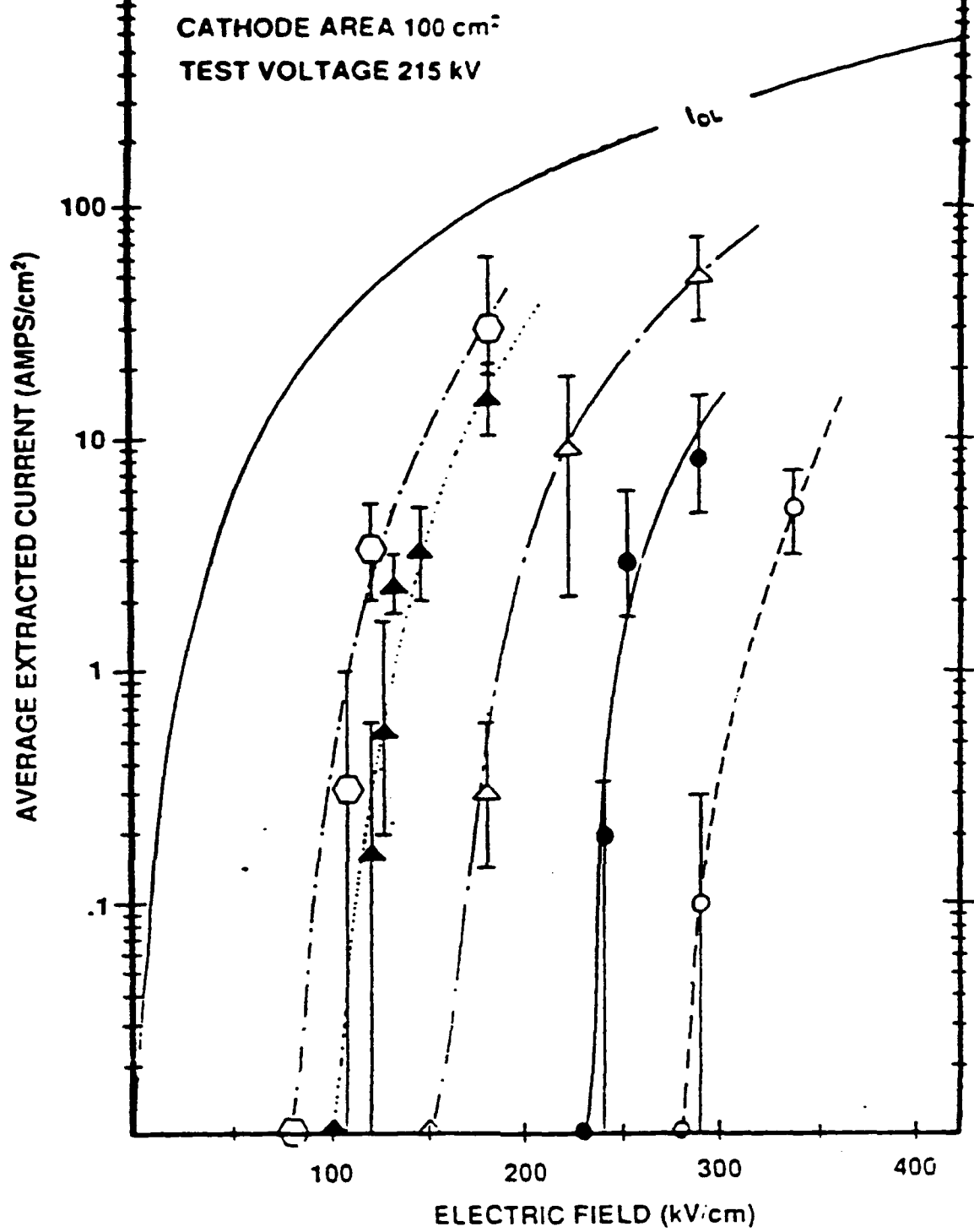


- - - ○ - - -  $\sqrt{125}$  FINISH
- - - ▲ - - - MIRROR FINISH
- - - △ - - - ELECTROPOLISHED
- - - ● - - - GREENED AND EXPOSED TO 1025°C DISPENSER CATHODE
- - - ○ - - - GREENED

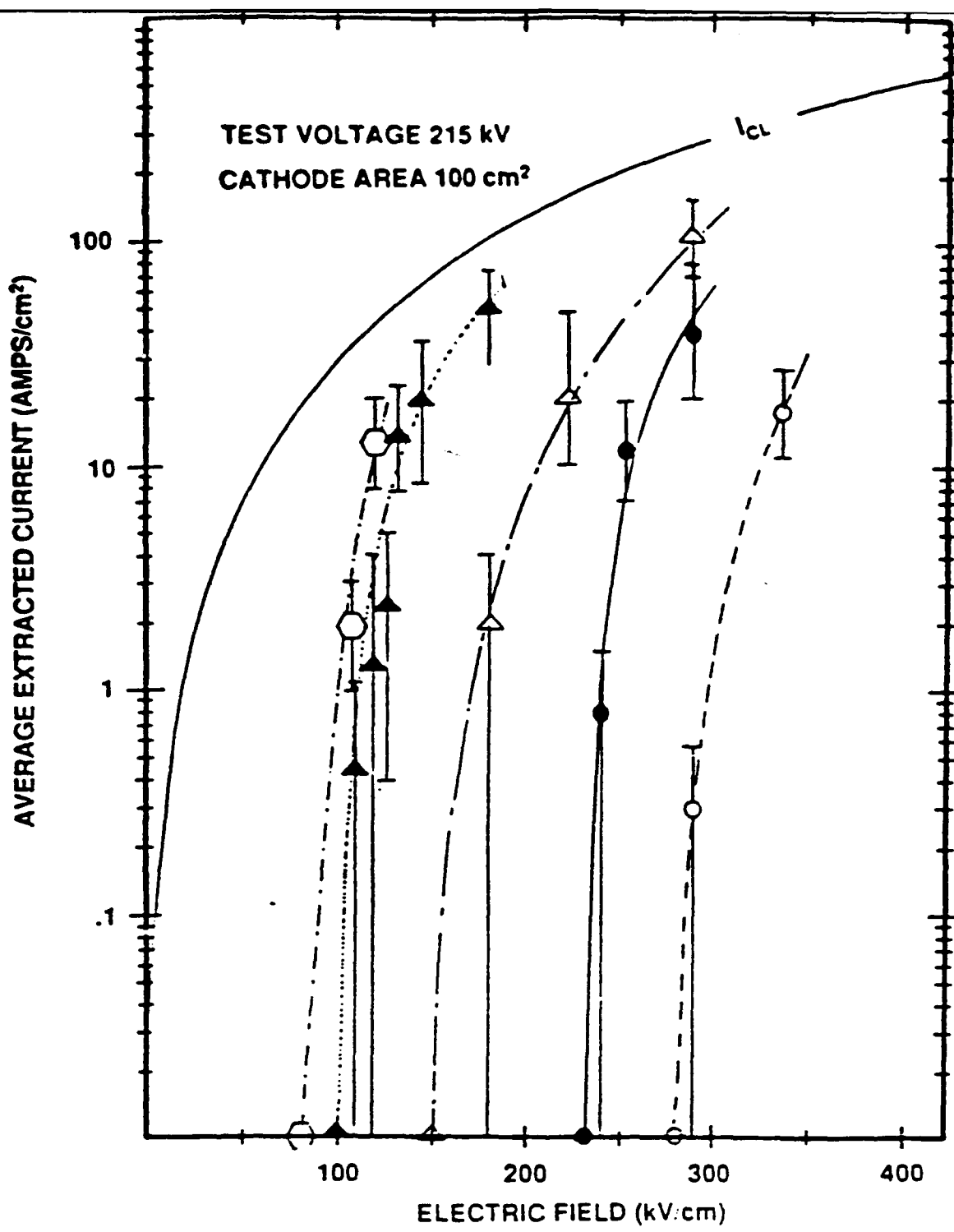
Figure 10.2: Percentage of Child-Langmuir current after 50 ns



- $\sqrt{125}$  FINISH
  - ▲--- MIRROR FINISH
  - △--- ELECTROPOLED
  - GREENED AND EXPOSED TO 1025°C DISPENSER CATHODE
  - GREENED
- Figure 10.3: Average extracted current density after 50 ns



- √125 FINISH
  - △— MIRROR FINISH
  - △— ELECTROPOOLISHED
  - GREENED AND EXPOSED TO 1025°C DISPENSER CATHODE
  - GREENED
- Figure 10.4: Average extracted current density after 100 ns



- $\sqrt{125}$  FINISH
- ▲--- MIRROR FINISH
- △--- ELECTROPOLISHED
- GREENED AND EXPOSED TO 1025°C DISPENSER CATHODE
- ◇--- GREENED

Figure 10.5: Average extracted current density after 200 ns